

8-2019

Understanding the Theory and Use of Resistive Welding Technology for Fiber-Reinforced Thermoplastic Composite Structures in Automotive Applications

Veera Aditya Choudary Yerra
Clemson University, vyerra@icloud.com

Follow this and additional works at: https://tigerprints.clemson.edu/all_dissertations

Recommended Citation

Yerra, Veera Aditya Choudary, "Understanding the Theory and Use of Resistive Welding Technology for Fiber-Reinforced Thermoplastic Composite Structures in Automotive Applications" (2019). *All Dissertations*. 2456.
https://tigerprints.clemson.edu/all_dissertations/2456

This Dissertation is brought to you for free and open access by the Dissertations at TigerPrints. It has been accepted for inclusion in All Dissertations by an authorized administrator of TigerPrints. For more information, please contact kokeefe@clemson.edu.

UNDERSTANDING THE THEORY AND USE OF RESISTIVE WELDING
TECHNOLOGY FOR FIBER-REINFORCED THERMOPLASTIC
COMPOSITE STRUCTURES IN AUTOMOTIVE APPLICATIONS

A Dissertation
Presented to
the Graduate School of
Clemson University

In Partial Fulfillment
of the Requirements for the Degree
Doctor of Philosophy
Automotive Engineering

by
Veera Aditya Choudary Yerra
August 2019

Accepted by:
Dr. Srikanth Pilla, Committee Chair
Dr. Paul Venhovens
Dr. Johnell Brooks
Dr. Gang Li
Dr. David Schmueser

ABSTRACT

Transportation accounts for 14% of global greenhouse gas emissions. With a projected rise in GDP for more than half of the global population, the demand for transportation is only going to increase sharply. It is essential to reduce the overall weight of the automobile and ensure that its constituent materials are being reused with the minimal energy consumption during treatment and conversion. This is especially critical for the heaviest components in an automobile – its structure and closures. In this regard, carbon fiber reinforced composites have high light-weighting potential for automotive structures. However, most OEMs use thermoset polymers as matrix material, which are not recyclable. This has led to a great push towards the use of thermoplastics as matrix material in the future. A key issue associated with this possibility is the need for an optimal joining mechanism – since while structural adhesives are the most common joining mechanism used at present, most of these adhesives are thermoset polymers themselves that are also expensive and have longer curing time. Additionally, when used with thermoplastic matrix materials, these adhesives bring forth the problem of compatibility.

The ability to be joined in fast, strong and repeatable methods is crucial for automotive structures, given that a typical body structure has between 150-400 individual parts, and their timely and strong joining is essential to ensure their applicability for mass production. In this context, the ability to be fusion bonded (or welded) is one of the key advantages of FRTPCs over thermoset composites. Welding thermoplastic reinforced composites can be segregated into three major categories: resistive implant welding (RIW), vibration welding, and electromagnetic welding.

Resistive implant welding is an attractive technology due to faster cycle times, lower cost, higher design freedom, and ease of automation. Most research till date primarily focuses on processing and optimizing RIW joints for FRTPCs with high-performance polymer matrix materials that are typically used in aerospace. This dissertation primarily focuses on understanding the processability and optimizing RIW joint for FRTPC materials with engineering-grade polymers.

Moreover, research to date also predominantly uses only lap shear strength to characterize these joints. However, this is not enough to adequately understand the mechanical behavior of welded joints. In this dissertation, both lap shear and peel strength were experimentally evaluated, and finite element models were created to simulate these joints under large non-linear loads such as crash tests. This exercise provided in-depth insights into effects on the component-level performance of resistive implant welded structures and their behaviors in large deformation load cases such as crash tests.

Acknowledgment

First and foremost, I would like to acknowledge my doctoral advisor Dr. Pilla, for technical guidance and support. Dr. Pilla's scientific knowledge, patience, and dedication were essential in keeping me motivated and curious throughout my doctoral studies. Besides this, Dr. Pilla has created a nourishing environment, in which I was exposed to research communities, various industrial partners, and real-world challenges, directly contributing to my professional and personal growth.

I would also like to acknowledge Dr. Venhovens for his support during my early doctoral research, for setting a research direction and being an aspirational figure. I sincerely appreciate his constructive feedback and mentorship during my graduate school.

I am thankful to Dr. Brooks, Dr. Li, and Dr. Schmueser, for serving as my committee members. Their time and feedback provided throughout this process are invaluable; I could not have asked for a better dissertation committee. I would also like to thank my colleagues from my research group and DOE-ULWC project for their support and guidance.

Last but not least, I would like to acknowledge the U.S Department of Energy (Project # DE-EE0007293) and Honda R&D North America for funding parts of this research and scholarships from Proforma, Altair and Draexlmaier for financially supporting through graduate school.

Dedication

I Have the most profound sense of gratitude to my parents and sister, without whom I would have never imagined pursuing higher education, let alone a doctorate degree. Their love, support, understanding, and sacrifices cannot be overstated. Therefore, I would like to dedicate my dissertation to my parents and sister.

List of Abbreviations

\$E	Economy
Δ	Difference
ABS	Acrylonitrile butadiene styrene
ASTM	American Society for Testing and Materials
BEVs	Battery electric vehicles
BiW	Body in white
CAD	Computer-aided design
CF	Carbon Fiber reinforcements
CH₄	Methane
CO₂	Carbon Dioxide
DOE	Design of experiments
DSC	Differential scanning calorimeter
D_{sf}	Stiffness Directionality
D_{st}	Strength Directionality
FE-C	Fuel economy City
FE-H	Fuel economy highway
FMVSS	Federal Motor Vehicle Safety Standards
FRTPC	Fiber-reinforced thermoplastics composites
G_{1c}	Fracture toughness in mode 1
GF	Glass Fiber reinforcements
GPA	Giga Pascal
HDV	Heavy-duty vehicles
HE	Heating element
HEVs	Hybrid electric vehicles
ICEVs	Internal combustion engine-only vehicles
IPCC	Intergovernmental panel on climate change
kWh	Kilo watt-hour
lbs	pounds
LDV	Light duty vehicle
LDV	Light Duty vehicles
LFT	Long fiber reinforced thermoplastics
LJS	Linear joining speed
LP_b	Lightweight Potential for beams
LP_p	Lightweight Potential for panels
LSS	Lap Shear strength

MDB	Moving deformable barrier
MPa	Mega Pascal
M_{sf}	Max Stiffness
M_{st}	Max Strength
N	Newtons
NI	National instruments
NOx	Nitrous Oxides
NVH	Noise, Vibrations, and Harshness
PA	Polyamides
PA 66	Polyamides 6-6
PC	Polycarbonate
PEEK	Polyether ether ketone
PEI	Polyetherimide
PET	Polyethylene terephthalate
PHEVs	Plug-in hybrid electric vehicles
PP	Polypropylene
PPS	Polyphenylene sulfide
RIW	Resistive implant welded
RP	Rigid Pole
RVE	Representative volume element
S	Seconds
SEM	Scanning electron microscope
SFT	Short fiber reinforced thermoplastics
Sq.m	square meter
Tg	Glass transition temperature
Tm	Melt temperature
TPH	Throughput per hour
UD	Unidirectional
UI	user interface
ULWC	Ultra-lightweight composite door
ε	Strain
σ	Stress

Table of Contents

1	INTRODUCTION.....	1
1.1	Motivation	1
1.2	Mass reduction	4
1.3	Why fiber-reinforced composites and particularly fiber-reinforced thermoplastics composites?	13
1.4	Joining thermoplastic composites from a bird’s eye perspective	17
2	LITERATURE REVIEW & GAPS.....	26
2.1	Overview of various fusion bonding technologies	26
2.2	Down selection of fusion bonding technology for automotive structures	29
2.3	Hypotheses.....	38
2.4	Literature review and Research Gaps.....	39
2.5	Pathway to verify research statements & address gaps	52
3	SELECTION AND MECHANICAL CHARACTERIZATION OF FIBER REINFORCED THERMOPLASTICS	57
3.1	Introduction.....	57
3.2	Types of fiber reinforcements.....	58
3.3	Manufacturing.....	61
3.4	Mechanical characterization.....	63
3.5	Comparison of FRTPC materials to Commonly used automotive structural material systems.	69
3.6	Summary	71

4	UNDERSTANDING HOW TO USE FRTPC MATERIALS AT SYSTEM LEVEL.....	73
4.1	Selecting an ideal candidate for the lightweighting study.	73
4.2	Development of an Ultra-lightweight FRTPC (ULWC) door frame.....	74
4.3	Summary	87
5	EXPERIMENTAL SETUP	88
5.1	Mechanical Design	89
5.2	Weld Automation and Data Acquisition.....	93
5.3	LabVIEW Program.....	95
6	IDENTIFYING PROCESSING WINDOW.....	98
6.1	Weld process & variables.....	98
6.2	Effect of process variables on joint performance	114
6.3	Key learnings.....	115
7	MECHANICAL CHARACTERIZATION	117
7.1	Mechanical characterization of RIW.....	117
7.2	Mechanical characterization of structural adhesive joints for comparison.....	126
7.3	Understanding strain rate dependency	129
7.4	Summary	132
8	TESTING, MODELING AND SIMULATION PATHWAY FOR RESISTIVE IMPLANT WELDING FOR LARGE NON-LINEAR FAILURE MODES .	134
8.1	Task 1: Identify and implement a modeling pathway for simulating resistive welded joints	134

8.2	Developing material models for adhesive joints.....	149
8.3	Understanding the system-level performance of resistive welded structures	152
9	EVALUATING SCALABILITY OF RESISTIVE WELDED JOINT.....	158
9.1	Understanding the effect of weld processing time on vehicle throughput of a body shop.....	158
9.2	Understanding Resilience to Contamination in the joint interface for Resistive Welded Joints.....	166
9.3	Evaluating reparability/ rework for resistive welded joints.....	174
10	CONCLUSION	180
10.1	Conclusions	180
10.2	Future work.....	185
11	BIBLIOGRAPHY.....	188

Table of Figures

FIGURE 1.1 GREENHOUSE GAS EMISSIONS BY ECONOMIC SECTORS. (IMAGE SOURCE ³).....	2
FIGURE 1.2 GREENHOUSE GASES DISTRIBUTION WITHIN THE UNITED STATES (DATA SOURCE ⁴ , YEAR: 2017).....	2
FIGURE 1.3 FUEL ECONOMY IMPROVEMENTS VS. RETAIL PRICE INCREMENT (IMAGE SOURCE ⁹).....	4
FIGURE 1.4 VEHICLE MASS VS. MPG FOR MY 2019 ICES WITHIN THE USA. (DATA SOURCE ¹¹)	6
FIGURE 1.5 VEHICLE MASS VS. MPGE FOR MY 2019 HEVS & PHEVS WITHIN THE USA. (DATA SOURCE ¹¹) ...	7
FIGURE 1.6 VEHICLE MASS VS. MPGE FOR MY 2019 BEVS WITHIN THE USA. (DATA SOURCE ¹¹).....	7
FIGURE 1.7 MASS VS. FUEL ECONOMY RELATION FOR ICEVS.	8
FIGURE 1.8 MASS VS. EQUIVALENT FUEL ECONOMY RELATION FOR BEVS.	9
FIGURE 1.9 HISTORIC TREND OF AVG LDV WEIGHT AND MATERIAL COMPOSITION (IMAGE SOURCE ¹²)....	10
FIGURE 1.10 CUMULATIVE WEIGHT REDUCTION FROM 1975 TO 2010. (IMAGE SOURCE ¹³)	12
FIGURE 1.11 ASHBY CHART FOR STRENGTH VS. DENSITY. (IMAGE SOURCE ¹⁶)	15
FIGURE 1.12: MECHANICAL INTERLOCKING FEATURES FOR COMPOSITE STRUCTURES. (IMAGE SOURCE ³¹)	20
FIGURE 2.1 RESISTIVE WELDING.....	27
FIGURE 2.2 ULTRASONIC WELDING.....	28
FIGURE 2.3 INDUCTION WELDING.....	29
FIGURE 2.4 CLASSIFICATION OF AUTOMOTIVE JOINTS REQUIREMENTS.	30
FIGURE 2.5 TOTAL FLANGE LENGTH FOR A BODY SIDE OUTER.....	32
FIGURE 2.6 NO. OF PUBLISHED ARTICLES VS. PUBLISHING YEAR FRO FRTPC.	41
FIGURE 2.7 FRTPC B-PILLAR DESIGN BY YARLAGADDA, S. ET AL., (IMAGE SOURCE ⁷⁴)	43
FIGURE 2.8 RESEARCH LIFE CYCLE OF RIW JOINTS.	44
FIGURE 2.9 TYPICAL FAILURE MODES FOR STRUCTURAL JOINTS.....	48
FIGURE 2.10 TENSILE SAMPLES FOR BULK CHARACTERIZATION OF ADHESIVE. (IMAGE SOURCE ⁸⁹)	49

FIGURE 2.11 TASKS FOR VERIFYING RS 1.....	52
FIGURE 2.12 TASKS FOR VERIFYING RS 2.....	53
FIGURE 2.13 TASKS FOR VERIFYING RS 3.....	55
FIGURE 2.14 TASKS FOR VERIFYING RS 4.....	56
FIGURE 3.1 SHORT FIBER AND LONG FIBER REINFORCED THERMOPLASTIC PELLETS.....	59
FIGURE 3.2 CARBON FIBER NON-WOVEN PREPREG MATERIAL.....	60
FIGURE 3.3 AUTOCLAVE MANUFACTURING CYCLE FOR UNI-DIRECTIONAL COMPOSITES.	62
FIGURE 3.4 AUTOCLAVE CYCLE FOR NON-WOVEN COMPOSITES.	62
FIGURE 3.5 CUSTOMER TEST COUPON INJECTION MOLD.	63
FIGURE 3.6 WOVEN TEST COUPONS WITH BONDED STRAIN GAUGES AND GLASS FIBER TABS.	64
FIGURE 3.7 FOOTPRINTS OF MATERIAL PERFORMANCE ATTRIBUTES IN SPIDER PLOTS.	68
FIGURE 3.8 ASHBY CHART FOR DENSITY VS. YOUNG'S MODULUS (IMAGE SOURCE ¹⁰⁸)	69
FIGURE 3.9 STRENGTH VS. DENSITY FOR AUTOMOTIVE MATERIALS.....	70
FIGURE 3.10 STIFFNESS VS. DENSITY FOR AUTOMOTIVE MATERIALS.....	71
FIGURE 4.1 STEEL DOORFRAME WITH HINGES AND COMPONENTS FROM THE OEM DOOR.....	74
FIGURE 4.2 WEIGHT DISTRIBUTION BY THE MATERIAL GROUP IN THE BASELINE DOOR.	75
FIGURE 4.3 WEIGHTS OF A MAJOR SUBASSEMBLY OF THE BASELINE DOOR.....	75
FIGURE 4.4 NONLINEAR LOAD CASES.....	77
FIGURE 4.5 INTERIOR TRIM COMPONENTS.....	78
FIGURE 4.6 FINAL SELECTED DESIGN.....	80
FIGURE 4.7 METAL ANTI-INTRUSION BEAM AND BELTLINE STIFFENER FOR ULWC.....	80
FIGURE 4.8 STRENGTH AND STIFFNESS ZONES ON THE DOOR.	81
FIGURE 4.9 OPTIMIZATION PROBLEM.....	82
FIGURE 4.10 OPTIMIZED THICKNESS DISTRIBUTION OF THE FRTPC PARTS.	83
FIGURE 4.11 FORCE-DISPLACEMENT PLOTS FOR ULWC DOOR VS. BASELINE DOOR.....	85

FIGURE 4.12 FMVSS 214: DEFORMATION PLOTS OF THE ULWC DOOR.	86
FIGURE 5.1 TYPICAL FAILURE MODES FOR STRUCTURAL JOINTS (IMAGE SOURCE ¹¹⁹).	88
FIGURE 5.2 WELDED COUPON GEOMETRY.	89
FIGURE 5.3 WELD FIXTURE DESIGN.	90
FIGURE 5.4 LOWER CLAMP.	90
FIGURE 5.5 FLOATING CLAMP.	91
FIGURE 5.6 ELECTRICAL CONNECTORS.	92
FIGURE 5.7 FULLY ASSEMBLED WELD FIXTURE.	93
FIGURE 5.8 WELD AUTOMATION AND DATA ACQUISITION.	95
FIGURE 5.9 LABVIEW PROGRAM (BACKEND).	96
FIGURE 5.10 LABVIEW PROGRAM FRONT END (UI FOR THE OPERATOR).	97
FIGURE 6.1 EFFECT OF INITIAL PRESSURE ON CONTACT.	100
FIGURE 6.2 CLAMPING SYSTEM HYDRAULIC LAYOUT.	101
FIGURE 6.3 SEM IMAGES OF WELD CROSS-SECTION AT 50 MICRONS FOR VARYING INITIAL PRESSURES.	102
FIGURE 6.4 RESISTANCE VS. TEMPERATURE MEASUREMENT.	103
FIGURE 6.5 TEMPERATURE VS. RESISTANCE FOR HEATING ELEMENTS.	104
FIGURE 6.6 LAP SHEAR STRENGTH VS NEAT POLYMER LAYER THICKNESS.	105
FIGURE 6.7 DSC PLOT FOR PA66 WITH CARBON FIBER REINFORCEMENTS.	106
FIGURE 6.8 VISUAL COLOR CHANGE (DEGRADATION) IN PURE PA66 AT ~290°C.	107
FIGURE 6.9 VOLTAGE AND CURRENT PROFILE.	108
FIGURE 6.10 TEST WELDS WITH A THERMOCOUPLE ON THE MESH CENTER.	109
FIGURE 6.11 FORCE-DISPLACEMENT PLOTS FOR DOE 1 UNDER LAP SHEAR.	111
FIGURE 6.12 STORAGE MODULUS AND VISCOSITY OF PA66.	112
FIGURE 6.13 MAIN EFFECTS PLOTS OF VARIABLES ON RESPONSES.	113
FIGURE 7.1 SEM SECTION OF THE WELD INTERFACE IN LFT CUPON.	118

FIGURE 7.2 SEM SECTION OF THE WELD INTERFACE IN NON-WOVEN CUPON.	119
FIGURE 7.3 SEM SECTION OF THE WELD INTERFACE IN WOVEN CUPON.	119
FIGURE 7.4 LAP SHEAR FORCE-DISPLACEMENT PLOT FOR LFT, NON-WOVEN AND WOVEN FRTPC.....	121
FIGURE 7.5 NON-WOVEN COUPONS AFTER FAILURE.....	122
FIGURE 7.6 WOVEN COUPONS AFTER FAILURE.	122
FIGURE 7.7 LFT COUPONS AFTER FAILURES.	123
FIGURE 7.8 CUSTOM DESIGNED AND MACHINE PEEL FIXTURE.	124
FIGURE 7.9 COUPON GEOMETRY (IMAGE SOURCE ¹³⁷).	125
FIGURE 7.10 INTERFACIAL FAILURE DURING DOUBLE CANTILEVER BEAM TEST.....	126
FIGURE 7.11 PLEXUS MA530 VS. 3M ADHESIVE LAP SHEAR PERFORMANCE.....	128
FIGURE 7.12 STRAIN RATE CLASSIFICATION(IMAGE SOURCE ¹³⁸).	129
FIGURE 7.13 STRAIN RATES VS. TIME FOR JOINT ELEMENTS IN AN FMVSS 214 RP.	130
FIGURE 7.14 RESISTIVE WELDING LAP SHEAR STRENGTH AT VARIOUS STRAIN RATES.	131
FIGURE 7.15 PLEXUS MA 530 LAP SHEAR STRENGTH AT VARIOUS STRAIN RATES.	132
FIGURE 7.16 RESTIVE WELDING VS. PLEXUS MA530.....	132
FIGURE 8.1 ADHESIVE MODELING USING BRICK ELEMENT.....	136
FIGURE 8.2 ADHESIVE SPRING (TYPE2) ELEMENTS.....	136
FIGURE 8.3 SHEAR AND NORMAL LOADING OF A COHESIVE BRICK ELEMENT.	137
FIGURE 8.4 STRESS-STRAIN PLOT FOR NON-WOVEN COUPONS IN 0°.	138
FIGURE 8.5 TENSILE: FORCE-DISPLACEMENT PLOTS FOR COUPON MATERIAL SIMULATION VS. TEST.	139
FIGURE 8.6 BENDING STIFFNESS CORRELATION.	140
FIGURE 8.7 MATERIAL CARD GENERATION PATHWAY FOR RESISTIVE WELDING.....	141
FIGURE 8.8 DOUBLE CANTILEVER BEAM TEST.....	142
FIGURE 8.9 FORCE-DISPLACEMENT PLOTS FOR DCB TEST RESISTIVE WELDING.	143
FIGURE 8.10 SCREEN GRABS FOR DIC.....	144

FIGURE 8.11 DIC STRAIN PLOTS FOR LAP SHEAR TESTS.	145
FIGURE 8.12 DIC STRAIN PLOTS FROM DCB TESTS.	146
FIGURE 8.13 LAP SHEAR: FORCE-DISPLACEMENT PLOTS.	147
FIGURE 8.14 DCB TEST: FORCE-DISPLACEMENT PLOT.....	147
FIGURE 8.15 MESH DEFORMATION OVERLAY ON ACTUAL TEST IMAGES (RESISTIVE WELDED).....	148
FIGURE 8.16 FINAL MODEL FOR RESISTIVE WELDED JOINTS.	148
FIGURE 8.17 STRESS-STRAIN PLOTS FOR PURE ADHESIVE (PLEXUS MA530).	149
FIGURE 8.18 LAP-SHEAR FORCE-DISPLACEMENT: SIMULATION VS. TEST.	150
FIGURE 8.19 DCB: FORCE-DISPLACEMENT PLOT, SIMULATION VS EXPERIMENTAL.....	151
FIGURE 8.20 MATERIAL CARDS FOR ADHESIVELY BONDED JOINTS.	151
FIGURE 8.21 BOUNDARY CONDITIONS.....	153
FIGURE 8.22 SIMPLIFIED RIGID POLE TEST.	154
FIGURE 8.23 IMPACTOR FORCE-DISPLACEMENT FOR RESISTIVE WELDED VS. ADHESIVES BONDED STRUCTURES.....	156
FIGURE 8.24 JOINT FAILURE PLOTS VS. INTRUSION.	157
FIGURE 9.1 BMW I3 STRUCTURAL FRAME.	159
FIGURE 9.2 BODY SHOP LAYOUT.	161
FIGURE 9.3 RESISTIVE WELDING BLOCK.	161
FIGURE 9.4 PLANT SIMULATION MODEL FOR THE UPPER MODULE BODY SHOP.	162
FIGURE 9.5 ANNUAL PRODUCTION VS. WELDING TIME.	163
FIGURE 9.6 DATA LOGGED FOR RIW WELD OF NON-WOVEN FRTPC (RUN2).	165
FIGURE 9.7 BODY SHOP CONTAMINATIONS.	167
FIGURE 9.8 WATER CONTAMINATES ON RESISTIVE WELDING.	168
FIGURE 9.9 OIL CONTAMINATION ON RESISTIVE WELDING.....	168
FIGURE 9.10 PEAK FORCE AT BREAK VS CONTAMINATION.....	170

FIGURE 9.11 NORMALIZED PEAK FORCE VS. CONTAMINATION.	170
FIGURE 9.12 STEAM EJECTION DURING THE WELDING PROCESS FOR 5 μ L WATER.	171
FIGURE 9.13 FORCE-DISPLACEMENT PLOTS FOR ALL TESTS WITH CONTAMINATIONS.	174
FIGURE 9.14 REWELD WITH OLD MESH.	176
FIGURE 9.15 REWELD WITH A NEW MESH.	177
FIGURE 9.16 FORCE-DISPLACEMENT PLOTS FOR REWELD STUDY.	178
FIGURE 9.17 WELD STRENGTHS FOR REWELDED COUPONS.	179
FIGURE 9.18 DE-BONDED COUPONS.	179

Table of Tables

TABLE 1.1 AUTOMOTIVE STRUCTURAL MATERIALS – A COMPARISON	14
TABLE 1.1.2: ADVANTAGES AND DISADVANTAGES OF MECHANICAL JOINING	19
TABLE 1.1.3: ADVANTAGES AND DISADVANTAGES OF MECHANICAL JOINING	22
TABLE 1.1.4: ADVANTAGES AND DISADVANTAGES OF MECHANICAL JOINING	24
TABLE 2.1 CYCLE TIMES OF VARIOUS FUSION BONDING TECHNOLOGIES FROM LITERATURE.....	31
TABLE 2.2 LAP SHEAR STRENGTH OF VARIOUS FUSION BONDING TECHNOLOGIES FROM LITERATURE.....	36
TABLE 2.3 DOWN SELECTION OF WELD PROCESSES.	38
TABLE 2.4 LITERATURE SORTED BY SUBSTRATE MATERIAL.....	47
TABLE 3.1 PROCESSING CONDITIONS FOR INJECTION MOLDING.	63
TABLE 3.2 SUMMARY OF MECHANICAL PROPERTIES OF FRTPC	67
TABLE 3.3 MATERIAL PERFORMANCE ATTRIBUTES.....	67
TABLE 3.4 SPECIFIC PROPERTIES OF FRTPC VS. METALS.	72
TABLE 4.1 OPTIMIZATION RESULTS OF ULWC DOOR.	83
TABLE 4.2 FMVSS 214 RP AND IIHS SI MDB PERFORMANCES.	86
TABLE 6.1 VARIABLES IN RIW PROCESS.....	99
TABLE 6.2 DSC TEST CONDITIONS AND RESULTS.....	107
TABLE 6.3 VARIABLE AND RESPONSES FOR DOE 1.	110
TABLE 7.1 LAP SHEAR STRENGTH FOR RIW JOINTS.....	121
TABLE 7.2 MODE ONE FRACTURE TOUGHNESS FOR RIW JOINTS	125
TABLE 7.3 MECHANICAL PROPERTIES FOR PLEXUS MA530.	128
TABLE 7.4 RIW VS. ADHESIVE, MECHANICAL PERFORMANCE.....	133
TABLE 9.1 FRTP BODY STRUCTURE ASSUMPTIONS.....	160
TABLE 9.2 ANNUAL PRODUCTION VS WELD TIME.	163
TABLE 10.1 SUMMARY OF FRTPC.	181

TABLE 10.2 SUMMARY OF THE RIW JOINT 182

1 INTRODUCTION

1.1 Motivation

1.1.1 *The rise of global atmospheric temperature*

Limiting average global temperature rise to less than 2°C over the pre-industrial era is a critical challenge of the 21st century¹. The Intergovernmental Panel on Climate Change (IPCC), a body of the United Nations (UN), has attributed this increase in temperature primarily to the emission of greenhouse gases (GHGs) in our atmosphere. To address this grave issue, 196 countries ratified the Paris agreement in 2015, acknowledging the serious risks and effects of climate change on our planet, and agreeing to take proactive measures that would aid in limiting the average global temperature rise to less than 2°C². In particular, they agreed to reduce the emission of major greenhouse gases due to anthropogenic activities – namely, carbon dioxide (CO₂), nitrous oxides (NO_x), methane (CH₄), and fluorinated gases. Of these, carbon dioxide is the most significant constituent, contributing up to 76% (of all GHGs) in volume globally³.

1.1.2 *Transportation's contribution to greenhouse gas emissions.*

The sources of GHG emissions can be classified based on end-use economic sectors, as shown in Figure 1.1. As shown, around 14% of global GHG emissions are attributable to transportation sector³. Remarkably, within the United States, the transportation sector accounted for 29% of U.S. GHG emissions in 2017⁴, i.e., twice of its share in global GHG emissions. Of this 29%, 16.8% of emissions arise from light-duty vehicles (LDVs), while 6.5% are from heavy-duty vehicles (HDVs), as shown in Figure 1.2.

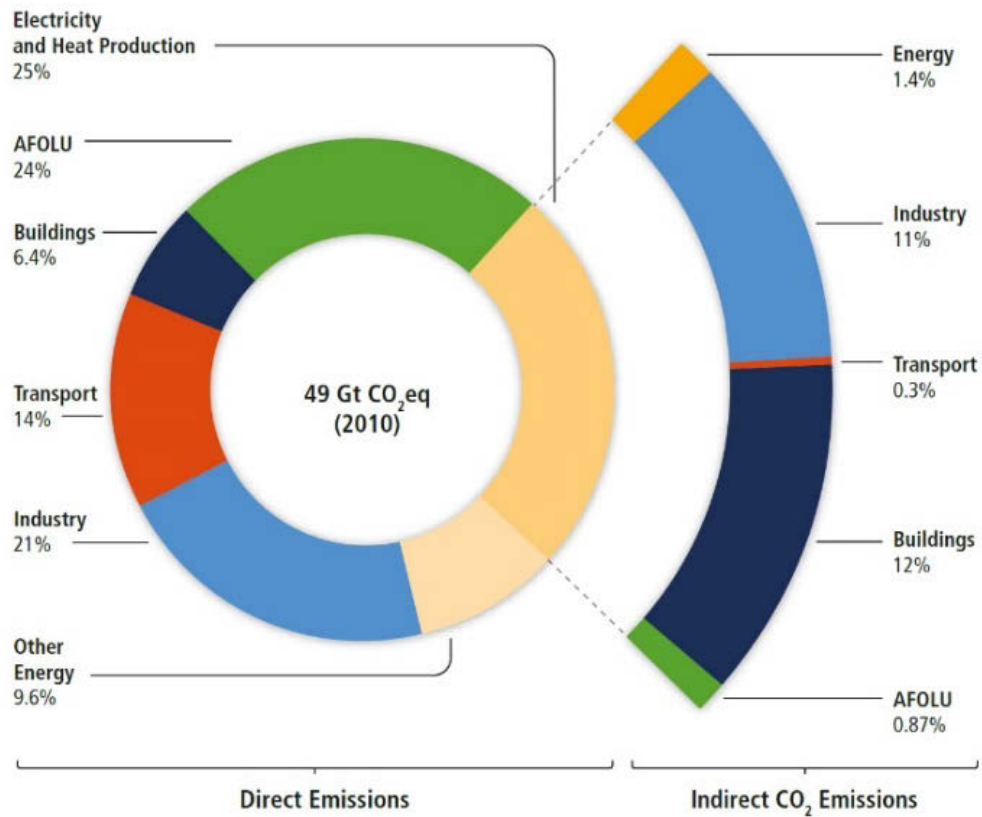


Figure 1.1 Greenhouse gas emissions by economic sectors. (Image source³)

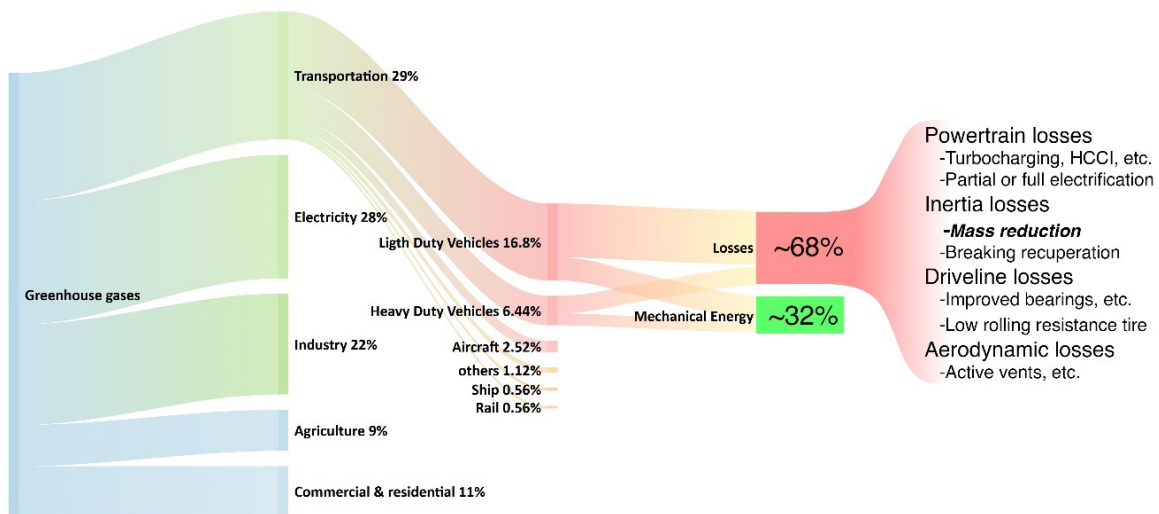


Figure 1.2 Greenhouse gases distribution within the United States (Data source⁴, Year: 2017).

1.1.3 Improving vehicle efficiency

While several approaches have been used to minimize transportation-related GHG emissions, the most effective solutions include hybridization/electrification, vehicular mass reduction, car-sharing/pooling, and improving public transport⁵. Of these solutions, improvements in public transportation and car-sharing are macro-level changes that involve governments, social acceptance, and long-term planning^{5,6}. On the other hand, hybridization/electrification and mass reduction are solutions that can be implemented at the automaker level⁷. Most countries enforce both these solutions by using fuel economy mandates, forcing automakers to improve vehicular efficiencies gradually. In fact, some countries have even gone a step further by issuing a blanket ban on manufacturing fossil fuel-powered vehicles in the upcoming decade (i.e., the 2030s)⁸.

Since hybridization and electrification of LDVs lead to a significant increase in cost for end-customers, it is essential for automotive manufacturers to balance the additional cost of new vehicle technologies with savings from fuel economy. As shown in Figure 1.3, R.A. Simmons et al.⁹ have plotted the relationship between various technologies for improving fuel economy and the net increment in retail price. As can be seen, for most hybridization technologies, the average consumer will never get the return on investment merely via increased fuel savings⁹.

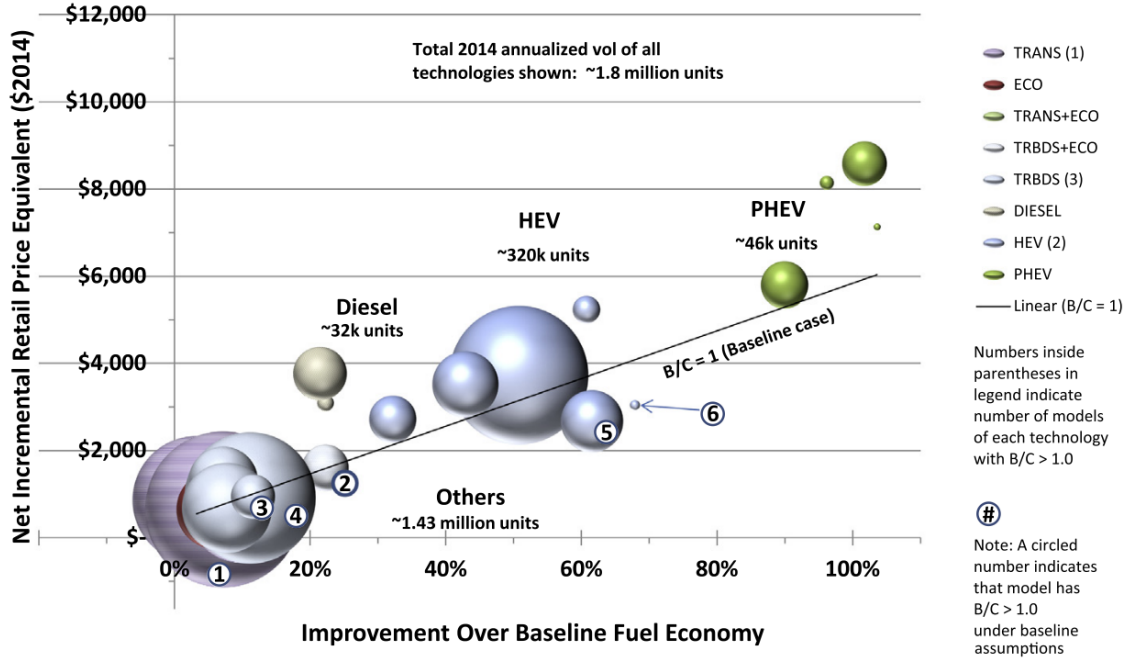


Figure 1.3 Fuel economy improvements vs. retail price increment (image source⁹)

1.2 Mass reduction

1.2.1 Impact of mass on vehicle efficiency

A lighter object has less inertia, thus requiring less energy to accelerate and sustain velocity. In addition to lower energy consumption, the other benefits of mass reduction are better handling, lower cost, and better safety¹⁰. Moreover, when a significant amount of mass is reduced from the overall vehicle structure, this reduction automatically trickles down to other subsystems as well. For example, a lighter body-in-white (BiW) will, in turn, require a lighter chassis. The combination of lighter BiW and lighter chassis will then require a smaller engine and fuel tank to meet the same performance targets as a larger (and heavier) vehicle. This effect is often referred to as *mass decompounding* or *inverting the mass spiral*¹¹.

To understand the effect of mass reduction on fuel economy, it is essential to separate LDVs into three categories, based on their propulsion types. These three categories are:

I. Internal combustion engine-only vehicles (ICEVs):

ICEVs use the traditional internal combustion engine (ICE) as a prime mover, with gasoline or diesel often powering these engines.

II. Hybrid electric vehicles (HEVs) and Plug-in hybrid electric vehicles (PHEVs):

HEVs and PHEVs often use an electric powertrain in tandem with the internal combustion engine (ICE). The torque augmentation from electric powertrain helps the ICE to operate in a more efficient envelope and recuperate kinetic energy during braking, thereby improving the overall vehicular fuel efficiency. Some HEVs with larger batteries can also run on the electric powertrain for a limited range. These vehicles typically have a provision for charging the battery using an external power source and are thus referred to as plug-in hybrid electric vehicles (PHEVs).

III. Battery electric vehicles (BEVs):

BEVs primarily depend on electric motors and high voltage battery systems for propulsion. A small subset of BEVs uses an ICE coupled to a generator as a range extender. Often, these range extenders are limited for the emergency driving range and are not the primary source of energy for the vehicle.

As can be seen in Figure 1.4, the fuel economy of ICEVs correlates with the vehicle mass, while HEVs and PHEVs do not exhibit a similar correlation (with vehicle mass). This disparity can be attributed to the variance in the degree of hybridization and small sample

sizes. Most hybridization technologies, if not all, are designed to improve fuel efficiency in city driving cycle, where the kinetic energy during braking is converted to electrical energy. Contrastingly, the number of braking zones in highway driving cycle is significantly less, thereby rendering these hybrid systems ineffective from the perspective of energy conversion, marking them as dead-weight in these driving scenarios. This trend can be observed in Figure 1.5, where certain data points have higher fuel economy in city driving cycle than that of the highway driving cycle.

Upon looking at the data of BEVs, a correlation can be observed between the vehicle mass and overall vehicle efficiency, as shown in Figure 1.6. While electric vehicles are significantly more efficient than ICEVs, HEVs, and PHEVs, their weight directly affects the vehicle range. Coupled with the high cost of batteries, this increases the incentive for automakers to invest in lightweighting.

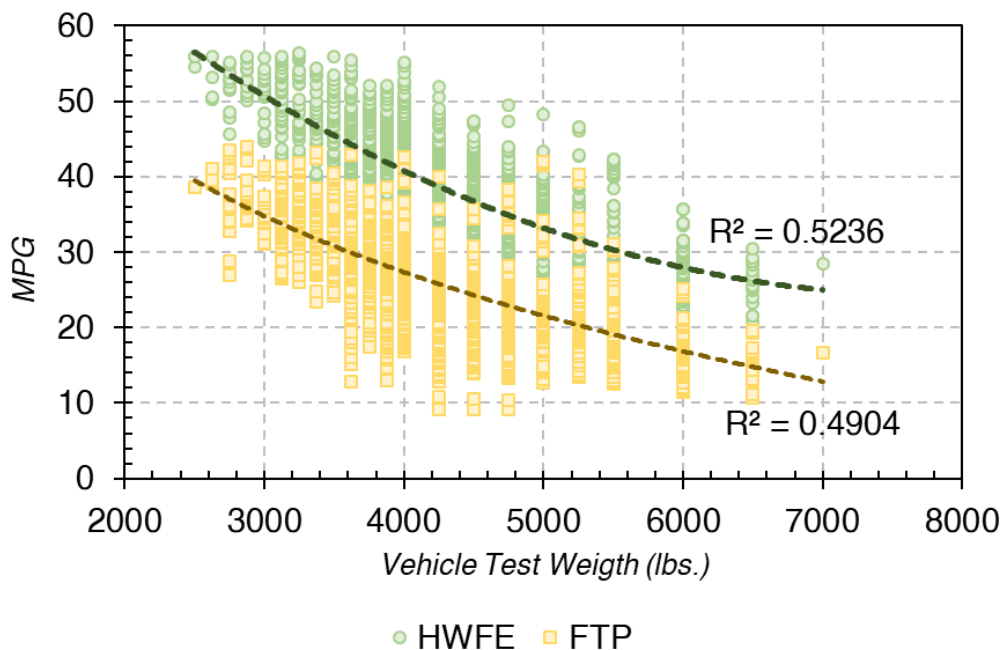


Figure 1.4 Vehicle Mass vs. MPG for MY 2019 ICEs within the USA. (data source¹¹)

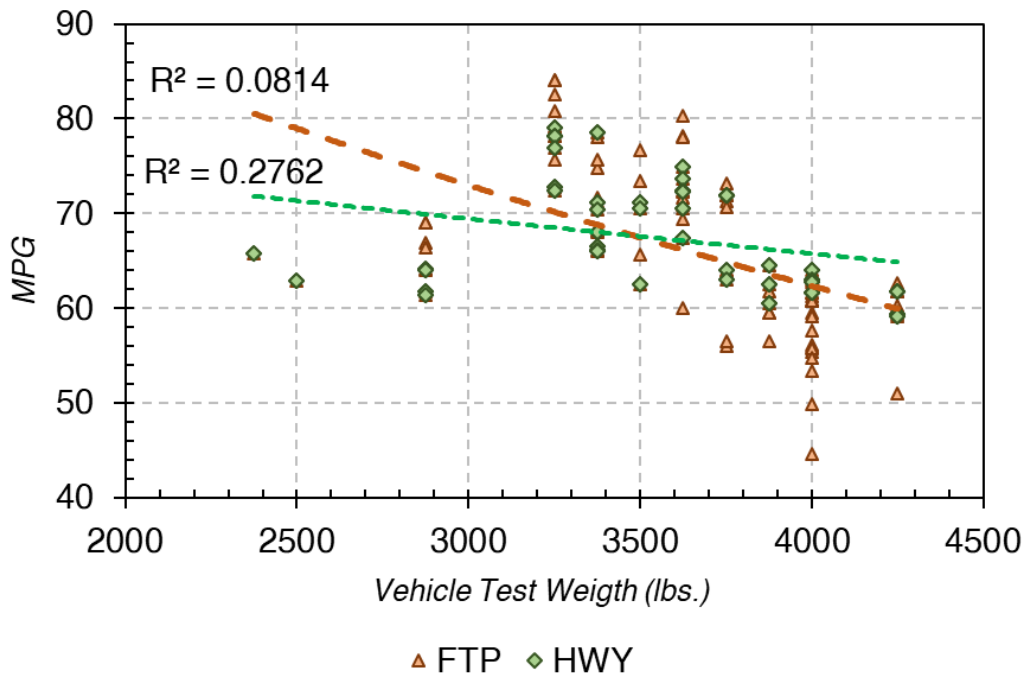


Figure 1.5 Vehicle Mass vs. MPGe for MY 2019 HEVs & PHEVs within the USA. (data source¹¹)

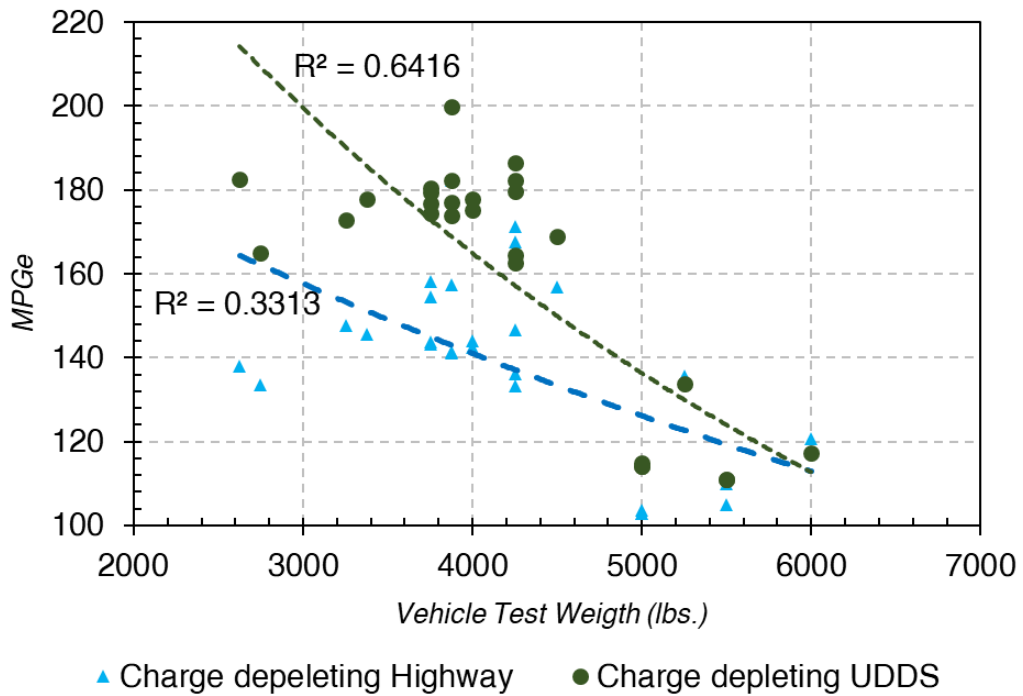


Figure 1.6 Vehicle Mass vs. MPGe for MY 2019 BEVs within the USA. (data source¹¹)

1.2.2 The sensitivity of vehicle mass on efficiency

I. For ICEVs

Using the fitted curves from Figure 1.4, the sensitivity between the percentage increase in mass and percentage decrease in fuel efficiency was calculated, as shown in Figure 1.7. On average, a reduction of 6% in city fuel economy and 5% in highway fuel economy was observed with 10% increase in mass for ICEVs.

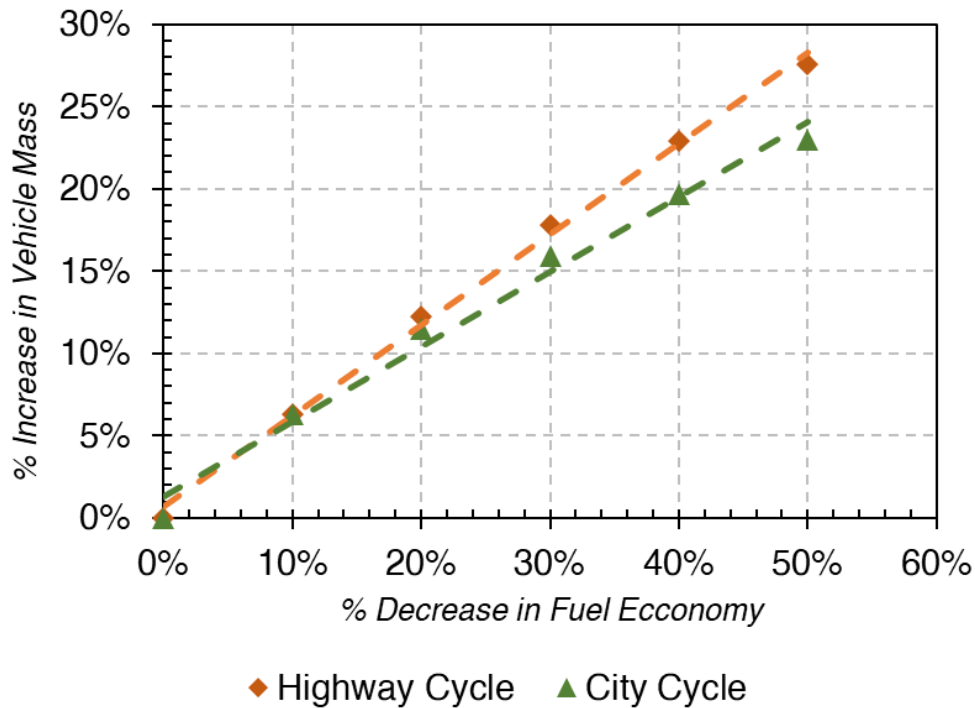


Figure 1.7 Mass vs. fuel economy relation for ICEVs.

II. For BEVs

Like for ICEVs, the fitted curves from Figure 1.6 were used to calculate the sensitivity (between mass and fuel economy). On average, for every 10% increase in mass, a reduction of 5% (for city driving cycle) and 3% (for highway driving cycle) in efficiency is observed for BEVs, as can be seen in Figure 1.8. To put this in perspective,

for every 10% increase in vehicle mass, an average of 4-5% reduction in driving range is observed for vehicles with battery capacity ranging between 75-100 KWh.

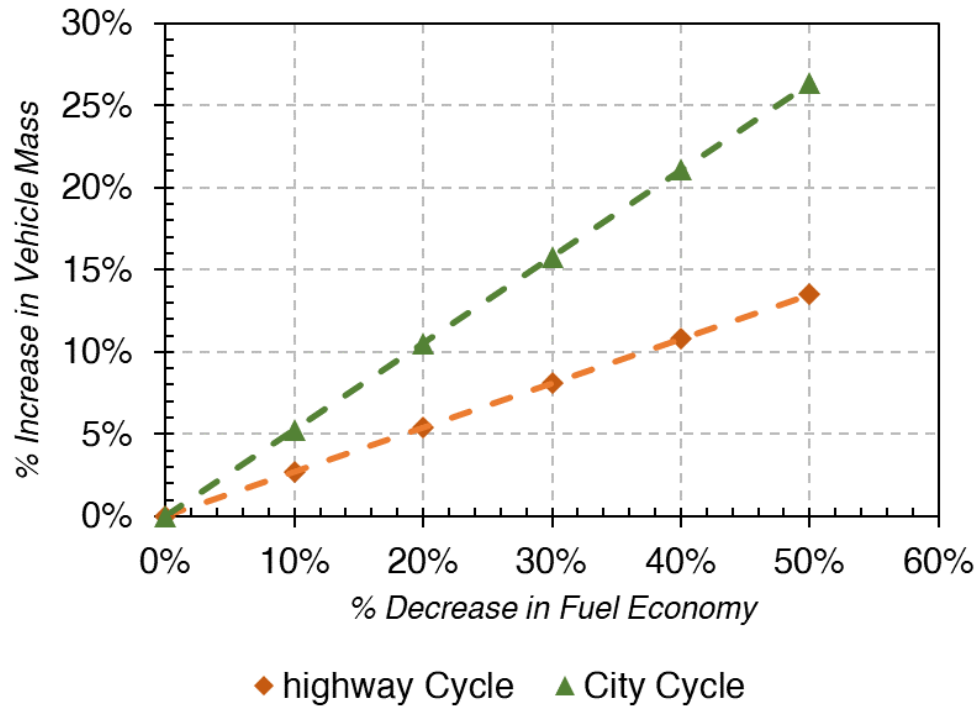


Figure 1.8 Mass vs. equivalent fuel economy relation for BEVs.

Given this direct correlation between fuel efficiency (as well as a driving range) and vehicle mass for LDVs, the incentive for lightweighting is often undisputed. Historically, automakers have used several approaches, such as downsizing, design optimization, and material substitution, to decrease vehicle mass. However, other requirements, such as meeting more robust crash tests, customers' preference for larger interior volumes, and the need for deploying additional equipment for emission controls, automated driver assistance systems, and high voltage batteries, have resulted in a gradual increase in average vehicle mass over the last three decades¹², as shown in

Figure 1.9. To overcome this mass creep, it is essential to focus on more drastic methods of mass reduction.

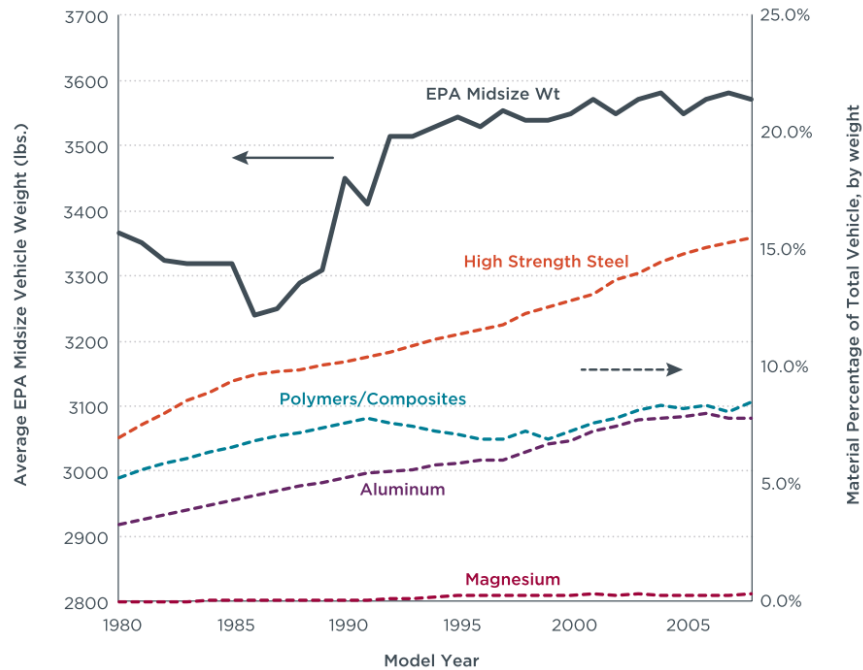


Figure 1.9 Historic trend of avg LDV weight and material composition (Image source¹²).

1.2.3 Mass reduction approach

Most vehicular mass reduction methods can be classified into the following three groups:

- I. Component downsizing (e.g., v8 to v6, rear-wheel drive to front-wheel drive)***
- II. Design optimization (e.g., Body on the frame to unibody)***
- III. Materials substitution (e.g., Mild steel to advance high strength steel, aluminum to carbon fiber composites)***

Component downsizing is one of the most effective ways of reducing the overall vehicle mass. However, in most cases, the allowable amount of downsizing is often limited by the performance and geometrical requirement of the vehicle. Hence, automakers typically try to shave every bit of unnecessary material using robust simulation and testing tools. This intense process of design optimization is a common practice in most vehicle development programs. Isenstadt, A. et al.¹³ have reported the historical contribution of various technologies for mass reduction (Figure 1.10). As can be seen, the mass reduction due to front-wheel drive transmission, change in construction type, and reduction in the number of cylinders have almost plateaued since the 1990s. However, the extent of mass reduction via the change in materials and manufacturing techniques has witnessed steady growth.

For further mass reduction (beyond component downsizing and design optimization), material substitution is the next forte. The words “*material substitution*” are often misunderstood as a process of merely replacing material “A” with “B”; such direct substitution may not necessarily be the best solution. Instead, for the effective lightweighting of a component, we need a holistic approach that considers all the new design freedoms and utilizes manufacturing processes offered by the new material system.

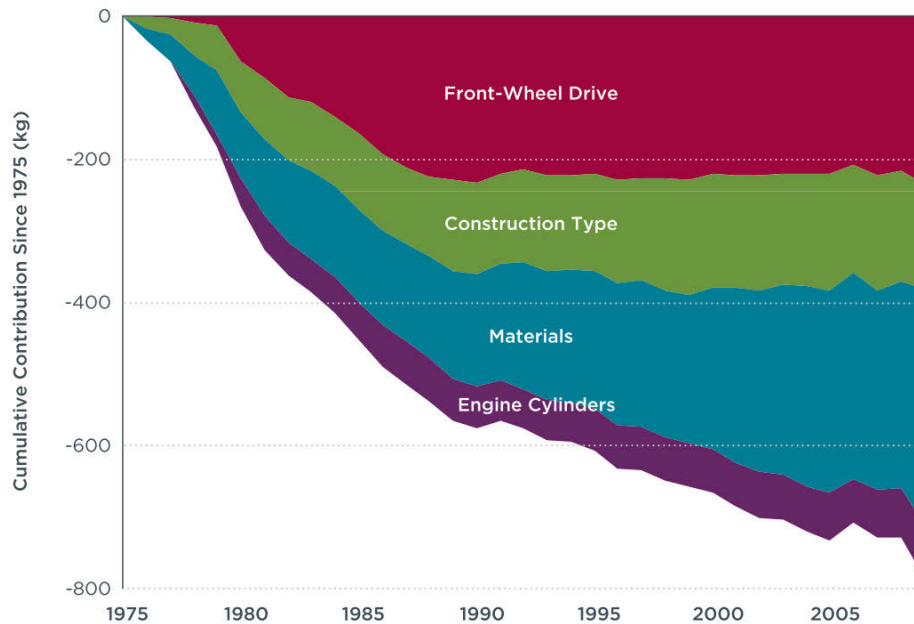


Figure 1.10 Cumulative weight reduction from 1975 to 2010. (image source¹³)

Typically, automotive structural materials can be broadly divided into three categories: (a) Ferrous metals (e.g., steel); (b) Nonferrous metals (e.g., aluminum); and (c) Composites or polymers. During the last decade, several new families of ferrous materials have been used for enhancing safety and reducing vehicle mass. The current state-of-the-art ferrous materials include TRIP (Transformation-induced plasticity) steels, TWIP (Twinning-Induced Plasticity) steels, and 3rd generation ultra-high-strength steels (UHSS). However, the inherent limitation of steel is its extremely high density and limited formability. These limitations, in turn, created the prospect of using nonferrous materials such as aluminum.

Aluminum structural components are generally manufactured using casting, extrusion or sheet metal forming. Over the past five years, the number of thin-walled aluminum castings in automotive structures has steadily increased¹⁴. However, the major

limitation with using aluminum alloys in automotive applications is the associated joining technology and higher cost. While steel can be spot-welded – a fast and economical joining technique – aluminum must be joined using either of metal inert gas (MIG) technique, bonding, or mechanical fastening, all of which are considerably slower than spot welding. Further, the formability limit for aluminum is much lower than that for steel, which reduces the design freedom.

Due to these limitations of aluminum, carbon fiber- and glass-fiber-reinforced polymers have gradually gained attention for use in high-performance automotive structures. The key advantages of using composite materials over metals are their: (a) Higher specific properties; (b) Anisotropy; and (c) Manufacturing flexibility. On the other hand, higher costs, longer manufacturing cycle times, and slow joining times are some prominent limitations of composites. Fiber-reinforced composites can be classified into two groups: (a) Thermoset composites; and (b) Thermoplastics composites.

Table 1.1 compares the aforementioned material systems for automotive structural applications.

1.3 Why fiber-reinforced composites and particularly fiber-reinforced thermoplastics composites?

A composite is a material system that is made from two or more constituents and has different material properties from those of its individual constituents. Examples of common composites include plywood, reinforced concrete, and reinforced plastics. As seen in the Ashby chart (Figure 1.11), composites such as carbon fiber-reinforced polymers (CFRPs) are stronger than most commonly used automotive metals or metallic alloys (such as magnesium, aluminum, and steel alloys), while also having lower densities.

Table 1.1 Automotive Structural materials – A comparison

	Steel	Aluminum	Thermoset Composites	Thermoplastic Composites
Lightweight potential	Medium	High	Very High	Very High
Material cost	Moderate	Medium	High	High
Reprocessing / recyclability	Good	Good	Bad	Good
Part manufacturing	Very Fast	Very Fast	Slow	Fast
Joining speed	Fast	Moderate	Very Slow	Very Slow
Number of parts per vehicle	290-430	350	160	No samples
Annual production volume (in 1000s)	45-90	45	40	No samples
Average takt time per vehicle	55-100 sec	120-200 sec	480 sec	No samples

Such higher specific properties¹⁵ enable composites as materials of high potential for use in structural applications in the automotive sector. Due to such high potential, CFRPs with thermoset matrix have been historically used for structural applications (such as body panels, closures, and composite tubs) in both performance and high-end vehicles. This has been primarily due to the easy availability and processability of thermosets, as well as, relatively, better properties.

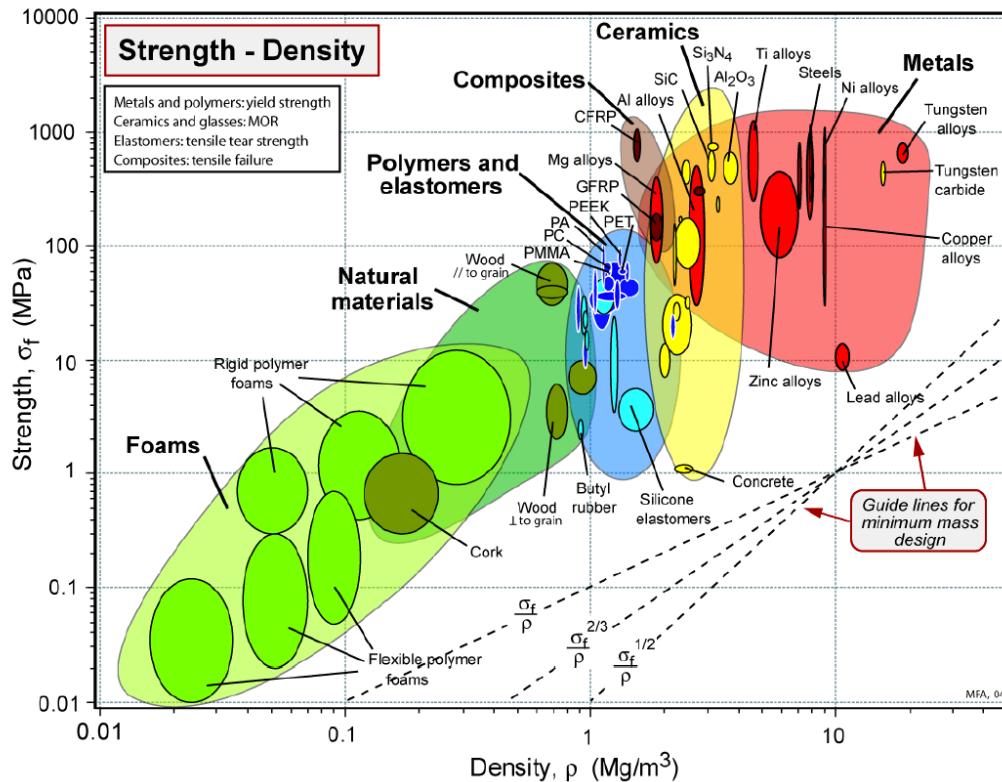


Figure 1.11 Ashby chart for strength vs. density. (image source¹⁶)

However, thermoset materials must be cured to polymerize and harden to their final shape – and this curing process is both slow and irreversible. Also, due to this curing mechanism, thermoset composites cannot be easily reprocessed or recycled¹⁷, which militates against the increasing requirement of recyclability of car components. Moreover, thermoset-based composites are typically (and preferably) joined in cars via adhesive bonding due to its excellent mechanical performance and low capital investment^{18,19}. Since most structural adhesives are based on thermosetting chemistry, the disadvantages of a curing/cross-linking mechanisms extend to the adhesives too: while structural adhesives can take between 2-6 hours to cure²⁰, spot welding of steel requires just a small fraction of this duration (< 30 seconds). This slow joining nature of adhesive bonding is an

additional and significant impediment towards its adaptation for mass production of vehicles, making it difficult to use thermoset-based composites on a larger scale in automotive structures.

Given the challenges mentioned above, associated with thermoset materials and their joining for automotive applications, there has been a growing interest in fiber-reinforced polymers involving thermoplastics as matrix material. While a few thermoplastic-based composites, such as carbon-fiber-reinforced polyether ether ketone (PEEK) and carbon-fiber-reinforced polyethyleneimine (PEI), have been previously used in the aerospace and space exploration industries, these have never been considered for automotive applications due to their extremely high cost and processing-related challenges²¹. However, the recent commercialization of novel processing techniques for fiber-reinforced polymers, such as compression molding and thermoforming, as well as the use of cheaper thermoplastic matrix such as polyamides, have together resulted in a renewed interest in the use of these systems in the automotive sector²². These developments have also ensured that thermoplastic-based composites exhibit similar levels of mechanical performance as thermoset-based composites, while also showcasing the benefits of thermoplastic materials, such as faster manufacturing cycle times, infinite shelf lives, better environmental resistance, improved toughness, and critically, recyclability^{23,24}. All these attributes make fiber-reinforced thermoplastic composites a highly desirable material system for automotive structural applications.

However, despite these advantages, two major limitations currently impede the use of thermoplastic-based composite systems in cars: high raw material cost, and slow joining speed²⁵. Of these, the higher cost of raw materials can be ascribed to the cost of carbon fiber reinforcement as well as the smaller supply chain and demand for these

composites. Moreover, the higher cost of carbon fiber reinforcement can, in turn, be attributed to the use of polyacrylonitrile (PAN) precursor and high energy requirement for carbonization of the precursor²⁶.

Substantial efforts are being made to reduce the cost of carbon fiber by using alternate precursors^{26,27} (such as lignin, pitch, and low-cost polymers) and more energy-efficient methods for carbonizing the fiber (e.g., using plasma arc furnace instead of convection oven²⁸). However, while existing research predominantly focuses on reducing the cost of thermoplastic-based composites, less attention is paid to the joining-related limitations associated with these systems. This is a major problem, since as shown in

Table 1.1, most automotive structures (currently manufactured) have around 150-400 individual parts, and the ability to join these parts structurally and quickly is a crucial requirement for desirable mechanical properties of an automotive structure. Moreover, apart from these mechanical performance requirements, mass-production of such joints necessitates that such joining is fast, repeatable, and easy to automate. Hence, this dissertation focuses on addressing these joining-related limitations, since it is only through effective redressal of both these limitations that the barriers for using these systems in mass-produced automotive structures can be significantly reduced.

1.4 Joining thermoplastic composites from a bird's eye perspective

At the highest level, most joints can be classified into two groups based on their joining intent as "*permanent*" and "*non-permanent*" joints. Within an automotive structure, most of the joints can be classified as *permanent joints*. However, with increasing environmental consciousness, it is essential to incorporate mechanisms (within joining

techniques) to disassemble these joints for recycling/repurposing, while also meeting all the performance and security requirements of a permanent joint. Apart from recycling, a certain degree of disassembly is also required to allow repair¹⁹. At present, most permanent joining technologies used for fiber-reinforced thermoplastics can be further classified into three groups: (a) Mechanical joints; (b) Adhesive joints; and (c) Welded joints.

1.4.1 Mechanical joining

Mechanical joints solely use mechanical force to create physical interlocking or frictional locking for joining individual parts. Common examples of mechanical joints include bolts, rivets, screws, and snap fits. The main advantages of mechanical joining are high speed, better out-of-plane performance, ease of disassembly, and no chemical alteration of parent material¹⁹. However, unlike for metals, composites are sensitive to localized loading, meaning that typical mechanical joining technologies, such as bolting, riveting, and screwing, are not desirable for structurally joining composite parts/components²⁹. To address this issue, much research has been undertaken on developing fasteners for composites, especially in the early 1980s, when several aircraft manufacturers sought to join composites using bolts and rivets mechanically³⁰.

In bolted, riveted, and screwed joints, the substrate material is subjected to very high localized shear and compression loading. In these loading modes, most of the force is transmitted to the matrix material. This causes premature delamination failures in the bearing region of composites²⁹. For this very reason, in most modern applications where mechanical joining is required for composites, it is accompanied by other joining techniques, such as adhesive bonding.

Apart from conventional mechanical joining solutions such as bolts, rivets, and screws, there is a growing interest in interlocking snap-fit features as a useful alternative. With the design flexibility offered by thermoplastics composites, it is feasible to incorporate surface features such as dovetails, balls, and sockets. Robert M.W. et al. has proposed several designs for such interlocking features³¹, as can be seen in Figure 1.12. While the concept of self-interlocking features is intriguing, no substantial work verifying their mechanical performance was found in the literature. Hence, finite element analysis (FEA) was used to verify the approximate mechanical strength of these features. With integrated post features and ball-socket features; mechanical performance is observed to be significantly lower (by 4-7%) compared to an adhesive-bonded joint. From this analysis, it is safe to assume that by themselves, these interlocking joints do not meet the requirements of structural joining. Hence, using these interlocking features as assembly aids in tandem with other joining technologies might be a more suitable and interesting approach, and has therefore been explored in this dissertation. Table 1.1.2 summarizes the advantages and disadvantages of mechanical joining.

Table 1.1.2: Advantages and disadvantages of mechanical joining

Advantages	Disadvantages
Fast cycle times	High-stress concentration on parent materials
High tolerance compensation ability	Lower in-plane shear performance
Easy Disassembly	The additional weight of the fastener
Better out of plane strength	Possibility for galvanic corrosion

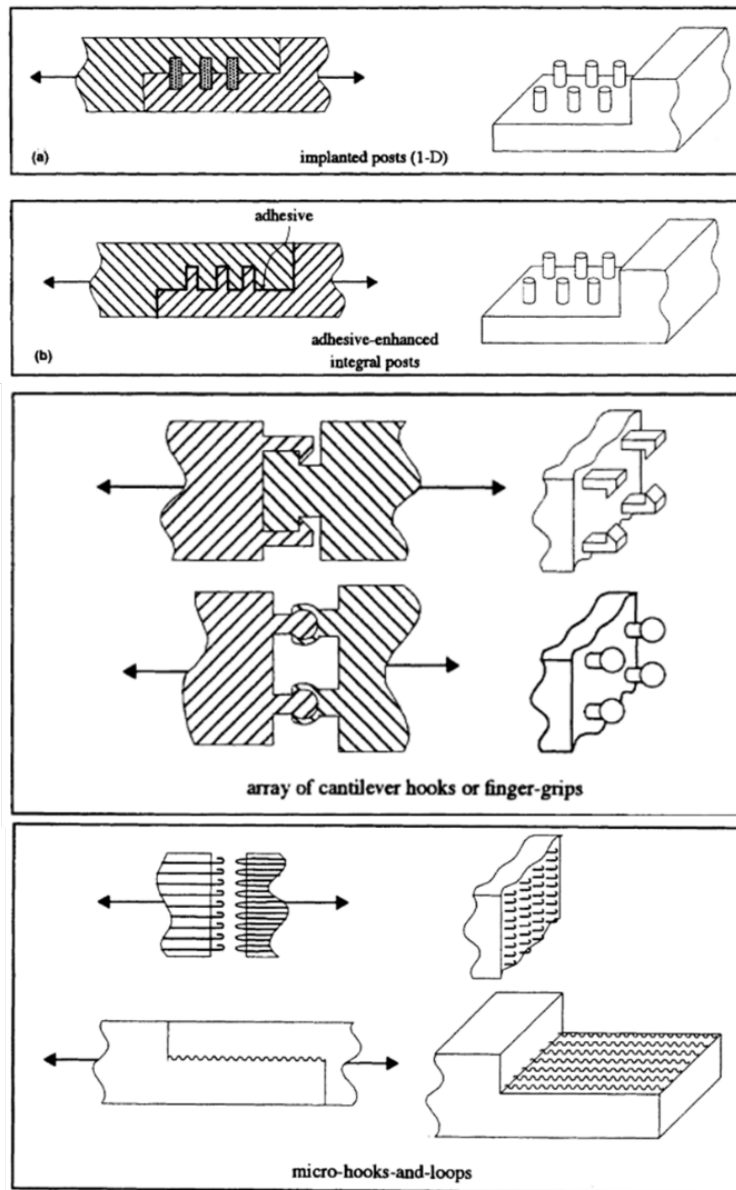


Figure 1.12: Mechanical interlocking features for composite structures. (Image source³¹)

1.4.2 Adhesive bonding

Adhesive bonding is the process of joining components (substrate) using a secondary material system (adhesive) via surface interactions. An adhesive bonds to the substrate either by chemical bonds, mechanical interlocking at the micro-scale, or a

combination of both mechanisms. A key advantage of adhesive joints is their large load transfer pathway: unlike mechanical joints, adhesive joints transfer load over a larger surface area, which in turn translates into well-distributed force on the load-bearing area of the substrate²⁸. Examples of conventional adhesive chemistries include epoxy, polyurethane, acrylic-based, methacrylate-based, cyanoacrylate, and silicone systems³². In addition to the base chemistry, most modern adhesives contain other components (less than 10% by volume) to modify various properties, such as adhesion promotion, thermal expansion, toughening, rheology and cure kinetics.

Several factors are critical to the selection of appropriate adhesive chemistry. One of these key factors is substrate compatibility. Most low-end thermoplastics (such as ABS, PP, PC, and PA) may be susceptible to stress cracking when in contact with solvents and adhesive systems with low molecular weight components³². A typical example of this effect is the whitening or blooming observed when cyanoacrylate adhesive comes in contact with PP³². Apart from chemical compatibility, thermoplastics are often more inert and have very low surface energy³³. Such low surface energy and inertness have an adverse effect on the bond strength of the joint³⁴. Upon considering these factors, only a few adhesive systems are suggested for bonding thermoplastic composites. In this dissertation (Chapter 7), various adhesive systems with different chemistries but similar strengths (as suggested by the manufacturer) were tested. Among these adhesive systems, modified methacrylate system performed significantly better than epoxy and polyurethane systems.

Another key factor to consider is that most adhesive systems are cured through chemical crosslinking, and reversing this crosslinked bond is difficult, if not impossible. Due to this, both end of life de-bonding and repairing are often challenging. The other major limitation of chemical crosslinking is its longer reaction time, with most structural

adhesive systems having curing time (for work handling) ranging from 10 minutes to 2 hours. Even after this duration, the cured joint is strong enough only to handle parts during assembly. To fully cure most adhesive systems to their full strength, additional time (ranging from 6 hours to 2 days) is often required. Table 1.1.3 summarizes the advantages and disadvantages of the adhesive bonding process.

Table 1.1.3: Advantages and disadvantages of mechanical joining

Advantages	Disadvantages
Better load distribution, and no stress concentration	Very long cycle times
Minimal weight penalty	Difficult to disassemble
Better fatigue performance	Difficult for non-destructive inspection
No galvanic corrosion	Sensitive to surface contamination and need extensive surface preparation

1.4.3 Fusion bonding

Fusion bonding or welding is a process where two components are joined together through chemical bonds under heat and pressure. In a typical fusion bonding process, both heat and pressure will cause a phase change from solid to melt phase, where atoms, ions or molecules attract each other and easily form a bond¹⁹. Fusion bonding is only possible in thermoplastic-based composites. Like adhesive bonding, most fusion bonding processes also use a large load transfer pathway to eliminate stress concentrations.

Fusion bonding is an established technology for pure thermoplastics that are used in most household and consumer electronics products. However, in composites, the very

high fiber content in polymer results in a drastic change in its thermal, electrical, and rheological properties, as well as in its surface structure. These changes drastically affect the process physics of conventional fusion bonding process³⁵. In the case of pure thermoplastic parts/components, fusion bonded joints can easily achieve the bulk properties of original part²⁵. Additionally, it is hard to introduce the reinforcement in the weld region during welding thermoplastic-based composites, which often leads to lower mechanical properties of the weld region vis-à-vis the bulk properties of the component³⁵.

Most common fusion bonding technologies are classified based on the heat source used. Three promising fusion bonding technologies for fiber-reinforced thermoplastic composites are: (a) Resistive welding; (b) Induction welding; and (c) Ultrasonic welding. Often, the cycle time for these welding processes is predominantly determined by two factors: (a) Heating time; and (b) Cooling time. Typically, most polymers have a narrow window for melt temperature, so it is essential that during the heating phase, the polymer in the interface region is within this narrow melt window. The time required to heat the polymer is often limited by the type of heat source used, the thickness of the component, and a total area of the joint.

With regard to cooling time, the degree of crystallinity of a polymer is directly related to the cooling ramp rates used³⁶. At faster cooling rates, the degree of crystallinity of the polymer decreases drastically, thereby affecting its overall mechanical properties. Due to this behavior, the cooling rate is often controlled to maintain a high degree of crystallinity.

With the recent interest in end-of-life recyclability, it is desirable to have this joint de-bond on command (i.e., when needed). Theoretically, this is possible for only a few

fusion bonding technologies. Table 1.1.4 summarizes the advantages and disadvantages of fusion bonding technologies.

Table 1.1.4: Advantages and disadvantages of mechanical joining

Advantages	Disadvantages
Better load distribution, and no stress concentration	Possibility of galvanic corrosion
Fast cycle times	Need more fixturing during the welding process
Very high mechanical properties	Energy-intensive process
De-Bonding for end of life recyclability is possible	

Down Selecting the Joining Approach

Mechanical fastening is not a preferred joining technology for fiber-reinforced polymers¹⁹; the local load concentration due to fasteners often leads to premature failure in the matrix material and act as crack initiation zone³⁷. Both fusion and adhesive bonding have larger load transfer area and thereby perform significantly better than mechanical joining. In addition to this, both adhesive and fusion bonding approaches have minimal additional weight when compared to mechanical joining.

With this, the two primary contenders for joining FRTPC materials are fusion and adhesive bonding. Two main limitations of adhesive bonding are a) long cycle times and b) challenging to separate/de-bond for end-of-life. Since most structural adhesives till date are based on thermosetting chemistry and rely on curing mechanics to solidify, their manufacturing cycle times are long. This long cycle time is highly undesirable for

automotive mass production and often act as a limiting factor for annual production volumes. Also, adding a thermoset adhesive for thermoplastic parts defeats the purpose of easy reprocessing/recyclability.

Given these limitations for both mechanical fastening and adhesive bonding, fusion bonding stands out as viable, joining technology for automotive thermoplastic composite structures.

In the subsequent chapter (Chapter 2), various fusion bonding processes are further elaborated in detail. When looking at these joining technologies from the perspective of automotive thermoplastic composite structures, resistive implant welding stands out due to its design and manufacturing freedom. Chapter 2 also summarizes the current state of research of resistive implant welding for fiber-reinforced thermoplastics and elaborates various research gaps.

2 LITERATURE REVIEW & GAPS

This chapter provides a brief overview of the various fusion bonding technologies adapted for thermoplastic composites. Based on the distinct advantages and drawbacks of these technologies, resistive implant welding (RIW) was chosen as the ideal candidate for automotive structures in this study. This chapter provides insights into the factors that led to this decision. Further, a thorough literature review was undertaken to identify the gaps associated with using RIW process for automotive structures and is presented in subsequent sections. Finally, two high-level hypotheses are proposed at the end of this chapter, along with a necessary research pathway and target metrics for validating the RIW process for automotive structures.

2.1 Overview of various fusion bonding technologies

Among the most promising fusion bonding technologies for fiber-reinforced thermoplastics are resistive welding, ultrasonic welding, and induction welding³⁵. A key difference between these technologies is the heat source used (to melt the polymer matrix) and the mechanism for joint consolidation. A brief description of all these technologies is provided in the subsequent sub-sections.

2.1.1 Resistive Implant Welding (RIW)

Resistive implant welding, also known as resistive welding or resistive fusion bonding, involves a porous conductive heating element that is sandwiched between two thermoplastic parts. Subsequently, the current is applied to the heating element, which in turn produces heat at the joint interface, as defined by Joule's law. Due to this heat, the material in contact with the heating element starts to melt and flow after the temperature

reaches a certain point (T_g for amorphous and T_m for semi-crystalline polymers). Upon ensuring the desired amount of material flow, current supply is shut down, and the joint is allowed to cool and solidify. During this entire process, clamping pressure is applied to the thermoplastic parts to ensure proper consolidation. Figure 2.1 shows a general schematic of the process, where the heating element is sandwiched between the two thermoplastic parts, and current is applied at the terminals of the heating element.

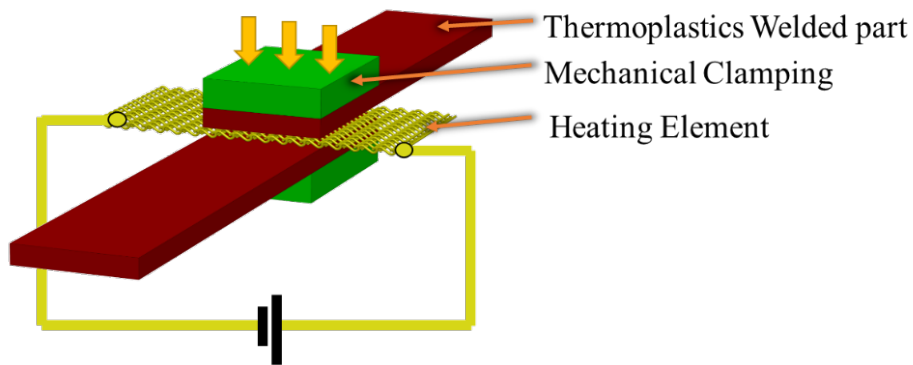


Figure 2.1 Resistive welding.

2.1.2 Ultrasonic welding

In the ultrasonic welding process, one of the workpieces (i.e., thermoplastic pieces) is mechanically vibrated at high frequency (20-40 kHz) using a welding horn, against the stationary workpiece (Figure 2.2). These high-frequency vibrations at the joint interface generate heat due to the surface and intermolecular friction³⁸. Once the material at the interface melts, oscillation is stopped, and the material is allowed to cool back to room temperature, thus causing the formation of the fused joint. Ultrasonic welding has been extensively used for joining commodity plastics^{39,40,41}. A large amount of research has also been conducted to adapt this process for fiber-reinforced thermoplastics^{38,40,42-45}.

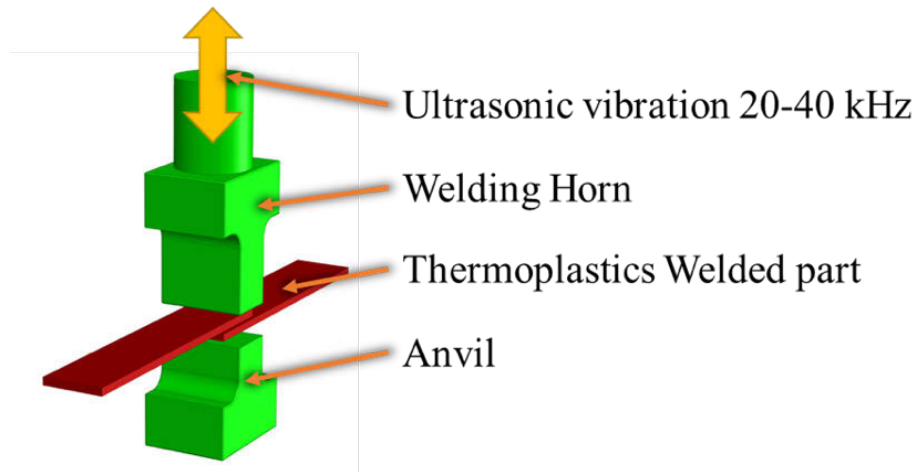


Figure 2.2 Ultrasonic welding.

2.1.3 Induction welding

Induction welding is similar to resistive welding, where the porous resistive heating element (in RiW) is replaced with a porous electromagnetic susceptor (Figure 2.3). The susceptor is the material that absorbs electromagnetic energy and converts it to heat. Typically used susceptor materials include stainless steel and other ferrous materials. Electromagnetic energy, such as microwave, is used to heat the susceptor till T_m for semi-crystalline and T_g for amorphous polymers. Once the material at the joint interface reaches this temperature, it flows through the susceptor. After attaining the desired amount of material flow, the electromagnetic source is turned off, and the bond region is cooled to solidify. Like for resistive welding, during this entire process, the parts are clamped together to ensure proper consolidation.

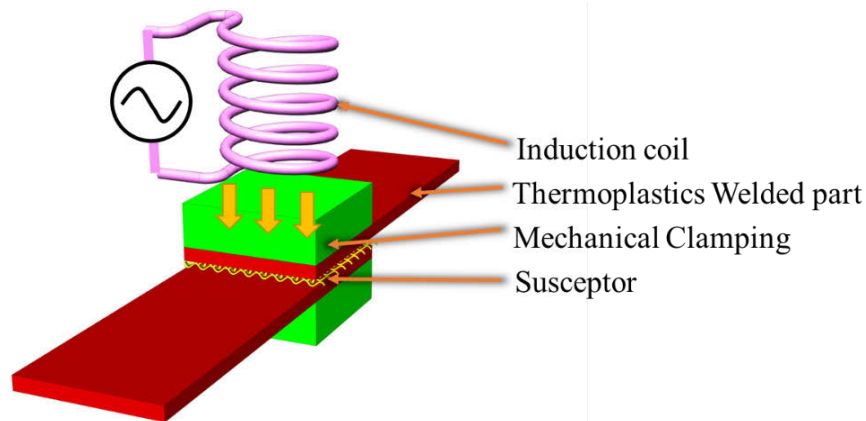


Figure 2.3 Induction welding.

2.2 Down selection of fusion bonding technology for automotive structures

Automotive structures are often complex to engineer, as they need to satisfy several requirements, such as stiffness, strength, crash energy management, occupant/component packaging, styling, cost, reparability, and recyclability. Due to these performance and geometric requirements, most automotive structures are manufactured from several hundred individual components that are subsequently joined. Such joints in automotive structures can be classified, based on their functional intent, into structural or nonstructural joints. This dissertation primarily focuses on using fusion bonding processes for structural joint applications.

The requirements for structural joints can be broadly classified into three categories (Figure 2.4): (a) manufacturability; (b) design freedom; and (c) mechanical performance. Furthermore, several individual metrics can be associated with these three categories (Figure 2.4). Of these, metrics such as ease of automation, quality control, cost, toughness, and NVH were not considered for down selection due to the lack of historical

information. Material compatibility was also not considered due to the similarity between the various fusion bonding technologies.

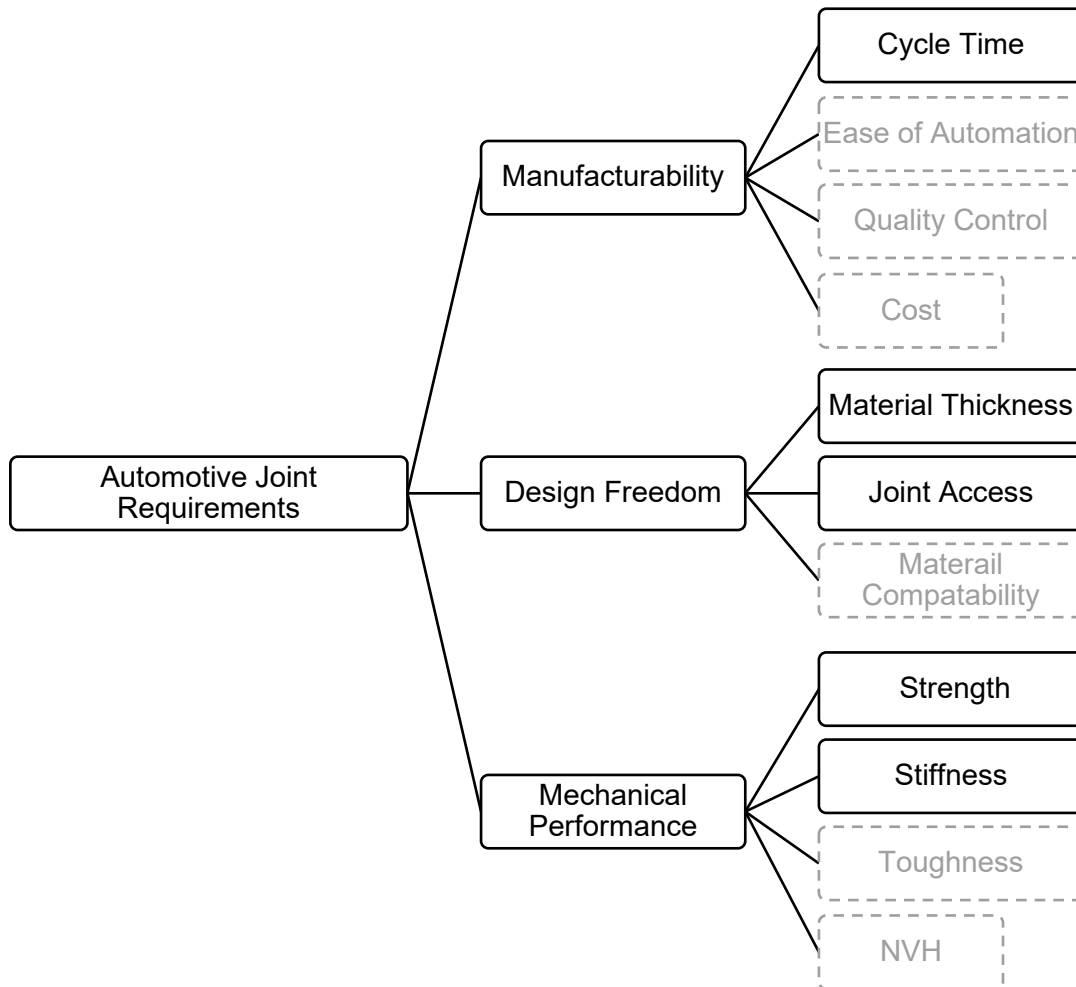


Figure 2.4 Classification of Automotive joints requirements.

2.2.1 Determining Cycle time

In the automotive industry, “Throughput per hour” (TPH) is commonly used to represent the target production rate of a body shop. TPH represents the total number of vehicles produced per hour. The typical TPH for most mass-produced passenger cars is

40 ± 15 units⁴⁶. Due to the higher cost of fiber-reinforced thermoplastic composites (FRTPCs), it is acceptable to assume that these materials will most likely be used in expensive vehicles. For such expensive vehicles, the typical TPH is 15-30 units. Using these TPH values, the maximum allowable cycle time for low-volume mass-produced vehicles are typically 120-240 s (Cycle time = 3600/TPH).

Table 2.1 Cycle times of various fusion bonding technologies from literature.

Welding Method	Author	Material	Cycle time (seconds or s)
Resistive Welding	Dube, M., et al ⁴⁷	CF-PEI	60
	Yerra, Veera Aditya Pilla, Srikanth ⁴⁸	CF-PA66	150
	Dubé, M. Hubert, P. ⁴⁹	CF-PEEK	200
	Shi, H. Villegas, I. F. ⁵⁰	GF-PEI	250
Induction welding	Ahmed, Tahira J., et al ⁵¹	CF-PEI	180
	Farahani, Rouhollah Dermanaki Dubé, Martine ⁵²	CF-PPS	90-110
Ultrasonic welding	Fernandez, I & Stavrov, D ³⁸	CF-PEI	6.5
	Irene Fernandez Moser, Lars, Et al ⁵³	CF-PPS	4.43

Literature shows that most fusion bonding processes have cycle times under 240s (Table 2.1). While these cycle times are promising, they do not entirely reflect the actual joining speed in a body shop. Hence, linear joining speed (LJS) is used as a metric to compare the various above-mentioned fusion bonding technologies. LJS reflects the total time required to join a flange of unit length.

To estimate the LJS for different fusion bonding technologies, we make the following three assumptions:

- Total flange length for a body side outer: 15,500 mm (Figure 2.5)
- Flange width: 25 mm
- Bond width: 20 mm

Based on these assumptions, the time needed for welding carbon-fiber-reinforced polyethyleneimine (PEI) as substrate material through the aforementioned fusion bonding techniques in available literature is as follows:

- Ultrasonic: 6.5 s for 381 mm² (Fernandez, I & Stavrov, D³⁸)
- Resistive Welding: 150 s (area independent) (Dube, M., et al⁴⁷)
- Induction Welding: 200 s (area independent) (Ahmed, Tahira J., et al⁵¹)

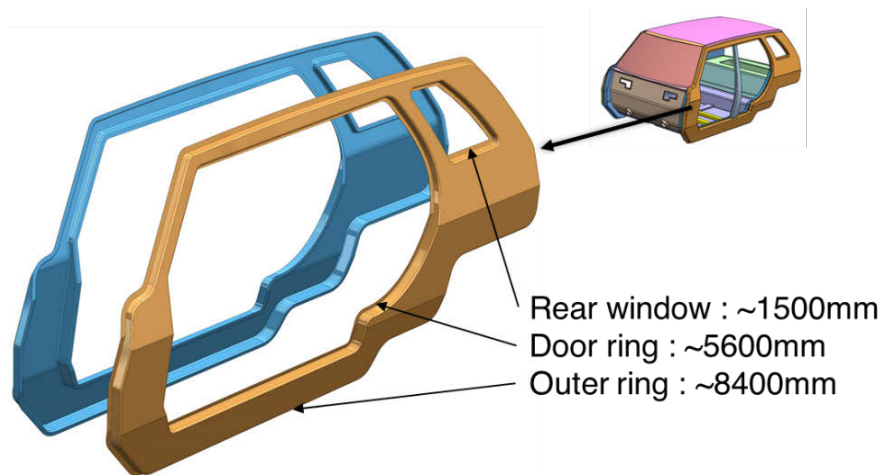


Figure 2.5 Total flange length for a body side outer.

The linear joining speed of the three fusion bonding techniques, based on the above-mentioned assumptions, is calculated and explained below.

With regard to ultrasonic welding, it is assumed that an industrial robot with an ultrasonic welder as the end effector is used to perform welding, while the components are held in weld fixtures. The welding robot welds the flanges in small segments and moves to the next location and repeats this sequential process. Due to the large size of the body side outer, typically two industrial robots are used on each side of the body shop. As calculated from Eq 1, the typical LJS for ultrasonic welding is around 3.175 mm/s.

$$LJS = \frac{\text{number of robots} \times 381 \div \text{width of the bond}}{(\text{Clamping time} + \text{Welding time} + \text{unclamping time} + \text{reindexing time})} \quad \text{Eq 1}$$

$$LJS (\text{ultrasonic welding}) = \frac{2 \times 381 \div 20}{(1.5 + 6.5 + 1 + 2)} = 3.175 \text{ mm/s}$$

Unlike ultrasonic welding, resistive implant welding (RIW) is a bulk joining process. Large joint lengths can theoretically be welded in a single sequence. The heating element can be separated into several segments to account for part complexity. However, weld current can be simultaneously applied on multiple segments of the heating element, thereby making the RIW process independent of total bond length. Generally, resistive welding process involves three steps: (a) Applying the clamping pressure; (b) Welding; and (c) Un-clamping the part. For body side outer, the LJS of RIW process can be calculated using Eq 2, and is obtained as 79.5 mm/s.

$$LJS (RIW) = \frac{\text{Total bond length}}{\text{Clamping time} + \text{welding time} + \text{unclamping time}} \quad \text{Eq 2}$$

$$LJS (RIW) = \frac{15,500}{10 + 180 + 5} = 79.5 \text{ mm/s}$$

Induction welding is very similar to RIW process, the critical difference being the source of (heat) energy used. Further, both the RIW and induction welding process share the advantages of being bulk joining processes. However, an important factor that affects

the induction welding process is the slightly slower rate of heating used due to higher losses during induction energy transfer. Hence, a similar equation to that for RIW process is used to calculate the LJS for induction welding (Eq 3), and the obtained LJS value is 72.1 mm/s.

$$LJS (Induction) = \frac{\text{Total bond length}}{\text{Clamping time} + \text{welding time} + \text{unclamping time}} \quad \text{Eq 3}$$

$$LJS (RIW) = \frac{15,500}{10 + 200 + 5} = 72.1 \text{ mm/s}$$

2.2.2 Effect of substrate thickness

In automotive structures, it is common practice to have parts with varying thickness for optimizing both performance and weight considerations. Since most composite automotive structures are typically between 1-5 mm thick, it is vital to select a joining process that is agnostic to substrate thickness. Hence, it is necessary to compare all three fusion bonding techniques in this aspect.

In ultrasonic welding, it is desirable to ensure that the thickness of the substrate (in contact with welding horn) be less than 6.35mm⁵⁴. This is because any increase in substrate thickness increases the energy propagation distance from the welding horn to weld interface, thereby significantly enhancing hysteresis losses (in the material) and in-plane dispersion of weld energy. For the very same reason, most ultrasonic welds are often limited to components with wall thickness less than 6.25 mm.

In the case of resistive implant welding, substrate thickness does not affect weld quality. However, the thermal mass of substrate increases with its thickness, resulting in higher energy requirement as well as the need for longer heating and cooling times during the entire weld process.

Lastly, in induction welding, a conductive coil is used to create an induction field near the joint interface. For thicker materials, the attenuation of the induction field drastically increases. Such attenuation is further exaggerated if the substrate material is conductive (i.e., has carbon fiber reinforcement)⁵³, making it challenging to focus the induction field on the joint interface, and thereby increasing the probability of bad welds.

In summary, ultrasonic welding and induction welding are sensitive to substrate thickness, while there is a negligible influence of substrate thickness on weld quality in case of resistive implant welding.

2.2.3 Mechanical performance of various fusion bonding technologies

Most fusion bonding technologies outperform commercially available structural adhesives for fiber-reinforced thermoplastic composites (FRTPCs). In ultrasonic welding, there is no foreign material (heating element or susceptor) at the joint interface, thereby increasing the active load transfer area. This higher load transfer area subsequently leads to better mechanical performance vis-à-vis other fusion bonding technologies, as shown in Table 2.2. Both RIW and induction welding processes have similar mechanical performance, which is on expected lines⁵¹. The slight decrease in weld strength in both RIW and induction welding processes can be attributed to the respective presence of porous heating element and susceptor in these techniques. For most metal heating elements and susceptors used in literature, only 35-50% of surface area is open for polymer flow^{47,55-57}.

Table 2.2 Lap shear strength of various fusion bonding technologies from literature

Bonding method	Author	Substrate Material	Lap shear strength (MPa)
Benchmark Adhesive (3M DP 190)	Yerra, Veera Aditya Pilla, Srikanth ⁴⁸	CF-PA66	5.9
Adhesive (3M DP 810)	Yerra, Veera Aditya Pilla, Srikanth ⁴⁸	CF-PA66	7.7
Benchmark Adhesive (Plexus MA 530)	This dissertation	CF-PA66	24.4
Benchmark Adhesive (Plexus MA 530)	Yarlagadda, S Heider, D, et al ²⁰	CF-PA66	22.6
Resistive Welding	Tan, S Zak, G ⁵⁸	GF-PP	20.0
	Warren, K. C. Et al. ⁵⁹	GF-PET	25.6
	Villegas, Irene Fernandez, et al ⁵³	Cf-PPS	23.3
	Hou, M., Ye, L. Mai, Y. W. ⁶⁰	CF-PEI	31.0
	Yerra, Veera Aditya Pilla, Srikanth ⁴⁸	CF-PA66	30.3
	Ageorges, C ⁶¹	CF-PEI	36.3
	Ahmed, Tahira J. Stavrov, Darko Bersee, Harald E.N. ⁵¹	CF- PEI	29.6
Induction welding	Villegas, Irene Fernandez, et al ⁵³	CF-PEI	27.3
	Ahmed, Tahira J. Stavrov, Darko Bersee, Harald E.N. ⁵¹	CF-PEI	31.0
Ultrasonic welding	Villegas, Irene Fernandez, et al ⁵³	CF-PEI	27.0
	Fernandez, I Stavrov, D ³⁸	CF-PEI	36.0
	Todd, Stephanie M ⁶²	CF-PEEK	35.0
	Schwartz, M M ⁶³	CF-PEI	38.0

The consequence of this low open area is that in most RIW and induction welding processes, less than 50% of the joint surface area is used for polymer-to-polymer bonding. From conventional wisdom, one might expect a similar reduction in joint strength with a reduction in the active load transfer area. However, this is not true; only a 5-15% reduction in bond strength is observed for either process when compared to ultrasonic welding. This can be attributed to the higher melt depth^{45,64} and load transfer via metal mesh for both RIW and induction melting processes.

In summary, ultrasonic welding outperforms RIW and induction welding by a small margin, while all fusion bonding technologies outperform commercially available structural adhesives. One forewarning is that here, only lap shear strength has been used to compare these technologies. This can be attributed to the lack of research on out-of-plane strength for fusion bonding technologies.

2.2.4 Summary

The requirement for sequential processing, and very slow linear joining speed (LJS) of ultrasonic welding renders this process undesirable for automotive mass production, irrespective of its superior mechanical performance. During induction welding, it is essential to not have any metal/conductive parts (other than the susceptor) within the induction field. However, most automotive fixtures are made from common metals, such as steel and aluminum. These requirements complicate the fixture design and increase the cost by forcing the use of ceramics and rigid polymers for fixturing.

From the metrics discussed above, RIW process offers a good trade-off between manufacturing cycle time, design freedom, and mechanical performance for automotive applications, as shown in Table 2.3.

Table 2.3 Down selection of weld processes.

Metric	Resistive welding	Induction welding	Ultrasonic welding
Cycle time	79.5 mm/sec ++	72.1 mm/sec +	3.2 mm/sec -
Effect of substrate thickness	None ++	Moderate +	High -
Mechanical Performance (LSS for CF-PEI)	36.3 +	31.0 +	38.0 ++

++ Very good + Good - Bad

2.3 Hypotheses

At the highest level, this dissertation proposes two hypotheses. In order to verify these hypotheses quantitatively, several secondary research statements are proposed in the following sub-sections. The idea is to test all of these hypotheses.

2.3.1 Hypothesis 1

“It is hypothesized that fiber reinforced thermoplastic composites can enable considerable mass reduction for automotive structures in terms of manufacturability, mechanical properties, and cycle times”

Hypotheses one implies the following statements:

- I. **Research statement (RS) 1:** Fiber-reinforced thermoplastics have better specific mechanical properties than most automotive structural materials.

- II. **RS 2:** Fiber-reinforced thermoplastic structures offer adequate applicability in terms of mechanical performance, design freedom (formability), and cycle time for mass-produced automotive structures.

2.3.2 Hypothesis 2

“It is hypothesized that resistive implant welding yields enhanced joining performance for fiber-reinforced thermoplastic composites in automotive structures.”

Hypotheses two implies the following statements:

- I. **RS 3:** Resistive welding can match or outperform the mechanical performance of any commercially available joining methods for fiber-reinforced thermoplastics.
- II. **RS 4:** This joining technology is scalable for part size and production volumes required for mass-produced automobiles.

2.4 Literature review and Research Gaps

This section of the dissertation explores research relevant to fiber-reinforced thermoplastics and RIW process in order to set a baseline understanding of both these aspects. Also, this section elaborates the various gaps in the literature, since these gaps must be carefully considered in order to verify the above-mentioned hypotheses.

2.4.1 State-of-the-art fiber reinforced thermoplastics (RS 1 & RS 2)

Fiber-reinforced thermoplastics were introduced on a commercial scale by Fokker aerospace, a Dutch aerospace company⁶⁵, in the late 1980s. Thermoplastic matrix

materials, such as poly-ether-ether-ketone (PEEK), poly-ether-imides (PEI), and poly-phenylene-sulfide (PPS), in conjunction with carbon fiber reinforcements, are some of the early FRTPCs available in commercial markets. These matrix materials offer excellent performance but are accompanied by higher costs and processing-related challenges⁶⁵. The advantages of such thermoplastic composites over their thermoset counterparts are higher toughness, better resistance to fire, lower manufacturing cycle times, and recyclability⁶⁶. However, competing material systems, such as thermoset composites, offer similar performance at a lower cost and with significantly easier processability when compared to these thermoplastic composites, with high performance polymer matrixes (PEEK, PPS and PEI). This explains the widespread use of fiber reinforced thermoset composites material systems in the 1980s and 1990s.

By the end of the 1990s, acknowledgment of environmental responsibility prevailed within the research community, leading to a resumed interest in FRTPCs, as reinforced by the steady growth in research publications and patents relevant to these systems (Figure 2.6). However, these publications and patents mostly restricted the use of FRTPCs to the aerospace sector, mainly due to the high cost of raw material.

However, with a substantial increase in the worldwide production of carbon fiber and a strong push for higher performance and fuel economy in automobiles⁶⁷, interest in composite materials as a lightweight material slowly gained traction in the automobile industry. In the 2000s, carbon fiber reinforced thermoset (epoxy) was widely adopted in motorsports and high-performance automobiles. However, higher costs and slow manufacturing cycle times of thermosets have prevented their widespread use in passenger vehicles.

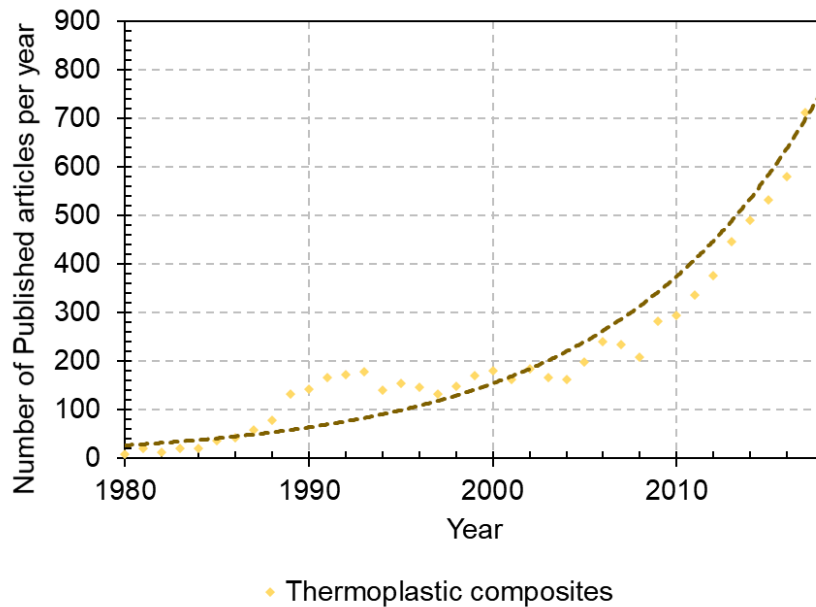


Figure 2.6 No. of published articles vs. Publishing year fro FRTPC.

In parallel, a substantial increase has been observed in research for improving the compatibility of carbon fiber reinforcement (via surface treatment) with low-cost engineering-grade thermoplastics, such as polyamides (PA), polymethylmethacrylate (PMMA), and polycarbonate (PC)⁶⁸. Surface treatments, such as nitric acid treatment⁶⁹, oxyflourination⁷⁰, and oxygen plasma treatment⁷⁰, have drastically improved the interfacial strength between the carbon fibers and polymer matrix. Due to such higher interfacial strengths, FRTPCs with engineering-grade thermoplastic matrix (PA) have been observed to exhibit mechanical performance^{71,72} comparable to that of thermoset matrix (epoxy)-based composites.

Interestingly, research published till date mainly focuses on optimizing the mechanical performance of carbon fiber reinforced polyamides by controlling processing parameters such as fiber volume fraction⁷², fiber morphology⁷¹, fiber surface treatment⁶⁸,

and fiber length⁷³. The resultant consequence is the creation of a large number of FRTPC material variants, whose mechanical properties range from being slightly better than pure polymer to being stronger than high strength steel. Further, these materials use different manufacturing processes and have varying design freedom, making it harder to decide on the material to be chosen. This confusion is sought to be addressed in this dissertation by mechanically characterizing all these major variations and organizing the information using easily understandable metrics (Chapter 3 & RS 1).

Till date, FRTPCs have been confined to semi-structural applications, such as interior brackets, semi-structural panels, and truck bed liners. However, the application scope of these material systems is much broader. Yarlagadda S. et. al⁷⁴ have successfully developed and tested a B-pillar with carbon fiber reinforced PA66 that meets challenging crash requirements during a side impact deformable barrier test while being 60% lighter than the baseline steel pillar. In this B pillar, they used unidirectional tape in 0° and 45°/-45° configuration to progressively buckle and retain adequate structural integrity after the crash test (Figure 2.7). However, this study suffers from two major limitations: (a) Non-inclusion of integration features, such as cut-outs for seat belt mechanism, bolt holes for rear door hinges, and striker plate for the front door; and (b) Non-consideration of other load cases, such as pole impact and seat belt anchorage. Despite these limitations, this study successfully illustrates the effectiveness of FRTPCs in automotive structures.

In this dissertation, a side-closure (car door) was chosen as a virtual test case. In this process, a baseline steel door was redesigned with FRTPC, and the decrease in weight was evaluated while keeping the static and crash performance of the door constant (Chapter 4). This virtual test case was undertaken to evaluate the limitations and application potential of FRTPCs.

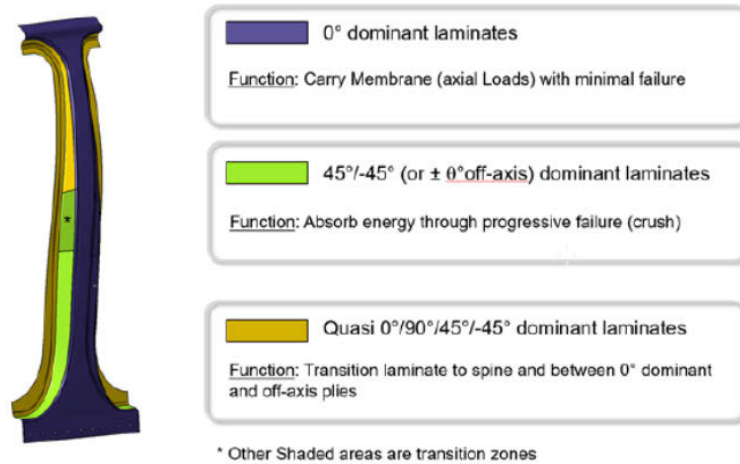


Figure 2.7 FRTPC B-Pillar design by Yarlagadda, S. et al., (Image source⁷⁴)

2.4.2 State-of-the-art in Resistive Implant Welding (RS3, RS4, & RS5).

There has been a keen interest in fusion bonding technologies for FRTPCs ever since their introduction³⁵. The life cycle of research of RIW process can be broadly classified into six phases (Figure 2.8). Most research for RIW processes to date generally falls under the first two phases (Feasibility and Processing). However, there are a few examples of research focusing on issues in the last two phases (i.e., series production research and application research), most of which focus primarily on aerospace applications and FRTPCs that use a high-performance polymer matrix. Thus, there is a vacuum of research on RIW joining of mid-tier FRTPCs for the last four phases. This dissertation tries to address these research gaps for joining mid-tier FRTPCs using the RIW process in the automotive context.

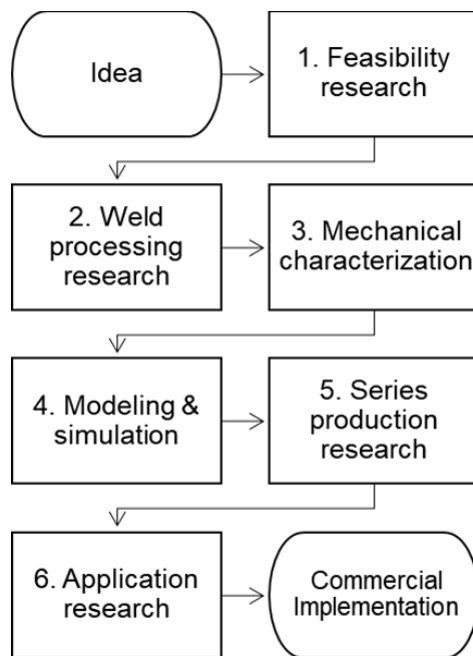


Figure 2.8 Research life cycle of RIW joints.

2.4.3 Feasibility and Processing research

Most applications/research to date primarily focus on joining high-performance polymer matrix materials (such as PEEK, PEI, and PPS) with continuous reinforcements (UD & Woven) ⁷⁵ (Table 2.4). Generally, such high-performance polymers are ~ 15-20 times more expensive than engineering polymers such as polyamides (for instance, PEEK costs ~ \$25/lbs, while PA 66 costs ~ \$1.4/lbs)⁷⁶. With such vast disparity in costs and greater processing-related challenges associated with high-performance polymers, only FRTPCs with engineering polymer matrix materials (such as PA6, PA66, and PC) can be viable for commercial, automotive applications.

Moreover, attributes such as melt viscosity^{77,78}, degree of crystallinity³⁶, and mechanical properties are significantly different for high-performance polymers and

engineering polymers. All these factors directly impact the performance and processing of RIW joints.

In a RIW joint, the primary load path between two substrates is the polymer matrix, so⁷⁵ any reduction in the mechanical performance of this matrix directly affects the mechanical performance of the joint. For reference, the modulus of PA 66 is ~ 2.1 GPa⁷⁹ (yield strength ~ 65 MPa)⁷⁹, whereas, for polymers like PEEK, it is ~ 4.5 GPa⁸⁰ (yield strength ~ 135 Mpa)⁸⁰. This massive reduction in mechanical properties warrants a question: *can the mechanical performance of RIW joints for substrates with materials such as CF-PA66 ever meet the performance of structural adhesives?*

The lower melt viscosity of engineering polymers⁷⁷ has both favorable and adverse effects on the welding process. Due to lower melt viscosity, the polymer can easily flow through the heating element and into surface crevasses, thereby decreasing the void content in the weld region. On the other hand, with lower melt viscosity, there is more probability for matrix squeeze out, as pointed out by Nonhof, C. J. et al.⁸¹, thereby leaving dry fibers in the weld region. The presence of any dry fiber in the weld region will adversely affect mechanical properties⁵⁶. Last but not least, low melt viscosity can often lead to fiber movement in the joint region, which is not desirable.

The other gap in the literature is the lack of research on the effect of reinforcement type on the mechanical performance of RIW joints. This gap can be attributed to the same reason: most composite materials used in aerospace applications have continuous reinforcements (Woven or UD). As shown in Table 2.4, most of the research on RIW process predominantly focuses on FRTPCs with continuous fiber reinforcements. In automotive applications, FRTPCs with discontinuous reinforcements, such as non-woven

and chopped injection molded (long fiber reinforced thermoplastics: LFTs & Short fiber reinforced thermoplastics: SFTs) are of keen interest due to their lower cost and higher design freedom. It is hypothesized that RIW joints of FRTPCs with discontinuous fiber reinforcement may have better mechanical properties than FRTPCs with continuous fiber reinforcement due to fiber migration and intertwining in the bond region. This behavior was earlier reported by Bates, P. J. et al.⁸² upon welding long glass fiber reinforced polypropylene. However, one limitation of this study was that mechanical performance was evaluated via lap shear compression test – unlike most other studies of similar nature on other material systems. Yet, the rare combination of the material tested and the test process itself makes it hard to compare this study with other research published till date.

Hence, to answer these unknown questions, this dissertation (Chapter 7) experimentally evaluates the mechanical properties of RIW joints of CF-PA66 and CF-PA6 substrates with various types of fiber reinforcements. Chapter 7 dwells deeply on this characterization process and discusses finite element models for these RIW joints.

Table 2.4 Literature sorted by substrate material.

Welding Method	Author	Reinforcement	Matrix	Matrix type	Reinforcement type
Resistive Welding	Tan, S, Zak, G ⁵⁸	Glass fiber	PP	Semi-Crystalline	Continuous
	Shi, H. Villegas, I. F., Bersee, H. E N ⁵⁶	Glass fiber	PEI	Amorphous	Continuous
	Hou, M. Ye, L. Mai, Y. W. ⁶⁰	Carbon fiber	PEI	Amorphous	Continuous
	Shi, Huajie, Villegas, Irene Fernandez, Et al ⁸³	Glass Fiber	PPS	Semi-Crystalline	Continuous
	Warren, K. C. Lopez-Anido, R. A. et al. ⁵⁹	Glass Fiber	PET	Semi-Crystalline	Continuous
	Ageorges, Christophe Ye, Lin ⁸⁴	Carbon Fiber	PEEK	Semi-Crystalline	Continuous
	Zammar, Imad Ali, Mantegh, Iraj, et al. ⁸⁵	Glass Fiber	PP	Semi-Crystalline	Continuous
	Villegas, Irene Fernandez, Bersee, et al. ⁸⁶	Glass Fiber	PEI & PPS	Semi-Crystalline	Continuous
	Dubé, M. Hubert, P. et al. ⁴⁷	Carbon Fiber	PEEK	Semi-Crystalline	Continuous
Induction Welding	Bates, P. J. Tan, S. Et al ⁸²	Glass Fiber	PP	Semi-Crystalline	Discontinuous
	Ahmed, Tahira J. Stavrov, Darko ⁵¹	Carbon Fiber	PEI	Amorphous	Continuous
	Matthews, D. Landgrebe, D. Drossel, W.-G. ⁸⁷	Glass Fiber	PA6	Semi-Crystalline	Continuous
Ultrasonic welding	Farahani, Rouhollah Dermanaki Dubé, Martine ⁵²	Carbon fiber	PPS	Semi-Crystalline	Continuous
	Fernandez, I, Stavrov, D ³⁸	Carbon Fiber	PEI	Amorphous	Continuous
	Wang, X. ⁴⁵	Carbon Fiber	PEEK	Semi-Crystalline	Continuous

Mechanical characterization.

Mechanical requirements of automotive structures are very diverse and often have conflicting objectives. For instance, the front module of an automotive structure must be stiff for good handling and NVH but must be less stiff and ductile for lowering deceleration during a frontal impact. These diverse mechanical requirements at the structural level translate directly to most joints within the body-in-white (BiW). Since most research published to date predominantly focusses on developing and optimizing weld processing, researchers often pick the lap shear tension test for mechanical evaluation. This choice of testing mode can be attributed to the simplicity of the test method. However, it does not provide the required information required to engineer BiW structures. Most adhesives, welded joints, or any area-based joining technology can experience any of the three failure modes, or even a combination of them (Figure 2.11). These failure modes are as follows:

- a) Mode 1: Normal loading or peel strength
- b) Mode 2: In-plane shear or lap shear strength
- c) Mode 3: Out of plane shear

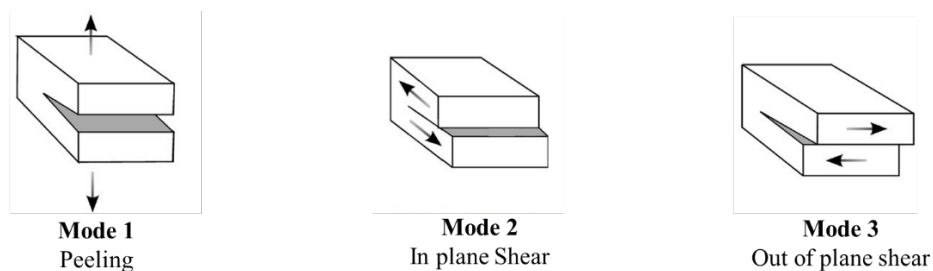


Figure 2.9 Typical failure modes for structural joints.

Due to geometric similarities between RIW joints and adhesive joints, using the methodology for characterizing adhesive joints is a good starting point. Mechanical

characterization of adhesives can be broadly divided into two approaches: (a) Bulk material characterization; and (b) In-situ material characterization⁸⁸.

In bulk material characterization, the adhesive is generally molded into standard test coupons and characterized independently of the substrate material (Figure 2.10). While doing so, some assumptions have to be made about the failure of the adhesive. These are (a) The failure is always cohesive; (b) The adhesive does not behave like a thin film, and (c) Strain-at-failure of adhesive must be higher than that for the substrate. Historically, this approach has worked well for characterizing and modeling structural adhesives for metal substrates and has produced sufficiently accurate results without the complexity of in-situ characterization⁸⁸. More often, most researchers often use a combination of both these approaches (bulk and in-situ characterization) to characterize adhesive performance⁸⁸ mechanically.



Figure 2.10 Tensile samples for bulk characterization of adhesive. (image source⁸⁹)

In in-situ characterization, the adhesive is tested with substrate materials. In these testing scenarios, identifying the true strain on the adhesive joint is highly challenging. The

force-displacement plots obtained from in-situ characterization include displacement in the substrate material, adhesive bond region, and interfacial stiffness between the adhesive and substrate. However, this approach yields results that are more representative of the real world performance⁸⁸.

In case of RIW joints, there is no possibility of bulk characterization for the following reasons: (a) First, the weld region can be independently produced without substrate materials; and (b) Second, the primary mode of failures are interfacial⁷⁵. For developing finite element models for RIW joints (or adhesive joints), both Mode 1: Peel strength and Mode 2: Lap shear strength are essential²⁰. However, as previously mentioned, most research, if not all, only tests Mode 2 (lap shear) performance. To address this aspect, in this dissertation, a double cantilever test approach is used to characterize Mode 1 performance.

For modeling RIW joints, a cohesive traction separation law might be a suitable approach⁹⁰. However, no literature is available that sheds light on the best approaches to develop non-linear finite element failure models simulation RIW joints. To address this issue, in Chapter 7, a methodology for in-situ mechanical characterization and finite element modeling approaches are further discussed in detail.

2.4.4 Summary of Gaps:

Gaps relevant to Hypothesis 1: Dealt with a broader manner

- i. No comparative database is publicly available on the mechanical performance of various FRTPCs, ranging from short fiber reinforced thermoplastics to unidirectional fiber-reinforced thermoplastics, characterized under identical testing

- conditions. In addition, there is no guide to aid the selection of specific FRTPCs with regard to mechanical performance requirements.
- ii. Most available examples for FRTPC automotive components are either semi-structural or representative design (i.e., these geometries are only a vague representation of the real parts, and often exclude integration features that might affect their performance)

Gaps relevant to Hypothesis 2: (Deep Dive)

- i. There is a lack of adequate research on understanding the processing and performance of RIW joints for FRTPCs with engineering polymer matrix (PA 66) and discontinuous fiber reinforcement.
- ii. There is a lack of sufficient understanding regarding the behavior of RIW joints under Mode 1 (Peel strength) fracture modes.
- iii. There is no research or methodology established to mechanically characterize, develop, and simulate finite element models of RIW joints in large non-linear load cases. (Automotive crash tests are an example of large non-linear load cases.)
- iv. While there is a good understanding about processing times of resistive implant welding, there is no proper understanding of research that evaluates its' influence at the manufacturing plant level, especially at the automotive body shop level.
- v. There is no understanding of the resilience of RIW process to common body shop contaminants.
- vi. There evaluation of joint repair strategies and it's effect on mechanical performance.

2.5 Pathway to verify research statements & address gaps

This section provides a brief overview of the approach used to verify the above-mentioned hypotheses (Section 2.3) with corresponding research statements and evaluation metrics. This pathway also acts as a guideline for the organization of this dissertation.

2.5.1 RS 1 (Chapter 3): *Fiber-reinforced thermoplastics have better specific mechanical properties than most automotive structural materials.*

- **Evaluating metrics for RS 1:**

- FRTPCs have better specific strength and specific stiffness in comparison to conventional automotive structural materials.

- **Tasks for RS 1:**

- Fiber-reinforced thermoplastics are a very diverse set of material systems. As seen in Figure 2.11, the first task in hand was to identify/select the subset of thermoplastic composites which are suitable for automotive structures. Subsequently, the next step was to procure commercially available material samples and conduct standardized mechanical characterization of these samples in accordance with ASTM standards. Using this data, the final task was to develop a database and finite element material cards for each of these material systems for further use in Chapter 4.

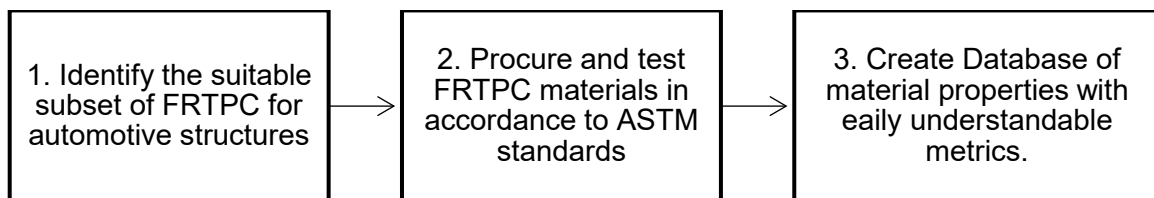


Figure 2.11 Tasks for verifying RS 1.

2.5.2 RS 2 (Chapter 4): Fiber-reinforced thermoplastics structures offer adequate manufacturability in terms of mechanical performance, design freedom, and cycle time.

- **Evaluating metrics for RS 2:**

- The redesigned automotive structure with FRTPCs should achieve significant mass reduction (> 40% reduction) in comparison to the baseline structure. Also, this redesigned structure should be manufacturable at similar annual production volumes.

- **Tasks for RS 2:**

- To categorically understand the effectiveness and lightweight potential of FRTPCs for automotive structures, a drivers side door (side-closure) was chosen as the virtual test case. The automotive door was a good candidate since its requirements range across geometrical fit, function, stiffness, and crash energy absorption. Within this section (Chapter 4), a steel baseline door was redesigned with FRTPC materials to meet functional, stiffness, and crash targets. Also, a virtual plant model was developed to estimate mass production cycle times. Figure 2.12 illustrates the three required tasks to verify RS 2.

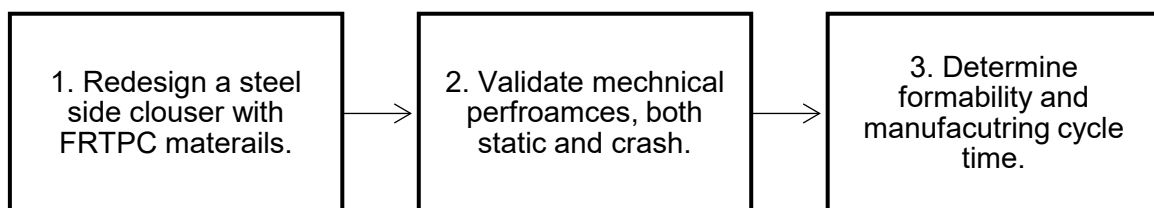


Figure 2.12 Tasks for verifying RS 2.

2.5.3 RS 3 (Chapter 5,6,7): Resistive welding can match or outperform the mechanical performance of any commercially available joining methods for fiber-reinforced thermoplastics.

- **Evaluating metrics for RS 3:**

- Mechanical properties of resistive implant welded joints were experimentally verified at the coupon level to see if these match or outperform properties of commercially available structural adhesives. Mechanical properties evaluated for these joints included the following: lap shear strength, in-plane stiffness, in-plane fracture energy, peel strength, out-of-plane stiffness, and out-of-plane fracture energy.

- **Tasks for RS 3:**

- Standard lap shear and double cantilever peel tests were required to characterize the mechanical performance of these joints. A custom weld fixture with sensors and controllable power supply was designed and built in-house. The goal of this fixture was to repeat the weld test with ease and consistency (Chapter 5). The processing variables for RIW process were sensitive to factors such as coupon material, weld area, heat loss during welding, and type of heating elements used. While the processing parameters from literature provided a good starting point, these did not produce optimum results for our in-house test setup. To address this, an optimization study was performed to understand the influence of individual parameters, and optimum processing windows were determined (Chapter 6). To compare the mechanical performance of RIW joints, three commercially available structural adhesives were also tested (Chapter 6). Using this test data, non-linear, elasto-plastic

material models for finite element analysis were generated (Chapter 7). These material models were used to simulate larger automotive components and understand the influence of joint performance at the systems' level (Chapter 8). The flowchart in Figure 2.13 provides an overview for verifying RS 3.

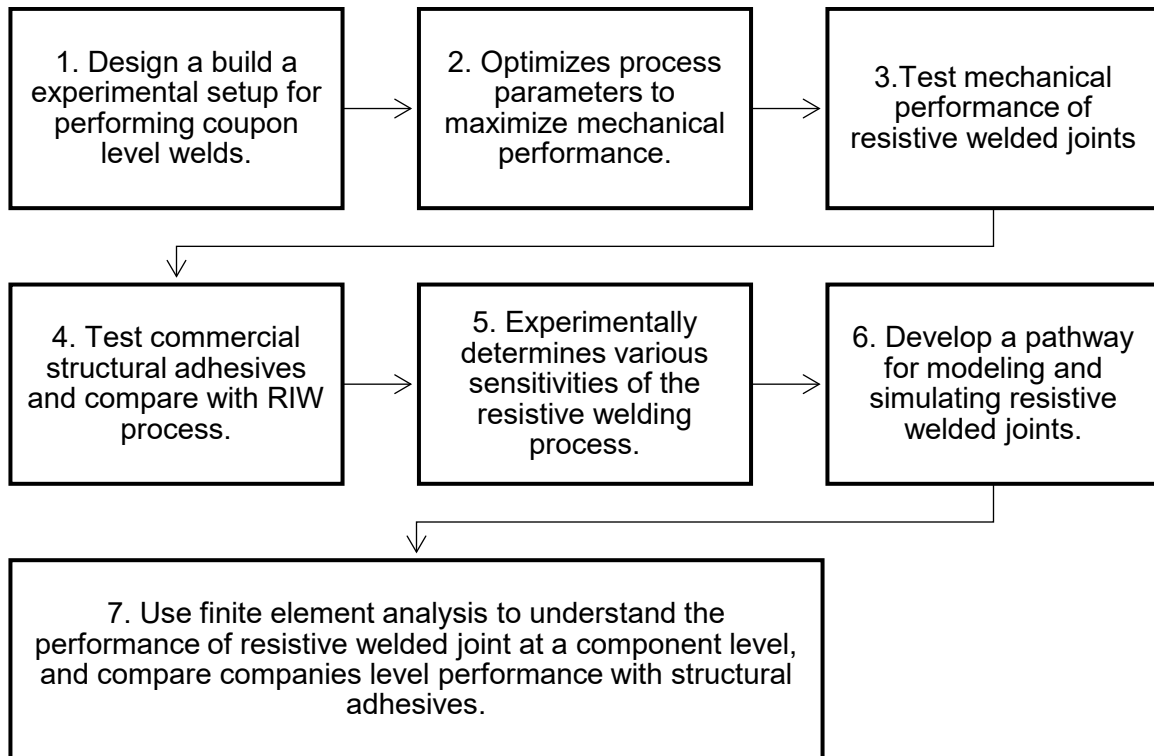


Figure 2.13 Tasks for verifying RS 3.

2.5.4 RS 4 (Chapter 9): This joining technology is scalable for part size and production volumes required for mass-produced automobiles.

- **Evaluating metrics for RS 4:**

- The evaluating metric was determining the feasibility of RIW process in terms of part size (typical automotive structures) and cycle time for low-volume production vehicle (less than 30,000 units annually produced).

- **Tasks for RS 4:**

- Using the existing research on various approaches for scaling the size of RIW joints, the best approach for automotive structures was proposed. Factors such as part complexity and part size were taken into consideration. Also, the effect of weld processing times on vehicle throughput per hour was determined for the automotive body shop (Figure 2.14).

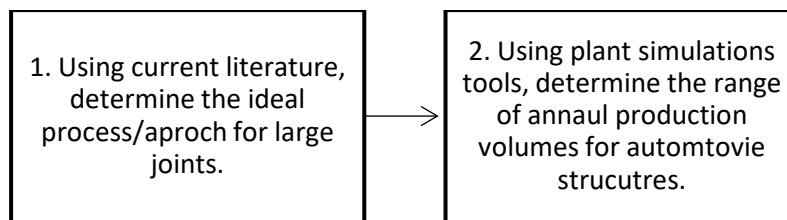


Figure 2.14 Tasks for verifying RS 4.

3 SELECTION AND MECHANICAL CHARACTERIZATION OF FIBER REINFORCED THERMOPLASTICS

3.1 Introduction

Parts manufactured from un-reinforced thermoplastic materials are ubiquitous in our day-to-day life, be it in household commodities or industrial equipment. There has been a great deal of maturity and diversity of compatible manufacturing technologies. (Extrusion, injection molding, thermoforming, etc.)⁷⁷. This vast legacy of knowledge and diversity in thermoplastic manufacturing has led to the development of FRTPC materials from various manufacturing standpoints, thereby resulting in the large variants of such materials. In fact, these variants make thermoplastics a more diverse field than their thermoset counterparts, even though thermosets have been in use for a longer duration.

Generally, thermoplastics require very high pressures and temperatures for processing, which often leads to distortion of fiber reinforcements. However, with the recent advent of better manufacturing simulation tools^{23,91-97} and material compatibilization techniques, for various forms of fiber-reinforced thermoplastics-based composites (FRTPCs) have been introduced. These reinforcements range from short chopped fibers to continuous tapes, depending on the intended manufacturing process. This diversity often makes it difficult for design engineers to pick the correct FRTPC material for their respective application. In addition to such diversity in mechanical performance, each form of FRTPC material is only compatible with certain manufacturing processes and has limited design freedom. Hence, it is essential to organize these material systems systematically, based on the desired mechanical and design performance.

3.2 Types of fiber reinforcements

FRTPC reinforcements can be broadly classified into five groups, based on reinforcement length, distribution, and manufacturing process employed.

3.2.1 *Short fiber reinforced thermoplastics (SFTs):*

Carbon fiber yarns are generally chopped to less than 5 mm in length and mixed with the polymer in a low shear extruder⁹⁸ and pelletized as SFT raw material. These pellets can be injection molded in a conventional injection molding machine. When these pellets are molded into a part, fiber length attrition is expected due to the shear forces in injection molding screw⁹⁹. This form of FRTPC offers the highest design freedom, lowest mechanical performance, and highest economic value when compared to other FRTPCs. As shown in Figure 3.1, the pellets to the right are short fiber reinforced thermoplastics; these are less than 5 mm long. These material systems are often not strong enough for structural applications and are generally used as a lightweight replacement for injection molded parts made from pure polymers. Typically, SFTs are manufactured using injection molding and bulk compression molding processes and do not possess any design limitation, barring the use of thin walls for complex 3D parts.

3.2.2 *Long fiber reinforced thermoplastics (LFT):*

LFTs are a relatively new set of materials that can be injection molded and provide excellent mechanical properties¹⁰⁰ (compared to SFTs). In these material systems, fibers are chopped to 10-25 mm in length¹⁰¹. One key difference between SFTs and LFTs is that the fiber is perfectly aligned to the length of pellets. This alignment improves processability and ensures higher fiber volume fraction within the pellets¹⁰². As previously noted, shear forces in the regular injection molding screw are quite high, thereby leading to fiber length

attenuation. To prevent this, a special low shear screw is used for molding this material¹⁰³. Also, the design of gate and runner systems in the mold plays a critical role in the final mechanical properties of the part. The pellets in Figure 3.1 (towards the left) are long fiber reinforced pellets. While these systems do offer good design freedom, it is a highly complex and challenging task to predict the strength of the final part. Indeed, over the last couple of years, there has been a significant research push towards simulating the manufacturing process and thereby predicting the mechanical properties of final LFT reinforced polymeric parts^{96,97}. In short, this material system promises to offer lightweight parts that can replace cast aluminum components within a vehicle structure. Like for SFTs, LFTs can be manufactured using both injection molding and bulk compression molding processes. They offer minimal design limitations, with thin walls desirable for simple 3D parts.



Figure 3.1 Short fiber and long fiber reinforced thermoplastic pellets.

3.2.3 *Non-woven fiber reinforced thermoplastics.*

These material systems are in the mid-range between SFTs and LFTs with regard to mechanical performance and cost. The raw material often comes in pre-impregnated

or co-mingled mats. Most of these materials are manufactured from recycled or scraped carbon fiber yarns. The average fiber length in these materials is around ~ 40-60 mm. Aqueous suspension and needle punching are the two most common processes used to manufacture this non-woven mats¹⁰⁴. These manufacturing processes are less energy-intensive and need less capital investment in comparison to woven and unidirectional tapes¹⁰⁵. Thermoforming, compression molding and autoclave can be used to manufacture parts from these systems. The parts are often limited to shell design, but these material systems can achieve shallow and blunt surface features as well. These materials are an excellent replacement for class “A” sheet metal parts that need considerable mechanical performances, such as hood skin and fenders.



Figure 3.2 Carbon fiber non-woven prepreg material.

3.2.4 Woven and unidirectional fiber-reinforced thermoplastics:

These materials are the upper echelon of performance composites. The two underlying characters of these material systems are their uniformity and very high fiber volume fractions. While the mechanical performance of these material systems is far superior to other forms of fiber-reinforced thermoplastics, the cost of raw material is

significantly higher. Thermoforming, compression molding and autoclave can be used to manufacture final parts from these material systems. However, these final parts can only have 2D shell features. However, these materials have higher specific properties than most aluminum used in automotive structures.

3.3 Manufacturing

Since the focus of this body of work is limited to automotive applications, an informed decision was made to limit the matrix material system to Polyamides 6-6 and Polyamide 6 for the reasons discussed in Section 2.4.1 of this dissertation (i.e., lower cost and easy processability). In fact, With this, the first task was to procure material samples from various suppliers. ASTM D3039¹⁰⁶, a standard test method for testing tensile properties of polymer matrix composites, was used to determine the mechanical properties of materials. While pre-manufactured plaques for LFTs and woven material were directly procured from the supplier, other material systems were only available in their raw material state. Non-woven and unidirectional composite coupons were prepared using an autoclave at the University of Delaware. The raw materials were placed on a flat steel tool (Figure 3.2) and vacuum bagged with Kapton film. This entire mold was then placed into the autoclave for preprogrammed pressure and temperature cycles, as shown in Figure 3.3 and Figure 3.4.

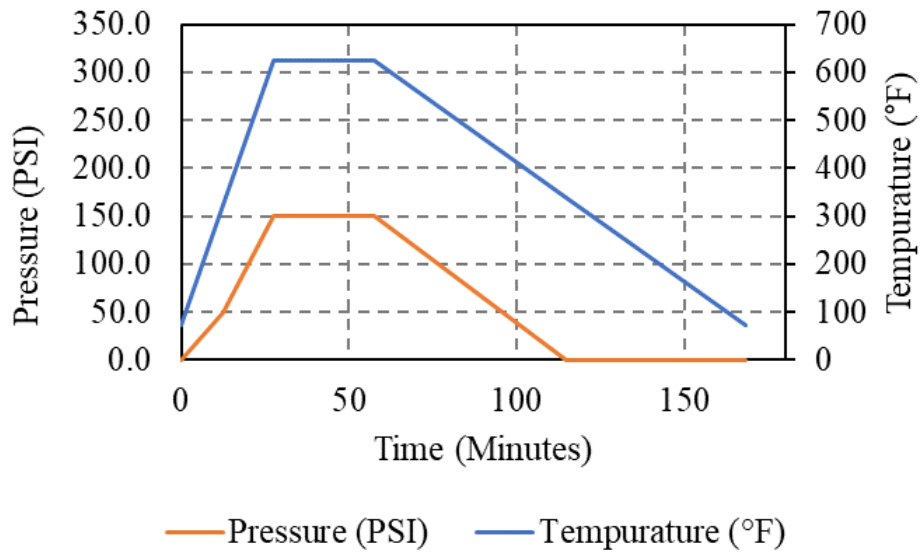


Figure 3.3 Autoclave manufacturing cycle for uni-directional composites.

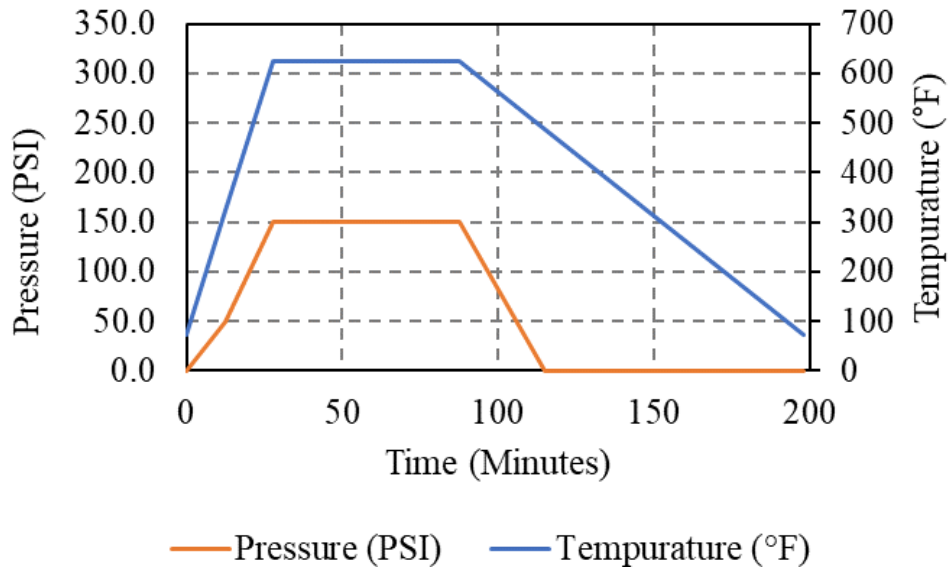


Figure 3.4 Autoclave cycle for non-woven composites.

The short fiber coupons were injection molded in-house using a custom machined injection mold, with cavities for Type 1 tensile coupon, rectangular plaque, and implant

specimen (Figure 3.5). Manufacturer-recommended processing conditions were used to injection mold these coupons, as shown in Table 3.1.

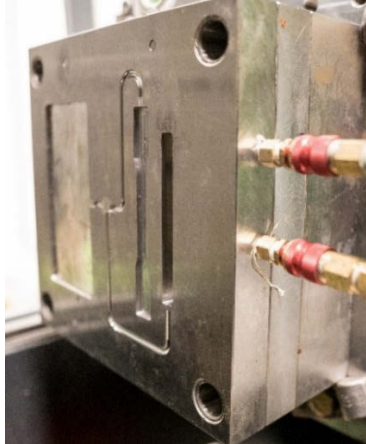


Figure 3.5 Custom Test coupon injection mold.

Table 3.1 Processing Conditions for injection molding.

Input	Value	Units
<i>Barrel rear zone temperature</i>	255	°C
<i>Barrel center zone temperature</i>	260	°C
<i>Barrel Front zone temperature</i>	264	°C
<i>Nozzle temperature</i>	275	°C
<i>Back Pressure</i>	50	psi
<i>Injection speed</i>	60	mm/sec

3.4 Mechanical characterization

Once the composite panels were manufactured, test coupons were cut from larger plaques using waterjet and vertical bandsaw. These test coupons were then tabbed, as recommended by the test standard ASTM 3039. A biaxial strain gauge was bonded to these coupons for accurately measuring strain and Poisson's ratio (Figure 3.6).



Figure 3.6 Woven test coupons with bonded strain gauges and glass fiber tabs.

Two Instron universal tensile testing machines with loadcells of 250 kN and 10 kN from the respective departments of Automotive Engineering and Material Science Engineering (both at Clemson University) were used to test the specimen. In addition to composites, pure Polyamide 6-6 coupon was also tested to give a better understanding of the effect of fiber reinforcement. Table 3.2 summarizes all mechanical properties of various composites, as obtained from ASTM D3039 tests.

From the force-displacement plots, ultimate tensile stress and elastic modulus in both 0° and 90° direction were measured. Using the equation below (Eq 4), ultimate tensile strength and elastic modulus were calculated. For every mechanical test, three repetitions were undertaken to ensure test repeatability.

$$UTS = \frac{p^{max}}{A} \quad Eq\ 4$$

UTS: ultimate tensile strength, (MPa)

P_{max}: Maximum force before the break, N

A: average cross-section area, mm²

$$E^{modulus} = \frac{\Delta\sigma}{\Delta\varepsilon} \quad \text{Eq 5}$$

E^{modulus}: elastic modulus, (GPa)

Δσ: Difference between two tensile stress points before yield point

Δε: Difference between two strain points before the yield point.

Getting information on cost proved to be difficult for some of the materials since these are currently not manufactured at an economic scale (i.e., higher volumes), whereas the cost of raw material is directly dependent on annual volumes. The approximate cost, as provided by material suppliers, is reported in Table 3.2. This cost is approximate when procured in volumes of 500,000 lbs. per year. While the number 500,000 lbs. looks very high, it only translates approximately to producing 2,000 vehicle structures per year. Seven attributes were used to compare these material systems in terms of structural requirements, as shown below. While the first five attributes are self-explanatory, the lightweight potential for beam and panels needs further explanation.

An automotive structure can be broadly divided into two major design elements: (a) beams; and (b) panels.¹⁰⁷ When designing beam-like structures, most of the external loading translates into stress in the principal direction, which is parallel to the length of the beam. By using material systems with high directionality, the mass efficiency of the beam can be improved. To reflect this, the lightweight potential for beam attribute (L_{pb}) favors material directionality and gives more preference to stiffness. On the contrary, while designing panels, it is desirable to have more isotropic material behavior. To reflect this,

the lightweight Potential for panels attribute (L_{Pp}) penalizes material directionality and pays equal importance to stiffness and strength.

Further, all these attributes were normalized, as shown in Table 3.3, and the spider chart for the same is shown in Figure 3.7. Figure 3.7 also elegantly illustrates the diversity in mechanical performance for various FRTPCs. Using this information, material cards for finite element analysis were generated. A few automotive components were picked to evaluate the effect of using FRTPC. Key material attributes were:

- *Max Stiffness (M_{sf})*: Maximum strength from either 0° or 90° directions.
- *Max Strength (M_{st})*: Maximum strength from either 0° or 90° directions.
- *Stiffness Directionality (D_{sf})*: Maximum stiffness (0°) \div Minimum stiffness (90°)
- *Strength Directionality (D_{st})*: Maximum strength (0°) \div Minimum Strength (90°)
- *Economy ($\$E$)*: $1 \div \text{Cost}$
- *Lightweight Potential for beams (L_{Pb})*: $[(0.7 \times M_{sf} * D_{sf}) + (0.3 \times M_{st} * D_{st})] \div \text{Density}$
- *Lightweight Potential for panels (L_{Pp})*: $[(0.5 \times M_{sf} * (1/D_{sf})) + (0.5 \times M_{st} * (1/D_{st}))] \div \text{Density}$

The spider plots in Figure 3.7 not only illustrate the range of variation in mechanical properties but are also a good tool for design engineers to quickly identify the correct subset of FRTPC materials, based on their respective mechanical performance.

Table 3.2 Summary of mechanical properties of FRTPC

Material	Density (g/cc)	0° Elastic Modulus (GPa)	0° Ultimate tensile strength	90° Elastic Modulus (GPa)	90° Ultimate tensile strength	Cost (\$/kg)
<i>Pure nylon (PA66)</i>	1.1	2.3	82.8	-	-	\$2.4
<i>Short Fiber reinforced thermoplastic</i>	1.4	7.9	166.5	-	-	\$15.4
<i>Long fiber reinforced thermoplastic</i>	1.4	30.0	300	15.7	150	\$24.2
<i>Non-woven reinforced thermoplastics</i>	1.5	28.4	455.7	18.0	305.3	\$33.1
<i>Woven fabric reinforced thermoplastics</i>	1.5	66.5	577.4	65.8	684.4	~\$41.9
<i>Uni directional thermoplastics tapes</i>	1.7	100.4	1450.0	4.8	30.9	\$50.2

Table 3.3 Material performance attributes.

Material system.	\$E	M_{sf}	M_{st}	D_{sf}	D_{st}	L_{Pb}	L_{Pp}
<i>Pure nylon</i>	636%	2%	6%	5%	2%	0%	13%
<i>Short fiber reinforced thermoplastics</i>	100%	8%	11%	5%	2%	0%	24%
<i>Long fiber reinforced thermoplastic</i>	70%	30%	21%	9%	4%	2%	27%
<i>Non-woven reinforced thermoplastics</i>	47%	28%	31%	8%	3%	2%	43%
<i>Woven fabric reinforced thermoplastics</i>	37%	66%	47%	5%	3%	3%	100%
<i>Uni directional thermoplastics tapes</i>	28%	100%	100%	100%	100%	100%	6%

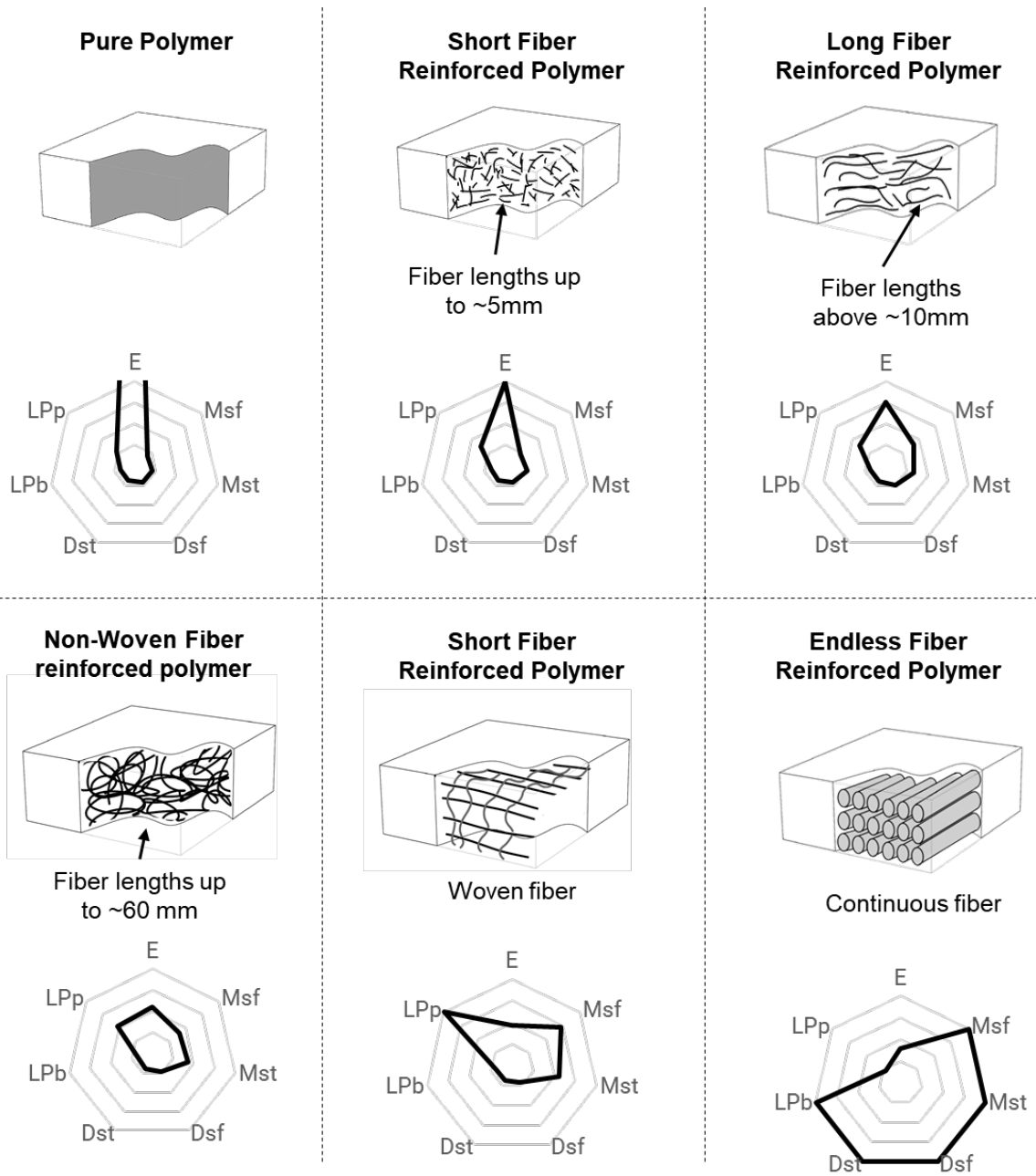


Figure 3.7 Footprints of material performance attributes in spider plots.

3.5 Comparison of FRTPC materials to Commonly used automotive structural material systems.

Ashby charts¹⁰⁸ are excellent tools to illustrate specific properties of materials and aid engineers in picking the suitable material for intended applications. Some of the most commonly used Ashby charts are Young's modulus vs. density and Ultimate tensile strength vs. density plots. Figure 3.8 is an example of an Ashby chart that compares several materials with respect to their density (ρ) and Young's modulus (E). In the lower right corner of this chart, there are three guidelines to aid material selection, each of which represents a different relationship between E and ρ . For example, when designing for stiffness, the appropriate guideline is $E/\rho = c$.

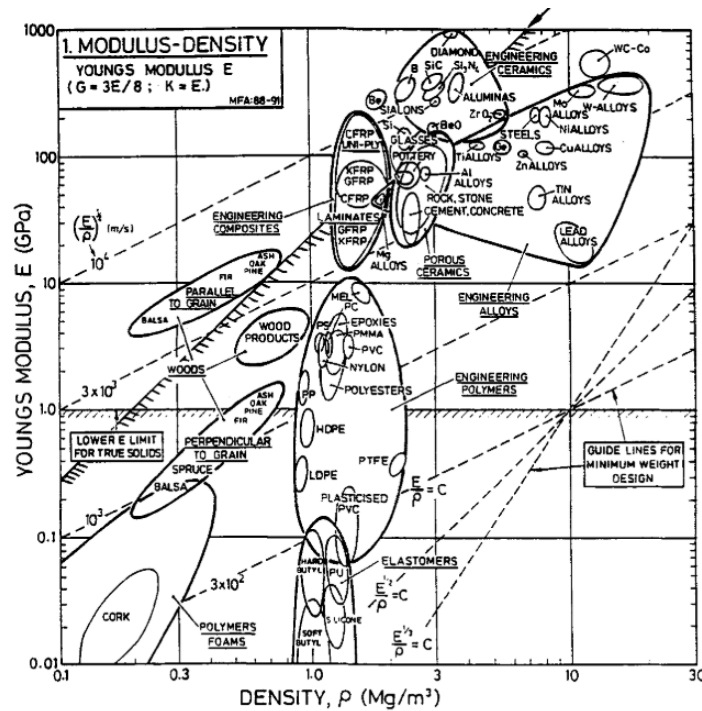


Figure 3.8 Ashby chart for Density vs. Young's modulus (image source¹⁰⁸)

Charts similar to Ashby charts were created in this work to effectively illustrate the potential of FRTPCs both in terms of their stiffness (E) and strength (UTS), as shown in Figure 3.9 and Figure 3.10. The data for these plots can be seen in Table 3.4.

As shown in Figure 3.9, when designing for strength, UD, woven, and non-woven FRTPCs were more effective than most metals barring one specific grade of steel (MS 1300). The more interesting observation is that LFT materials performed better than most grades of aluminum and magnesium, thereby making this material system a great replacement for aluminum and magnesium-cast parts. However, when designing for stiffness, only woven and UD FRTPCs performed better than most metals. It is also important to note that most metals only outperformed non-woven and LFT FRTPCs by a razor-thin margin.

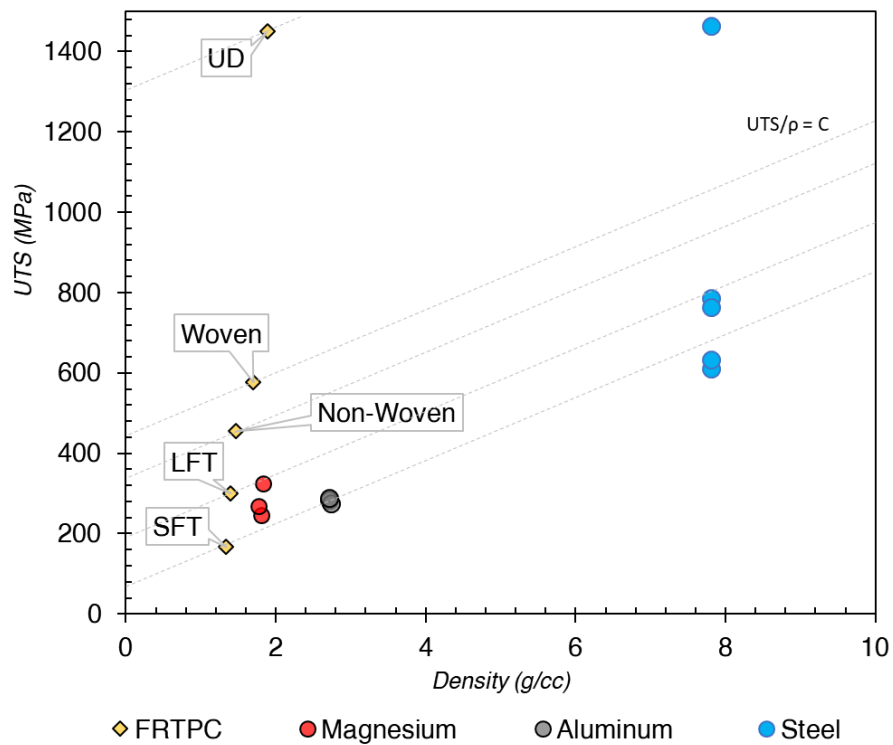


Figure 3.9 Strength vs. Density for automotive materials.

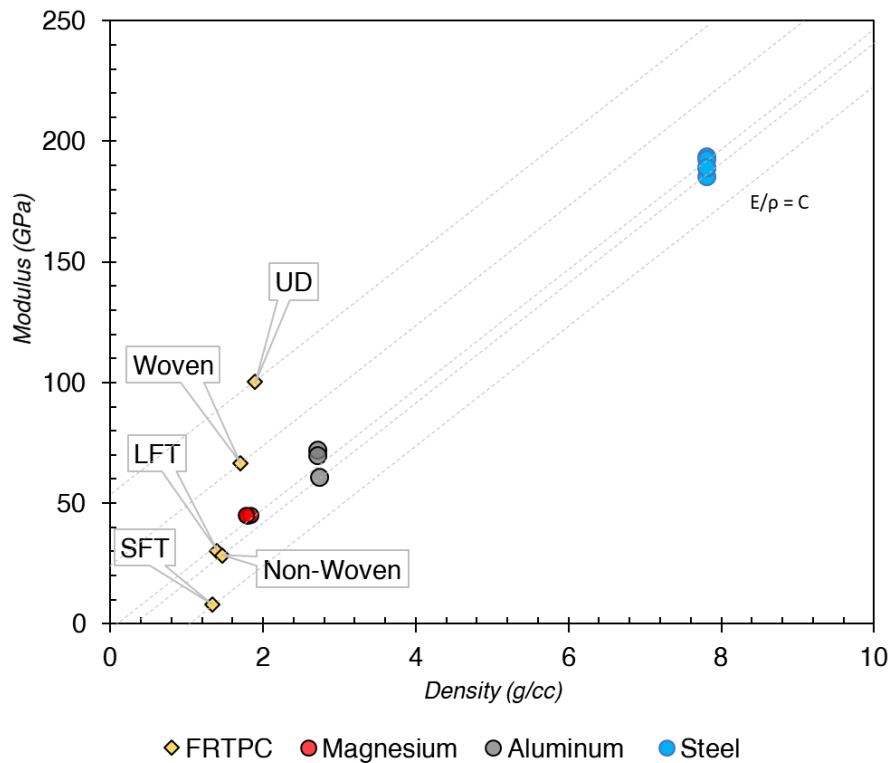


Figure 3.10 Stiffness vs. Density for automotive materials.

3.6 Summary

In summary, based on the data presented in this chapter, it can be inferred that FRTPC materials with engineering grade polymer matrix and continuous fiber reinforcement can enable meaningful mass reduction, and ensure better specific stiffness and specific strength when compared to common automotive structural materials. Also, low-cost discontinuous fiber-reinforced thermoplastics have better specific properties than most common casting grade aluminum and magnesium, making them an attractive replacement for casted parts within the automotive structure.

Table 3.4 Specific properties of FRTPC vs. metals.

Family	Material Or grade	Density gm/cc	Modulus GPa	Specific Modulus GPa*CC/g	Strength MPa	Specific Strength (MPa*CC/gm)
FRTPC PA66 & carbon fiber	SFT	1.3	7.9	<u>5.9</u>	166.5	<u>124.7</u>
	LFT	1.4	30.0	<u>21.4</u>	300.0	<u>214.3</u>
	Non-Woven	1.5	28.4	<u>19.4</u>	455.7	<u>311.1</u>
	Woven (2X2 twill)	1.7	66.5	<u>39.1</u>	577.4	<u>339.7</u>
	UD	1.9	100.4	<u>53.1</u>	1450.0	<u>767.2</u>
Polymers	PA66	1.1	2.3	<u>2.1</u>	82.8	<u>72.6</u>
Steel	DP 600	7.8	193.8	<u>24.8</u>	611.9	<u>78.3</u>
	DP 800	7.8	185.6	<u>23.8</u>	785.5	<u>100.6</u>
	TRIP 600	7.8	192.8	<u>24.7</u>	632.3	<u>81.0</u>
	TRIP 700	7.8	189.3	<u>24.2</u>	763.4	<u>97.7</u>
	MS 1300	7.8	189.2	<u>24.2</u>	1464.7	<u>187.5</u>
Aluminum	AA 5023	2.7	72.0	<u>26.6</u>	285.0	<u>105.2</u>
	AA 6022	2.7	60.9	<u>22.3</u>	275.0	<u>100.7</u>
	AA 6111	2.7	70.0	<u>25.8</u>	290.0	<u>107.0</u>
Magnesium	AZ31	1.8	44.8	<u>24.9</u>	245.0	136.1
	ZK60	1.8	45.0	<u>24.6</u>	325.0	<u>177.6</u>
	AM50	1.8	45.0	<u>25.4</u>	268.0	<u>151.4</u>

The data source for E and ρ for metals ¹⁰⁸⁻¹¹⁵

4 UNDERSTANDING HOW TO USE FRTPC MATERIALS AT SYSTEM LEVEL

Apart from a better understanding of the FRTPC material family, it is also essential to understand how these systems can affect the basic design of automotive structures and their subsequent performance. Hence, the overarching goal of this chapter is to identify the right FRTPC candidate for the automotive structure (via redesigning) and to understand the shortcomings and virtues of FRTPC material systems. This exercise of design development will also help us later evaluate the effect of RIW joints at the systems level (Chapter 7).

4.1 Selecting an ideal candidate for the lightweighting study.

Automotive body structure (or BiW) is the heaviest component of a vehicle, thus making it a key target for several lightweighting studies. However, due to the sheer complexity of BiW in terms of load cases, the number of parts, and complexity of the design, selection of a simpler system would make more sense for this study. At the same time, it is essential that this selected system still experiences diverse load cases, such as static stiffness, strength, and crash induced failure, in order to effectively evaluate these material systems. Keeping these aspects in mind, automotive closures may be a good candidate for this study due to the following reasons:

- a) They have very diverse performance requirements, ranging from stiffness to crash energy management¹¹⁶.
- b) They are relatively easier to design and simulate compared to developing an entire body structure.

- c) They still contribute to 35-50% of the total structural weight¹¹⁷.
- d) The disruption to existing infrastructure is relatively minimal. Therefore FRTPC closures have increased commercialization prospects.

4.2 Development of an Ultra-lightweight FRTPC (ULWC) door frame.

For this virtual test case, a driver-side door from a mid-size luxury crossover was chosen. The entire process of developing the virtual test case can broadly be divided into five stages: (a) Baseline Benchmarking; (b) Design requirements; (c) Development; (d) Optimization; and (e) Simulation.

4.2.1 Baseline Benchmarking

The baseline steel door represents the state-of-the-art in terms of lightweighting and performance for conventional steel frame behind the glass architecture. A teardown benchmarking study was performed on the steel door to determine the weight of each component and get a better understanding of the design, manufacturing, and assembly, during which a fully assembled door was disassembled to the last nut and bolt (Figure 4.1.). Each of these components was then weighed to create a detailed bill of materials.

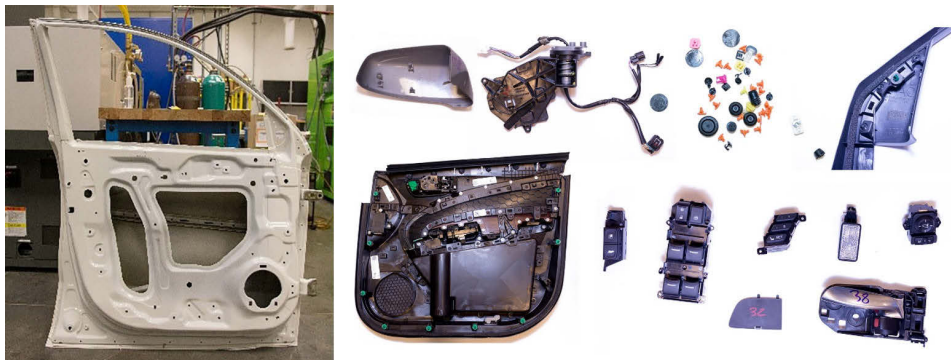


Figure 4.1 Steel doorframe with hinges and components from the OEM door.

The door comprised of 54 parts (excluding fasteners) that can be classified as either being made from rigid polymers, metals, or elastomers, as shown in Figure 4.2. The door frame is the heaviest component of the entire door assembly, contributing ~ 49% of its total mass, while the trim, electronics, and windows contribute another 31% (Figure 4.3). Metals constitute a majority of the total door mass (~ 62%), wherein the door frame consists of regular cold drawn steel and high-strength steel (Figure 4.3).

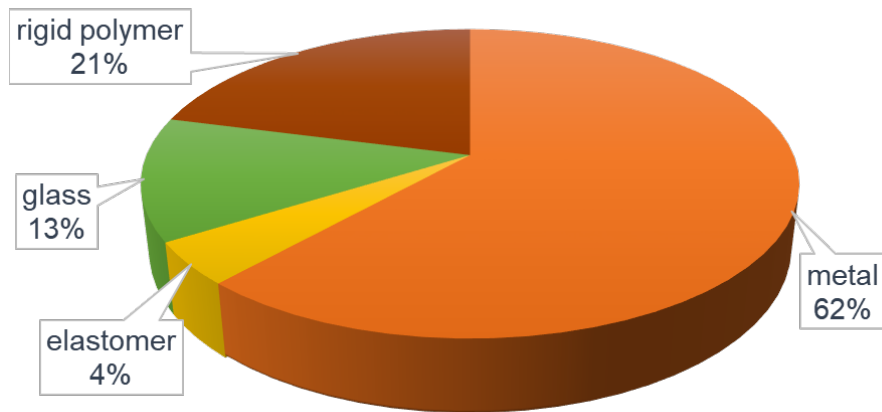


Figure 4.2 Weight Distribution by the material group in the baseline door.



Figure 4.3 Weights of a major subassembly of the baseline door.

4.2.2 Design requirements

To effectively compare the lightweighting potential offered by FRTPCs, the ultra-lightweight FRTPC (ULWC) door must either meet or surpass the baseline metal door in terms of mechanical performance, crash safety, fit, and finish.

The design requirements for the ULWC door are as follows:

I. Mechanical requirements

a. Static load cases:

These load cases represent the daily use and misuse of the door frame over its life span. Six individual load cases were provided by the vehicle manufacturer: (a) Door sag closed (DSC); (b) Door sag open (DSO); (c) Door over opening; (d) Beltline stiffness; (e) Sash stiffness near latch; and (f) Sash stiffness near hinge. All these load cases have well-defined boundaries and loading conditions. The qualification criterion is to have less or equal deflection in the ULWC door frame than the target metrics.

b. Nonlinear load cases:

These load cases represent crash tests affecting the door frame, as mandated or recommended by the National Highway Traffic Safety Administration (NHTSA) and the Insurance Institute for Highway Safety (IIHS). A total of three crash tests were picked for evaluating the ULWC door frame (Figure 4.4).

- **FMVSS 214 static test:** A cylindrical impactor (diameter: 300 mm), connected to hydraulic ram, is used to quasi-statically deform in the lateral direction for 18 inches. During this 18-inch stroke, the reaction force on the hydraulic ram is monitored. The

force-displacement curve of the impactor is used to calculate the crush resistance of the door frame.

- **IISH SI MDB:** The moving deformable barrier (MDB) impacts the car perpendicularly at 50 kmph. Such configuration, along with the higher barrier bumper height and mass, makes this test more challenging than the FMVSS 214 deformable barrier test. Due to the increased bumper height, a larger portion of the impact energy is transferred through the door frame than via the BiW.
- **FMVSS 214 Rigid pole:** In this crash mode, the vehicle is mounted on a mobile platform and is impacted with a rigid pole at 75° to the length of the vehicle at a speed of 32 kmph. A 5th percentile side-impact female dummy was selected to position the vehicle for the crash test. In this configuration, the B-pillar is furthest from the impact location, thereby forcing the door frame to absorb the larger chunk of impact energy.

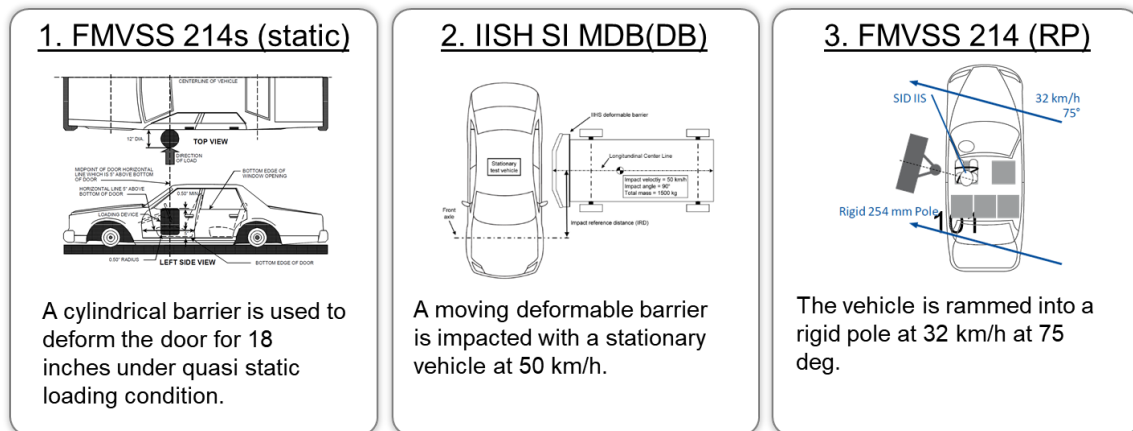


Figure 4.4 Nonlinear Load cases.

c. Sealing requirements

One of the critical requirements of this study entailed developing a door to interface with existing BiW. The baseline door has two weather-strips and two wind deflectors, and so the ULWC door must use the same weather-strips and sealing surfaces to maintain a

good seal with the existing BiW. Doing this will also give realist geometrical constraints for the ULWC door design.

d. Noise, vibration and harshness requirements (NVH).

The door frame acts as a critical route for transmitting vibration, structural bound, and air bound noise into the passenger cabin. However, for this redesign, NVH performance was not evaluated directly. Instead, modal analysis was performed to ensure that the excitation modes of ULWC door are higher than those of the baseline door and that the total leakage area (of ULWC door) is also lower than that of the baseline door.

4.2.3 Concept Development

An iterative process was used in developing and evaluating conceptual designs for the ULWC door. From the very beginning, it was clear that design optimization or material substitution alone would not be the most effective way to reduce mass. Hence, it was essential to understand the requirements from systems' perspective for developing a door frame that meets these requirements using the least number of parts.

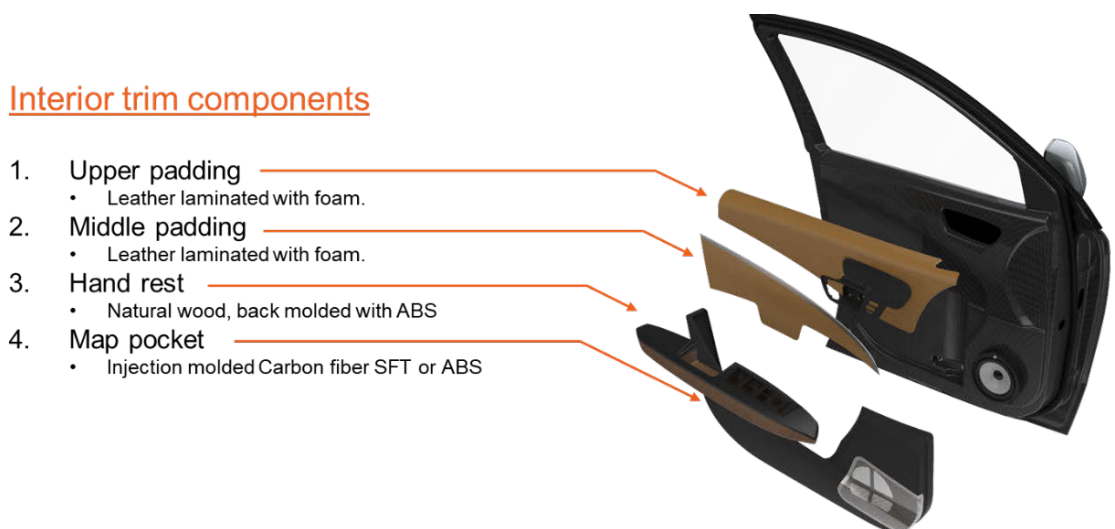


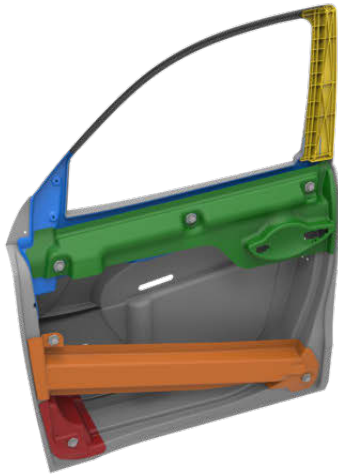
Figure 4.5 Interior trim components.

In order to maximize such part consolidation and mass reduction, an integrated frame approach was used. In the ULWC door, the structural frame also acts as an interior trim panel (Figure 4.5). This is possible due to higher design freedom and good surface quality offered by woven FRTPCs. Unlike the baseline door, the “class A” panel is non-structural and is mechanically attached later in the assembly process, as doing so enables greater access to the internal door parts for associates in the assembly plant, while also easing repairability.

In the initial design (Figure 4.6), the structural door frame consisted of six FRTPC components. Even though this door met all performance requirements, the FRTPC anti-intrusion beam was similar in mass to that of a steel beam. To achieve ductile behavior for the anti-intrusion beam, the fibers had to be oriented in $45^{\circ}/-45^{\circ}$ directions to increase shear rotation in the fibers. By doing so, only ~50% of the fiber strength was utilized. Hence, it made logical sense to replace the FRTPC anti-intrusion beam with a steel beam similar to that in the baseline door. This anti-intrusion beam is a good example for parts which require higher toughness as well as higher elongation, and FRTPCs are generally ineffective for such parts. Considering this limitation, the anti-intrusion beam (orange in Figure 4.7) and the outer beltline stiffener (green in Figure 4.7) were replaced with metal parts.

Moreover, in the current configuration, most structural parts are bonded using structural adhesives. In Chapter 9, these bonds are replaced with RIW joints, and the improvement in the performance of the new door frame is evaluated. Laminate systems used in the inner panel and inner beltline stiffener are a combination of woven and UD carbon fiber-PA66 materials characterized in the previous chapter.

Structural components of inner panel



1. Inner Frame

- Thermoformed Inner panel with integrated trim.
- Material: Non-Woven fabric with UD reinforcements.

2. Anti intrusion beam

- Thermoformed hat section with a spine.
- Material: UD tapes in mostly $\pm 45^\circ$.

3. Inner beltline stiffener

- Thermoformed shell part with mounting interface for the inner components.
- Material: Non-Woven fabric with UD reinforcements.

4. Outer beltline stiffener

- Thermoformed shell part with mounting interface for the inner components.
- Material: Non-Woven fabric with UD reinforcements.

5. Lower hinge stiffener

- Thermoformed shell part.
- Material: Non-Woven fabric.

6. Sash reinforcement

- LTF/SFT injection molded
- Material: Nylon with chopped carbon fiber.

Figure 4.6 Final selected design

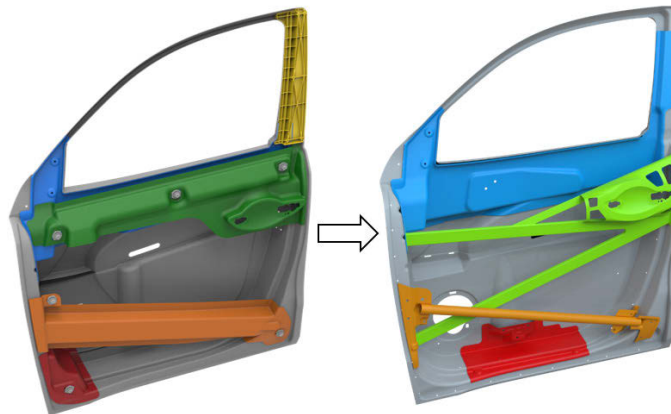


Figure 4.7 Metal anti-intrusion beam and beltline stiffener for ULWC

4.2.4 Performance Analysis.

In the initial part of the concept development phase, critical zones within the door frame that contribute to overall stiffness were identified, as shown in Figure 4.8. This

knowledge was used to appropriately design and size different zones within the door frame for optimal performance. The most critical area is the hinge side of the door frame – a zone that is crucial in transmitting the load from the door to BiW. Ply boundaries were created using these zone shapes for optimization, and Altair Optistruct was used to determine the optimal laminates for static load cases. The objective of this optimization was to minimize mass while meeting all stiffness requirements in order to satisfy these static load cases.

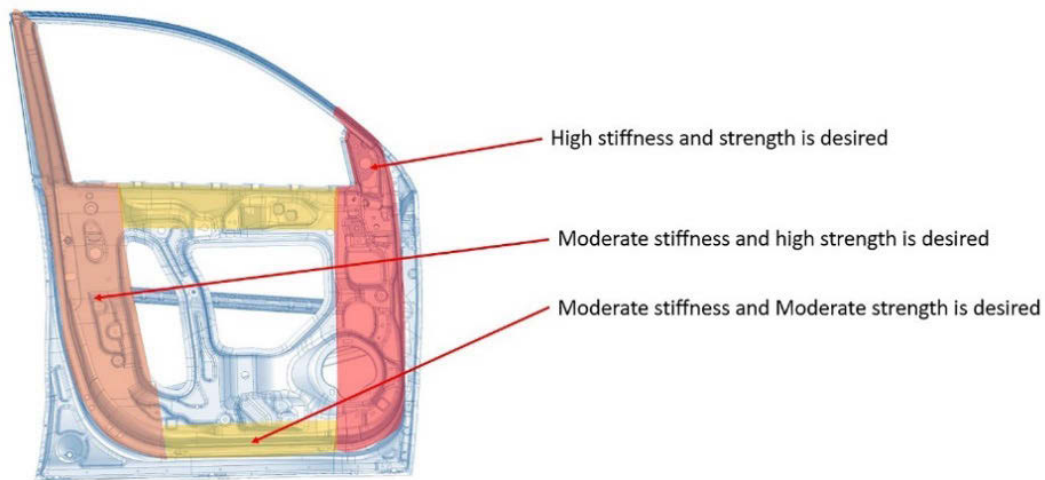


Figure 4.8 Strength and stiffness zones on the door.

A three-step optimization process, involving free-size, size, and shuffle optimization steps, was then established. In the first step, a very thick laminate was used as an input to the optimization problem, during which the optimizer removed lazy plies (i.e., plies which do not contribute to stiffness). In the second step, size optimization was performed to assign discrete values to each ply in the component. In the final step, shuffle optimization was used to optimize the stacking sequence of the plies in laminates.

In free-size optimization, all components except the anti-intrusion beam and beltline stiffener were included in the objective function for mass reduction. The exclusion of these two parts from the optimization for the static load was necessary, as these were sized to meet the crash requirements. For free-size optimization, two types of constraints were applied: (a) Displacement constraints; and (b) Laminate thickness constraints.

The displacement constraints were determined from the stiffness requirements provided by the vehicle manufacturer, while the laminate thickness constraints considered the manufacturable thickness of FRTPC materials. The minimum required thickness for a composite component was 1.2 mm, and hence this value was considered as the minimum thickness, as it was also informed by other performance criteria such as NVH and manufacturability (Figure 4.9).

The static performance of the optimized ULWC door frame can be seen in Table 4.1. The ULWC door meets or outperforms the stiffness targets, while also achieving a 45% reduction in structural mass. The thickness of the inner panel and beltline stiffener varies from 5.33 mm to 1.2 mm (Figure 4.10). The optimization results reinforce the initial assumption of the hinge and latch side of the door panel being the thickest laminate.

Optimization problem:

Minimize total mass (objective function):
 $M_1 + M_2 + \dots + M_i$ (i: door component number)

Subject to (constraints):

$$DS < \begin{cases} 6 \text{ mm for near closed position} \\ 5 \text{ mm for fully open position} \end{cases}$$

Sash A < 3.5 mm
 Sash B < 4.0 mm
 $T_{\text{initial}} > T_i > T_{\text{man}}$ where T: total thickness of component i
 T_{initial} : initial thickness
 T_{man} : min. manufacturable thickness
 Ply thickness = 0, 0.15 mm, or 0.3 mm (for size-optimization)

Figure 4.9 Optimization problem.

Table 4.1 Optimization results of ULWC door.

Targets (From the manufacturer)				Baseline steel Door	ULWC Door (V11)
<i>Structural frame mass</i>				15.1	8.3
<i>Door Sag - Fully open</i>	<	5	mm	3.5	2.89
<i>Sash Rigidity at point A</i>	<	3.5	mm	0.93	2.9
<i>Sash Rigidity at point B</i>	<	4	mm	0.91	2.29
<i>Beltline stiffness-Inner panel</i>	<	1.5	mm	1.34	0.59
<i>Window regulator (Normal)</i>	<	1	mm	6.88	0.73
<i>Mirror Mount rigidity in X</i>	<	0.92	mm	0.57	0.92
<i>Mirror Mount rigidity in Y</i>	<	2.25	mm	0.86	0.97
<i>Door Over opening</i>	<	Baseline	mm	24.7	18.52
<i>Speaker mount stiffness</i>	<	Baseline	mm	0.35	0.18

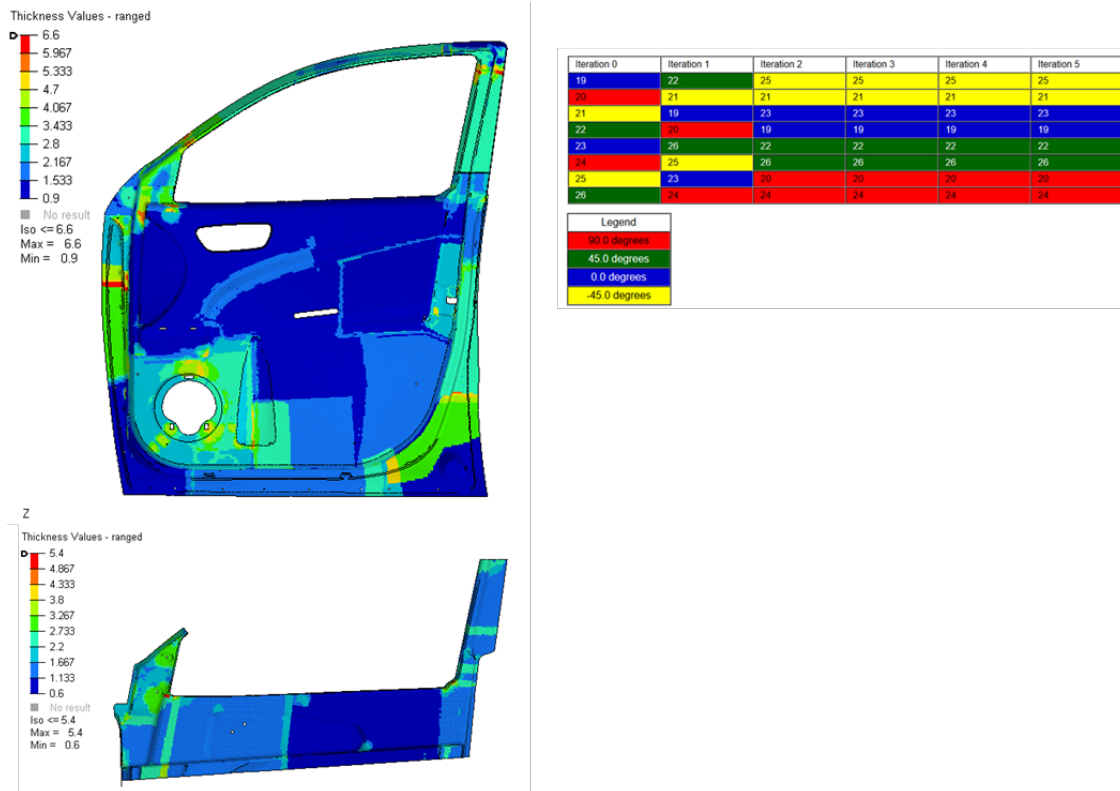


Figure 4.10 Optimized thickness distribution of the FRTPC parts.

4.2.5 Non-Linear Load Cases

Energy absorption capacity is critical for ensuring that the door frame meets the federal and OEM specified crash requirements. Metal structures generally exhibit slow progressive failures, which is desirable for maximizing energy absorption. Contrastingly, most carbon fiber composites have a morphology that is characteristically brittle, thus resulting in abrupt fractures and possessing very little energy absorption capacity. The use of a thermoplastics matrix, instead of thermoset matrix, can mitigate/delay this failure to a certain degree²⁰. While this effect is highly desirable for the crash test, it is also accompanied by a reduction in stiffness, thus requiring careful design of the laminates to utilize the best of both effects.

Hence, FMVSS 214 static¹¹⁸ was selected for preliminary analysis to verify crash performance due to its overall simplicity of the test boundary conditions and simulation. Due to this simplicity and fast simulation turnaround, several issues were identified, and necessary design changes were made to address the root causes. One of the key challenges was the premature failure of the adhesive between the anti-intrusion beam and the inner panel on the hinge side. The steel end plate on the hinge side was redesigned with larger bond overlaps and two additional bolts. Any changes made to resolve the crash performance issue were incorporated back into the static optimization problem since even though this feedback loop increased the number of iterations, it was essential to minimize the use of any unnecessary material(s).

The force-displacement plots for FMVSS 214 simulations are shown in Figure 4.11. LS-Dyna predictions show that all simulations meet the requirements of the FMVSS 214 static test in all the stages. LS-Dyna deformed plots of ULWC door deformation show

progressive damage, with the failure modes being in the following order: (a) Anti-intrusion beam buckling; (b) Belt-line stiffener buckling; (c) Side walls of the inner panel folding inwards; (d) Crack initiation at the hinge side of the inner panel; and finally (e) Major crack initiation in the lower section of inner panel, leading to final failure (Figure 4.12).

The force-displacement of ULWC door was observed to be significantly higher than that for the baseline steel door in the FMVSS 214 static test. This requirement of higher crush resistance was necessary for the ULWC door to meet the FMVSS Rigid pole test. Furthermore, the ULWC door also meets the requirements for other crash modes (FMVSS 214 Rigid pole and IIHS Si MDB tests), as seen in Table 4.2.

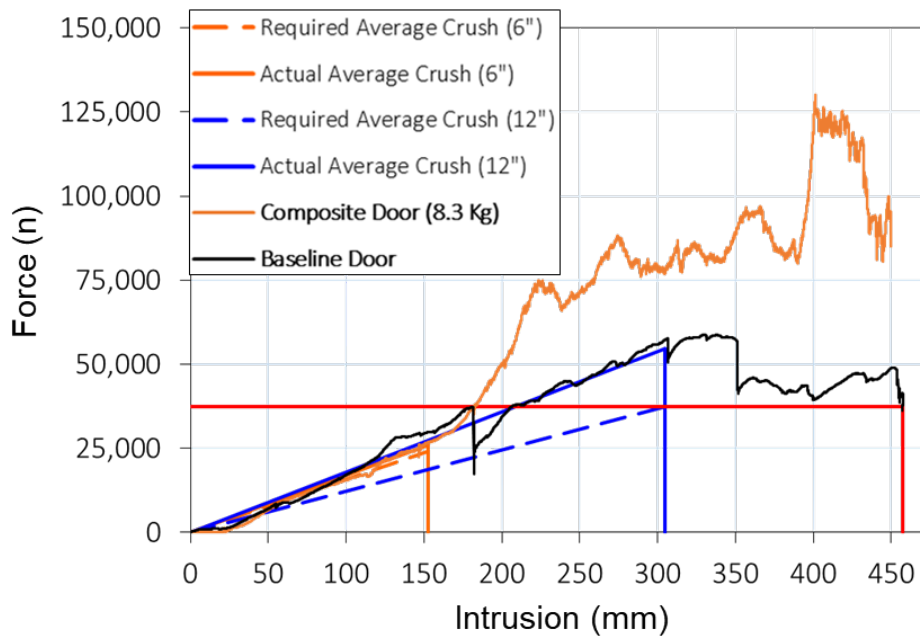


Figure 4.11 Force-Displacement plots for ULWC door vs. Baseline door.

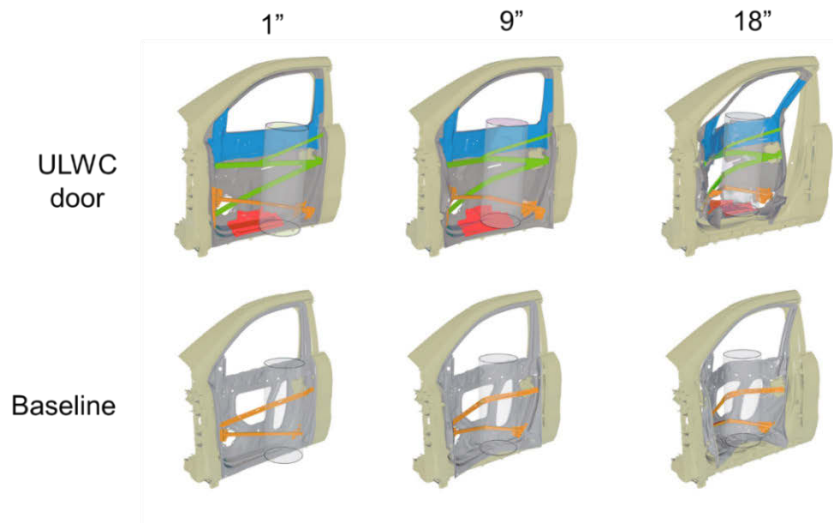


Figure 4.12 FMVSS 214: Deformation plots of the ULWC door.

Table 4.2 FMVSS 214 RP and IIHS SI MDB performances.

	Key Performance Indicator	Baseline [mm]	Composite [mm]	Difference [mm]	Difference [%]
IIHS SI MDB	Occupant survival space	134.3	140	5.7	4.20%
	Maximum intrusion at roof	62.1	48.16	-13.94	-22.45%
	Maximum intrusion at window sill intrusion	279	233	-46	-16.50%
	Intrusion at hip location of the dummy	175.6	125.64	-49.36	-28.10%
	Maximum intrusion at lower door region	210.4	205.76	-4.64	-2.20%
FMVSS 214 RP	Maximum intrusion at B-pillar	150.9	164	13.1	8.68%
	Maximum intrusion at sill intrusion	293.4	287.6	-5.8	-1.98%
	Maximum intrusion at roof	254	259.8	5.8	2.28%
	Maximum intrusion at window sill intrusion	434.5	438.1	3.6	0.83%
	Intrusion at Hip location of the dummy	355.3	336.5	-18.8	-5.29%
	Maximum intrusion at lower door region	440.3	443.1	2.8	0.64%
<ul style="list-style-type: none"> • Success (Green) <ul style="list-style-type: none"> • Below baseline target values (<b) • Tolerable (Yellow) <ul style="list-style-type: none"> • More than baseline values but smaller than 10 % difference (>b, <b+10%) • Failure (Red) <ul style="list-style-type: none"> • More than 10% above baseline value (>b+10%) 					

4.3 Summary

In summary, FRTPCs offer a very high lightweighting potential for automotive structures, as shown by the ~ 45% of structural mass reduction achieved for the ULWC door vis-à-vis the baseline steel door. For this ULWC door, the PA-66 (a mid-tier engineering polymer) was used as the polymer matrix with woven and UD carbon fiber as reinforcement. This further reinforces the hypothesis that FRTPCs with engineering polymer matrix exhibit adequate performance for automotive structures, and the use of more expensive FRTPCs with high-performance polymer matrix materials (such as PEEK, and PPS) is not necessary for automotive applications.

5 EXPERIMENTAL SETUP

To minimize variability in test coupons, it was initially decided to build a custom weld fixture with a high degree of automation and repeatability. Keeping this in mind, the first task in hand was to select welded coupon geometries. The mechanical performance of all joining technologies can be classified into three failure modes¹¹⁹, as seen in Figure 5.1. For this study, Mode 1 (peel) and Mode 2 (lap shear) failure modes are selected. The Mode 3 failure (out of plane shear) performance was not measured, as generally it is very similar to Mode 2 failure and is typically not required to develop a finite element model. Most literature published till date validates the performance of resistive welding joints only in Mode 2 failure (lap shear), this can be attributed to complexity in testing joints in Mode 1 loading.

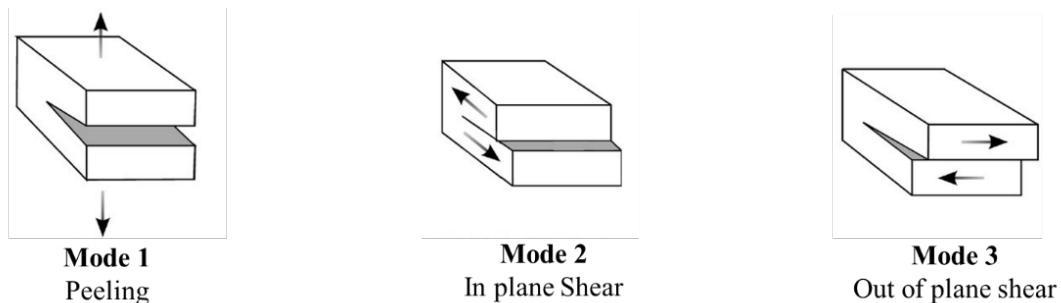


Figure 5.1 Typical failure modes for structural joints (Image source¹¹⁹).

To characterize both Mode 1 and Mode 2 behavior, a double cantilever test and ASTM D5868 standardized lap shear test method were respectively selected. The two required geometries for these tests are shown in Figure 5.2. In both cases, the welded area is 25.4 mm × 25.4 mm (1 sq. inch).

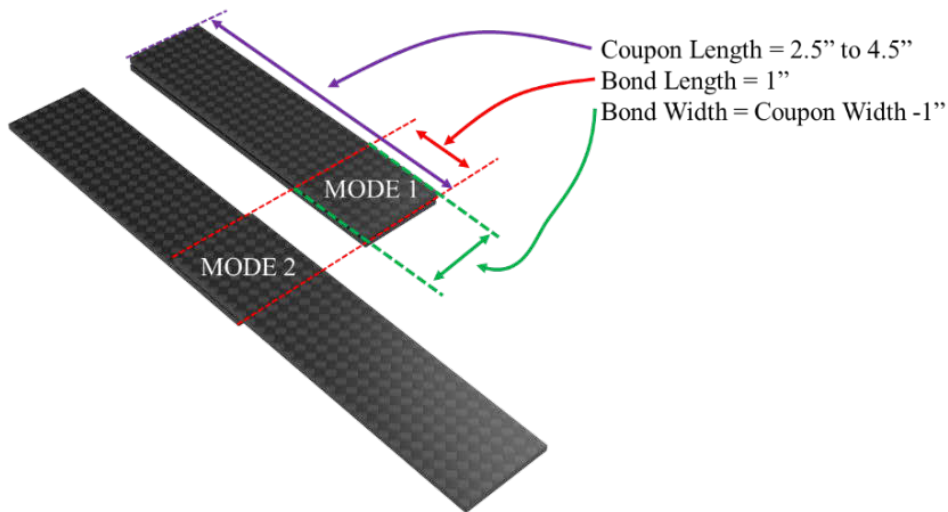


Figure 5.2 Welded coupon geometry.

After selecting the coupon geometries, the next goal was to develop a weld fixture that can produce repeatable welds with a high degree of automation. To ensure the safety of the operator, it was decided to perform welds under 8 volts, which in turn meant that the current required to perform these welds were significantly higher. The weld fixture development can be divided into mechanical design and control/data acquisition.

5.1 Mechanical Design

Some of the key considerations for the mechanical design of the weld fixture was minimizing fixture deformation during the welding process and maintaining good electrical and thermal insulation. Aluminum 6061 was used for structural parts of the weld fixture, as shown in Figure 5.3. For insulation, glass-mica ceramic was used as primary insulation material due to its low thermal expansion coefficient and excellent insulation properties. These ceramic plates were machined with alignment features to align the coupon during

the weld properly. The weld fixture could essentially be divided into three major assemblies: lower clamp, floating clamp, and electrical connector bridges.

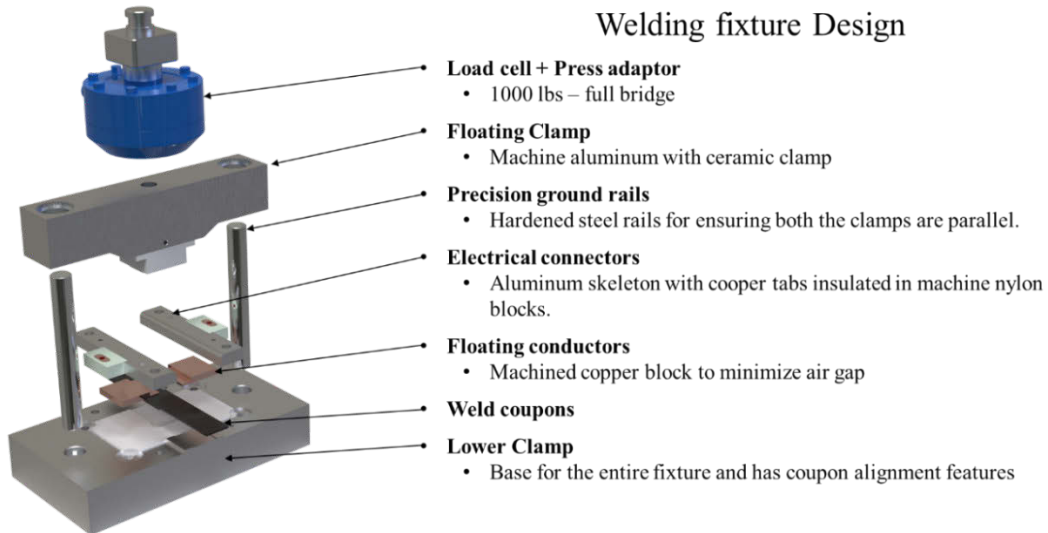


Figure 5.3 Weld fixture design.

5.1.1 Lower clamp

This is the base of the weld fixture. The lower clamp plate has a machined nylon insulator press-fitted in the aluminum base. The ceramic insulator plate is aligned and adhesively bonded to the nylon insulation block. Two precision ground guide rails are also press-fitted in the lower plate, as shown in Figure 5.4.

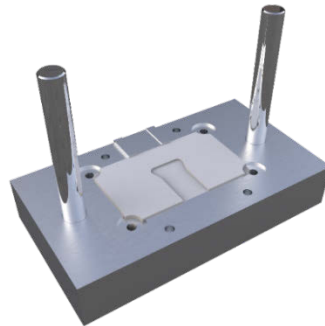


Figure 5.4 Lower clamp.

5.1.2 *Floating clamp*

This part is the movable clamp with slides on the ground rails. On the underside of the clamp, a machined nylon adaptor was used to attach the ceramic plate to the aluminum structures. On the top of the clamp, a 1000 lbs. Load cell was attached to monitor welding pressure throughout the process, as shown in Figure 5.5. A thermocouple was also attached to the surface of the ceramic plate to monitor the contact temperature between the fixture and coupon during welding.

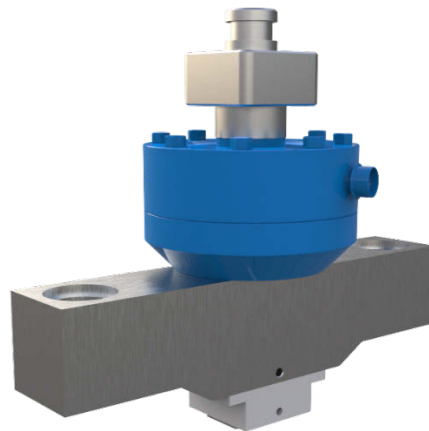


Figure 5.5 Floating Clamp.

5.1.3 *Electrical connector bridges*

These connectors were responsible for securing the heating element in place and applying current to perform the weld. A machined aluminum block was used as the structural skeleton to which a machined nylon insulator was press-fitted. A machined copper tab was sized to handle the current of more than 120 amps and was press-fitted to the nylon block. Together, this arrangement was strong enough to apply sufficient clamping force on the heating element. Under the electrical connector bridge, a floating

copper block was used to make sure that no parts of the heating element were exposed to air, to preventing overheating as shown in Figure 5.6. The floating copper block also acted as a heat sink for the heating element, which was outside the weld region.

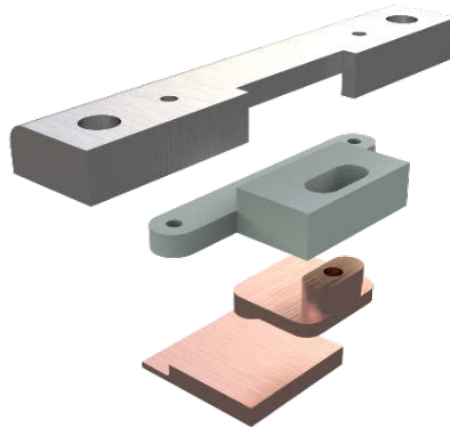


Figure 5.6 Electrical Connectors.

Once the entire welding fixture was assembled, a metalized glass fiber polyimide heat insulation tape was applied to all areas in proximity to the weld (other than the ceramic region), as shown in Figure 5.7. In the subsequent revisions of the weld fixture, the electrical connector bridges were attached on a compressed spring and wingnuts in the front. This made the test setup completely tool-less and significantly shortened the setup time.

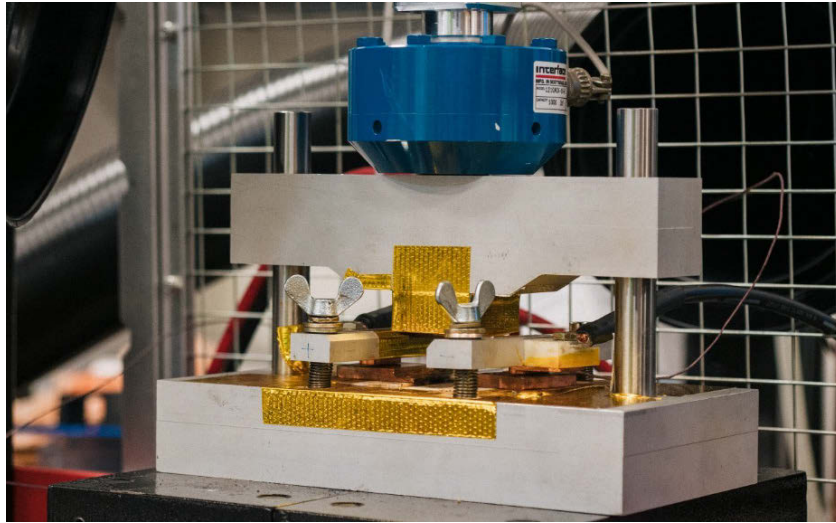


Figure 5.7 Fully assembled weld fixture.

5.2 Weld Automation and Data Acquisition.

The weld fixture had three thermocouples, a load cell, and a programmable power supply. To control and acquire data from all sensors, LabVIEW was used. In addition to the weld fixture, a P3 strain recorder, National Instruments Compact Rio, and Keysight 6682a programmable power supply were used to acquire data and supply welding power. The electrical schematic of the weld fixture is shown in Figure 5.8.

5.2.1 Data Acquisition:

- a. **Temperature:** The weld fixture had two thermocouples attached permanently to the underside of the top clamp and the positive floating connector block. The third thermocouple was occasionally used to monitor the temperature in the mesh center while establishing process parameters.
- b. **Load cell:** A 1000 lbs. full bridge load cell was used to monitor clamping pressure on the weld. The load cell was connected between the floating clamp and the

hydraulic press. P3 strain recorder was used to acquire data on the force from the load cell. The strain recorder was connected to the NI Compact Rio via an analog signal channel.

- c. **NI Compact Rio:** This is a compact, logical processing FPGA unit from National Instruments. The real-time module from NI was flashed on this device to act as a high-speed data acquisition system. NI 9213, a temperature input module with cold-junction compensation was used to interface the thermocouple with Compact Rio. NI 9201 analog input module was used to interface with the P3 Strain recorder. The advantage of using a Compact Rio was its ability to timestamp measured data, thus ensuring proper sync between multiple sources.

5.2.2 Weld Power Control

- a. **Power supply:** A Keysight 6682a programmable power supply was used to supply weld current for the fixture. The power supply was rated for an output of 21 V and 210 Amps. For welding tests, less than 8% of the power supply output was used. This ensured that the weld test was repeatable over a long duration without overheating the power supply. One of the challenges of using this power supply was its outdated interface. The power supply uses a GPIB interface for which native drivers were not available. A custom driver code was written using LabVIEW's visa module. The underlying protocol for this GPIB interface was SCPI command line for reading and writing data from the power supply. The power supply was also set to follow the voltage control command from the LabVIEW program, with a virtual safety current limit of 35 amps, to prevent any temperature

rise in power cables and electrical connectors. The power cables between the power supply and weld fixture were sized to handle up to 110 amps at 60 volts DC.

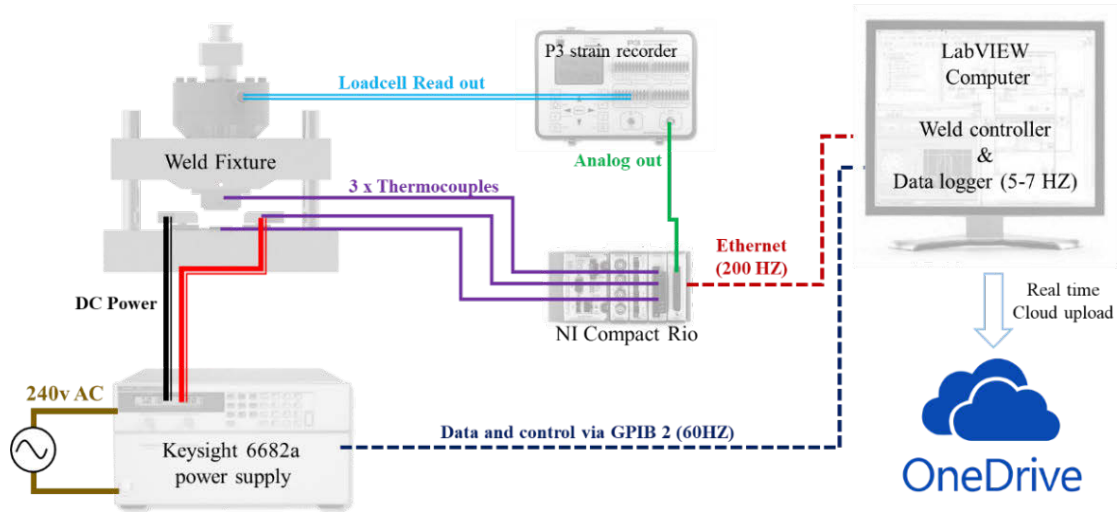


Figure 5.8 Weld automation and Data Acquisition.

5.3 LabVIEW Program.

LabVIEW 2018 was used to develop a weld controller and data acquisition system. As seen in Figure 5.9, the LabVIEW program can be divided into five sections. The first section of the program had blocks to acquire data from compact Rio, remove noise from it, and scale the signal, respectively. These data streams were then logged using a “write to measurements” block. The other section of the code was used to generate voltage sweep profiles as requested by the operator and write to power supply drivers at 75 Hz. These power supply drivers could write the requested voltage to the power supply and read the actual voltage and current at its terminals. The last module of the code was to interface with the front-end control panel, as shown in Figure 5.10, to take inputs for the welding process and communicate sensor readouts in real-time.

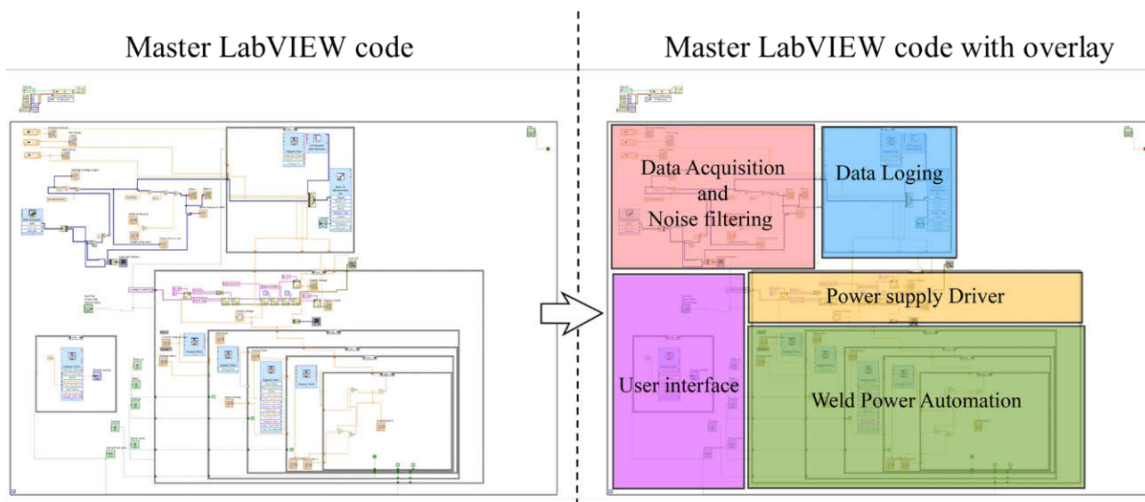


Figure 5.9 LabVIEW program (backend).

The weld power profile was programmed by defining voltages and times; using these inputs, the controller linearly interpolated values between any two defined points. This was done by inputting in the top right corner of the front-end user interface, as shown in Figure 5.10. The green lights corresponding to the values showed progress during the welding process. A warning system was also implemented to alert the operator if clamps were released to remove the coupon when it was too hot to touch. The following data streams were logged during every weld: top clamp surface temperature, positive floating clamp temperature, mesh center temperature (when available), clamping pressure, weld voltage, and weld current. After each welding test, a time-stamped spreadsheet with all the sensor readouts is automatically saved to the local computer.

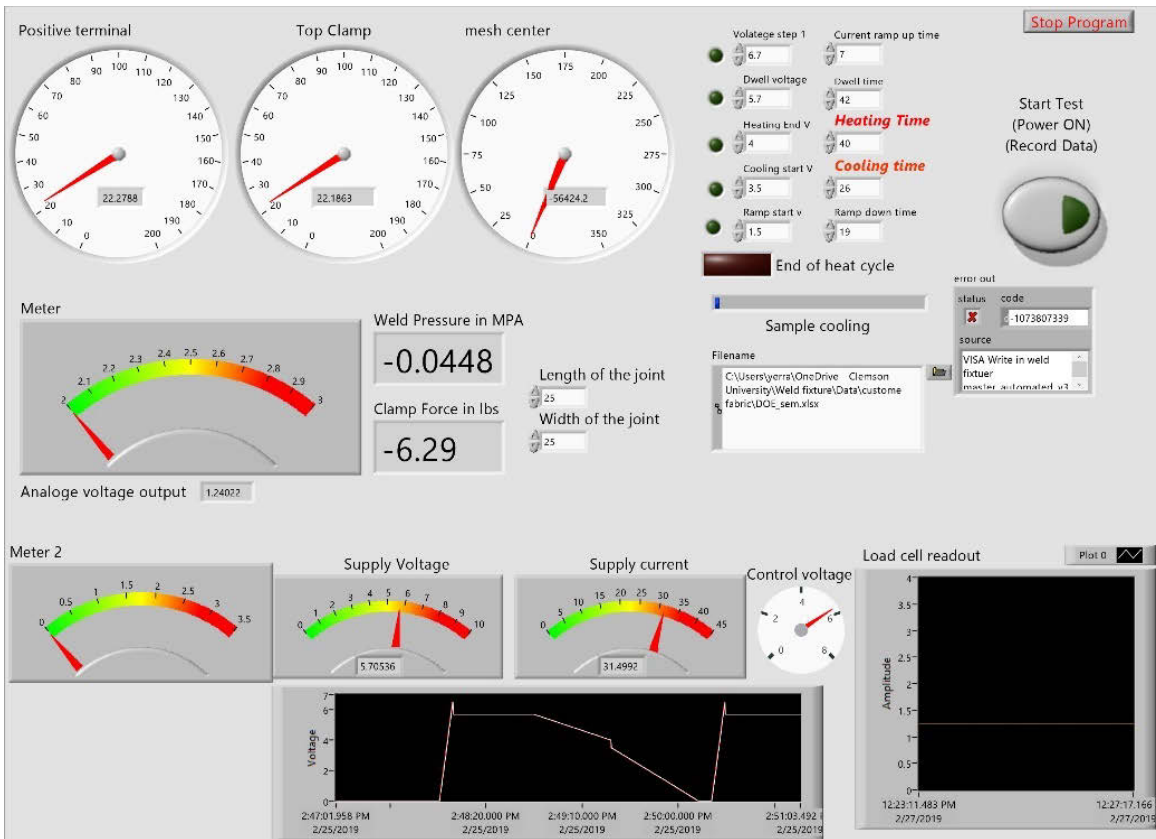


Figure 5.10 LabVIEW program front end (UI for the operator).

6 IDENTIFYING PROCESSING WINDOW

As mentioned in Chapter 2, the primary focus of this chapter is to understand and identify processing windows for RIW joints of FRTPCs with engineering polymer matrix material. Polyamide 6-6 was chosen as the matrix due to its low cost, adequate strength, and extensive use within the automotive sector, especially as unfilled polyamides¹²⁰.

Since most of the innovation for FRTPCs has emerged from the aerospace industry, there has been an implicit bias in research on FRTPCs involving high-performance polymer matrix materials. This bias also translates into research on resistive implant welding of such materials, with two exceptions to this being the evaluation of melt flow behavior of glass fiber reinforced polypropylene during RIW process⁵⁸, and the investigation of effect of weld pressure and mesh geometry for glass fiber reinforced polyethylene terephthalate⁵⁹.

6.1 Weld process & variables

The RIW process can be divided into five phases: (a) Clamping; (b) Heating; (c) Consolidation; (d) Cooling; and (e) Part removal. Each of these phases has several independent variables, as shown in

Table 6.1. In this section, a systematic approach is used to identify optimum processing variables for welding FRTPCs with PA 6-6 matrix, based on both existing literature and experimental evaluation.

Table 6.1 Variables in RIW process.

Welding phase	Variables.	Approach
<i>Clamping</i>	I. Type of clamping control	From literature
	II. Clamping force	Experimental
<i>Heating</i>	III. Heating element material selection	From Literature
	IV. Quantity of pure resin in the weld interface	Experimental
	V. Weld temperatures	Experimental
	VI. Heating time	Experimental
<i>Consolidation</i>	VII. Consolidation time	Experimental
<i>Cooling</i>	VIII. Cooling time	Experimental
<i>Part removal</i>	IX. Unclamping temperature	Experimental

6.1.1 Type of Clamping control.

Till date, most control strategies for clamping force can be classified into two categories: (a) Constant force method; and (b) Constant displacement method.

In the constant displacement method, initial welding pressure is applied, and the position of the clamping block is fixed. When heat is applied at the joint interface, thermal expansion of the substrate material results in a sharp increase in clamping force⁶⁰, with this increase being more pronounced in semi-crystalline polymers⁵⁶. Due to this sharp increase, the polymer matrix is squeezed out of the interface during the welding process, which often leads to reduced weld strength^{56,60,61}. To prevent this, most researchers^{60,61} suggest using lower initial clamping pressure. However, the downside of this approach is poor heat transfer through conduction during the initial heating. In contrast, at higher clamping pressures, the heating element sinks into the pure polymer layer, thereby

increasing the surface area for heat transfer, as shown in Figure 6.1. Apart from this, the other drawback of using lower initial clamping pressure is inadequate consolidation pressure during the cooling phase of welding process. During cooling, the substrate material starts to recrystallize, leading to significant shrinkage in the substrate material¹²¹. The lack of adequate clamping pressure during this phase can lead to warpage in finished joints¹⁰¹.

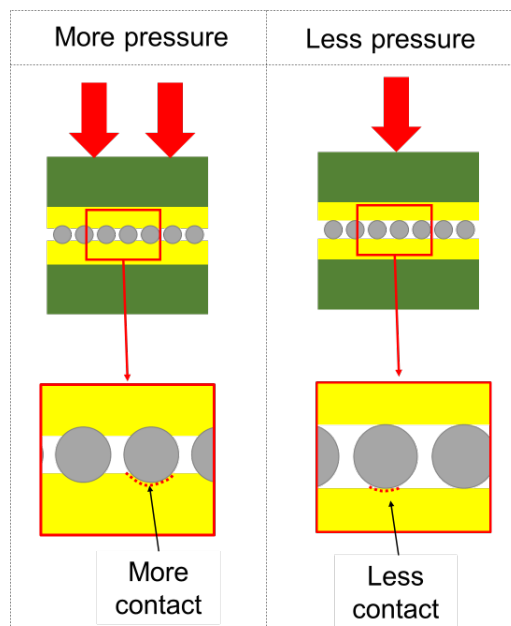


Figure 6.1 Effect of initial pressure on contact.

Given these conflicting requirements for clamping pressure, a constant pressure method has been proposed by Ageorges⁶¹, where the welding pressure is actively monitored and adjusted throughout the process using a closed-loop controller. Using this approach, Ageorges⁶¹ and other researchers^{50,82,122} were able to produce better quality welds with lower polymer squeeze out and void content. However, some major limitations of this approach are: (a) Difficulty in controlling final weld thickness; (b) Increase in

complexity of weld fixture design and cost; and (c) Highly challenging nature of scaling up this process for larger joints⁷⁵.

In this dissertation, a hybrid approach was used to control clamping pressure that was applied using a hydraulic cylinder connected to an accumulator (Figure 6.2). This system helped to passively smoothen and minimize the pressure spikes and drops in the welding process, while not requiring any complex active controllers and load cell on weld fixtures. However, a load cell was included in this setup to monitor pressure during the welding process. When implemented commercially, this load cell can be eliminated, and the clamping pressure can be directly measured by monitoring the output pressure of accumulator. The other reason for selecting such a hydraulic layout was that it could easily be scaled to larger joints at lower costs when compared to constant pressure systems.

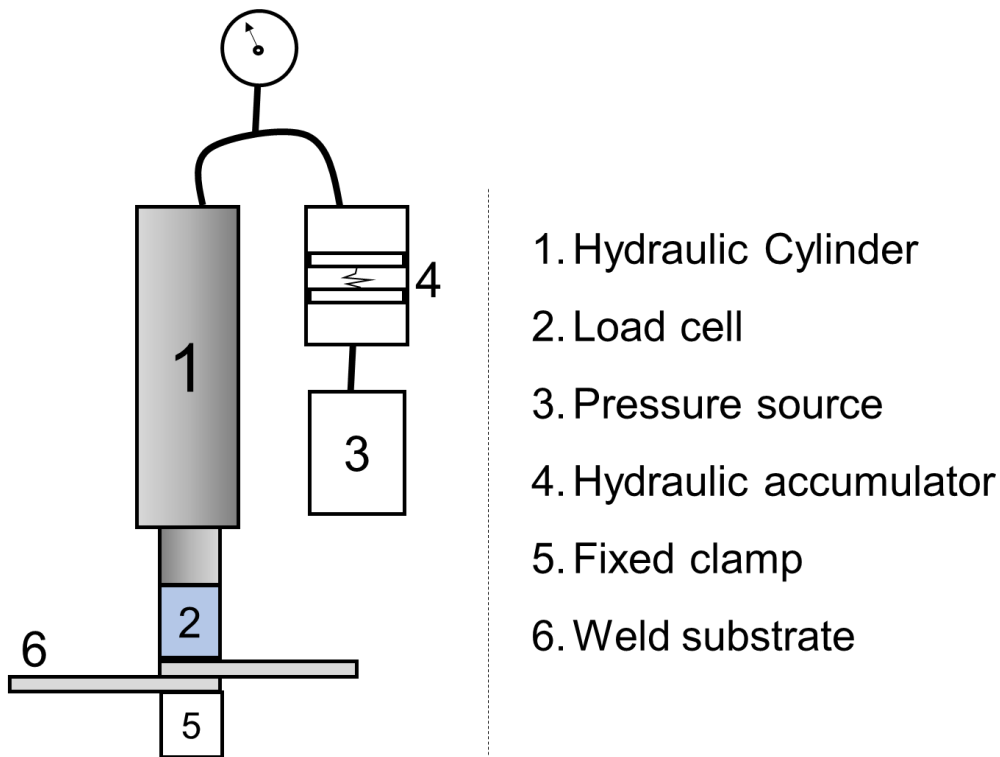


Figure 6.2 Clamping system hydraulic layout.

6.1.2 Clamping force.

Clamping pressures used in most literature^{47,49,55,83,86} till date range between 0.5-2.5 MPa. Using the initial welding conditions, three welds with clamping pressures of 0.50, 0.75, and 1.00 MPa were performed. The welded coupons were cut in the center of mesh region using an abrasive diamond cutter, were sputter-coated with silver (Ag), and subsequently, SEM images were taken from their cross-section. Clamping pressures of 0.50 MPa and 0.75 MPa were observed to cause significant void content in the weld region (Figure 6.3). To avoid such voids, the acceptable pressure window for this evaluation was set in the range of 1.00-2.50 MPa.

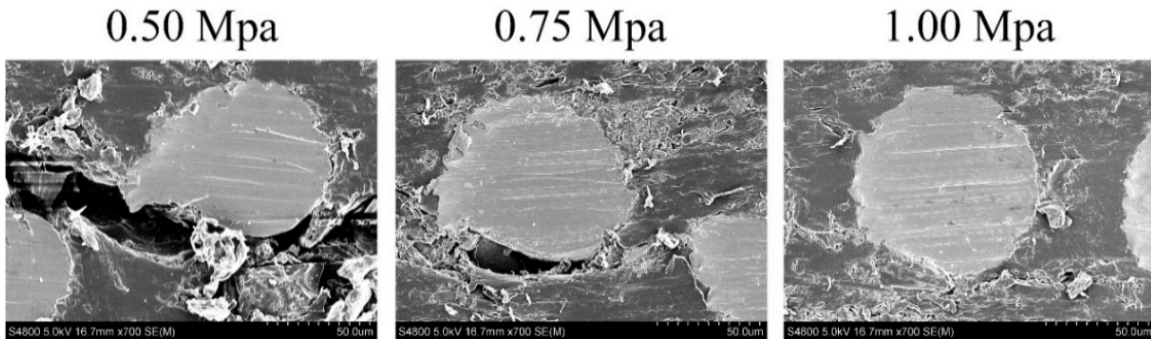


Figure 6.3 SEM images of weld cross-section at 50 microns for varying initial pressures.
(The grey circle is a single wire of the heating element).

6.1.3 Heating element material

The two most common heating elements (HEs) used in literature are stainless steel mesh^{47,49,53,55,57,82,122,123} and carbon fiber fabrics^{52,61,124}. RIW process with stainless steel HEs has consistently produced better joints with fewer voids and dry spots. Moreover, the change in resistance of stainless steel HE with an increase in temperature is significantly lower than that for carbon fiber HE^{47,49,60}, so its use often leads to a more predictable

outcome. To understand the effect of temperature on resistance, a thermocouple was attached to both HEs (Figure 6.4), and resistance between the contacts was measured over 25-300°C (Figure 6.5). Even though the initial resistance of carbon fiber HE is higher than that of stainless steel HE, it drastically drops with increase in temperature. In fact, at 200°C, carbon fiber HE has less than half the resistance of stainless steel HE. Such low resistance at higher temperatures makes the carbon fiber HE less efficient for the welding process. In addition to these issues, the best lap shear strength obtained for carbon fiber HEs was only 24% of that for stainless steel HE.

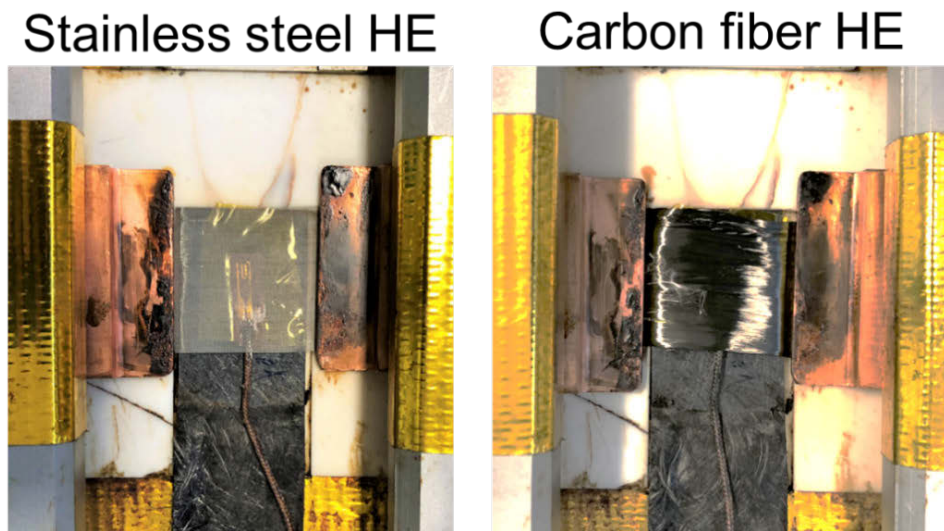


Figure 6.4 resistance vs. temperature measurement.

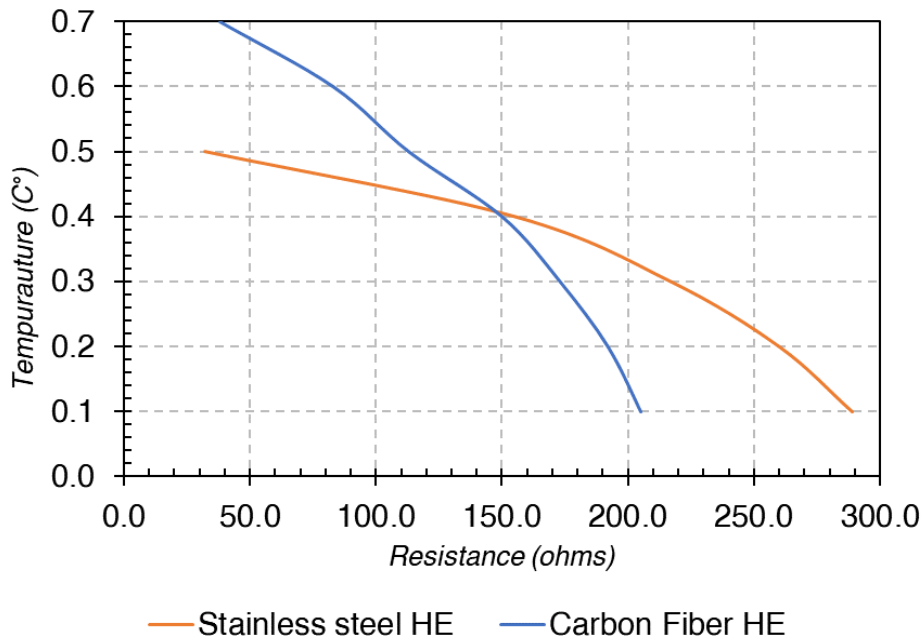


Figure 6.5 Temperature vs. resistance for heating elements.

6.1.4 Quantity of pure resin in the weld interface

One challenge when welding FRTPCs with carbon fiber reinforcement is the phenomenon called current leakage^{49,53}. When the HE comes in contact with carbon fiber reinforcements in FRTPCs, current leaks from the HE to reinforcements within the substrate. This causes the overall resistance between connectors to drop, thus reducing the temperature at the joint interface and also making the process inefficient. To prevent these effects, two approaches were evaluated: (a) Coating the HE with ceramics⁴⁹; and (b) Using neat polymer film on both sides of HE^{60,64}. Of these two approaches, the presence of polymer film not only helps to eliminate current leakage but also improves the contact area between HE and substrate. Hence, the neat film approach was used in this dissertation to prevent current leakage.

However, no literature till date has determined the optimum thickness of this neat polymer film. Therefore, a quick experimental evaluation was undertaken by varying the thickness of neat polymer film at the joint interface and testing the lap shear strength of RIW joints (Figure 6.6). Since weld tests with neat films (thickness: 50 μm) performed the best, the 50- μm neat film thickness was used in the weld regions for subsequent evaluations. To achieve this thickness, two 25- μm neat polymer films were used on either side of the stainless steel HE.

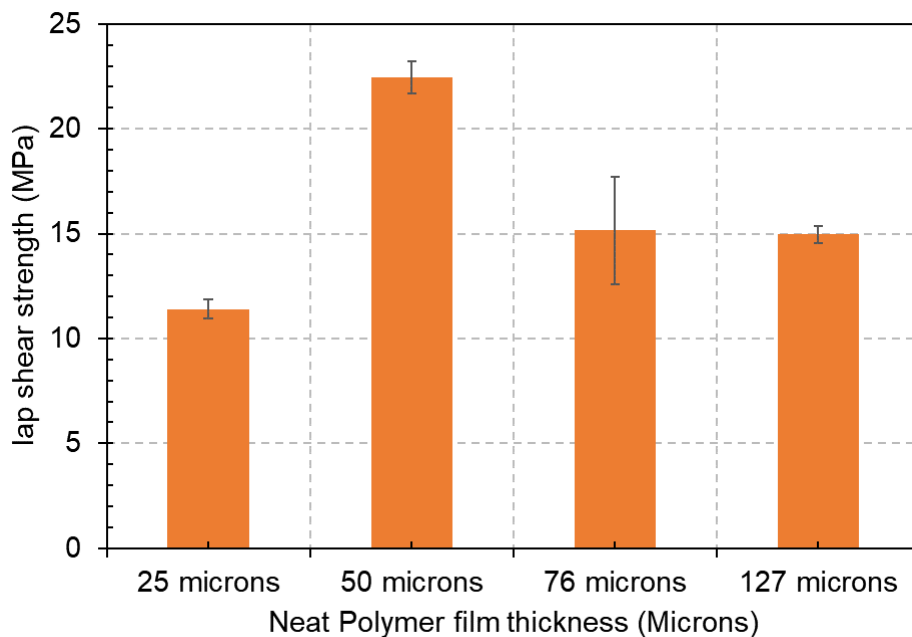


Figure 6.6 Lap shear strength vs neat polymer layer thickness.

6.1.5 Weld temperatures

To determine the ideal weld temperature for FRTPCs, a thermal analysis of the polymer matrix is necessary. With accurate melt temperature and processing windows for the polymer matrix, an informed decision on welding temperature can be made.

Thermal analysis of PA 6-6 carbon fiber composite

Differential scanning calorimeter (DSC) was used to determine the melt and glass transition temperatures for matrix material¹²⁵ (Figure 6.7). Melt peaks were observed at ~ 261.2°C and ~ 52.4°C (corresponding to glass transition temperature). The exothermic peak between 246.3°C and 224.8°C indicated the recrystallization temperature range of the polymer. Yet, upon closer inspection, it was understood that data from DSC alone is insufficient, and that additional information, such as degradation temperature, viscosity, and storage modulus profile, is also needed to define the welding temperature profiles.

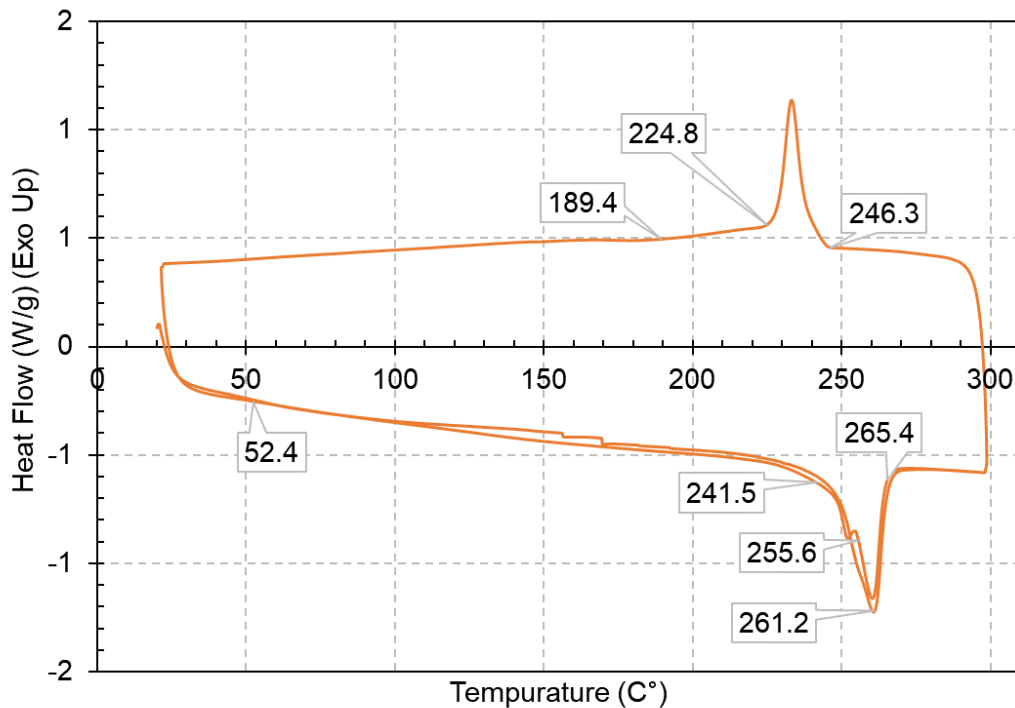


Figure 6.7 DSC plot for PA66 with carbon fiber reinforcements.

To prevent any thermal degradation/oxidation of PA 6-6, it is commonly suggested to keep the processing temperature under 300°C¹²⁶, but upon verifying this, visual color

change in PA 6-6 was observed around 287-293°C (Figure 6.8). For this very reason, the upper limit for weld temperature was set at 285°C in this study (Table 6.2).

Table 6.2 DSC test conditions and results.

	Attribute	Value
Test Conditions	Cycle	Heat – Cool -Heat
	Temperature range	20° to 300° C
	Temperature ramp	20°c/min
	Atmosphere	Nitrogen
Results	Glass transition temperature (Tg)	52.4°C
	Melt Temperature (Tm)	261.2°
	Recrystallization peak	246.3° to 224.8° C
Weld parameters	Welding temperature range	285° to 260° C
	Controlled cooling lower limit	189.4° C



Figure 6.8 Visual color change (degradation) in pure PA66 at ~290°C.

It is also important to control the cooling rate of the weld region until it reaches the lower limit of recrystallization temperature^{127,128}. In semi-crystalline polymers such as PA

6-6, the cooling rate is one of the most critical factors for controlling crystallinity³⁶. To increase the degree of crystallinity in the polymer, it is essential to actively control the cooling rate by gradually ramping the power to the HE.

6.1.6 Heating time, consolidation time, cooling time, and clamping pressure.

Having determined all other variables, a full factorial design of experiments (DOE) was conducted to determine optimal processing time and clamping pressure for maximizing the RIW weld performance of PA 6-6 composites.

To determine the weld power requirements for RIW process, several samples with thermocouples at the joint interface were used (Figure 6.10). After manually adjusting and testing various voltage/current profiles (Figure 6.9), it was determined that ~ 91.2 watts (141.3 kWh/sq.m) of power is needed to reach the desired welding temperature window (260-285°C) for this test configuration.

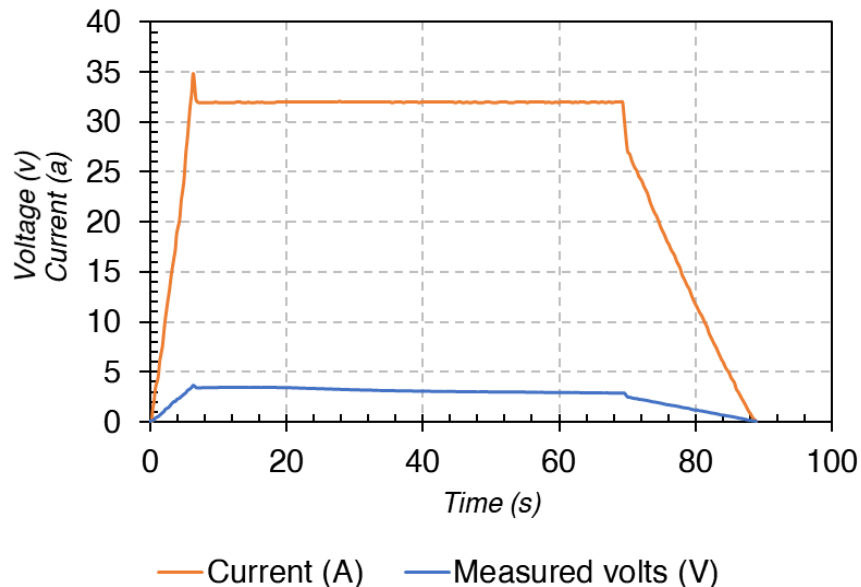


Figure 6.9 Voltage and current profile.

Using this weld power requirement as a constant, a DOE with variables such as heating time, cooling time, and initial clamping pressure was created to understand the influence on mechanical performance (Table 6.3). In most studies, the performance of welded joint is only described by lap shear strength, but it is important to look at other attributes such as stiffness, toughness, and elongation at break in order to better understand the influence of these different variables^{36,47,60,129–131}.

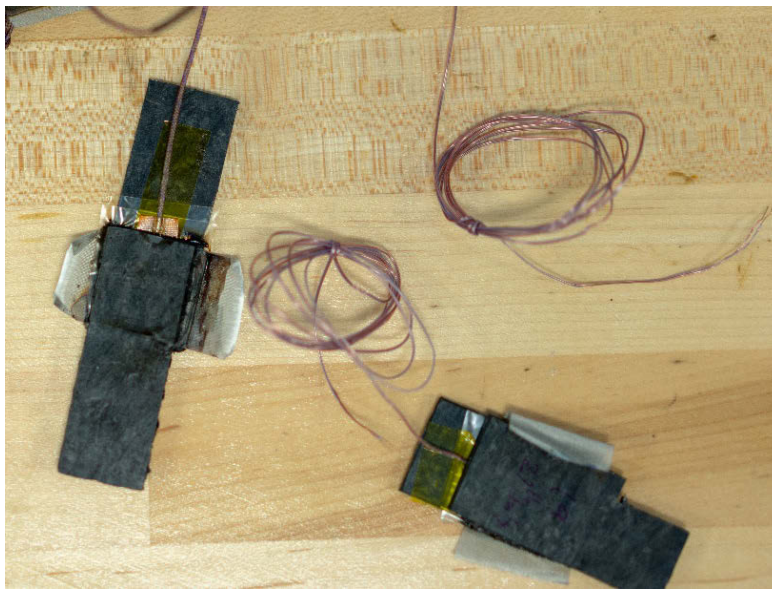


Figure 6.10 Test welds with a thermocouple on the mesh center.

Keeping this in mind, a full factorial DOE with three midpoints was evaluated with variables and responses (Equation 5). Using the data collected from the DOE, the effects of variables were studied (Table 6.3). Figure 6.11 also shows the individual force-displacement plots for all test welds. From this test data, response-interaction plots were generated in Minitab to illustrate the effect of different variables on the overall joint performance. This influence of weld process variables has been discussed in Section 6.2 of this chapter.

DOE : $F(\text{variables}) = \text{responses}$

(1)

$f(\text{heating time, cooling time \& intial pressure})$

= max force at break, stiffness, toughness, elongation at break.

Table 6.3 Variable and responses for DOE 1.

Variable				Responses			
Run order	Initial Pressure (MPA)	Heating time (Sec)	Cooling time (Sec)	Max force (KN)	Stiffness (KN/mm)	Energy (Joule)	Elongation at break (mm)
1	1.00	55	130	10.9	12.2	5.4	0.9
2	1.75	40	100	15.6	11.0	12.8	1.5
3	1.75	40	100	13.3	11.1	9.1	1.3
4	1.00	55	70	8.4	9.9	2.9	0.7
5	1.00	25	70	10.9	11.0	6.2	1.1
6	2.50	55	70	14.1	12.1	9.2	1.2
7	1.75	40	100	9.8	9.8	4.6	0.9
8	2.50	25	70	14.2	11.3	10.5	1.4
9	2.50	25	130	11.4	11.5	6.0	1.0
10	2.50	55	130	11.9	11.3	7.2	1.1
11	1.00	25	130	11.3	10.9	6.7	1.1

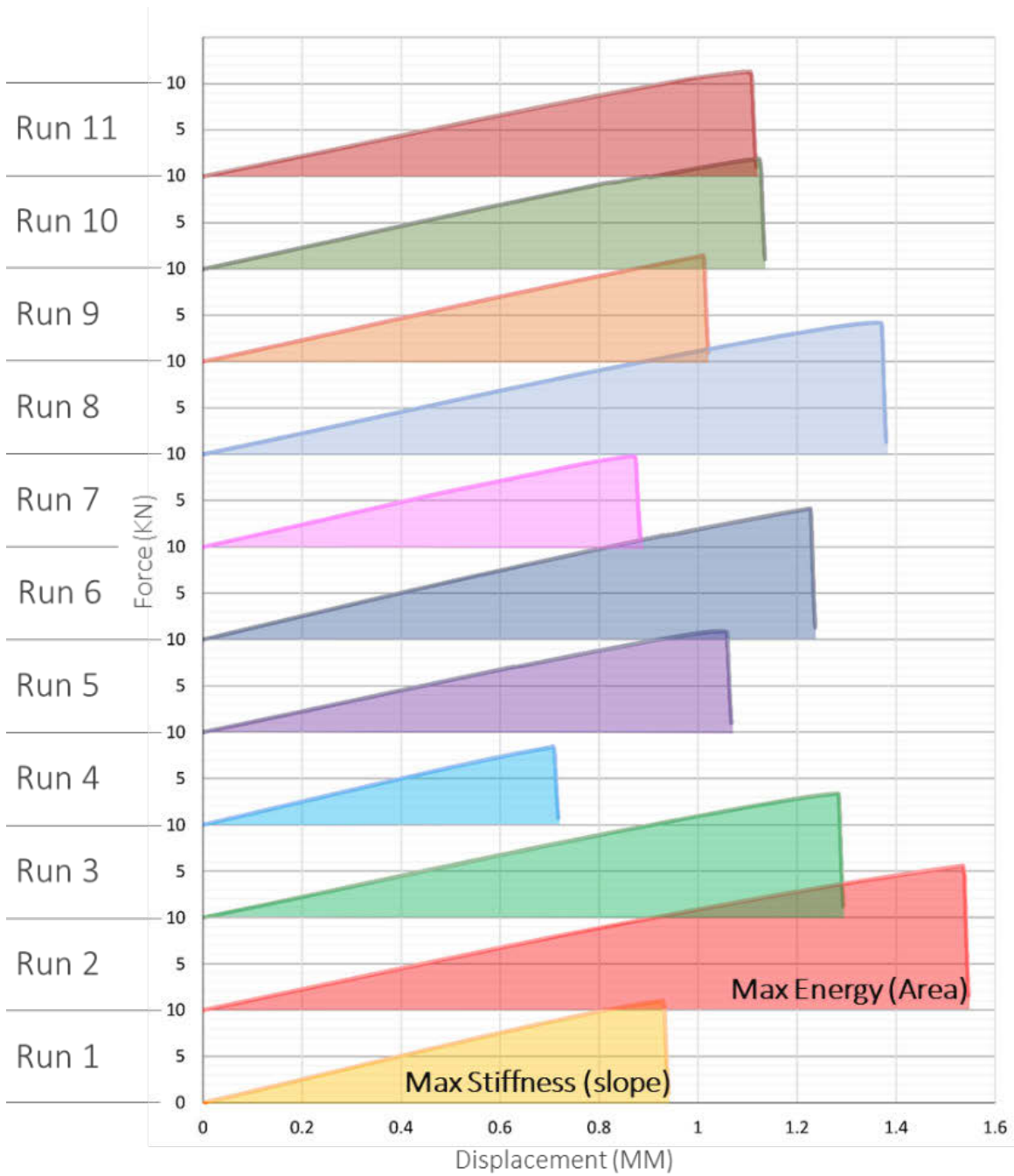


Figure 6.11 Force-displacement plots for DOE 1 under lap shear.

6.1.7 Unclamping temperature (or part ejection)

Last but not least, it is also necessary to determine the safe temperature for removing the welded joint from the welding fixture (to prevent warpage or distortion). For most polymers, the glass transition temperature can be used for part removal. However, PA 6-6 has a very low T_g of $\sim 54.2^\circ\text{C}$, so waiting for the weld to cool down to this temperature will drastically increase welding time. Since minimizing weld time is critical for automotive production, there is a motivation to determine the highest safe temperature for part ejection. A melt rheometer was used to determine the response of viscosity and storage modulus v/s temperature (Figure 6.12). From Figure 6.12, we can observe that there is a slight drop in storage modulus and viscosity of PA 6-6 at 190°C , and then a drastic drop after 240°C . From this data, one can conclude that it is safe to handle the welded coupons after cooling them down to below 190°C . However, for operational safety, these welded joints were let to cool down to 100°C before part ejection. In a commercial setting, where maintaining short cycle times is crucial, the welded parts can be ejected once they cool down to $\sim 180^\circ\text{C}$.

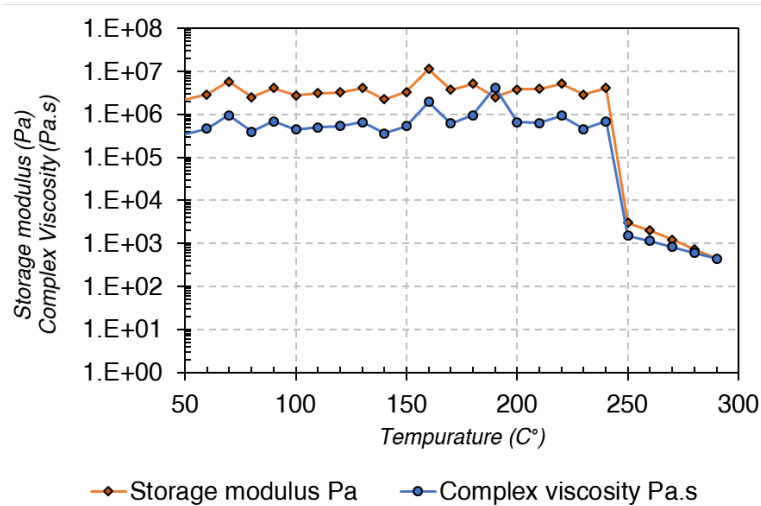


Figure 6.12 Storage Modulus and Viscosity of PA66.

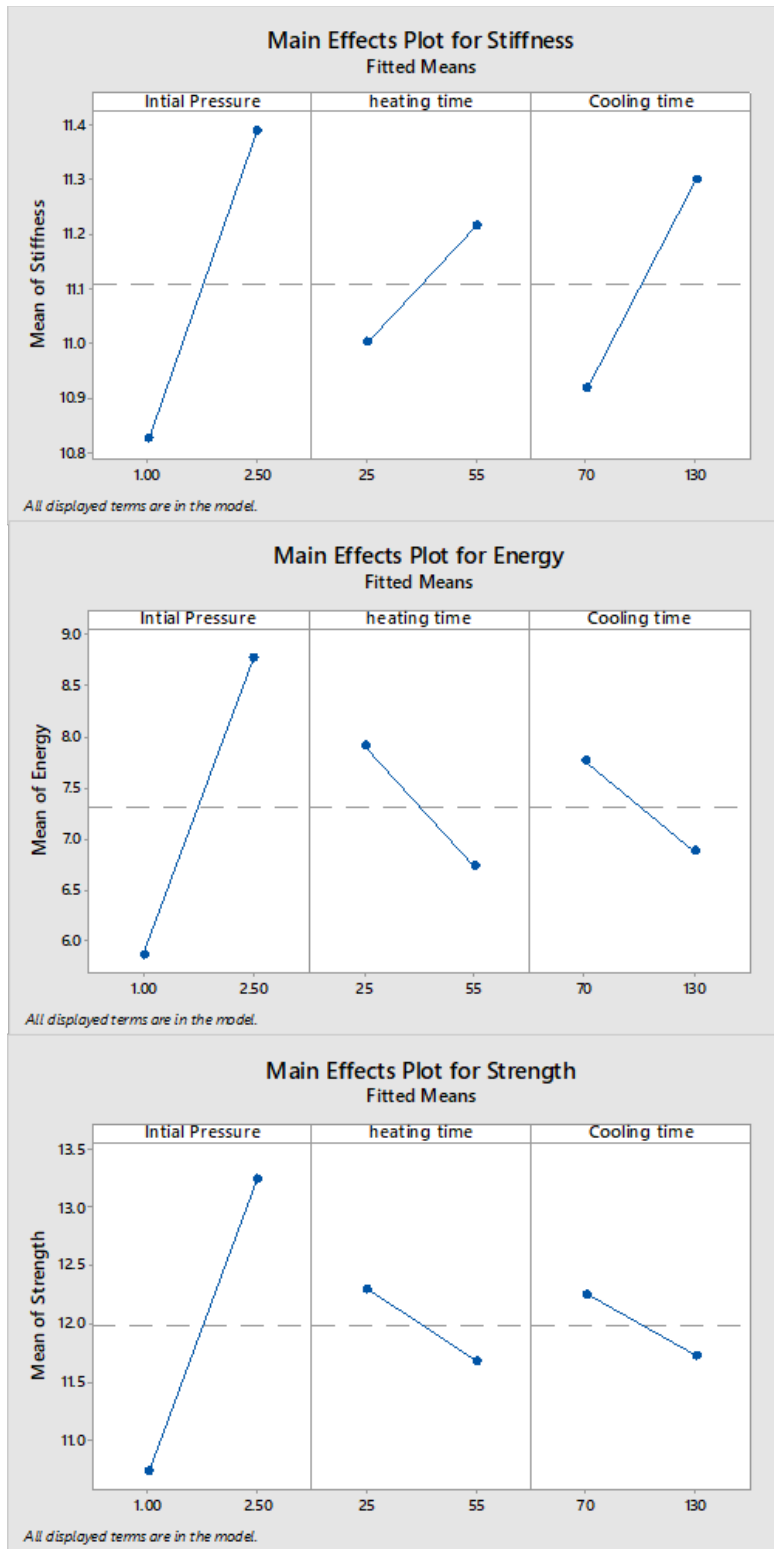


Figure 6.13 Main effects plots of variables on responses.

6.2 Effect of process variables on joint performance

6.2.1 Effect on joint stiffness:

I. Clamping pressure:

With an increase in clamping pressure, the stiffness of joint generally increased (Figure 6.13), which could be attributed to the decrease in void content, and possibly also the decrease in pure resin content, in the weld region. The latter explanation holds since with higher clamping pressure; pure resin is squeezed out, thereby decreasing the resin content and increasing the fiber volume fraction in the weld region. Such an increase is typically associated with an increase in stiffness¹³².

II. Heating time:

There is a positive correlation between heating time and the stiffness of weld (Figure 6.13). This is because with longer heating time, the depth of polymer melt increases, which helps the fibers and HEs to move within the weld region and consolidate more tightly, thereby increasing fiber intertwining in the weld region.

III. Cooling time:

With an increase in the cooling time, the weld is gradually cooled from melt temperature to glass transition temperature. In semi-crystalline polymers, slower cooling rate leads to a higher degree of crystallinity³⁶. Moreover, with a higher degree of crystallinity, polymeric stiffness typically increases. One key takeaway from this is that active control of the cooling rate of the welded joint is very critical to its mechanical performance.

6.2.2 Effect on strength and toughness (energy):

The behavior response for strength and toughness are very similar; for this very reason, the effect of weld variables on these attributes are merged.

I. Clamping pressure:

Similar to the effect on stiffness, clamping pressure has a positive correlation with weld strength and fracture energy, which can be attributed to the effect of this pressure on minimizing void contents and improving the overall weld quality.

II. Heating time:

Increase in heating time reduces the strength and fracture energy of welded joint, which might be due to a slight thermal degradation of the polymer in the weld region. Also, as previously explained, an increase in fiber volume fraction makes the joint more brittle, thus decreasing the fracture energy and overall strength.

III. Cooling time:

The rate of cooling plays a critical role in strength and fracture energy. By rapidly cooling the polymer, the degree of crystallinity decreases drastically. Since amorphous polymers are known to exhibit ductile behavior, this increase in cooling rate leads to more amorphous regions in the polymer, thereby increasing the elongation at break, which in turn affects its fracture energy and strength.

6.3 Key learnings

1. Accurate control of heating element temperature is critical, as it helps prevent any thermal degradation in polymers – even minimal thermal degradation can lead to a significant loss in mechanical properties of the RIW joint.

2. Cooling rates play an important role in determining joint performance, as the degree of crystallinity for a polymer is a function of the cooling rate. Also, it is possible to use the cooling rate to tune a joint for either high stiffness or high strength. For example, slow and gradual cooling during the RIW process generally yields a stiffer joint.
3. The pressure window for good welds is between 1.00-2.50 MPa. At pressures above 2.50 MPa, weld coupons were observed to be severely distorted, and dry fibers were exposed, while for weld pressures under 1.00 MPa, void content in the proximity of HE was very high.
4. The optimized lap-shear strength obtained was 24.1 MPa (15.82 kN peak force) for a non-woven CF-PA 6-6 composites. This is an acceptable result, considering that the structural adhesive (Plexus MA 530: 21.2 MPa) failed at approximate 87% of the welded joint strength.
5. The cycle time for optimum weld settings is approximately 140 s for non-woven CF-PA66 material.
6. The approximate weld power density (for both heating and controlled cooling) for welding FRTPCs with PA 6-6 matrix is ~ 141.3 kWh/sq.m. Not only is this less than the power requirements for many high-performance polymers, but it is better than even the requirement for mid-tier polymers such as PET⁵⁹ (215 kWh/sq.m). Further, this power requirement can be significantly reduced by having better thermal insulation around the weld.
7. The minimum initial clamping pressure required for welding FRTPC with PA 6-6 matrix is approximately 1 MPa to avoid voids.
8. The optimum thickness of the neat polymer film for these welds is 50 microns (two 25 microns films on either side of the stainless steel HE).

7 MECHANICAL CHARACTERIZATION

7.1 Mechanical characterization of RIW

The primary focus of this chapter is to evaluate and compare the mechanical performance of RIW joints with the best commercially available adhesive systems. Most literature focuses only on evaluating the lap shear strength, but doing so will not give a holistic understanding of the joint performance. In fact, to develop finite element models for these joints, it is necessary to have both their lap shear and peel strength. For this characterization, three FRTPCs with different reinforcement types were chosen as the substrate material. Using processing parameters from Chapter 6, these coupons were welded for lap shear and peel tests.

7.1.1 *Substrate material systems:*

- I. LFT injection molded:
 - a. Matrix: PA-66
 - b. Reinforcement: Long carbon fiber, AS4
 - c. Substrate manufacturing: Injection molding
 - d. Coupon thickness: 2.1 mm
- II. Non-Woven FRTPC:
 - a. Matrix: PA-66
 - b. Reinforcement: Ultralong recycled standard modulus carbon fiber
 - c. Substrate manufacturing: Autoclave
 - d. Coupon thickness: 2 mm
- III. Woven FRTPC:
 - a. Matrix: PA-66
 - b. Reinforcement: Woven 2 × 2 twill – AS4 carbon fiber
 - c. Substrate manufacturing: Autoclave
 - d. Thickness: 3.0 mm

7.1.2 Weld processing

Seven welds were made per substrate material system (four lap shear and three peel). Most weld parameters for welding process were kept similar to those of Run 2 in Chapter 6, barring the aerial power density for a woven substrate that was adjusted for the higher thickness in order to compensate for the higher thermal mass at the joint interface. The fourth weld lap shear coupon was not meant for mechanical testing but to verify the weld quality. This verification was done by placing a thermocouple at the joint interface and ensuring that weld temperatures did not reach the polymer degradation temperature. After welding, a small section was cut using a diamond section saw, and then sputter-coated with Ag for imaging in a scanning electron microscope (SEM). The maximum temperatures at the weld interface were observed to be around $\sim 270\text{-}282^\circ\text{C}$ – below the degradation temperature (285°C).

As can be seen in the SEM images, no large voids were observed in any of the three welded coupons (Figure 7.1, Figure 7.2, and Figure 7.3) when compared to those of the RIW weld.

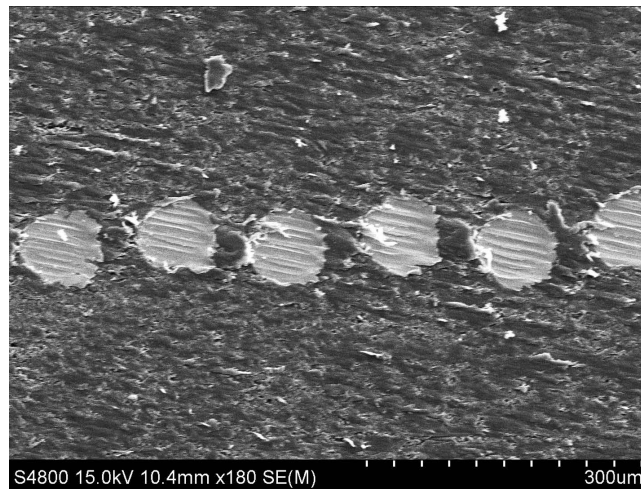


Figure 7.1 SEM section of the weld interface in LFT coupon.

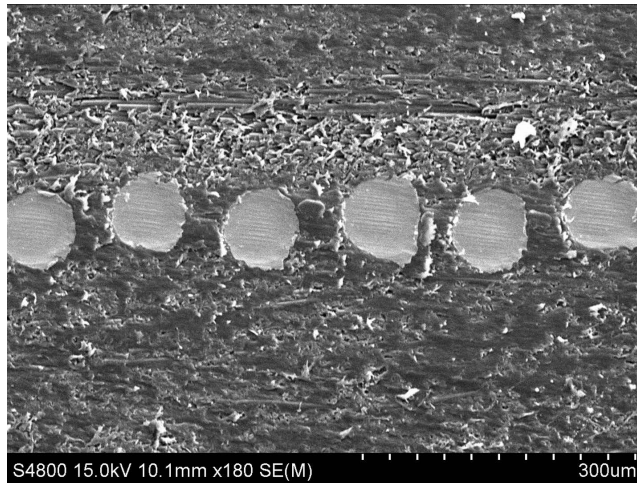


Figure 7.2 SEM section of the weld interface in Non-woven cupon.

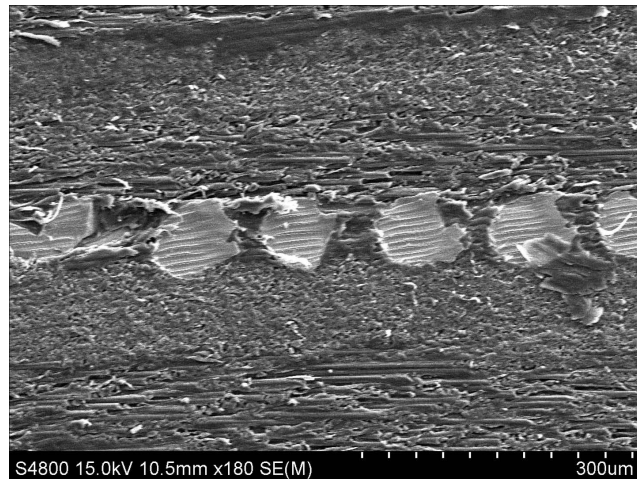


Figure 7.3 SEM section of the weld interface in woven cupon.

Weld process parameters:

- I. Initial Clamping pressure: 2.0 MPa
- II. Heating time: 40 s
- III. Target weld temperature: 280°C
- IV. Cooling time: 100 s
- V. Aerial power density:

- a. For LFT : 141 kWh/ sq.m
 - b. For non-woven: 141 kWh/ sq.m
 - c. For woven : 210 kWh/ sq.m
- VI. Max current: 35 amps
- VII. Neat resin thickness: 50 μ m
- VIII. Heating element:
- a. 316 Stainless steel mesh
 - b. 200 \times 200 mesh size
 - c. 40 μ m wire dia.
 - d. 46% open area

7.1.3 Lap shear strength test.

A universal tensile testing machine with serrated hydraulic jaws was used to test these coupons. Two glass-fiber epoxy tabs were bonded to the ends of the welded coupon to ensure that the weld is parallel to the crosshead travel axis.

Test conditions

- Test method: ASTM D5686 -01 (2014)
- Crosshead speed: 13 mm/min¹³³
- Formula: Lap shear strength (MPa) = (Peak force at break (kN) \div bond area (sq.mm))
- Weld Geometry: 25.4 mm \times 25.4 mm bond area (as recommended by ASTM)

Results

Once prepared, these welded coupons were tested at room temperature. The force and displacement of crosshead were recorded at every 20 ms during the test and using this data, lap shear strength of the joints was calculated. While the non-woven and woven joints failed interfacially at the joint region (Figure 7.5 and Figure 7.6), LFT welded coupons

always showed failure in the coupon material (Figure 7.6). For this reason, accurate strength of the weld could not be determined for the LFT reinforced thermoplastics system. However, this performance is still acceptable, since the welded joints in LFT materials are generally stronger than the parent material itself.

Table 7.1 Lap shear strength for RIW joints.

	LFT	Non-Woven	Woven	units
<i>Sample 1</i>	12.0	13.8	19.6	kN
<i>Sample 2</i>	11.2	14.3	16.8	kN
<i>Sample 3</i>	10.5	15.3	18.0	kN
<i>Avg Peak force</i>	11.2	14.5	18.1	kN
<i>Avg lap shear</i>	17.4	22.4	28.1	MPa
<i>St. deviation</i>	1.2	1.2	2.2	MPa

*Coupon failure occurred in LFT material

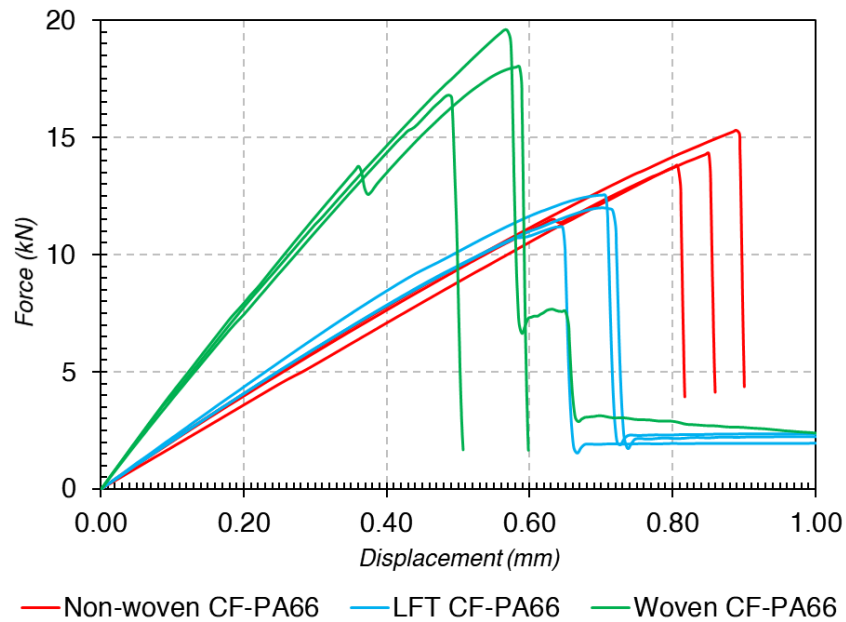


Figure 7.4 Lap shear force-displacement plot for LFT, Non-woven and Woven FRTPC.



Figure 7.5 Non-Woven coupons after failure.

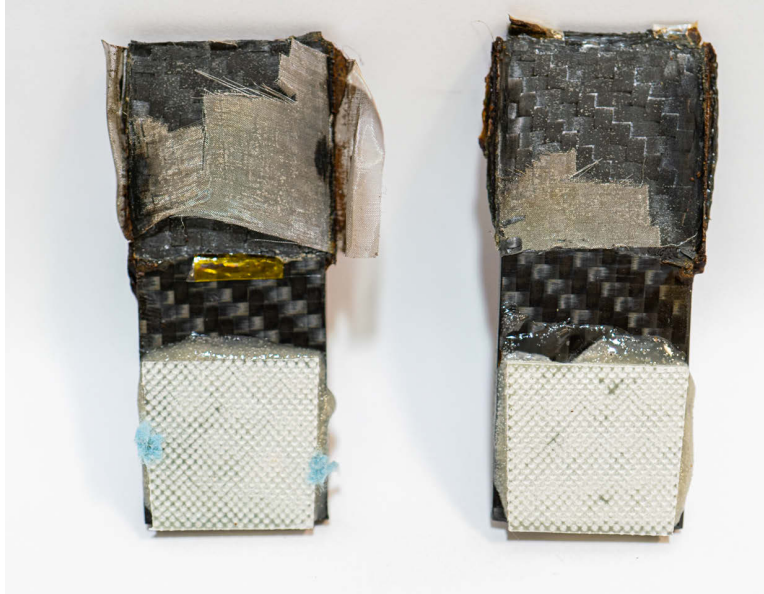


Figure 7.6 Woven coupons after failure.



Figure 7.7 LFT coupons after failures.

7.1.4 Peel strength test.

For characterizing the peel strength (Mode 1) for RIW and adhesive joints, the double cantilever beam (DCB) test was chosen as it is among the most commonly used methods to determine the peel and normal strength for adhesives and composites^{134–136} via in-situ approach. A custom fixture (Figure 7.8) was designed and properly constrained the DCB coupon in a conventional tensile testing machine. The DCB coupons were rigidly attached to the pivot block via an M6 screw with a large washer.

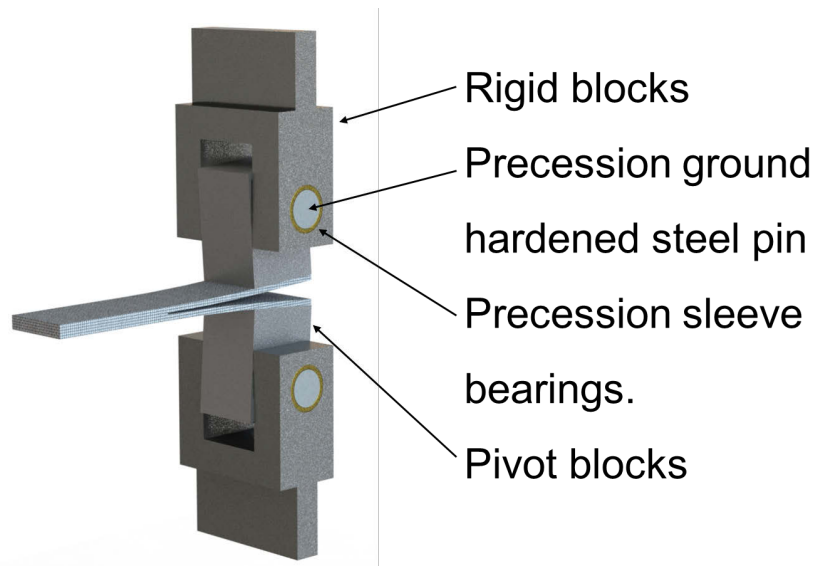


Figure 7.8 Custom designed and machine peel fixture.

Test conditions

- Test method: DCB peel strength test (ASTM D5528 with loading block)¹³⁷
- Crosshead speed: 15 mm/min
- Formula: $G_{1C} = (3 \cdot P \cdot \delta) \div (2 \cdot b \cdot a)$
 - P: Avg load (n)
 - b: Width of the joint (mm)
 - δ : Load point deflection.
 - a: length of crack
- Weld Geometry: 25.4 mm × 25.4 mm bond area

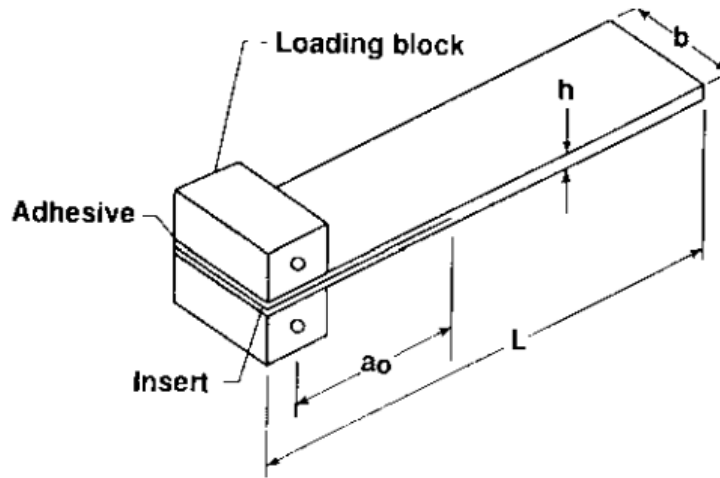


Figure 7.9 Coupon geometry (image source¹³⁷).

Results

Similar to lap shear tests, these tests were conducted at room temperature. During the test, force-displacement data was logged at time intervals of 20 ms. Using this force-displacement data, the average peel strength for RIW joints for the three FRTPC coupons was calculated (Table 7.2). To determine the crack propagation length, video DIC was used (more on this is explained in Section 8.1.4)

Table 7.2 Mode one fracture toughness for RIW joints

	LFT	Non-Woven	Woven	units
<i>Sample 1 -G_{1C}</i>	0.116	0.242	0.192	kJ/m ²
<i>Sample 2 -G_{1C}</i>	0.103	0.237	0.242	kJ/m ²
<i>Sample 3 -G_{1C}</i>	0.137	0.225	0.275	kJ/m ²
<i>Avg P -G_{1C}</i>	0.119	0.235	0.236	kJ/m ²
<i>St.dev -G_{1C}</i>	0.017	0.009	0.042	kJ/m ²

Similar to lap shear, RIW joint for both non-woven and woven carbon fiber reinforcements performed much better than LFT system. However, the difference between

woven and non-woven FRTPCs material was insignificant. In all cases, the joint failed interfacially between the heating element and substrate material (Figure 7.10).



Figure 7.10 Interfacial failure during Double cantilever beam test.

7.2 Mechanical characterization of structural adhesive joints for comparison.

To understand and set the context for the mechanical performance of RIW joints, commercially available structural adhesives were tested. The goal was to meet the mechanical performance of the best adhesive systems. Generally, fast curing adhesives used in automotive mass production result in a sacrifice of mechanical performance for faster curing times. A conscious decision was made to skip these fast curing adhesives

and pick a system which offers better mechanical performance irrespective of its curing time. After talking to various suppliers and subject matter experts, 3M DP 810 methacrylate system and 3M DP190 epoxy system were picked. During initial tests, these systems severely underperformed than manufacturer-recommended properties, which was attributed to surface preparation requirements. It is also important to note that the very low surface energy of polyamides (matrix material) and their chemical inertness also contribute to such behavior. To address these performance issues, two surface preparation methods were identified: (a) Sandblasting; and (b) Plasma etching. For sandblasted coupons, a pneumatic sandblasting unit was used with 80 grit glass beads at 40 psi pressure. For plasma-etched samples, coupons were placed in a plasma cleaner at 100% power for 10 min in a Harrick PDC-32G. Among the two types, sandblasted coupons performed marginally better.

Unsatisfied with this adhesive performance, a new adhesive system was identified for setting the baseline target: Plexus MA530, a methacrylate-based adhesive system from ITW polymers. This adhesive is specially formulated to work with fiber reinforced thermoplastics composites in structural applications. The coupons were sandblasted to improve surface roughness, and the adhesive was applied using a hand applicator with bond thickness of 0.7 mm. This bond thickness was controlled using acrylic sheets as a spacer. Once the adhesive was applied, the coupons were left for 8 h at room temperature and were then transferred in an oven at 60°C for 24 h. It was recommended to let the coupons rest at room temperature for an additional 48 h to fully cure the adhesive. This prolonged cure cycle ensured that the adhesive was entirely cured before testing. All coupons were prepared and tested using identical standard testing methods used in the previous section for RIW joints.

The Plexus systems performed far superior compared to the 3M adhesive systems (Figure 7.11). Similar results have been reported by Yaralagadda. S et al.²⁰, who identified the Plexus system as among the better performing adhesives for FRTPCs.

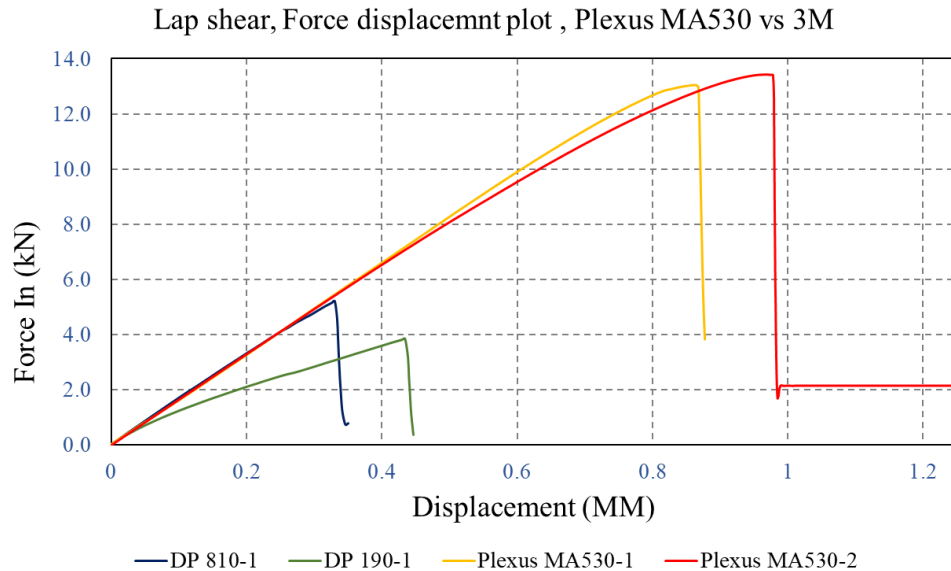


Figure 7.11 Plexus MA530 vs. 3M adhesive lap shear performance.

After selecting this adhesive, an in-situ evaluation for lap-shear strength and Mode 1 fracture toughness testing was conducted (similar to RIW) using the non-woven carbon-fiber PA-66 material. The results for these tests are summaries in Table 7.3.

Table 7.3 Mechanical properties for Plexus ma530.

	Lap Shear Strength		Mode 1 Fracture toughness	
<i>Sample 1</i>	18.044	Mpa	0.293	kJ/m2
<i>Sample 2</i>	20.210	Mpa	0.282	kJ/m2
<i>Sample 3</i>	20.807	Mpa	0.298	kJ/m2
<i>Avg P</i>	19.687	Mpa	0.291	kJ/m2
<i>St.dev</i>	1.454	Mpa	0.008	kJ/m2

7.3 Understanding strain rate dependency

No studies have sought to evaluate the strain rate dependency of resistive welded joints for polyamides. Since it is important to verify that no significant reduction in mechanical performance is observed during high or low strain rate loading, this study was conducted using both resistive welding and Plexus MA 530 structural adhesive at three different strain rates. Due to limitations of the universal tensile testing machine, the maximum test speed was limited to 500 mm/min. These strain rates fall under quasi-static to medium rate (Figure 7.12). To set a context for strain rates in automotive structures, Figure 7.13 shows the typical strain rate (5.0 e1/sec or $\sim 1600 \text{ mm/sec}$ crosshead speed) experienced by joint elements in FMVSS 214 rigid pole test simulation in the FRTPC door from Chapter 4.

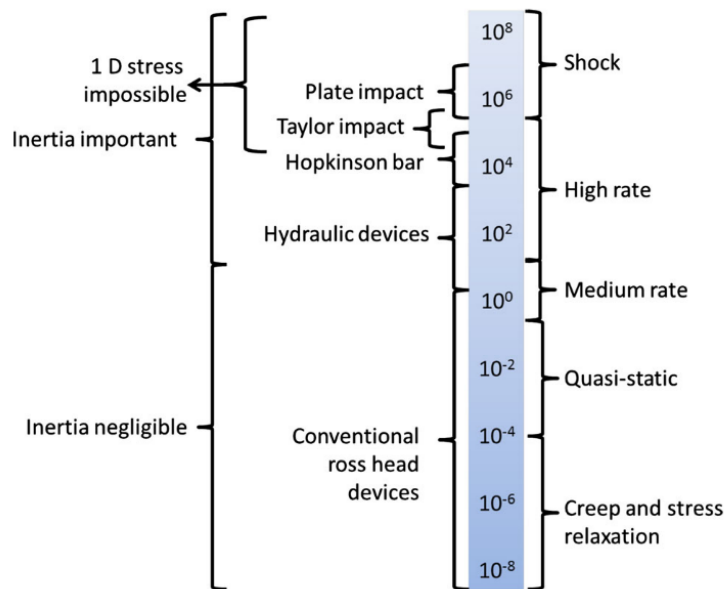


Figure 7.12 Strain rate classification(image source¹³⁸).

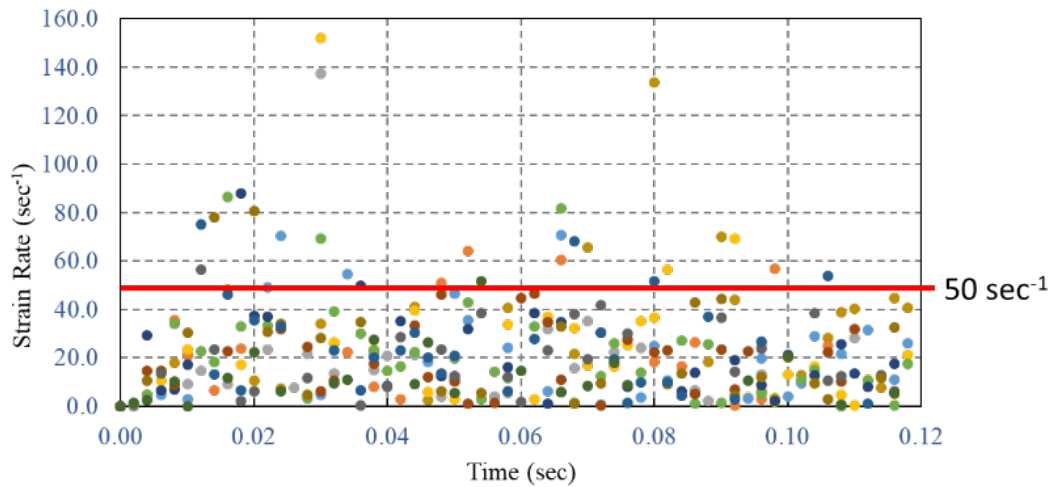


Figure 7.13 Strain rates vs. time for joint elements in an FMVSS 214 RP.

Experiment overview

For these experiments, non-woven random carbon fiber mat was used as the coupon material, and mechanical properties were tested in lap-shear mode using ASTM 5868 standardized lap shear test.

Joining methods

1. Resistive implant welding with stainless steel mesh.
2. Methacrylate-based adhesive, Plexus MA 530

Test speeds:

1. Crosshead speeds & strain rates. (typical strain rate in a crash test = $5.0 \text{ e}^1/\text{sec}$)
 - a. 5 mm/min ($8.33 \text{ e}^{-2} \text{ mm/sec}$); strain rate : $2.08 \text{ e}^{-3}/\text{sec}$
 - b. 50 mm/min ($8.33\text{e}^{-1} \text{ mm/sec}$); strain rate : $2.08 \text{ e}^{-2}/\text{sec}$
 - c. 500 mm/min (8.33 mm/sec); strain rate : $2.08 \text{ e}^{-1}/\text{sec}$

Results:

A clear strain rate dependency trend was observed for resistive welding: with an increase in strain rate, a decrease in joint strength is noticed (Figure 7.14). Also, the effect of joint stiffness for resistive welding showed no trends and was not significant. It is well established that the strength of semi-crystalline polymers has an inverse relationship to strain rate¹³⁹. Since the major load transfer path is through the polyamide polymer, this behavior is justified. When the Plexus MA 530 was tested at the same strain rates, the 50 mm/min crosshead test exhibited the best strength and stiffness compared to all other strain rates. According to literature¹⁴⁰, methacrylate – the major constituent of the Plexus MA 530 – exhibits a strain hardening behavior; however, the adhesive lap shear test did not reflect this (Figure 7.15). With the adhesive system performing at its best close to ASTM recommended test-speed, it would be safe to assume that stiffness/toughness modifiers added in the adhesive system are tuned to perform better at ASTM test speeds. This is often a common practice for structural adhesive manufacturers to tune the adhesive performance to a particular strain rate. In conclusion, the resistive welding outperformed the adhesive system at all tested strain rates (Figure 7.16).

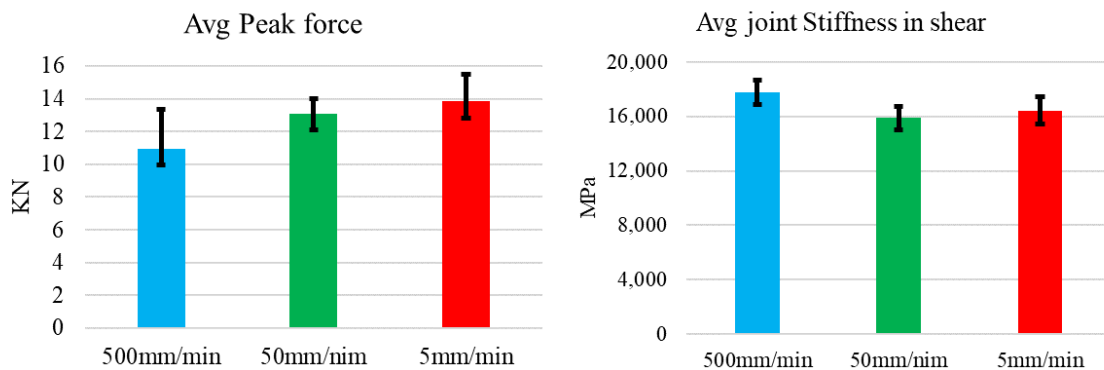


Figure 7.14 Resistive welding lap shear strength at various strain rates.

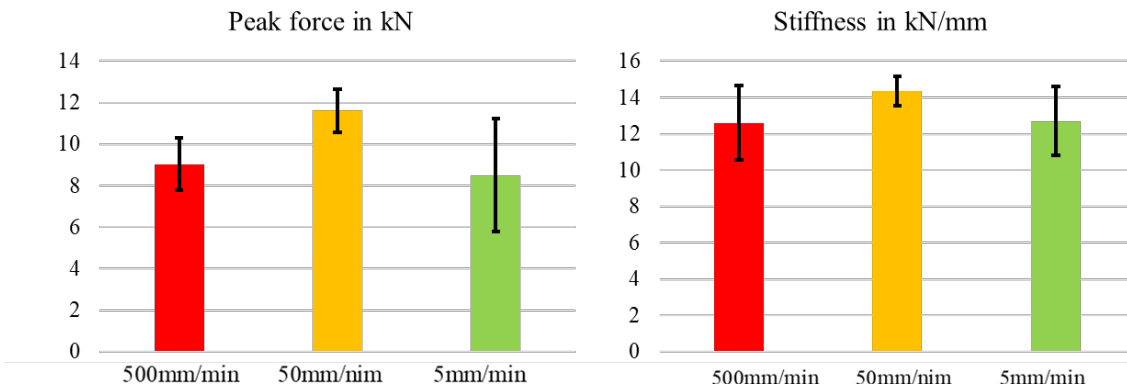


Figure 7.15 Plexus MA 530 lap shear strength at various Strain rates.

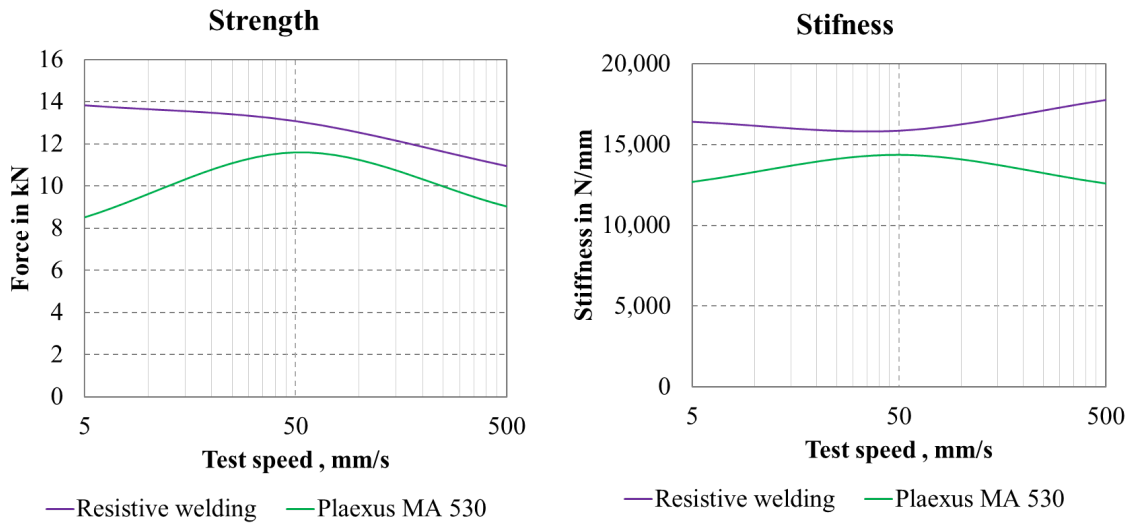


Figure 7.16 Restive welding vs. Plexus MA530.

7.4 Summary

In summary, the RIW joints outperform the adhesive in lap-shear performance (Mode 2), and the adhesive bonding outperforms the RIW joint in peel performance (Mode 1), as shown in Table 7.4. In this comparison, the RIW performance of injection-molded LFT materials are ignored since these material systems are generally not used with the primary stress.

It is common practice to design automotive structural joints to be under shear loading primary (mode 2). However, in real-world scenarios, most automotive structural joint experience both shear and peel loads. With this, it is tough to determine which of these joints will perform better in automotive structures. Chapter 8 uses finite element simulation methods to model these joints and simulate them in an automotive component to answer this very same question.

Table 7.4 RIW vs. Adhesive, mechanical performance.

	RIW (LFT)	RIW (Non-woven)	RIW (woven)	Plexus	
Mode 1 (Peel)	.119 + 017	0.235 + .009	.236 + .042	0.291 + .008	kJ/m2
	41%	81%	81%	100%	normalised
Mode 2 (lap shear)	17.4 + 1.2	22.4 + 1.2	28.1 + 2.2	19.7 + 1.4	Mpa
	62%	80%	100%	70%	normalised

8 TESTING, MODELING AND SIMULATION PATHWAY FOR RESISTIVE IMPLANT WELDING FOR LARGE NON-LINEAR FAILURE MODES

Finite Element Analysis (FEA) plays a significant role in accelerating the vehicle development process. With the introduction of explicit finite element methods, complex full vehicle crash simulations can be simulated relatively faster. In general, vehicle crash simulations are highly non-linear and contain complex elemental contacts and ruptures¹⁴¹. Accurate modeling of the joints between parts is critical in predicting vehicle responses in a crash test. In recent years, the use of structural adhesives has drastically increased in vehicle structures. Cohesive zone modeling is broadly used to accurately model this adhesive failure and responses¹⁴². When developing a new joining solution for automotive structures, it is essential to develop robust modeling methods to capture accurate failure and deformation.

The two major tasks outlined in this chapter are:

1. **Task 1:** Identify and implement a modeling pathway for simulating resistive welded joints, along with experimental characterization and verification.
2. **Task 2:** Understand the effect on system-level performance of a resistive welded automotive composite structure.

8.1 Task 1: Identify and implement a modeling pathway for simulating resistive welded joints

Most automotive joining technologies can be modeled using some combination of these numerical formulations: (a) Rigid/Springs (1D); (b) Beams (1D); and (c) Shell/Brick

(2D/3D)¹⁴³. Joining technologies, such as spot welds and rivets, can be modeled accurately using one-dimensional numerical formulation such as rigid and spring elements. These one-dimensional formulations are computationally efficient and stable¹⁴⁴. Adhesive failures often are progressive and anisotropic. To accurately capture this behavior, 3D brick elements were used, even though these elements are computationally intensive to solve.

The goal for this study is to develop a material characterization pathway for simulating resistive welded joint from experimental data and compare its performance with a structural adhesive.

8.1.1 *Material models in Radioss for Area connectors.*

In Radioss, area connectors can be simulated by a series of spring elements (Type 2 adhesive spring) or brick elements (adhesive contact), as shown in Figure 8.1. The adhesive spring (Type 2 adhesive spring) connector formulation is a relatively new method for modeling complex adhesive behavior and is implemented using a series of one-dimensional springs (Figure 8.2). The computational efficiency for these modeling approaches is significantly higher than that for brick elements. This contact formulation was co-developed by Ford Motor Company with Altair to expedite full car crash simulations¹⁴⁵. One major limitation of this connector formulation is its requirements for extensive testing data and multiple verification loops. Hence, the adhesive contact (brick) approached was picked for modeling the resistive welded joints.

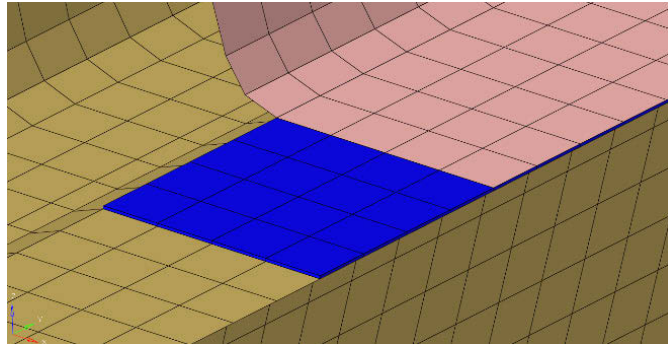


Figure 8.1 Adhesive modeling using brick element.

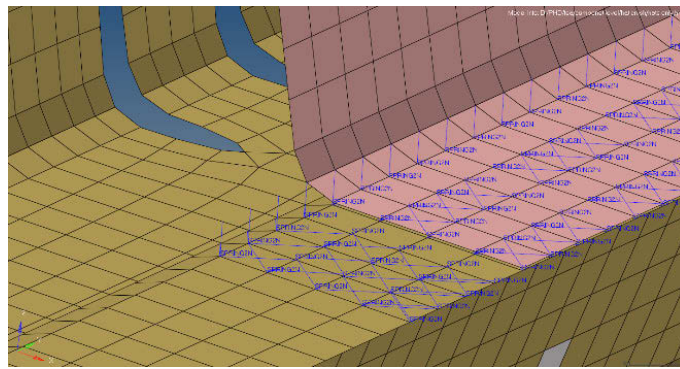


Figure 8.2 Adhesive spring (type2) elements.

8.1.2 Material model

“MAT/LAW/59” was identified as an appropriate material model for simulating resistive welding and adhesive bonding in Radioss¹⁴⁶. Either elastic or elastoplastic behavior in normal and shear directions can be defined using this material model, as shown in Figure 8.3. The softening and hardening characteristics can be controlled using a plastics behavior curve as input in both normal and tangential directions. The model by itself does not have any way to capture rupture and element deletion. However, this was solved by using a “FAIL/CONNECT” property card in tandem to the LAW59 material model. The FAIL/CONNECT property card allows users to define failure criteria in both normal and shear directions¹⁴⁷. The failure criteria for modeling rupture via element

deletion can be either “delete at maximum elongation” or “delete at maximum energy”. In this regard, the number of iterations to fit the model response can be drastically reduced if we can experimentally determine true strain at failure.

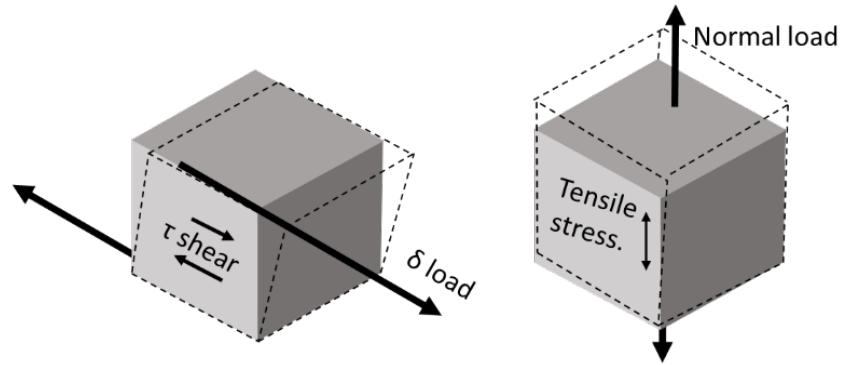


Figure 8.3 Shear and Normal loading of a cohesive brick element.

Before developing the material model for joints, it is important to verify that the material model for coupon material behaves similarly to the test-obtained data. For all tests in this chapter, non-woven carbon fiber PA 6-6 coupons were used. Using the material data from Chapter 2, a simple elastoplastic model was developed to simulate the non-woven coupon materials.

MAT/LAW2 (Johnson-cook model) was used to simulate the coupon material. In the recent version of Radioss solver, a new simplified data option is included for auto-fitting the elastoplastic behavior (a,b,n parameters). This new input method uses yield stress and ultimate tensile stress or strain. While the MAT/LAW2 simulates the deformation response, it does not simulate the rupture of the elements. This was achieved by including the FAIL/TENSSTRAIN card to delete elements experiencing strains beyond a set limit.

The following inputs for the coupon material model were derived from the stress-strain plot (Figure 8.4):

- Initial density: 1.5×10^{-9} tons/mm³
- Young's modulus: 22474.13 N/mm²
- Poisson's ratio: .33
- Yield stress: 406 N/mm²
- Ultimate tensile stress: 408.877 N/mm²
- Strain at UTS: 0.0175 mm/mm

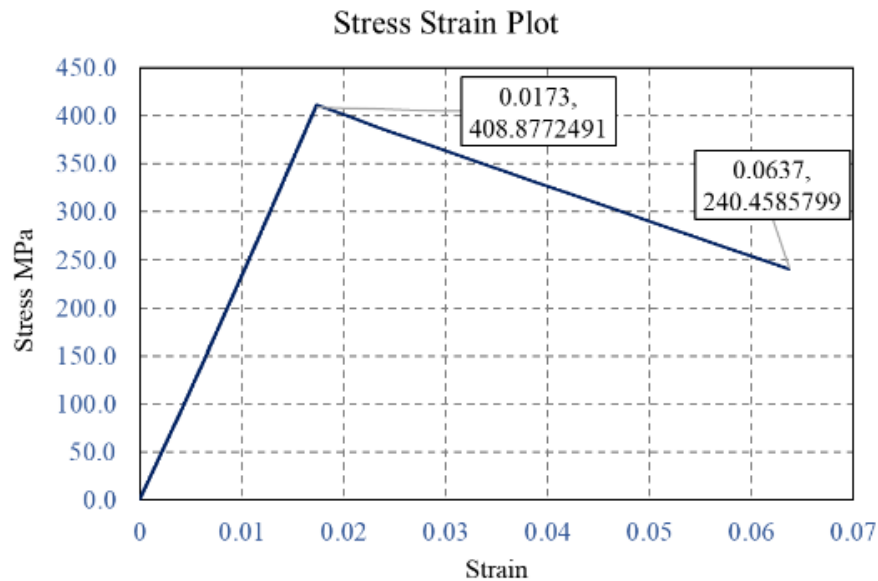


Figure 8.4 Stress-strain plot for Non-Woven coupons in 0°.

The behavior of the coupon material was tested under two loading modes: tension, and double cantilever, to ensure that the material model deformed and ruptured for obtaining experimental data. A tensile test was simulated with the same coupon

dimensions, and force-displacement plots were compared to validate model correlation (Figure 8.5).

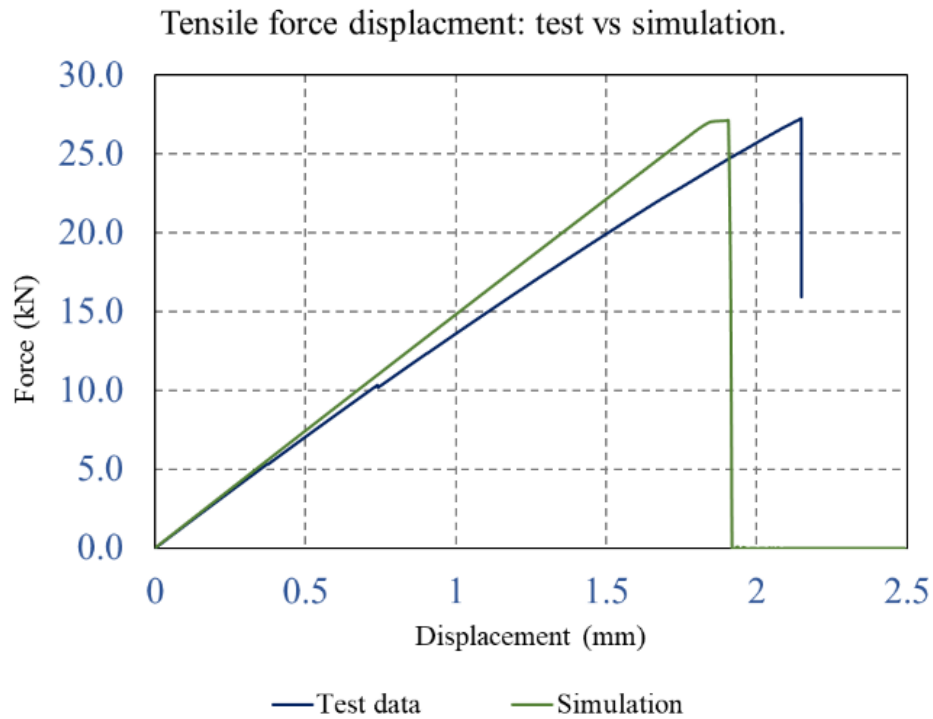


Figure 8.5 Tensile: Force-displacement plots for coupon material simulation vs. test.

The first 17 mm in the double cantilever test can be used to verify the bending stiffness of the material. A good correlation was observed between the test and simulation data, as shown in Figure 8.6. With these verifications, it was confirmed that the material model behaved similarly to the test data.

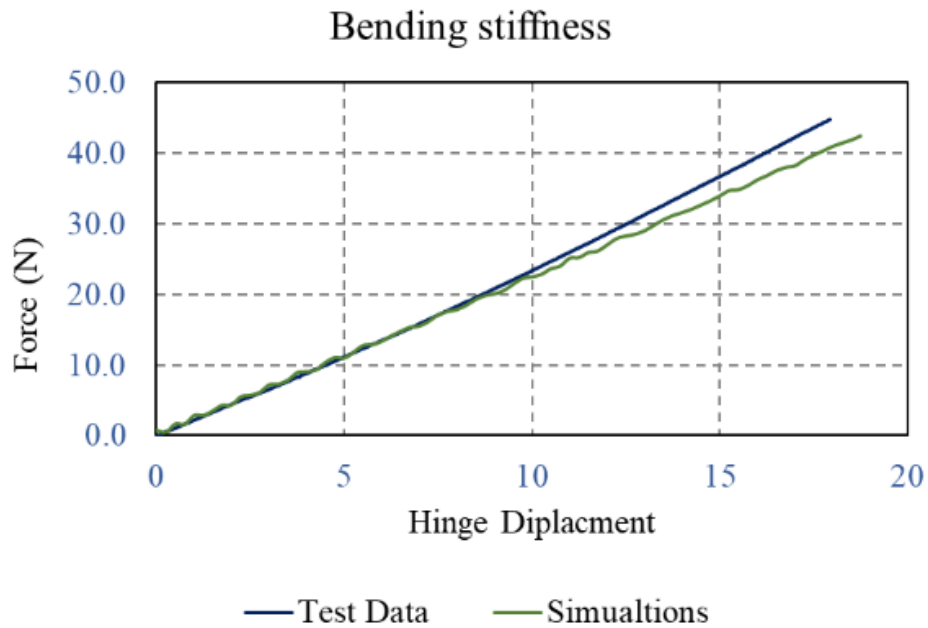


Figure 8.6 Bending Stiffness Correlation.

8.1.3 Testing and modeling pathway for resistive welded joints.

One of the key challenges in developing material models for resistive welding was to test the behavior under normal loading conditions experimentally. When characterizing the adhesive, this can be easily done by casting a coupon with pure adhesive and testing this coupon under tensile loading. However, since this approach is impractical for testing welded joints, an indirect approach, such as the double cantilever beam test, was used to characterize behavior under normal loads. The overall testing to simulation pathway is shown in Figure 8.7.

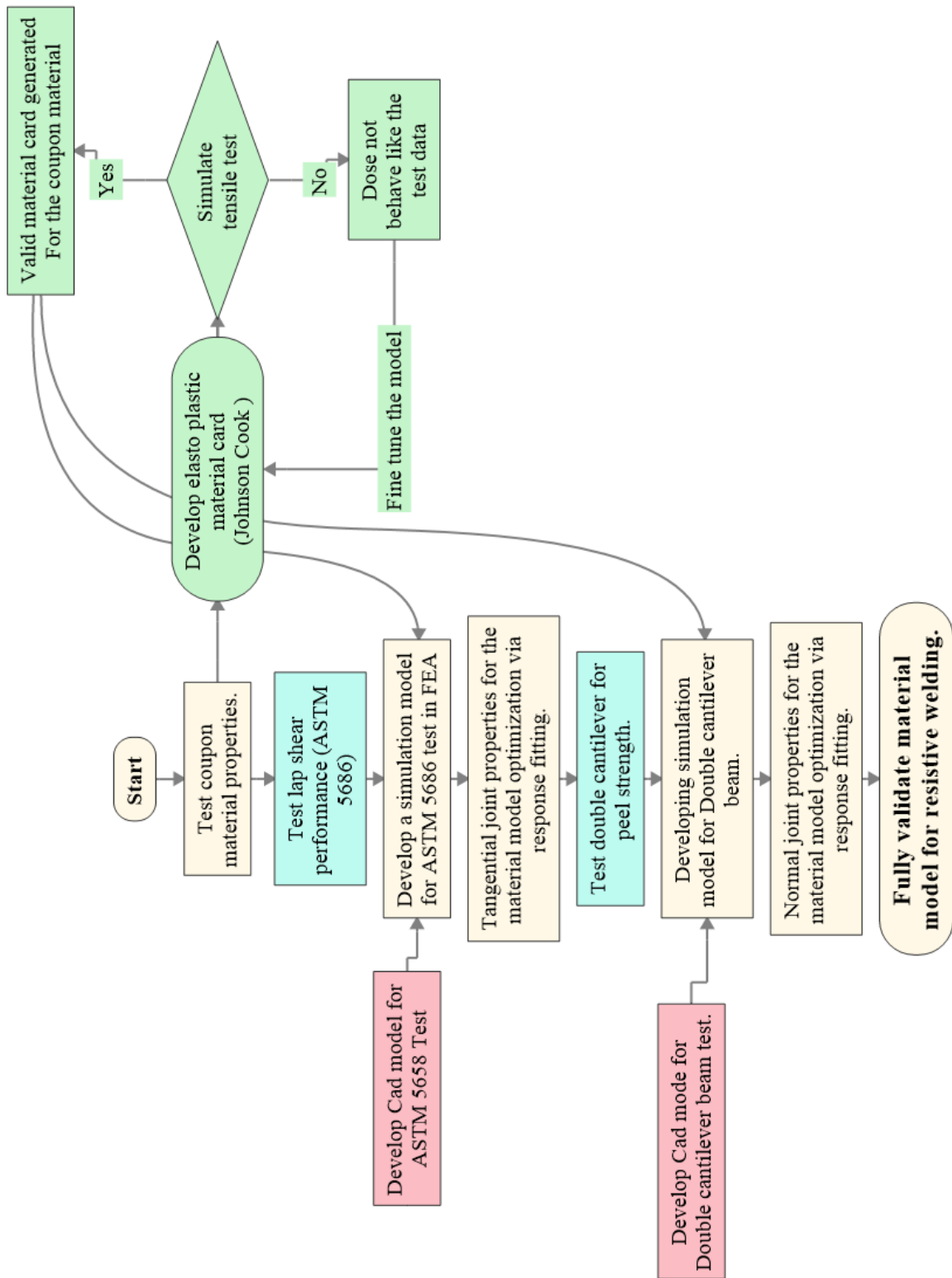


Figure 8.7 Material card generation pathway for resistive welding.

8.1.4 Experimental evaluation.

In addition to the lap shear tests mentioned in Chapter 2, double cantilever beam (DCB) tests were performed. A custom test jig was machined to fix the weld coupons in the universal tensile testing machine (Figure 8.8). Digital image correlation technique was used to determine localized strain and crack propagation. The resistive welded coupons exhibited a brittle crack propagation behavior, as seen in the force-displacement plots (Figure 6.11). The bond area for the DCB test was 25.4 mm × 25.4 mm, and coupon dimensions were 25.4 mm × 114 mm.

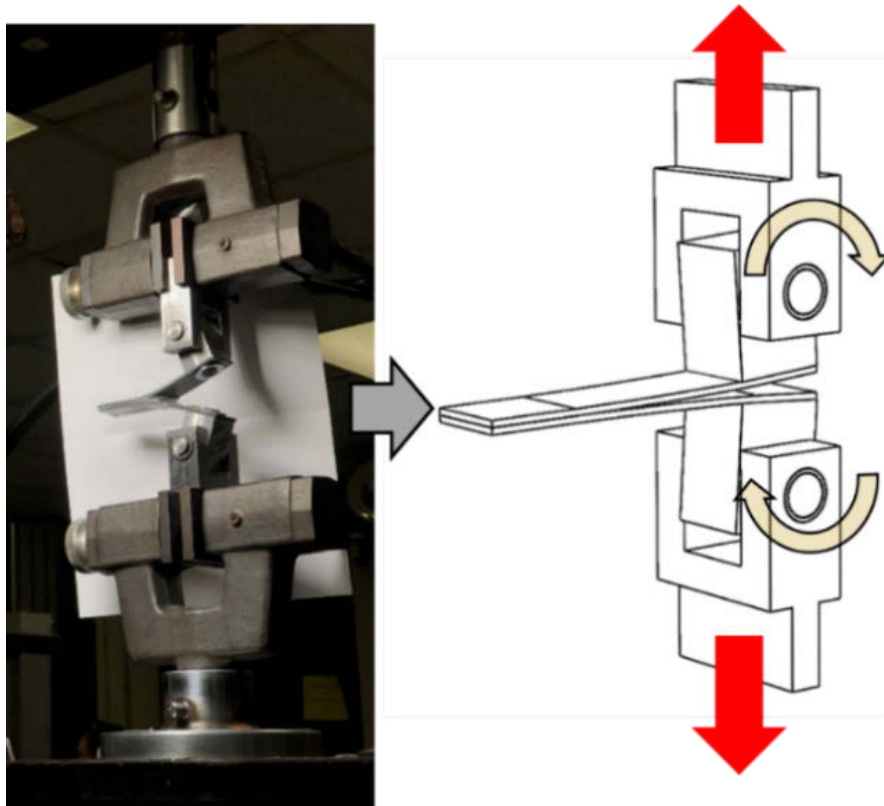


Figure 8.8 Double cantilever beam test.

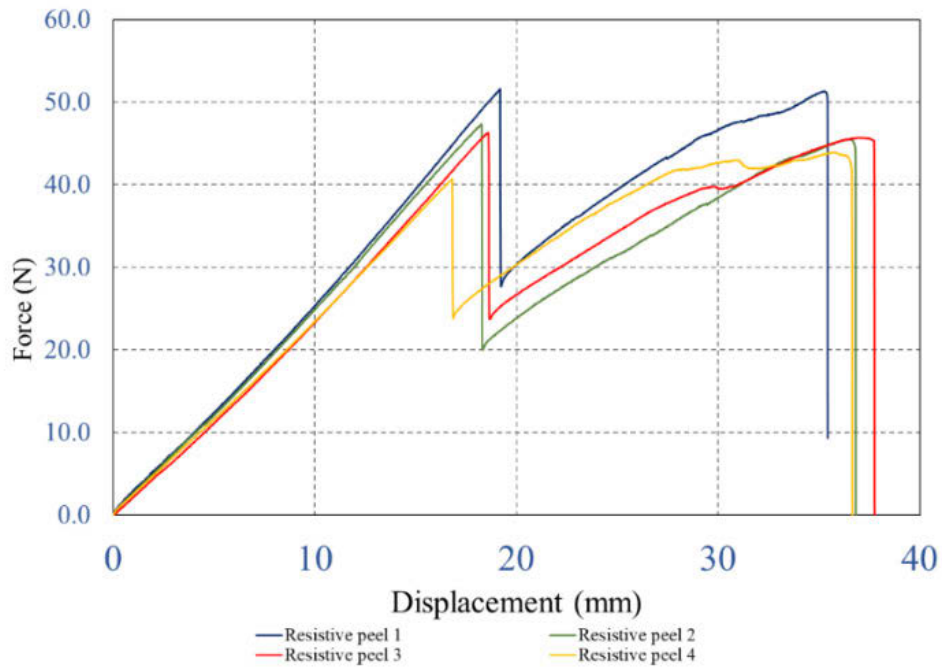


Figure 8.9 Force-displacement plots for DCB test resistive welding.

FEA models were developed for both the lap shear and BCD tests to fit the material weld parameters, while trying to match the output response. Due to the brittle nature of the resistive welded joints, an elastic model with failure criteria was used for simulations. For the material model, we need elastic and shear moduli. These parameters will determine the slope of the line. To capture the failure of these welds, a maximum strain criterion is used. To determine the starting point for the strain limits at fracture, digital image correlation (DIC) was used. The weld coupons were painted with a specular pattern, and a video of the test was captured using a macro lens at 30 Hz (Figure 8.10). These videos were converted to individual frames and imported as deformation stages into GOM® Correlate. Using the specular pattern on the coupon's material, the deformation map is created.

Screen grabs from Raw video for digital Image correlation

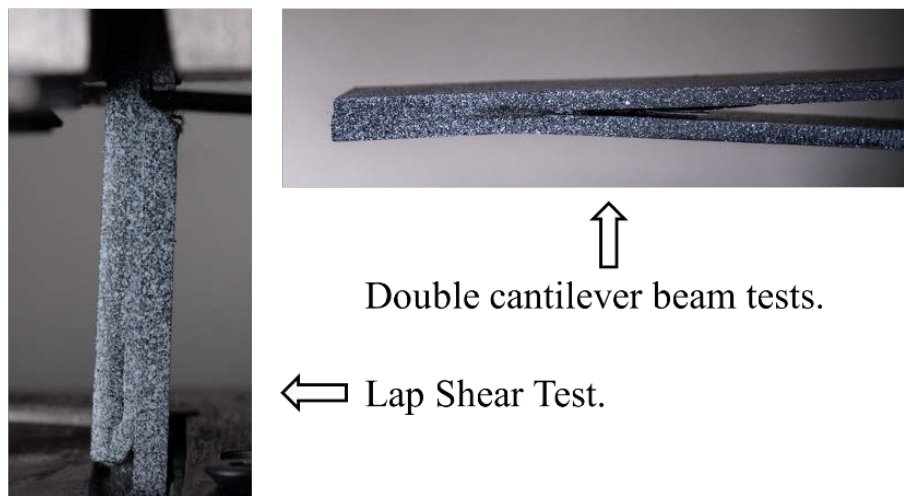


Figure 8.10 Screen Grabs for DIC.

Using the deformation maps, localized strain (just before failure) can be identified. Using the measured strain value as a starting point, the material models were tweaked until the output response matched the test data. The stiffness of the response simulation was used to tweak Young's and shear modulus. Once a decent correlation was achieved for stiffness response between the test data and simulation, strain limits were tweaked to match the failure points. Indeed, the strain data from DIC helped to match simulation and test data with relative ease. In the lap shear mode, strain rates up to .175 units were observed in the resistive welded region but in adhesively bonded coupons, strains up to 0.465 units were observed. While these strains offered a good starting point for modeling failure, they could not be directly used in simulation. This was predominantly due to two reasons:

1. It was hard to isolate the resistive weld region from the coupon materials; these strain numbers also reflected the deformation of coupon material in proximity to the weld

interface. This was predominantly due to the limitation of resolution and magnification in DIC plots. To accurately capture the strain value, we will need to use a tracking microscope and micro specular patterns.

2. The other cause was the geometric simplification used in FEA modeling. The thickness of the weld region is less than $50\ \mu\text{m}$, and it is not practical to model such thin elements without having stability issues. Moreover, to maintain reasonable nodal timesteps, the thickness of the element was restricted to a minimum of $0.5\ \text{mm}$.

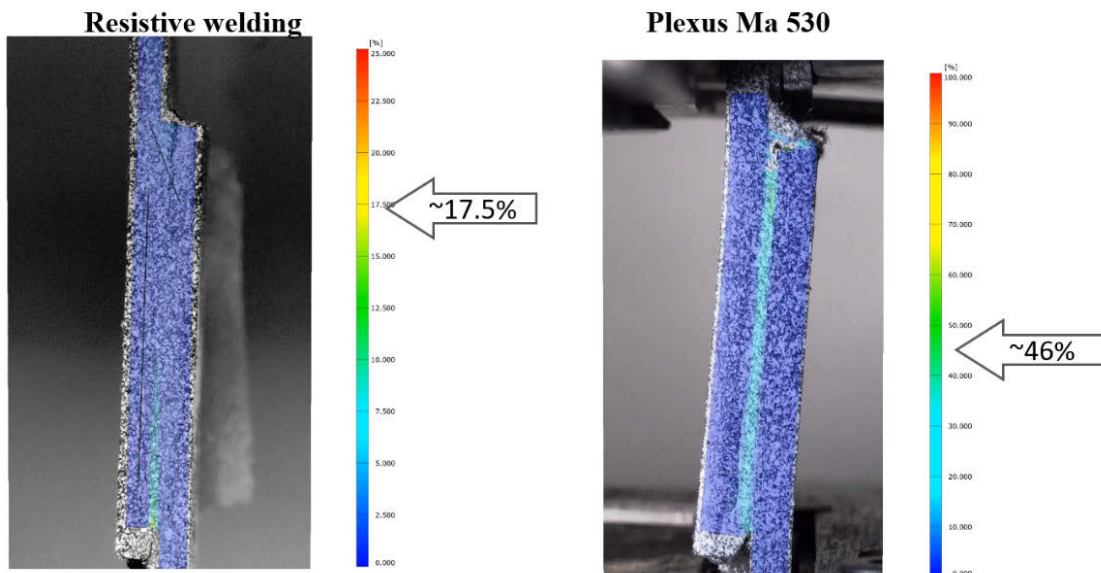


Figure 8.11 DIC strain plots for lap shear tests.

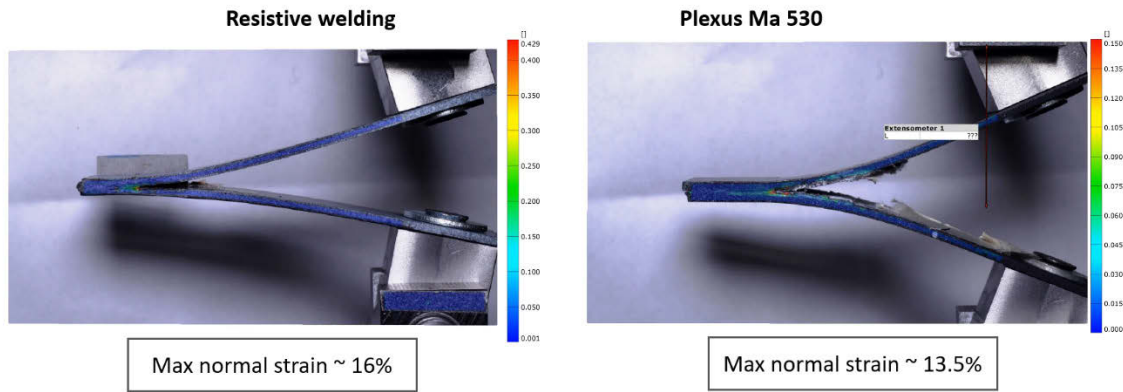


Figure 8.12 DIC strain plots from DCB tests.

8.1.5 Final fitted model:

After several iterations, a good correlation was achieved between the simulation and test data for both lap shear and double cantilever beam tests (Figure 8.13 and Figure 8.14). In order to simplify these simulations, the weld material was assumed to be planar isotropic and strain rate independent. The second assumption is not true for the work described in Chapter 2, but it is commonly acceptable to ignore strain rate dependency in quasi-static loading conditions. In addition to the force-displacement plots, the deformation of the FEA model in DCB test also provides a good correlation when overlaid with experimental results (Figure 8.15). The final data card for the resistive welded joints can be seen in Figure 8.16.

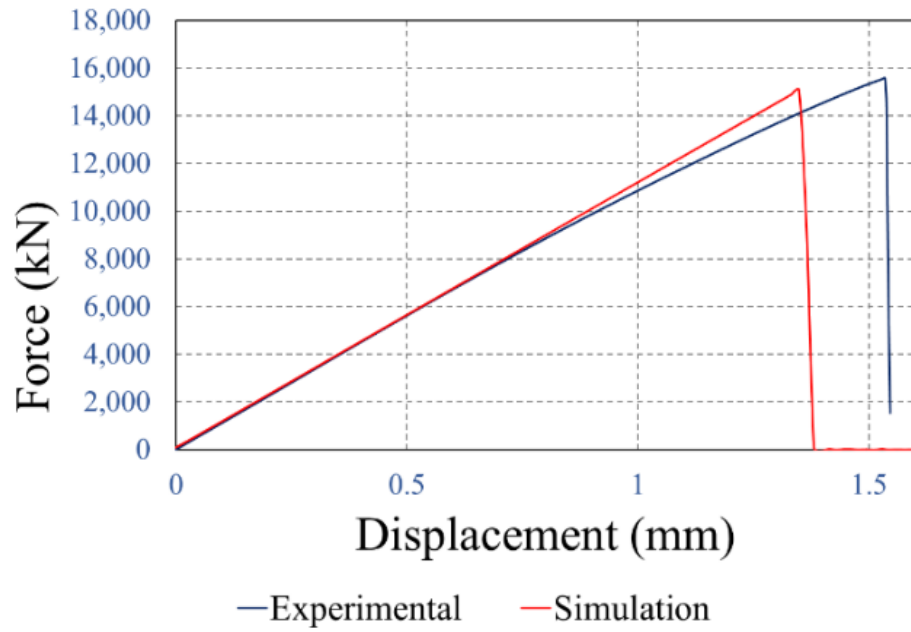


Figure 8.13 Lap shear: force-displacement plots.

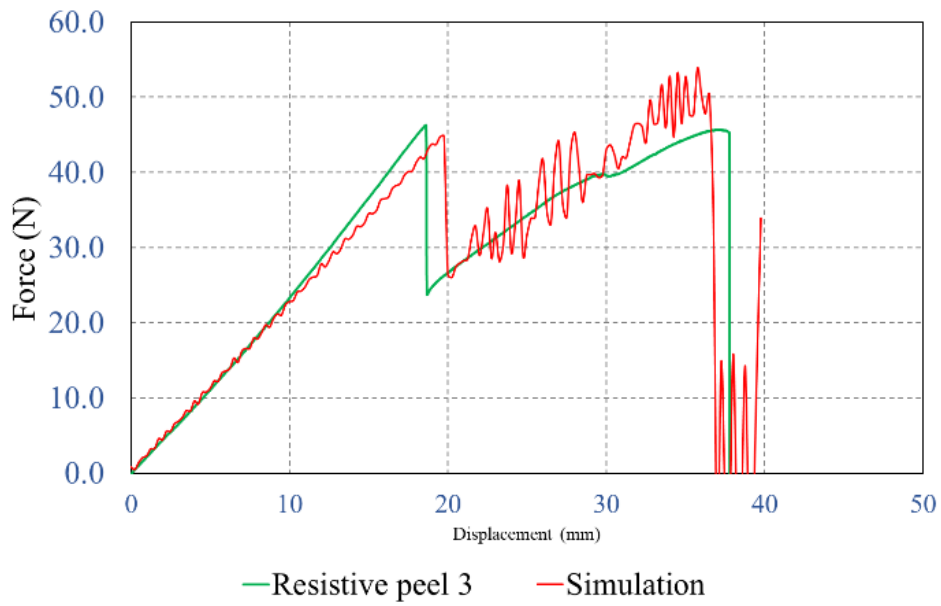


Figure 8.14 DCB test: Force-displacement plot.








Time step	Mesh overlay	Time step	Mesh overlay
T = 0		T=2.9e-1	
T=5.5e-2		T=3.57e-1	
T=1.2e-1		T=3.8e-1	
T=1.8e-1			

Figure 8.15 Mesh deformation overlay on actual test images (resistive welded).




MAT/LAW59		FAIL/CONNECT-Layer 1		FAIL/CONNECT-Layer 2	
Name	Value	Name	Value	Name	Value
Solver Keyword	/MAT/LAW59/	Solver Keyword	/FAIL/CONNECT/	Solver Keyword	/FAIL/CONNECT/
ID	3	Mat_Id	{3} layer 1	Mat_Id	{5} layer 2
Name	Weld	Name	layer 1 fail connect	Name	Layer 2 fail connect
Color		Color		Color	
Include	[Master Model]	Include	[Master Model]	Include	[Master Model]
Defined	<input checked="" type="checkbox"/>	Defined	<input checked="" type="checkbox"/>	Defined	<input checked="" type="checkbox"/>
User Comments	Hide In Menu/Export	Card Image	FAIL_CONNECT	Card Image	FAIL_CONNECT
Card Image	M59_CONNECT	Epsi_max_N	0.0255	Epsi_max_N	0.047
Regular_OR_encrypted_flag	Regular	Exp_N	0.0	Exp_N	0.0
RefRho_Option	<input type="checkbox"/>	Alpha_N	0.0	Alpha_N	0.0
Rho_Initial	1.2e-009	R_funct_ID_N	<Unspecified>	R_funct_ID_N	<Unspecified>
E	870.0	I_fail	0: Uni-directional failure with i = 33 for normal direction a...	I_fail	0: Uni-directional failure with i = 33 for normal direction a...
G	890.0	Ifail_so	1: The solid element is deleted, when one integration poi...	Ifail_so	1: The solid element is deleted, when one integration poi...
Imass		ISYM		ISYM	
Icomp		Epsi_max_T	0.063792	Epsi_max_T	0.063792
Ecomp	0.0	Exp_T	0.0	Exp_T	0.0
Nb_funct	0	Alpha_T	0.0	Alpha_T	0.0
Fsmooth	1: Strain rate filtering	R_funct_ID_T	<Unspecified>	R_funct_ID_T	<Unspecified>
Fout	0.0	EI_max	0.0	EI_max	0.0
ALE CFD Formulation	NONE	EN_max		EN_max	
HEAT_input	<input type="checkbox"/>	ET_max		ET_max	
		N_n		N_n	

Figure 8.16 Final model for resistive welded joints.

It is important to note that these material properties were only valid for this coupon material and thickness. The stiffness of the coupon is directly related to its thickness, and from Chapter two, it is experimentally proven that weld performance is directly related to coupon performance. When simulating vehicle structures with resistive welded joints, it is critical to experimentally evaluate every combination of material and thickness variation in the structure. This can immediately become tedious when simulating systems with many parts and variances.

8.2 Developing material models for adhesive joints.

Using a similar pathway as above, a material model was generated for the adhesive joints. One key difference was that the behavior to normal loads was tested directly using pure adhesive coupons. The pure adhesive was cast in a silicone dog bone mold and subjected to the same curing cycle as bonded coupons. Once these coupons were fully cured, they were tested on an Instron with 10 kN load cell. The stress-strain plots for the adhesive are shown in Figure 8.17.

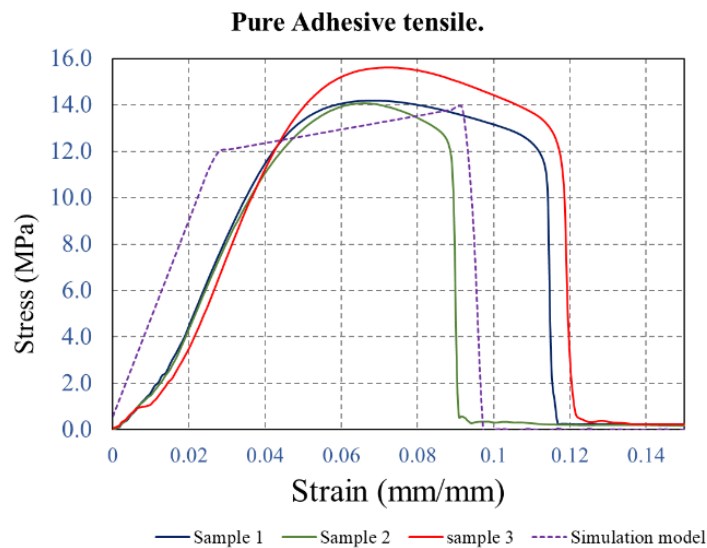


Figure 8.17 Stress-strain plots for pure adhesive (Plexus MA530).

For fitting the tangential performance of the adhesive bond, a similar pathway was used as resistive welding. Unlike resistive welded joints, adhesive bonds yield like ductile materials; hence, it is essential to capture this performance of the joint to accurately predict the behavior of a bonded structure. Due to the yielding nature of adhesive bonds, an elastoplastic material model was used to simulate the bond region. Figure 8.18 shows the lap-shear force-displacement data both for simulation and test coupons. As can be seen, there is a good correlation between the test data and simulations, under lap-shear loading. In the DCB test, the goal was to match the initial slope and overall area under the curve. However, as can be observed in Figure 8.19, there is an adequate correlation between the test data and simulation results. The final material models for the adhesive-bonded joint can be seen in Figure 8.20.

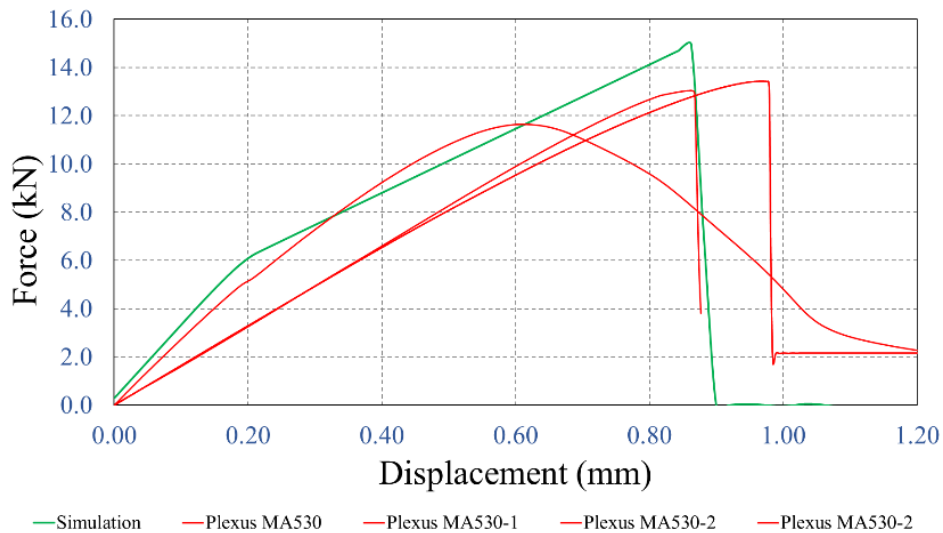


Figure 8.18 Lap-shear force-displacement: simulation vs. test.

DCB test: Force-displacement plots

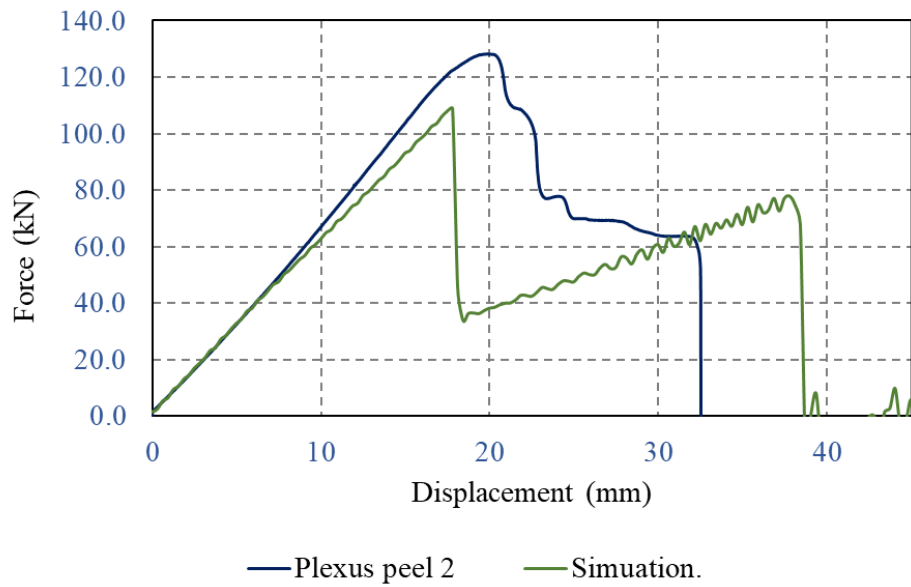


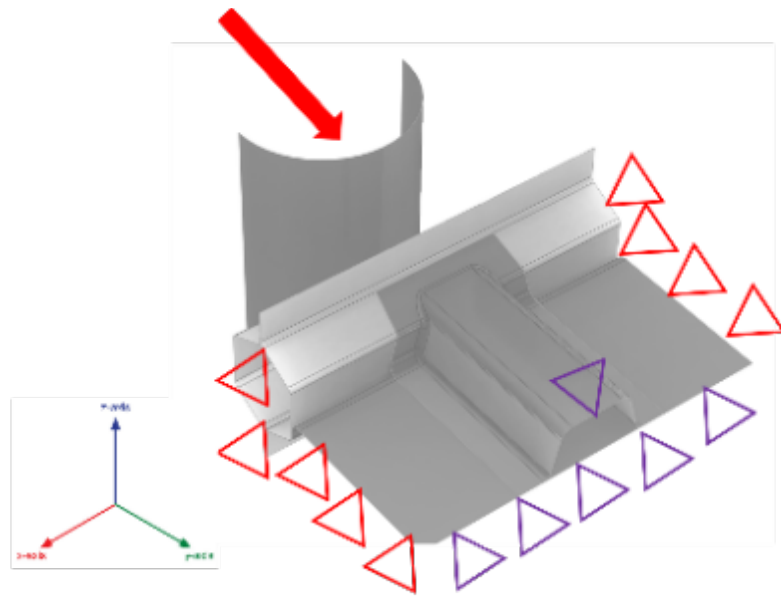
Figure 8.19 DCB: force-displacement plot, simulation vs experimental.

MAT/LAW59		FAIL/CONNECT	
Name	Value	Name	Value
Solver Keyword	/MAT/LAW59/	Solver Keyword	/FAIL/CONNECT/
ID	3	Mat_Id	{3} plexus elasto plastic
Name	plexus elasto plastic	Name	layer 1 fail connect
Color		Color	
Include	[Master Model]	Include	[Master Model]
Defined	<input checked="" type="checkbox"/>	Defined	<input checked="" type="checkbox"/>
User Comments	Hide In Menu/Export	Card Image	FAIL_CONNECT
Card Image	M59_CONNECT	Epsi_max_N	0.165
Regular_OR_encrypted_flag	Regular	Exp_N	0.0
RefRho_Option		Alpha_N	0.0
Rho_Initial	1.2e-009	R_funct_ID_N	<Unspecified>
E	380.0	L_fail	0: Uni-directional failure with i = 33 for normal direction a...
G	335.0	Ifail_so	1: The solid element is deleted, when one integration poi...
Imass		ISYM	
Icomp		Epsi_max_T	0.485
Ecomp		Exp_T	0.0
Nb_funct	1	Alpha_T	0.0
Data: Y_funct_ID_N, ...		R_funct_ID_T	<Unspecified>
Fsmooth	1: Strain rate filtering	EI_max	0.0
Fcut	0.0	EN_max	
ALE CFD Formulation	NONE	ET_max	
HEAT_Input	<input type="checkbox"/>	N_n	
		N_t	
		-	

Figure 8.20 Material cards for adhesively bonded joints.

8.3 Understanding the system-level performance of resistive welded structures

At coupon level, the resistive welded joints are more brittle in relation to adhesively bonded joints. On the contrary, the strength and stiffness of joints are significantly higher than those of the adhesives. While it is not possible to predict performance at a system level, but by using previously developed material models for the non-woven composite and joining technologies, we can simulate a typical crash scenario and study the performance from a system level. For this study, implementing a full car simulation under a crash mode is impractical due to limited computation resources. Hence, a simple model descriptive of rocker beam, floor panel, and floor cross-beam was modeled, and a 300-mm rigid pole impactor was used to simulate a load case similar to FMVSS 214 rigid pole (Figure 8.22). The boundary conditions for the floor panel are shown in Figure 8.21. With the floor panel carefully constrained, the rigid impactor was displaced into the car by 100 mm. The reaction force on the impactor was used to compare the effect of joining solutions.



 Constraint in Tx & Ry  Constraint in Ty & Rx

Figure 8.21 Boundary Conditions.

Simulation details:

- Part material: Non-woven carbon fiber
- Joining technology:
 - Case 1: Resistive welding
 - Case 2: Adhesive bonding (Plexus ma530)
- Solver: Radioss 2018
- Time scaling: 1000x

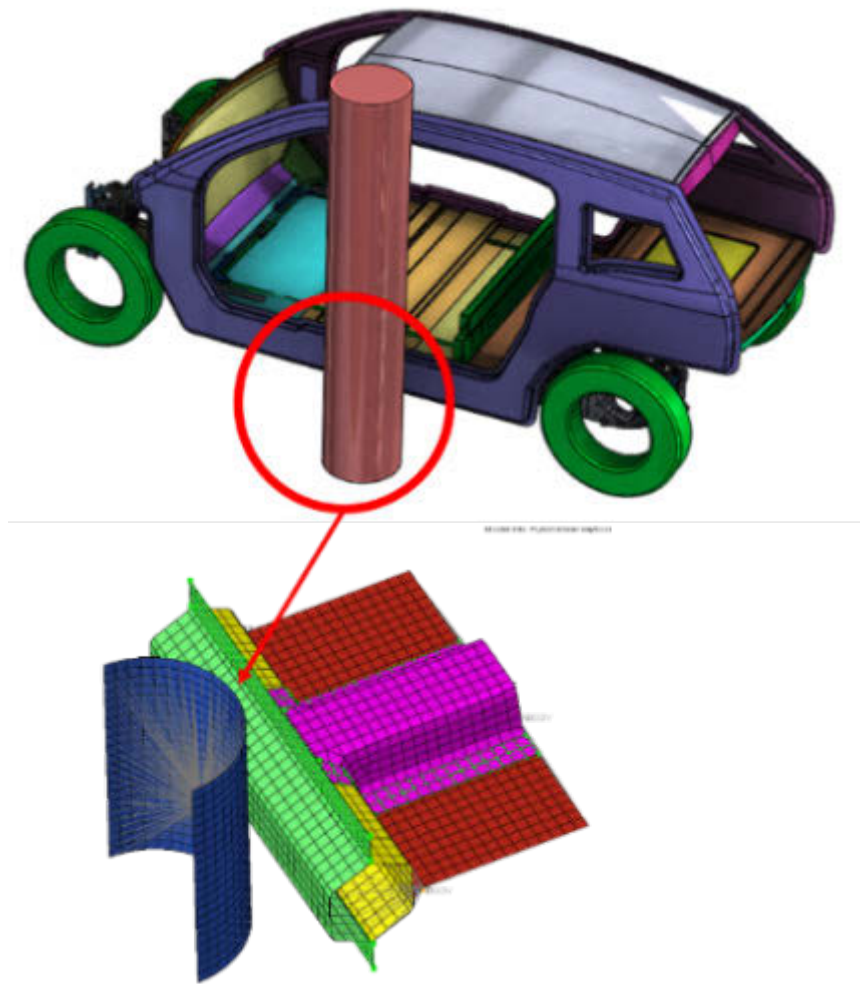


Figure 8.22 simplified rigid pole test.

8.3.1 Results:

The force-displacement curve of the impactor is shown in Figure 8.23, and the joint failure plots at several time steps are shown in Figure 8.24.

- In the initial section (up to 20 mm intrusion), both cases performed similarly,
- The first failure in the joint region occurred on the resistive welded case at 27 mm intrusion.

- By 32 mm of intrusion, the weld between the floor cross-member and rocker fully failed. On the contrary, there is still significant adhesive bond in Case 2.
- At 70 mm intrusion, the floor cross-section member completely separated from the floor panel in the adhesive-bonded case (Case 2), while being intact in the resistive welded case.
- At the end of the simulation, the resistive welded structure has a reaction force 6500 N versus 3414 N in the adhesive-bonded structure.

8.3.2 Conclusion

Both structures performed similarly in terms of the total energy observed. The resistive welding absorbed approximately 3% more energy than the adhesive-bonded structure, which was contrary to our expectation given the brittle nature of resistive welded joints. The other significant difference was that at the end of the intrusion, the resistive welded structure offered twice as much resistance than adhesively bonded structure, meaning that at the end of the crash, the resistive welded structure has more structural integrity than the adhesive-bonded structure.

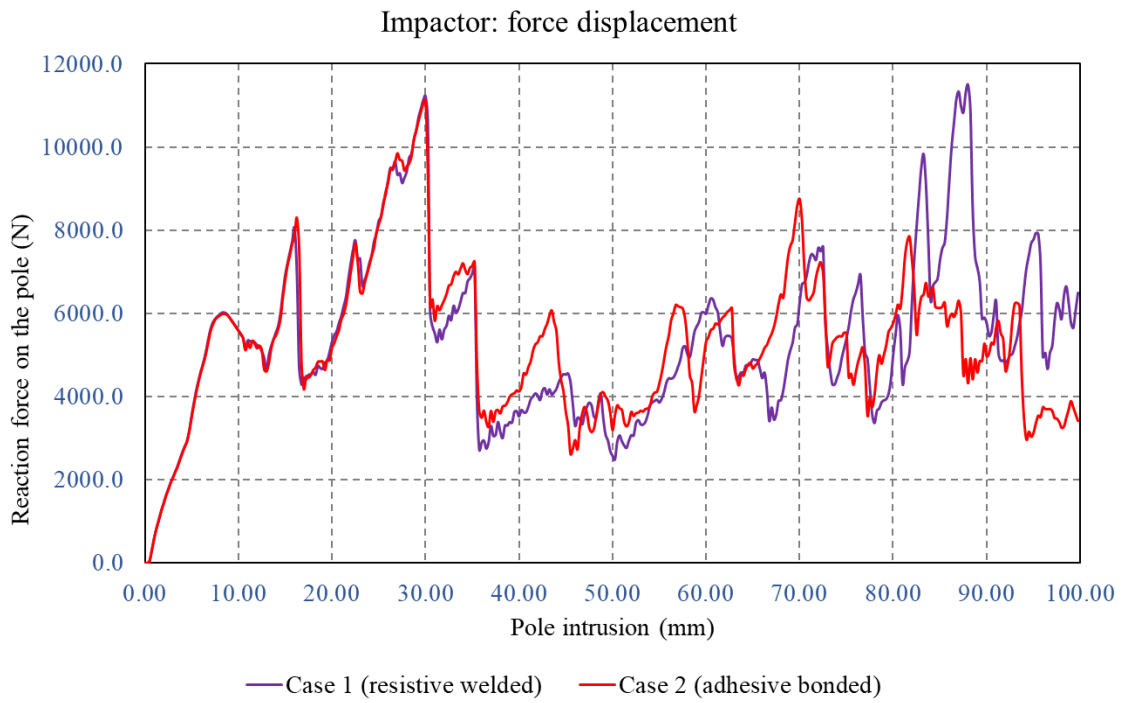


Figure 8.23 Impactor force-displacement for resistive welded vs. adhesives bonded structures.

Case1 :Welded

Case2 :Adhesive

20mm

32mm

70mm

100mm

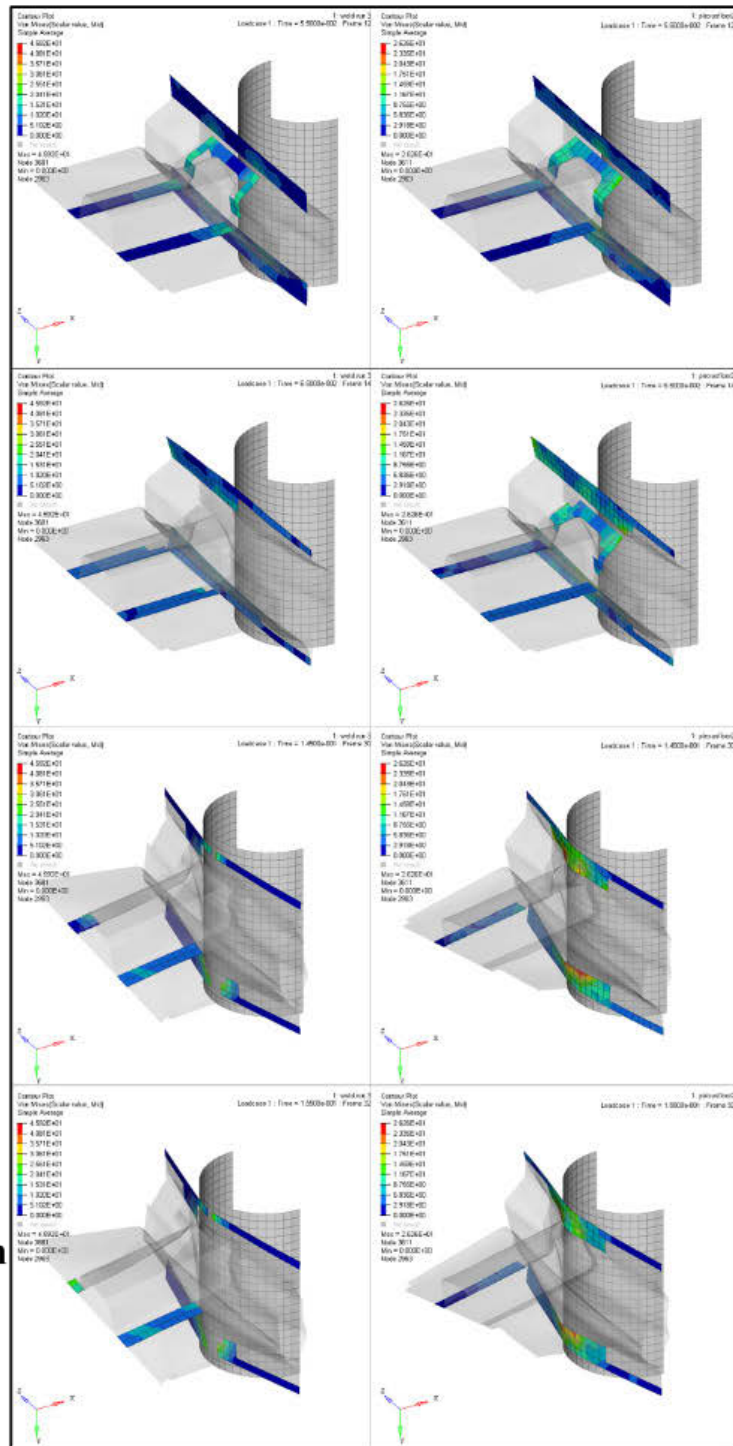


Figure 8.24 Joint failure plots vs. intrusion.

9 EVALUATING SCALABILITY OF RESISTIVE WELDED JOINT.

As previously discussed in Chapter 2, most research till date is focused on processing and optimizing the RIW process. The goal of this chapter is to look beyond these aspects and analyzing the next phase of research regarding scaling and commercializing this process for FRTPCs. Hence, this chapter evaluates the following issues that are relevant to the scaling of the RIW process for mass production.

1. At the plant level, what is the effect of weld processing time on vehicle throughput in a body shop?
2. How sensitive is the RIW process to typical contamination in the body shop?
3. If say, the RIW process is used on an automotive structure, how will repairing and recycling be approached?

9.1 Understanding the effect of weld processing time on vehicle throughput of a body shop.

A plant simulation approach was used to evaluate the effect of weld processing times on the throughput of the body shop. To accurately develop a body shop layout, detailed information for parts size, assembly sequences and flange lengths are needed.

The BMW i3 structural frame design offers a good starting point for a composite-intensive body structure. The structure is divided into two modules: the upper module is the occupant survival space that is predominantly made from carbon fiber reinforced epoxy, while the lower modules house the battery pack, powertrain, and suspension components (Figure 9.1). For this case study, a CAD model was developed similar to the

upper module of the BMW i3, since this structure can be easily manufactured with FRTPC materials. Using the BMW i3 occupant module as a guide also ensured that this CAD model is realistic. This upper module had 34 large FRTP parts, for which the primary joining method was resistive implant welding.

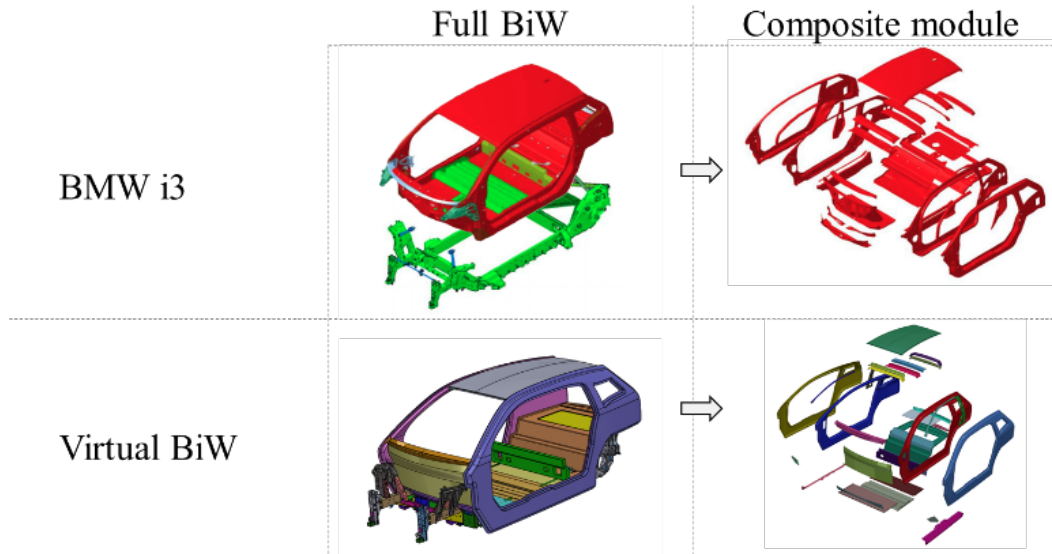


Figure 9.1 BMW i3 Structural frame.

For this composite structure, a plant model was designed using discrete object modeling method in Siemens Tecnomatix. This plant model represents a composite body shop for the upper module, and this exercise enabled us to accurately determine the total bond length and assembly sequence. In addition to developing the plant model, certain assumptions were made regarding the annual production volumes and cycle times, as shown in Table 9.1. While ~ 35,000 BMW i3 are manufactured annually, slightly higher production volumes were assumed for the FRTP structure vehicle. This assumption of an increase in production is predominantly due to the slightly lower cost for FRTP (over fiber-reinforced thermosets) and significantly faster manufacturing cycle times. The body-shop can be divided into four sub shops, as shown in Figure 9.2.

Table 9.1 FRTP body structure assumptions.

Parameter	Units	BMW i3 upper module	FRTP upper module
<i>No. Of major parts</i>	Number	34	34
<i>Dimensions of the BiW</i>	L × W × H in mm	3250 × 1940 × 1580	3250 × 1940 × 1580
<i>Annual production</i>	units/year	35,000	40,000
<i>Body Shop throughput</i>	units/hour	18	25
<i>Cycle Time</i>	Minutes: seconds	3:20	2:24
<i>Annual Production hours</i>	Weeks × Days × shifts × hours	48 × 5 × 1 × 8	48 × 5 × 1 × 8

Each body side outer assembly has three panels which are welded together and sent to the main assembly line. Similarly, the three roof cross members, each made from two panels, are assembled in a subassembly shop before it is sent to the main assembly line. Each resistive welding operation was modeled using two discrete blocks, as shown in Figure 9.3. The first block was an assembly function block, which represents the process of collecting all the components needed for assembly. Once all the components reach the block, an assembly countdown timer was assumed to start. After the completion of this time, this block passed all its contents to the next block. The second block was a single process block that emulated resistive welding.

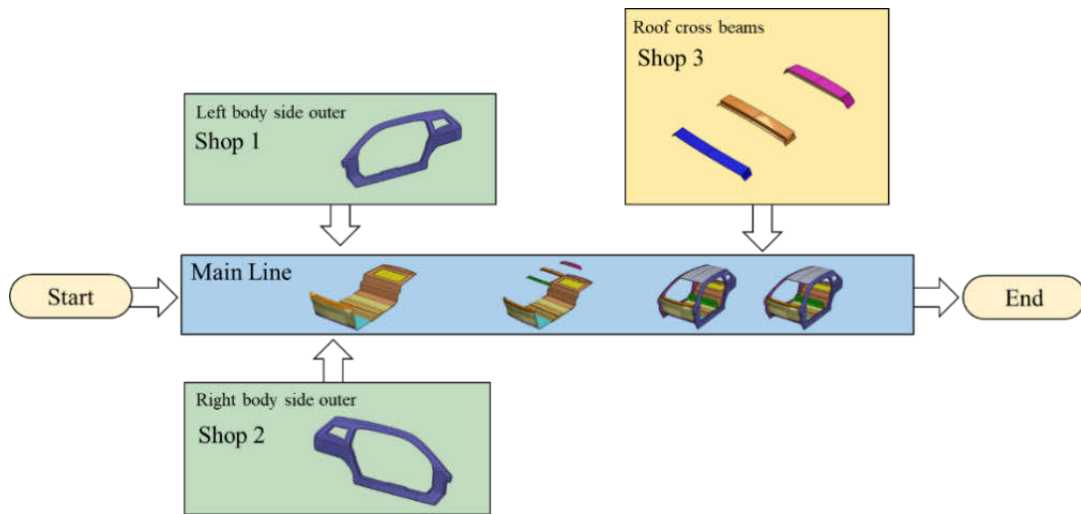


Figure 9.2 Body shop layout.

Once the process timer was complete, this block passed down all their components to the next operation. Together these blocks simulated collecting all the components needed for assembly, fixturing, clamping, and welding operations.

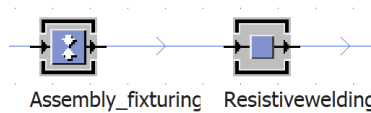


Figure 9.3 Resistive welding block.

The entire body shop for the upper module was modeled using these fundamental blocks (Figure 9.4). Using this plant model, the influence on throughput per hour with regard to variation in welding time is calculated.

9.1.1 Assumptions:

- **Loading time: 40 s** – This time represents the time required to load and clamp the parts to a welding fixture.

- **Unloading time: 20 s** – This time represents the time required to unload and place the parts on the conveyer belt.
- **Conveyor speed: 0.25 m/s** – This is the average conveyor speed in the body shop.

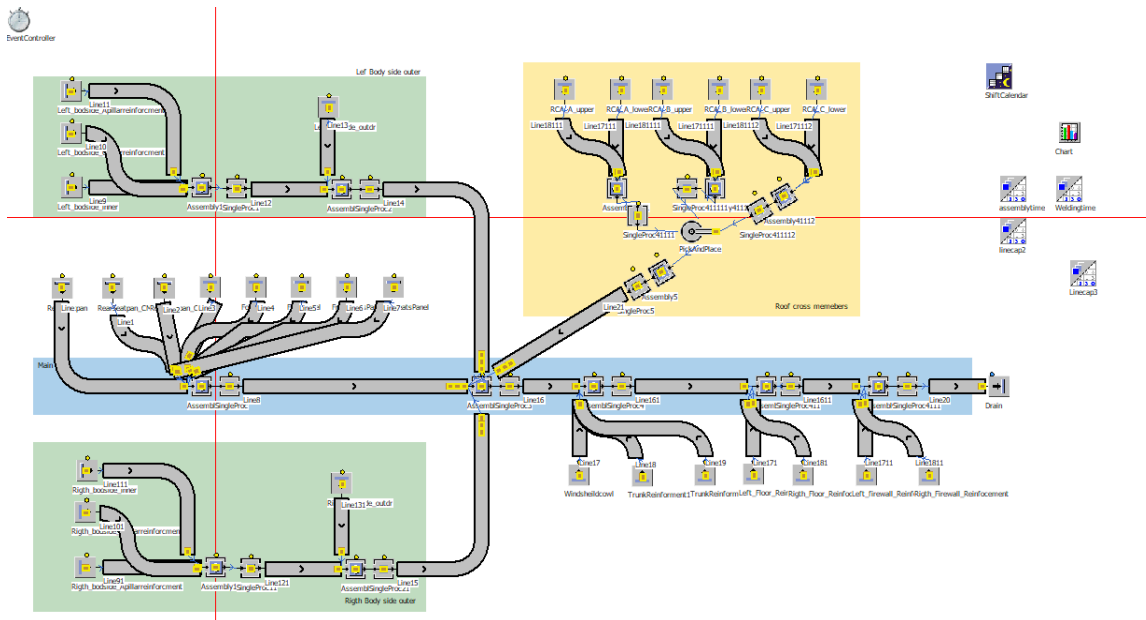
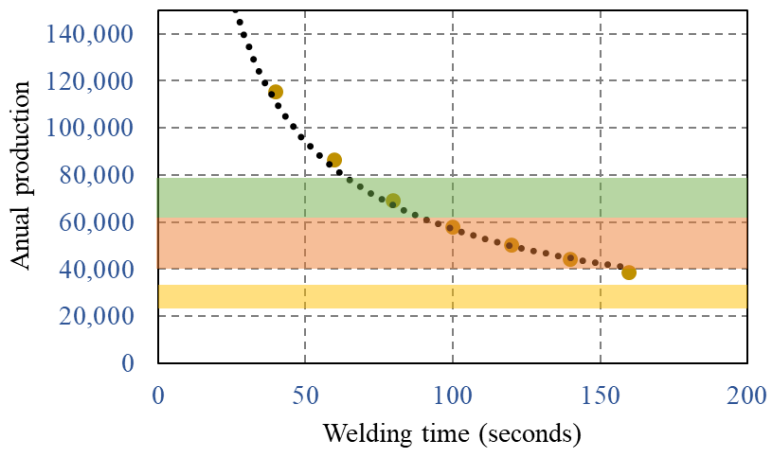


Figure 9.4 Plant simulation model for the upper module body shop.

9.1.2 Results:

The initial assumption that joining speed is linearly proportional to annual production volumes was not valid. When targeted for mid-production volume cars with an annual production volume less than 50,000 units, the required joining speed was obtained as 120 seconds. For higher production volumes up to 100,000 units per year, it was found to be necessary to increase production hours by having two shifts per day – a much prevalent practice in the automotive industry. For production volumes higher than 120,000 units per year, welding speed was needed to be faster than 100 seconds (Table 9.2)

Annual production vs welding time



- Similar to BMW 3ers (steel)
- Similar to Audi A8 (Aluminum)
- Similar to BMW i3 (CFRP)

Figure 9.5 Annual production Vs. Welding time.

Table 9.2 Annual production vs Weld Time.

TPH (Units)	Welding time (sec)	Annual production volume (units)
90	20	172,800
60	40	115,200
45	60	86,400
36	80	69,120
30	100	57,600
26	120	49,920
23	140	44,160
20	160	38,400

In Chapter 6, the total welding time for RIW process was ~ 140 s. However, this welding time is not a good representation of what one can expect in a commercial process.

To determine a more realistic welding time for the commercial process, a closer look at the temperature profiles of the weld interface is required. Figure 9.6 is a plot with all the data logged during a RIW weld test for non-woven FRTPC substrate from Chapter 6 (Run 2). From the rheometer test (Section 6.1.7), it was determined that the welded joint was safe to handle upon cooling down to below 190°C. However, to increase the degree of crystallinity, the cooling rate at the joint interface had to be controlled till 189°C. Hence, it is fair to assume that in a commercial process, the part is ejected when the joint interface reaches 185°C (including an additional 4-5°C as safety factor), which in turn will reduce the total welding time to ~ 110.5 s. This 29.5 s reduction in welding time roughly translates to an increase in throughput per hour by four units, or an additional 7,680 units of production on an annual basis – as shown below.

To further reduce welding time, a possible solution is to incorporate self-clamping features within the part. These features are similar to snap fits and apply the required clamping force on the weld interface. To verify the feasibility of this feature, a quick study was performed in FEA for 2D shell parts. However, incorporating these features for applying such high clamping force on the weld interface would have resulted in an increase in part weight by 3-4 times, thereby defeating the primary purpose of using FRTPC composites for mass reduction.

In summary, with the welding parameters from this dissertation, it is possible to build FRTPC intensive vehicles with annual production volumes ~ 50,000 units per shift.

- **Case 1:** Welding time = 140 s
 - TPH from the plant model = 23 units per hour
 - Annual production per shift = 44,160 vehicles

- **Case 2:** Reduced welding time by the hot ejection of the part = 110.5 s
 - TPH from plant model = 27 units per hour
 - Annual production per shift = 51,840 vehicles.

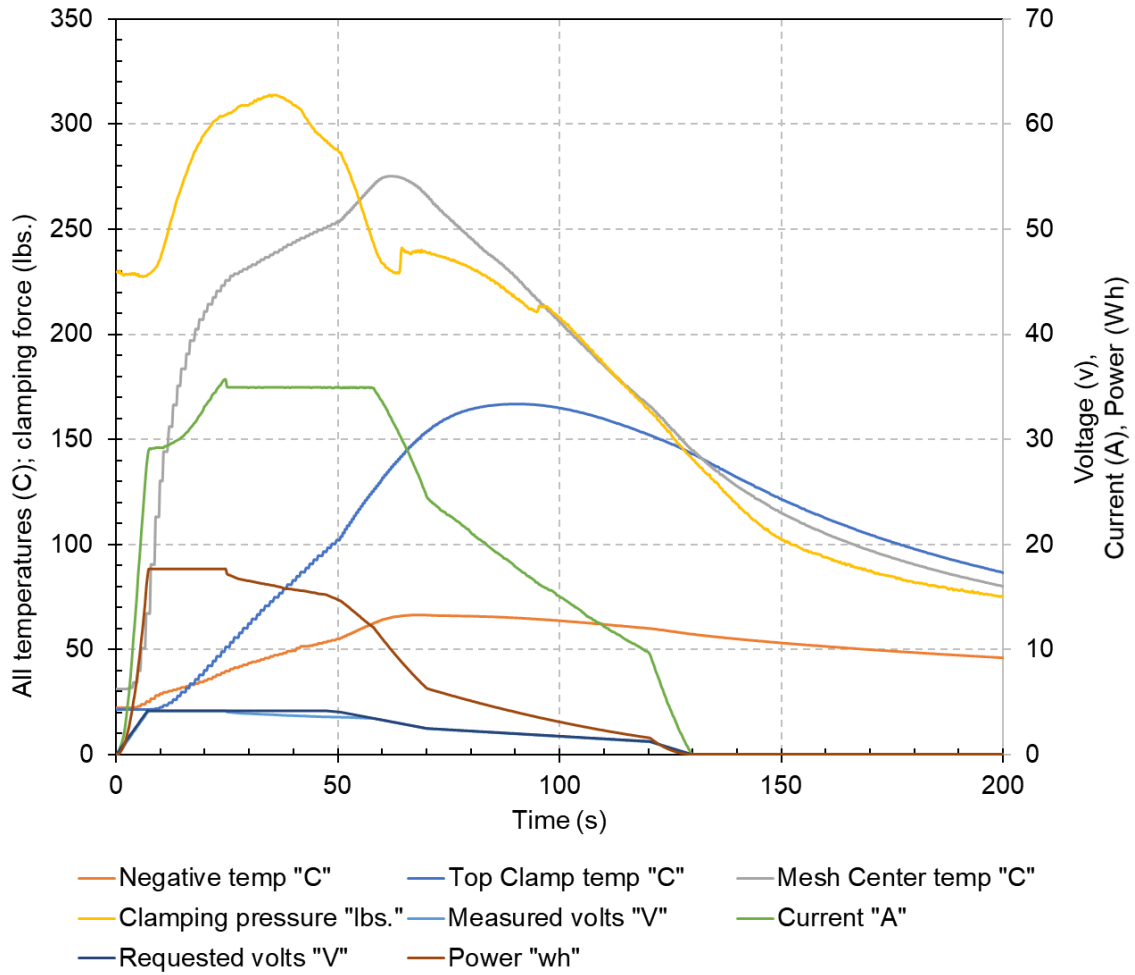


Figure 9.6 Data logged for RIW weld of non-woven FRTPC (Run2).

9.2 Understanding Resilience to Contamination in the joint interface for Resistive Welded Joints.

It is broadly believed that resistive welding is more resistant to contamination. However, a study is yet to be undertaken to ascertain this fact⁷⁵. While the environment inside the body shop is generally controlled, it is not up to the standards of a cleanroom. This makes the joining of composite parts – typically via adhesive bonding – an issue, since this process is sensitive to surface contamination¹⁴⁸. Hence, this operation should be performed in a clean room environment within the body shop to prevent any contamination of the adhesive joints; the operation of these cleanroom sections is an expensive process that increases manufacturing cycle time.

Contaminations are classified as particle-based, water-based, and oil-based. The results of this paper encompass analyses of water- and oil-based contamination, as detailed in Figure 9.7. One of the most common methods of contamination within a body-shop is water-based contamination, which may manifest from moisture residue, improper cleaning, and condensate droplets. While moisture residue is the most common form of water contamination, its consistent replication at the laboratory scale is challenging. Therefore, a droplet form of contamination was selected for this study. Oil-based contaminations are generally from the fixture moments, robots and other hydraulic devices in proximity. These oil contaminations assume the form of either a droplet or smudge. In this analysis, a droplet is selected as the method of contaminations, with a micropipette used in the conveyance.

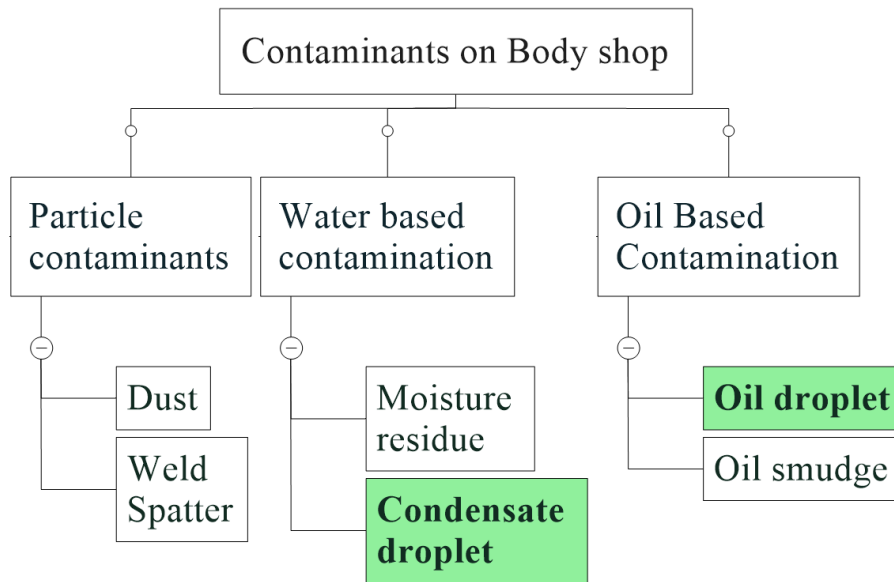


Figure 9.7 Body Shop contaminations.

9.2.1 Introducing contaminants

A micropipette was used to place the contaminant with oil and water droplets on a microbalance and weighed to ensure an accurate displacement of both oil and water via the micropipette. Each of these samples was cleaned using acetone and dried to eliminate any random contamination. For the resistively welded sample, the droplet was placed between the pure polymer film and top coupon. In the adhesively bonded coupon, contamination was added between the adhesive and top coupon. The water contaminant formed a smaller droplet due to high surface tension (Figure 9.8), unlike the oil droplet (Figure 9.9).



Figure 9.8 Water contaminates on resistive welding.

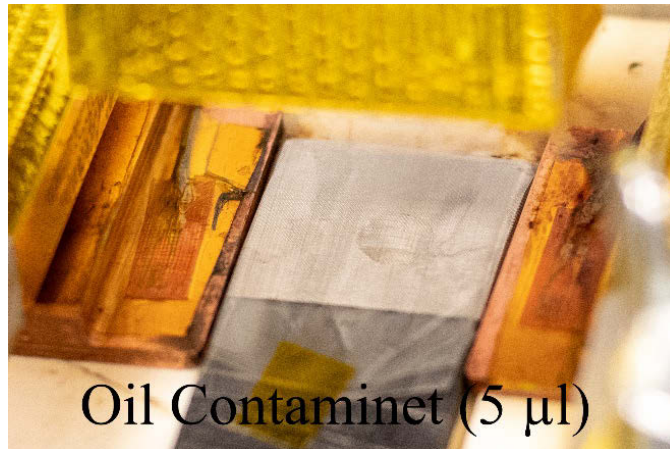


Figure 9.9 Oil Contamination on resistive welding.

9.2.2 *Experiment overview*

For these experiments, non-woven random carbon fiber mat was used as coupon material, and mechanical properties were tested in lap-shear mode using ASTM 5868 standardized lap shear test.

1. **Joining methods**

- a. Resistive implant welding with stainless steel mesh.

- b. Epoxy-based adhesive, 3M DP190
- c. Methacrylate-based adhesive, 3M DP810
- d. Methacrylate-based adhesive, Plexus MA 530

2. Contamination:

- a. Distilled water:
 - i. Volume one: 6 μ l
 - ii. Volume two: 9 μ l
- b. Hydraulic oil (SAE type #32)
 - i. Volume one: 5 μ l
 - ii. Volume two: 8 μ l

Force-displacement plots for all 40 data points were recorded, which indicated the performance of adhesives to be significantly below the manufacturer-recommended lap shear strength value. Such underperformance is perhaps attributable to the very low surface energy of nylon and good surface finish of coupons. A quick evaluation of the effect of surface treatments, such as flaming and sanding, indicated insignificant improvement in performance from these processes. The peak force at the break for all 40 data points is shown in Figure 9.10.

To further compare the loss in property against baseline performance, the average lap shear strength for two replicates was normalized with baseline (clean joint) performance for each joining method as shown in Figure 9.11.

Contamination vs Peak force

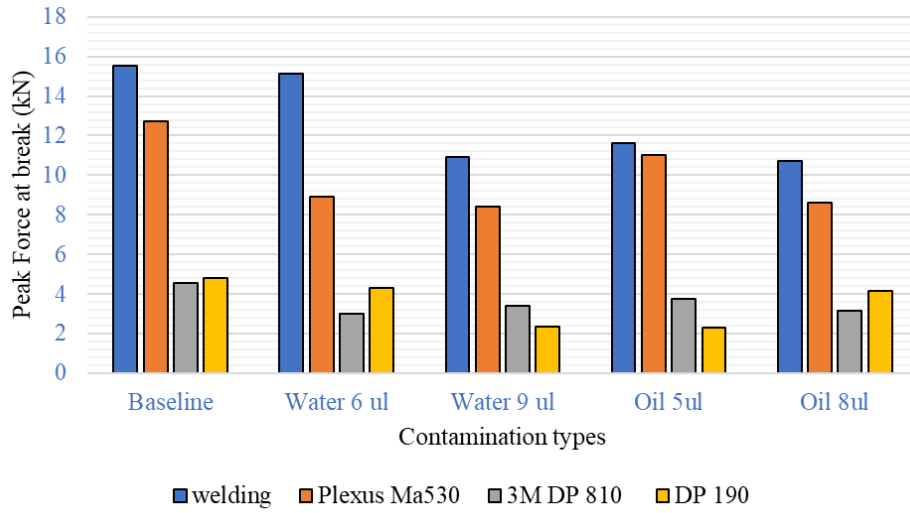


Figure 9.10 Peak force at break vs contamination.

Contamination vs Normalized Peak force

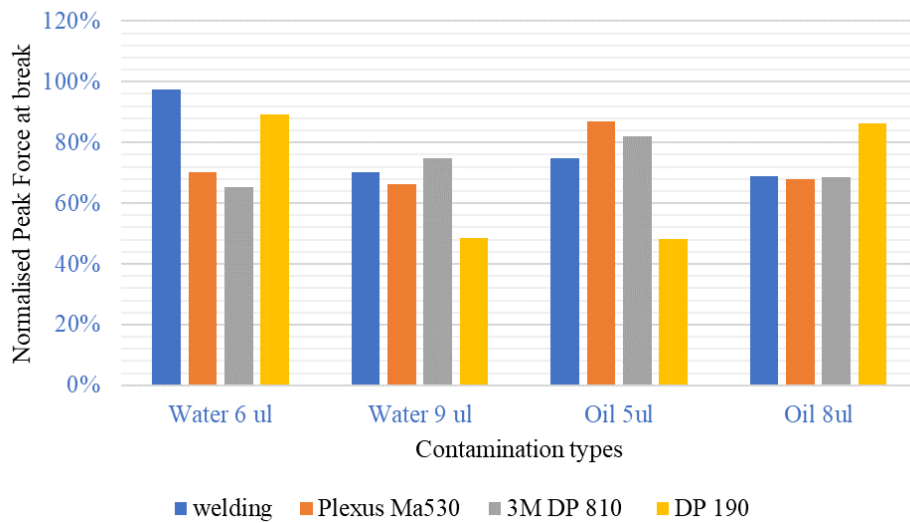


Figure 9.11 Normalized peak force vs. contamination.

As indicated in Figure 9.11, the effect of contamination is significant on both 3M adhesives, unlike for both Plexus MA530 adhesives and resistive welding. While this observation is true when observing the peak force at the break, a more thorough analysis is required, especially to understand the actual effect of contamination for the entire region in force-displacement curves (Figure 9.13).

9.2.3 Observations.

1. Resistive welding

- Steam ejection was observed during the welding process for 5 μl water. Although repeatable, the effect of resistive welding upon contamination also exhibited a consistent effect upon weld strength.
- Presence of 6 μl water caused a negligible effect on weld strength, with steam vapor observed during the welding process at the joint interface (Figure 9.12).
- Oil contamination had a significant effect on weld strength, with residues present at the joint interface after the joint was fractured. However, an increase in the volume of oil contaminant had a much lesser effect on joint performance.
- All fractures were interfacial failures.

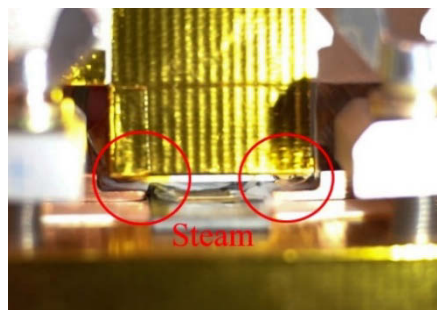


Figure 9.12 Steam ejection during the welding process for 5 μl water.

2. DP 190 Epoxy based adhesive

- Contamination in epoxy-based adhesive affected both strength and stiffness of the joint, with the water diffusing into the polymer network and hydrolyzing chemical bonds within the epoxy network¹⁴⁹. This phenomenon has been previously reported as well, with water contaminants reducing the joint stiffness and thus increasing the elongation at break.
- Addition of oil increased the stiffness of joint, possibly due to the effect of crosslinking performance of the epoxy on its efficiency. However, elongation at break was significantly lower when compared to the baseline.
- Although all fractures except those from oil contamination were interfacial, cohesive failures occurred in the presence of 8 μ l oil contaminant.

3. DP 810 methacrylate-based adhesive

- The acrylic-based adhesive was the most sensitive to contaminants.
- Oil contaminations exhibited a significant effect on the strength of adhesive systems, with > 50% reduction in strength observed.
- No significant effect on joint stiffness was observed, perhaps due to the lack of any chemical interaction between the contamination and adhesive.
- Oil and water residues were present after fracture of the joint at the interface.
- All fractures were mostly interfacial, with small parts of adhesives stuck on both coupons.

4. Plexus MA 530 methacrylate-based adhesive

- This adhesive system performed the best in relation to other adhesive systems.
- Both cohesive and interfacial failures were observed in this adhesive system.
- Unlike other adhesive systems, contamination influenced the failure mechanism, with coupons having oil contaminants tending to fail cohesively.

- There was a significant effect on joint stiffness, indicating some chemical interaction between the contamination and adhesive.
- This adhesive system was very resilient to oil contamination, and also exhibited a lesser reduction in properties on introducing oil contaminant vis-à-vis other systems.

In summary, resistive welding was more resilient to water-based contamination, while adhesive systems were more resilient to oil-based contamination by a very small margin (Figure 9.11). One key observation is that contamination in both resistive welding and 3M DP810 had an insignificant effect on joint stiffness. Irrespective of this, resistive welding outperformed all other systems with both water and oil-based contamination. Thus, when implemented in a body shop, resistive welding might need fewer cleaning processes and significantly lesser environmental control, thereby significantly lowering manufacturing complexity and cycle time.

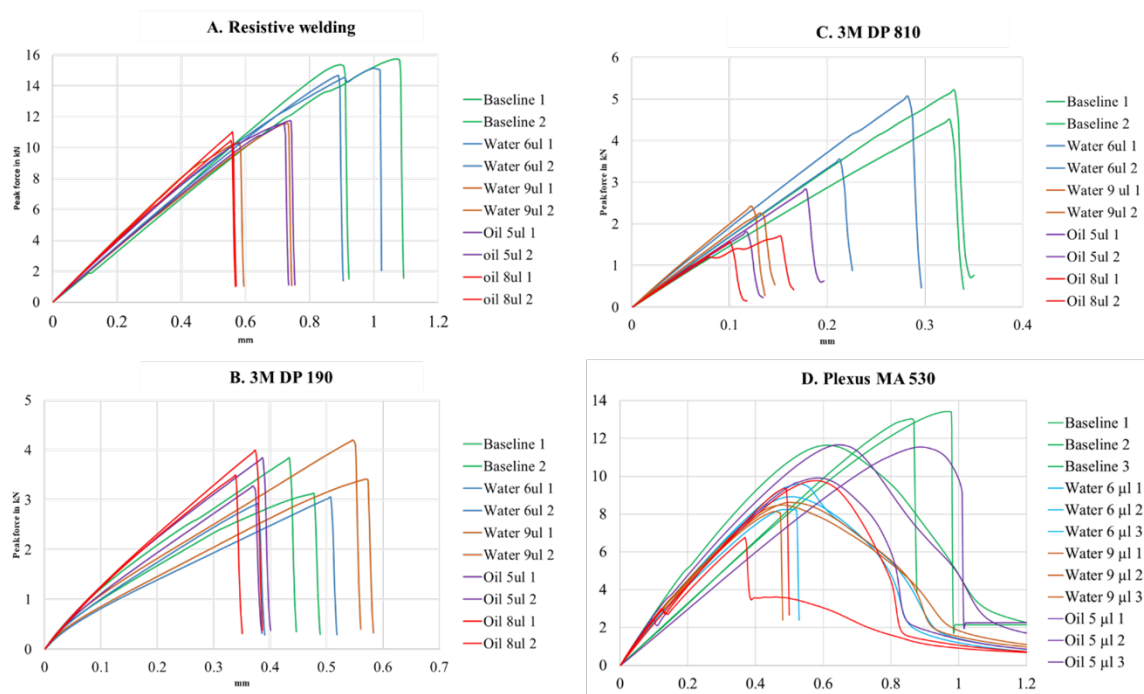


Figure 9.13 force-displacement plots for all tests with contaminations.

9.3 Evaluating reparability/ rework for resistive welded joints.

The total number of motor vehicle crashes in the U.S.A for the year 2016 was ~ 7,277,000, out of which ~ 5,065,000 were classified as property damage only¹⁵⁰. Depending on the age of the vehicle, only 5% (vehicles newer than one year) to 30% (vehicles older than ten years) of these crashes were flagged as a total loss of the vehicle¹⁵¹. This means that a significant portion of these vehicles are involved in non-fatal crashes and can be repaired.

Given this background, one of the key requirements for automakers is to design while keeping in mind the reparability of the structural frame. In this regard, the ability to de-bond a panel on command is crucial. However, this has always been a challenge for composite structures, since debonding a structural adhesive is very difficult without damaging the adjacent parts.

Theoretically, in resistive welding, the heating element can be used to reheat the joint interface and then carefully de-bond the damaged part without damaging any adjacent parts. Once the damaged part is removed, the joint region can be prepped, and a replacement part can be welded back. If this can be achieved without any significant loss in mechanical properties, replacing resistively weld parts will become easier than conventional steel structures since no cutting and patching is required. To evaluate this hypothesis, a coupon level study was conducted as described below.

9.3.1 Experiment overview

For these experiments, non-woven random carbon fiber mat was used as the coupon material, and mechanical properties were tested in lap-shear mode using ASTM 5868 standard lap shear test method.

1. Joining methods

- I. Resistive implant welding with stainless steel heating element.

2. Test Cases:

- I. Baseline weld
- II. Reweld with the old heating element
- III. Reweld with the new heating element

The initial weld was performed, and the coupon was allowed to cool down to room temperature. The welded coupon was assembled back onto the weld fixture with the heating element terminal securely clamped by electrical connectors. Weld current was then switched on, and only the heating portion of the welding profile was run. After heating

for 10-15 s, the top coupon was gently de-bonded, following which two approaches were used to reweld the coupon:

I. **Approach 1:** Reweld with the old heating element

Once the top coupon was de-bonded, a new layer of pure nylon film was added on the old heating element. The new coupon was placed on the old welding stack and rewelded (Figure 9.14).

Reweld with the old heating element

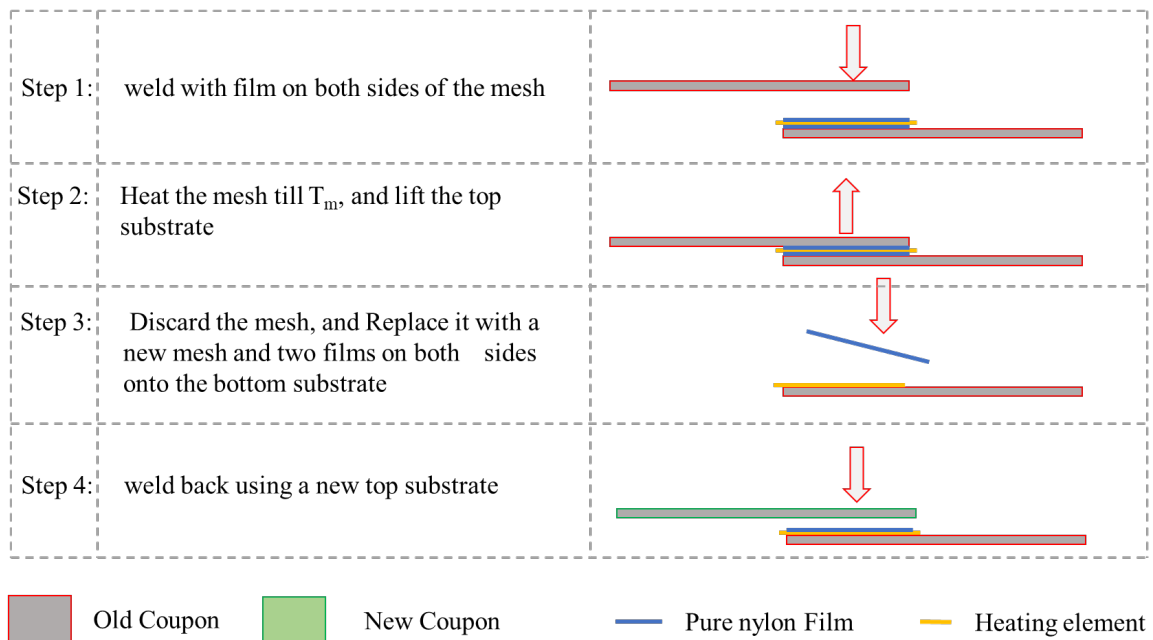


Figure 9.14 Reweld with old mesh.

II. **Approach 2:** Reweld with a new heating element

Once the top coupon was de-bonded, the old heating element was removed from the bottom coupon. After removing the heating element, the weld surface was scraped with a razor and wiped with acetone to remove any residue.

A new heating element, sandwiched between two nylon films, was added to the joint interface along with the new top coupon. The weld was repeated in a similar fashion to the baseline welding process, as shown in Figure 9.15.

Reweld with the New heating element

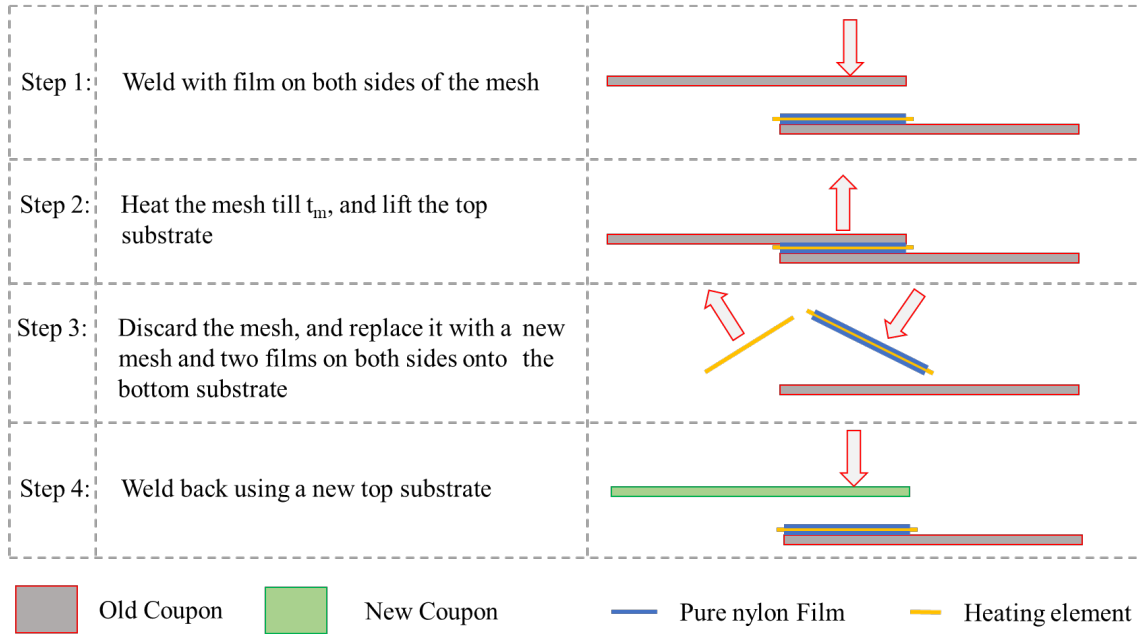


Figure 9.15 Reweld with a new mesh.

Both the baseline and rewelded coupons were tested using the ASTM 5868 lap shear test. Figure 9.16 depicts the force-displacement plots for this test.

9.3.2 Results

Stiffness of the rewelded joint did not undergo any significant change, as shown in the above-mentioned force-displacement plots. However, unlike stiffness, there was a drop in the strength of the rewelded joints. Compared to the baseline, rewelded joints with the new mesh had approximately 8% reduction in average weld strength, while those with

the old mesh had approximately 18% reduction in average weld strength (Figure 9.17). Indeed, the difference between the three weld strengths was statistically insignificant. However, the observed reduction in average weld strength can be attributed to thermal degradation of the polymer melt in the joint region as well as fiber distortion created during de-bonding operations (Figure 9.18). Thermal degradation of the polymer can be alleviated by optimizing the temperature ramps and dwell times, which in turn may enhance the reweld strength like at baseline joints.

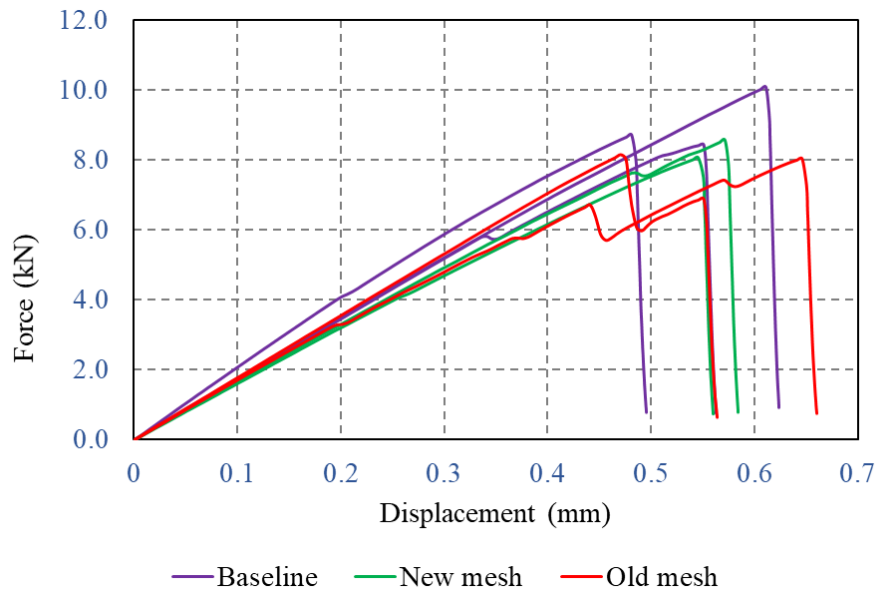


Figure 9.16 Force-displacement plots for Reweld study.

Summary

In conclusion, reprocessing resistive welded joints was observed to be feasible, with possibly no impact to adjacent parts. Using the embedded heating element, the polymer in the weld region was successfully melted and the weld was de-bonded. The reweld performance upon using a new heating element was almost similar to the baseline

weld performance after taking into account the standard deviation. Therefore, in practice, it is possible to de-bond and rework resistive welded joints with ease and while ensuring no significant loss in mechanical performance.

Baseline strength vs Reweld strength

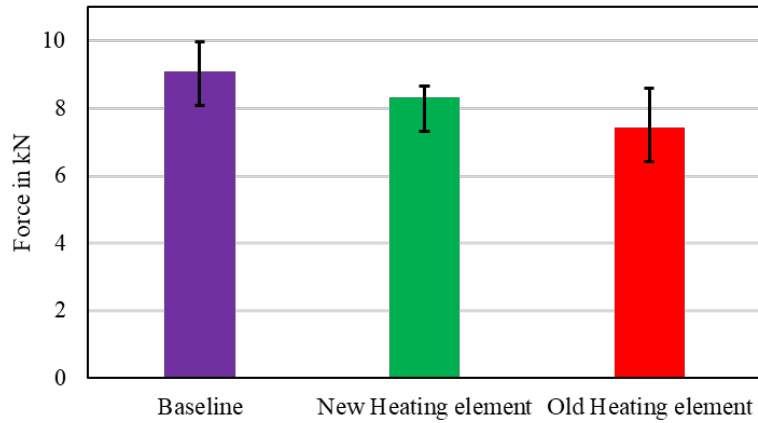


Figure 9.17 Weld strengths for rewelded coupons.

De-bonded Coupons



Lower Coupon (reweld)



Top Coupon (discard)

Figure 9.18 De-bonded Coupons.

10 CONCLUSION

10.1 Conclusions

The primary goal of this dissertation is to minimize barriers for the usage of FRTPC materials for mass-produced automotive structures. To effectively achieve this goal, two critical things needed to be addressed: (a) Ensuring that FRTPCs have better specific properties than most automotive structural materials; and (b) Ensuring that these materials can be joined structurally with very fast cycle times.

Historically, the focus of most research was limited to FRTPCs with high-performance polymers such as PEEK, PEI, and PPS. However, the very high cost of these composites made them untouchable for automotive applications. From an economic standpoint, FRTPCs with engineering (mid-tier) polymers such as PA6 and PA6-6 are within the regime of automotive structures. However, the overarching question was whether these materials met the mechanical requirements of an automotive structure or not. Chapter 3 exactly addresses this question by procuring and testing several types of FRTPCs with PA 6-6 matrix for mechanical performance. Using this data from Chapter 3, in Chapter 4, these material systems were simulated in an automotive structure to evaluate whether they met the required mechanical performance while achieving reasonable mass reduction. An automotive side closure (Door) was developed with FRTPCs (with PA-66 matrix), and approximately 45% reduction in structural mass was achieved. Few key comparison points between steel and FRTPC automotive structures are summarized in Table 10.1.

Table 10.1 Summary of FRTPC.

Attribute	Steel structures	FRTPC structures (PA66 /AS4)
Mass reduction potential	0	~45%
Part consolidation potential	0	~ 35 to 40%
Manufacturing cycle time	~15 to 20 seconds	~120 to 180 Seconds
Cost per lbs. saved	\$0	~ \$ 5
Corrosion resistance	Poor	Very good
Capital investment	High	Moderate
Manufacturing energy consumption	High	Moderate
Strength	450 to 1500 MPa	166 to 1449 MPa
Elastic modulus	~210 GPa	8 to 100 GPa

However, the ability to join these materials with very low cycle times and strengths is also vital for their usage in mass production. This dissertation explores various fusion bonding technologies for FRTPCs and recommends resistive implant welding as the best process for automotive structural joining applications. Chapter 2 (Section 2.2) begins on this aspect by using a top-down approach to determine targets for resistive implant welding. Further, to experimentally validate and verify various research statements made in this dissertation, an instrumented welding test rig was developed and manufactured in house (Chapter 5).

In a resistive welded joint, the polymer matrix is the weakest link in the load path between the joint parts. With the decision to use mid-tier polymer, there was a significant drop in the mechanical properties of this weakest link. In addition to this, the melt viscosity of these polymers is significantly lower than that of high-performance polymers. Due to

these factors, the pressing question was whether resistive implant welding could match or outperform the current commercial joining technology (adhesive bond).

Table 10.2 Summary of the RIW joint

Attribute	Adhesive Bonding (Plexus MA530)	RIW joints (PA66 /AS4)
Mode 1 fracture toughness	.291 KJ/m ²	.235 KJ/m ²
Mode 2 Strength	22.4 MPa	19.7 MPa
Joining cycle time	110 to 150 seconds	120 minutes (work handle, 48 hours full cure)
Sensitivity to water contamination	High	Low
Sensitivity to oil contamination	Moderate	Moderate
Sensitivity to strain rates	Yes	Yes
Performance delta in crash mode (component level)	0	+ 8%

Chapter 6 primarily focuses on developing and optimizing weld process for FRTPCs with PA 66 matrix. Several approaches for temperature control, clamping pressure modulation, and heating element configurations, were evaluated. Several designs of experiments were conducted to develop optimum processing windows for maximizing the mechanical performance of the resistive welded joints.

Using this understanding on weld processing, several RIW joints for various FRTPCs, such as LFT injection-molded CF-PA66, non-woven discontinuous CF-PA66, and woven CF-PA66 materials, were evaluated and compared against the best performing commercially available adhesive system. The RIW joints outperformed adhesive systems by a significant margin in Mode II loading (in-plane shear or lap shear), but slightly underperformed in Mode I loading (out of plane force or peel). It is common knowledge that most automotive joints are designed to be loaded in Mode II conditions (in-plane

shear). However, it was not possible to conclude that the RIW joints performed better or same as adhesive systems just by evaluating these coupon-level performances. It is also important to note that these adhesive systems represent the very best in mechanical performance for FRTPC materials and while having longer curing time (2 hours for handling and 48 hours for full cure). This very long curing time renders these adhesives unusable for automotive mass production. RIW joint performance in relation to structural adhesives is summarized in Table 10.2.

For this very same reason, finite element analysis methods were used to evaluate these joining technologies at an automotive component level. However, there is no existing research on material testing to modeling pathway for RIW joints.

In Chapter 8, using the current framework to model and simulate adhesives as a starting point, testing-to-simulation pathways were developed for RIW joints. For most existing approaches, bulk properties of the joining material (adhesive or weld interface) is critical. However, due to the nature of RIW joints, it was impossible to test the joint interface in isolation of substrate materials physically. Therefore, in this chapter, a model-fitting approach was used to develop FE models (cohesive zone models). Digital image correlation techniques were used to estimate the local strain behavior of welded coupons by using these local strain limits as starting points, while the number iterations for modeling fitting were drastically cut short.

In addition to this, FE models (cohesive zone models) for the test adhesive were also developed. Using these FE models, the performance of an automotive side sill was evaluated in the side impact pole test. From these evaluations, it is fair to conclude that

the RIW joints for FRTPC (with PA66 matrix) slightly outperformed structural adhesives in large deformation load cases.

In this work, the focus was also on understanding the effect of welding time of a RIW joint on the throughput of automotive body shop using a virtual plant simulation model. Using this model, it was concluded that at current welding times, it was possible to achieve an annual production volume of 100,000 units with two shifts per day. In addition to this, when commercializing this process, it was important to acknowledge that high standards of environmental control are not cost-effective or common in the automotive body shop. Water condensate and oil smudges are some of the common contaminants found in the automotive body shop. In Chapter 9, it was experimentally determined that the RIW joint with water or oil contamination performs better than the tested adhesive system.

When these joints are implemented in automotive structures, it is essential to have some mechanism to debond and rejoin these joints. The lack of an easy approach to achieve the same for adhesives is among its major drawbacks. In this dissertation, the existing heating element was used to heat the joint interface to melt temperature, thereby significantly weakening the weld. In this process, the parts could be debonded without any damage. Using a new heating element, a new coupon was welded back to the old coupon without any significant property loss. This technique can also be used at the end of life of automotive structures to disassemble parts and separate the embedded heating element from the FRTPC material for recycling.

In summary, this dissertation addresses several gaps in understanding the performance of FRTPCs and RIW joining process in an automotive context. Using these technologies can enable significant mass reduction for automotive structures.

10.2 Future work

While this body of work testifies the systematic evaluation of a novel joining technology for FRTPCs, the observations and inferences open several opportunities for further exploration. Some of the proposed research opportunities are highlighted here:

10.2.1 Using multiscale modeling to capture variance in weld performance

One of the major challenges with the resistive welded joint is its sensitivity to coupon material and coupon geometry. When implementing this joining technology in large structures, it will get tedious to repeat testing and model development for every joint combination. By using a multi-scale modeling approach, the performance variance of resistive welding can be simulated, thereby minimizing the number of tests required and streamlining the simulation of these joints. A representative volume element (RVE) approach can be used at micro-scale to simulate the interaction between the heating element, voids, and the polymer melt. Similar approaches have been used previously to model the effect of fiber reinforcement on polymer matrix materials¹⁵².

10.2.2 Developing comingled carbon fiber -polymer heating elements

Despite better performance from metallic heating elements, certain attributes such as low density and corrosion resistance make nonmetallic heating elements attractive. One of the major limitations for carbon fiber heating element is very high permeation resistance. In addition to this, this permeation resistance increased when clamping

pressure was applied to the welding stack. Conventional wisdom suggests spreading the carbon fibers, but doing so will lead to having un-melted polymer in the weld region. The best technique to uniformly distribute polymer resin is via filament commingling. In this process, a pre-selected amount of carbon fiber and polymer fibers can be uniformly distributed into a yarn. From this yarn, a UD tape can be manufactured and used as a heating element. While these joints may be relatively brittle than welds with metallic heating elements, their advantage in weight and corrosion resistance can make them attractive for select applications.

10.2.3 Validate simulation correlation at a mixed-mode loading and component level

To truly validate any simulation model, it is necessary to correlate simulation with actual tests at multiple levels. In the current body of work, the correlation was only done at a coupon level. To truly validate this material and simulation process, a component level correlation is necessary. A typical practice is to use simple geometries, such as a closed hat section under simply supported beam configuration or axial crumpling configuration. By comparing the responses from experiments and simulation, a high level of confidence can be attained with the simulation pathway.

11 BIBLIOGRAPHY

1. IPCC. *Global Warming of 1.5 °C - SR15. Ippc - Sr15* (2018).
2. UNFCCC. Conference of the Parties (COP). ADOPTION OF THE PARIS AGREEMENT - Conference of the Parties COP 21. *Adopt. Paris Agreement. Propos. by Pres. 21932*, 32 (2015).
3. Edenhofer, O. *et al.* Technical Summary. *Clim. Chang. 2014 Mitig. Clim. Chang. Contrib. Work. Gr. III to Fifth Assess. Rep. Intergov. Panel Clim. Chang.* 33–107 (2014). doi:10.1103/PhysRevD.70.106002
4. Desai, M. & Camobreco, V. Inventory of U.S.Greenhouse Gas Emissions and Sinks 1990-2017. (2019).
5. Edenhofer, O., Pichs-Madruga, R., Sokona, Y., Minx, J.C., Farahani, E., Kadner, S., Seyboth, K. *Climate Change 2014 Mitigation of Climate Change Summary for Policymakers and Technical Summary, Working Group III Contribution to the Fifth Assessment Report of the Intergovernmental Panel on Climate Change (IPCC). Annual Review of Environment and Resources 40*, (2015).
6. Atabani, A. E., Badruddin, I. A., Mekhilef, S. & Silitonga, A. S. A review on global fuel economy standards, labels and technologies in the transportation sector. *Renew. Sustain. Energy Rev. 15*, 4586–4610 (2011).
7. Anderson, S. T., Parry, I. W. H., Sallee, J. M. & Fischer, C. Automobile fuel economy standards: Impacts, efficiency, and alternatives. *Rev. Environ. Econ. Policy 5*, 89–108 (2011).

8. ICTSD. International Trade Governance and Sustainable Transport: The Expansion of Electric Vehicles. (2017).
9. Simmons, R. A., Shaver, G. M., Tyner, W. E. & Garimella, S. V. A benefit-cost assessment of new vehicle technologies and fuel economy in the U.S. market. *Appl. Energy* **157**, 940–952 (2015).
10. Singh, H. Mass Reduction for Light-Duty Vehicles for Model Years 2017-2025. *Rep. No. DOT HS 811 666* (2012).
11. Bjelkengren, C. The Impact of Mass Decompounding on Assessing the Value of Vehicle Lightweighting. *Development* (2006).
12. Lm, P. I. D., Mascarin, A. & Associates, I. Vehicle Lightweighting : Mass Reduction Spectrum Analysis and Process Cost Modeling Overview Timeline. (2016).
13. Isenstadt, A. *et al.* Lightweighting technology development and trends in U.S. passenger vehicles | International Council on Clean Transportation. *Ricardo Strateg. Consult. Mater. Doug Richman (Aluminum Assoc.* (2016).
14. Dai, Q., Kelly, J. & Elgowainy, A. Vehicle Materials : Material Composition of U . S . Light-duty Vehicles. (2016).
15. Mangino, E., Carruthers, J. & Pitarresi, G. The future use of structural composite materials in the automotive industry. *Int. J. Veh. Des.* **44**, 211 (2007).
16. Ashby, M. F. Material and process selection charts. *CES EduPack Resour. Bookl.* 2 42 (2010).
17. Fukui, R. *et al.* Recycle of Carbon Fiber Reinforced Plastics. 44–49 (2005).

18. Daniels, J. Design implications of adhesive bonding in car body construction. *Int. J. Adhes. Adhes.* **4**, 5–8 (1984).
19. Messler, R. W. Joining composite materials and structures: Some thought-provoking possibilities. *J. Thermoplast. Compos. Mater.* **17**, 51–75 (2004).
20. Yarlagadda, S. *et al.* Multi-material joining for carbon fiber thermoplastic B-pillar. *Spe Antec* **240**, (2017).
21. Folkes, M. J. *Advances in thermoplastic matrix composite materials. Materials & Design* **12**, (2003).
22. Whitten, W. K. *Composites Composites. Science* **32**, (1977).
23. Stack, R. M. & Lai, F. Development in Thermoforming Thermoplastic Composites. (2011).
24. Muzzy, J. D. & Kays, A. O. Thermoplastic vs. thermosetting structural composites. *Polym. Compos.* **5**, 169–172 (1984).
25. Yousefpour, A., Hojjati, M. & Immarigeon, J.-P. Fusion Bonding/Welding of Thermoplastic Composites. *J. Thermoplast. Compos. Mater.* **17**, 303–341 (2004).
26. Mainka, H. *et al.* Lignin - An alternative precursor for sustainable and cost-effective automotive carbon fiber. *J. Mater. Res. Technol.* **4**, 283–296 (2015).
27. Baker, D. A. & Rials, T. G. Recent advances in low-cost carbon fiber manufacture from lignin. *J. Appl. Polym. Sci.* **130**, 713–728 (2013).
28. Hartshorn, S. R. *Structural adhesives : chemistry and technology.* (Plenum Press, c1986., 1986).

29. Smith, L. J. H. MECHANICALLY FASTENED JOINTS FOR ADVANCED COMPOSITES - PHENOMENOLOGICAL CONSIDERATIONS AND SIMPLE ANALYSES.
30. Annual, A. *et al.* *Acronyms and Abbreviations*.
31. Robert W, M. J. & Genc, S. Integral micro-mechanical interlock joints for polymer-matrix composite structures. *J. Thermoplast. Compos. materials* **11**, (1998).
32. Copyright. in *Woodhead Publishing Series in Welding and Other Joining Technologies* (ed. Dillard, D. A. B. T.-A. in S. A. B.) iv (Woodhead Publishing, 2010).
doi:<https://doi.org/10.1016/B978-1-84569-435-7.50021-3>
33. OWENS, D. K. & Nemours, E. I. du P. de. Estimation of Estimation of Surface Free Energy of Polymers. *J. Appl. Polym. Sci.* **13**, 1741–1747
34. Dimethyl, P. *et al.* Studies on Surface Wettability of Studies on Surface Wettability of Poly (Dimethyl) Siloxane (PDMS) and Glass Under Oxygen-Plasma Treatment and Correlation With Bond Strength. **14**, 590–597 (2014).
35. Ageorges, C., Ye, L. & Hou, M. Advances in fusion bonding techniques for joining thermoplastic matrix composites: A review. *Compos. - Part A Appl. Sci. Manuf.* **32**, 839–857 (2001).
36. Ageorges, C., Ye, L., Mai, Y.-W. & Hou, M. Characteristics of resistance welding of lap-shear coupons. Part III. Crystallinity. *Compos. Part A Appl. Sci. Manuf.* **29**, 921–932 (1998).
37. Zhao, T. *et al.* Mechanical behaviour of thermoplastic composites spot-welded and mechanically fastened joints: A preliminary comparison. *Compos. Part B Eng.* **112**,

224–234 (2017).

38. Fernandez, I. & Stavrov, D. Ultrasonic Welding of Advanced Thermoplastic Composites : an Investigation on Energy Directing Surfaces.
39. Kalpakjian, S. 1928-author., Schmid, S. R. . author. & Sekar, K. S. V. writer of supplementary textual content. *Manufacturing engineering and technology / Serope Kalpakjian, Steven R. Schmid.* (2014).
40. Tolunay, M. N., Dawson, P. R. & Wang, K. K. Heating and bonding mechanisms in ultrasonic welding of thermoplastics. *Polym. Eng. Sci.* **23**, 726–733 (1983).
41. Natesh, M. *et al.* Experimental and numerical procedure for studying strength and heat generation responses of ultrasonic welding of polymer blends. *Meas. J. Int. Meas. Confed.* **132**, 1–10 (2019).
42. Volkov, S. & Kholopov, Y. . Technology and equipment for ultrasonic welding of polymer based composite structures.
43. Harras, B., Cole, K. & Vu-Khanh, T. Optimization of the ultrasonic welding of PEEK-carbon composites. *J. Reinf. Plast. Compos.* **15**, 174–182 (1996).
44. Palardy, G. & Villegas, I. F. On the effect of flat energy directors thickness on heat generation during ultrasonic welding of thermoplastic composites. *Compos. Interfaces* **6440**, 1–12 (2016).
45. Wang, X. FEM Investigation of the Temperature Field of Energy Director During Ultrasonic Welding of PEEK Composites. *J. Thermoplast. Compos. Mater.* **19**, 593–607 (2006).

46. Moon, D. H., Cho, H. I., Kim, H. S., Sunwoo, H. & Jung, J. Y. A case study of the body shop design in an automotive factory using 3D simulation. *Int. J. Prod. Res.* **44**, 4121–4135 (2006).
47. Dube, M. *et al.* Metal mesh heating element size effect in resistance welding of thermoplastic composites. *J. Compos. Mater.* **46**, 911–919 (2012).
48. Yerra, V. A. & Pilla, S. Understanding Resilience to Contamination in the Joint Interface for a Resistive Welded Joint in Fiber Reinforced Thermoplastics. *SAE Tech. Pap. Ser. 1*, 1–6 (2019).
49. Dubé, M., Hubert, P., Yousefpour, a. & Denault, J. Current leakage prevention in resistance welding of carbon fibre reinforced thermoplastics. *Compos. Sci. Technol.* **68**, 1579–1587 (2008).
50. Shi, H., Villegas, I. F. & Bersee, H. E. N. Strength and failure modes in resistance welded thermoplastic composite joints: Effect of fibre-matrix adhesion and fibre orientation. *Compos. Part A Appl. Sci. Manuf.* **55**, 1–10 (2013).
51. Ahmed, T. J., Stavrov, D. & Bersee, H. E. N. An Experimental Investigation into Resistance and Induction Welding for Aerospace Structures: A Comparison. in *ASC Structures, Structural Dynamics, and Materials Confere 1 - 4 May 2006, Newport, Rhode Island AIAA* 1–10 (2006).
52. Farahani, R. D. & Dubé, M. Novel Heating Elements for Induction Welding of Carbon Fiber/Polyphenylene Sulfide Thermoplastic Composites. *Adv. Eng. Mater.* **19**, 1–10 (2017).
53. Villegas, I. F., Moser, L., Yousefpour, A., Mitschang, P. & Bersee, H. E. N. Process

- and performance evaluation of ultrasonic, induction and resistance welding of advanced thermoplastic composites. *J. Thermoplast. Compos. Mater.* **26**, 1007–1024 (2013).
54. Guide, A. R. Ultrasonic welding. *Ultrasonics* **2**, V (1964).
 55. Villegas, I. F. & Bersee, H. E. N. Characterisation of a metal mesh heating element for closed-loop resistance welding of thermoplastic composites. *J. Thermoplast. Compos. Mater.* **28**, 46–65 (2015).
 56. Shi, H., Villegas, I. F. & Bersee, H. E. N. A displacement-detection based approach for process monitoring and processing window definition of resistance welding of thermoplastic composites. *Compos. Part A Appl. Sci. Manuf.* **74**, 1–9 (2015).
 57. Requena, I. G., Lobera, a. S. & Fernández, L. M. V. Characterizing of Meshes for Resistance Welding of High Temperature Reinforced Laminate Thermoplastic (RLT). *Procedia Eng.* **63**, 556–563 (2013).
 58. Tan, S. & Zak, G. Resistive Implant Welding of Glass Fiber Reinforced Polypropylene Compounds. *Engineering* (2006). doi:10.4271/2006-01-0332
 59. Warren, K. C., Lopez-Anido, R. A., Freund, A. L. & Dagher, H. J. Resistance welding of glass fiber reinforced PET: Effect of weld pressure and heating element geometry. *J. Reinf. Plast. Compos.* **35**, 974–985 (2016).
 60. Hou, M., Ye, L. & Mai, Y. W. An Experimental Study of Resistance Welding of Carbon Fibre Fabric Reinforced Polyetherimide (CF Fabric/PEI) Composite Material. *Appl. Compos. Mater.* **6**, 35–49 (1999).
 61. Ageorges, C. Experimental investigation of the resistance welding of thermoplastic-

- matrix composites. Part II: optimum processing window and mechanical performance. *Compos. Sci. Technol.* **60**, 1191–1202 (2000).
62. Todd, S. M. Joining thermoplastic composites. *Soc. Adv. Mater. Process Eng.* 383–392 (1990).
 63. Schwartz, M. M. Joining of composite materials. *ASM Int* **1994**, 35–88 (1994).
 64. Eveno, E. C. & Gillespie, J. W. Resistance Welding of Graphite Polyetheretherketone Composites: An Experimental Investigation. *J. Thermoplast. Compos. Mater.* **1**, 322–338 (1988).
 65. Offringa, A. R. Thermoplastic composites—rapid processing applications. *Compos. Part A Appl. Sci. Manuf.* **27**, 329–336 (1996).
 66. Schijve, W. Fokker 50 thermoplastic main undercarriage door: design and cost effectiveness of thermoplastic parts. *J. Adv. Mater.* **25**, 2–9 (1994).
 67. Kelly, J. C., Sullivan, J. L., Burnham, A. & Elgowainy, A. Impacts of Vehicle Weight Reduction via Material Substitution on Life-Cycle Greenhouse Gas Emissions. *Environ. Sci. Technol.* **49**, 12535–12542 (2015).
 68. Yao, S. S., Jin, F. L., Rhee, K. Y., Hui, D. & Park, S. J. Recent advances in carbon-fiber-reinforced thermoplastic composites: A review. *Compos. Part B Eng.* **142**, 241–250 (2018).
 69. Zhang, G. *et al.* The surface analytical characterization of carbon fibers functionalized by H₂SO₄ / HNO₃ treatment. **6**, 0–9 (2007).
 70. Park, S., Seo, M. & Lee, Y. Surface characteristics of fluorine-modified PAN-based

- carbon fibers. **41**, 723–730 (2003).
71. Botelho, E. C., Scherbakoff, N. & Rezende, M. C. Study of polyamide 6/6 synthesis carried out by interfacial polymerization on carbon fibre. *Polym. Int.* **51**, 1261–1267 (2002).
 72. Botelho, E. C., Figiel, Rezende, M. C. & Lauke, B. Mechanical behavior of carbon fiber reinforced polyamide composites. *Compos. Sci. Technol.* **63**, 1843–1855 (2003).
 73. Karsli, N. G. & Aytac, A. Composites: Part B Tensile and thermomechanical properties of short carbon fiber reinforced polyamide 6 composites. *Compos. Part B* **51**, 270–275 (2013).
 74. Gillespie, J. W., Haque, B. Z. G. & Tierney, J. J. Keuthage 2. 1–10
 75. Stavrov, D. & Bersee, H. E. N. Resistance welding of thermoplastic composites-an overview. *Compos. Part A Appl. Sci. Manuf.* **36**, 39–54 (2005).
 76. Young, R. J. & Chung, C. I. Introduction to Polymers. *J. Eng. Mater. Technol.* **104**, 297 (2009).
 77. Sailer, C. & Handge, U. A. Melt viscosity, elasticity, and morphology of reactively compatibilized polyamide 6/styrene-acrylonitrile blends in shear and elongation. *Macromolecules* **40**, 2019–2028 (2007).
 78. Bangarusampath, D. S. *et al.* Rheology and properties of melt-processed poly(ether ether ketone)/multi-wall carbon nanotube composites. *Polymer (Guildf)*. **50**, 5803–5811 (2009).

79. Majumdar, B., Keskkula, H. & Paul, D. R. Mechanical behaviour and morphology of toughened aliphatic polyamides. *Polymer (Guildf)*. **35**, 1399–1408 (1994).
80. Albérola, N. D., Mélé, P. & Bas, C. Tensile mechanical properties of PEEK films over a wide range of strain rates. II. *J. Appl. Polym. Sci.* **64**, 1053–1059 (1997).
81. Nonhof, C. J., Riepen, M. & Melchers, A. W. Estimates for process conditions during the vibration welding of thermoplastics. *Polym. Eng. Sci.* **36**, 2018–2028 (1996).
82. Bates, P. J., Tan, S., Zak, G. & McLeod, M. Shear strength and meltdown behavior of reinforced polypropylene assemblies made by resistance welding. *Compos. Part A Appl. Sci. Manuf.* **40**, 28–35 (2009).
83. Shi, H., Villegas, I. F., Oceau, M.-A., Bersee, H. E. N. & Yousefpour, A. Continuous resistance welding of thermoplastic composites: Modelling of heat generation and heat transfer. *Compos. Part A Appl. Sci. Manuf.* **70**, 16–26 (2015).
84. Ageorges, C. & Ye, L. Simulation of impulse resistance welding for thermoplastic matrix composites. *Appl. Compos. Mater.* **8**, 133–147 (2001).
85. Zammar, I. A., Mantegh, I., Huq, M. S., Yousefpour, A. & Ahmadi, M. Intelligent Thermal Control of Resistance Welding of Fiberglass Laminates for Automated Manufacturing. **20**, 1069–1078 (2015).
86. Shi, H., Villegas, I. F. & Bersee, H. E. N. N. Analysis of void formation in thermoplastic composites during resistance welding. *J. Thermoplast. Compos. Mater.* **30**, 0892705716662514 (2017).
87. Matthes, D., Landgrebe, D. & Drossel, W.-G. Inductive heating of glass fibre-reinforced thermoplastics using fibre- and wire-shaped stainless steel susceptors.

J. Thermoplast. Compos. Mater. (2015). doi:10.1177/0892705715583179

88. Dolev, G. & Ishai, O. Mechanical Characterization of Adhesive Layer in-situ and as Bulk Material. *J. Adhes.* **12**, 283–294 (1981).
89. Banea, M. D., Da Silva, L. F. M. & Campilho, R. D. S. G. Moulds design for adhesive bulk and joint specimens manufacturing. *Assem. Autom.* **32**, 284–292 (2012).
90. Scheider, I. & Brocks, W. The Effect of the Traction Separation Law on the Results of Cohesive Zone Crack Propagation Analyses. *Key Eng. Mater.* **251–252**, 313–318 (2009).
91. Wang, P., Hamila, N. & Boisse, P. Thermoforming simulation of multilayer composites with continuous fibres and thermoplastic matrix. *Compos. Part B Eng.* **52**, 127–136 (2013).
92. Huang, P. Y., Tsai, Y. C., Chen, Y. De & Hwang, S. F. Thermoforming of woven carbon fiber thermoplastic composites. *Proc. 2018 IEEE Int. Conf. Adv. Manuf. ICAM 2018* 93–96 (2019). doi:10.1109/AMCON.2018.8614985
93. Guzman-Maldonado, E., Hamila, N., Naouar, N., Moulin, G. & Boisse, P. Simulation of thermoplastic prepreg thermoforming based on a visco-hyperelastic model and a thermal homogenization. *Mater. Des.* **93**, 431–442 (2016).
94. Wang, Q., Maze, B., Tafreshi, H. V. & Pourdeyhimi, B. Simulating through-plane permeability of fibrous materials with different fiber lengths. *Model. Simul. Mater. Sci. Eng.* **15**, 855–868 (2007).
95. Hou, M., Friedrich, K. & Scherer, R. Optimization of stamp forming of thermoplastic composite bends. *Compos. Struct.* **27**, 157–167 (1994).

96. JOHNSON, A. F. & PICKETT, A. K. Numerical simulation of the forming process in long fibre reinforced thermoplastics. 233–242
97. Adam, L., Depouhon, A. & Assaker, R. Multi-Scale Modeling of Crash & Failure of Reinforced Plastics Parts with DIGIMAT to LS-DYNA interface. *7th Eur. LS-DYNA Conf. c*, 1–9 (2009).
98. Fu, S. Y., Lauke, B., Mäder, E., Yue, C. Y. & Hu, X. Tensile properties of short-glass-fiber- and short-carbon-fiber-reinforced polypropylene composites. *Compos. Part A Appl. Sci. Manuf.* **31**, 1117–1125 (2000).
99. Gupta, V. B., Mittal, R. K., Sharma, P. K., Mennig, G. & Wolters, J. Part I : Reduction in Fiber Length During Processing. *Polym. Compos.* 8–15 (1989). doi:10.1007/s10040-016-1436-5
100. Hassan, A. *et al.* Interfacial shear strength and tensile properties of injection-molded, short- and long-glass fiber-reinforced polyamide 6,6 composites. *J. Reinf. Plast. Compos.* **30**, 1233–1242 (2011).
101. Balaji Thattai parthasarathy, K., Pillay, S., Ning, H. & Vaidya, U. K. Process simulation, design and manufacturing of a long fiber thermoplastic composite for mass transit application. *Compos. Part A Appl. Sci. Manuf.* **39**, 1512–1521 (2008).
102. Ranganathan, N., Oksman, K., Nayak, S. K. & Sain, M. Effect of long fiber thermoplastic extrusion process on fiber dispersion and mechanical properties of viscose fiber/polypropylene composites. *Polym. Adv. Technol.* **27**, 685–692 (2016).
103. Wolf, H. J. Screw plasticating of discontinuous fiber filled thermoplastic: Mechanisms and prevention of fiber attrition. *Polym. Compos.* **15**, 375–383 (1994).

104. Chen, T., Liao, J., Liu, G., Zhang, F. & Gong, Q. Effects of needle-punched felt structure on the mechanical properties of carbon/carbon composites. *Carbon N. Y.* **41**, 993–999 (2003).
105. Chen, X., Chen, L., Zhang, C., Song, L. & Zhang, D. Three-dimensional needle-punching for composites - A review. *Compos. Part A Appl. Sci. Manuf.* **85**, 12–30 (2016).
106. ASTM-American Society for Testing and Materials. ASTM D3039/D3039M: Standard Test Method for Tensile Properties of Polymer Matrix Composite Materials. *Annu. B. ASTM Stand.* 1–13 (2014). doi:10.1520/D3039
107. Malen, D. E. *Fundamentals of automobile body structure design.* (2011).
108. Ashby, M. *et al.* Materials selection in mechanical design To cite this version : HAL Id : jpa-00251707. **03**, (1993).
109. Hu, X. H., Choi, K. S., Sun, X. & Golovashchenko, S. F. Edge Fracture Prediction of Traditional and Advanced Trimming Processes for AA6111-T4 Sheets. *J. Manuf. Sci. Eng.* **136**, 021016 (2014).
110. Sakurai, T. The Latest Trends in Aluminum Alloy Sheets for Automotive Body Panels. *KOBELCO Technol. Rev.* **28**, 22–28 (2008).
111. Embury, J. D. *et al.* Tensile and bending properties of AA5754 aluminum alloys. *Mater. Sci. Eng. A* **316**, 52–59 (2002).
112. Tamarelli, C. M. The evolving use of advanced high-strength steel for automotive applications. *Steel Mark. Dev. Inst.* 42 (2011). doi:10.1007/s11947-009-0181-3

113. Smerd, R. *et al.* High strain rate tensile testing of automotive aluminum alloy sheet. *Int. J. Impact Eng.* **32**, 541–560 (2006).
114. Huh, H., Kim, S. B., Song, J. H. & Lim, J. H. Dynamic tensile characteristics of TRIP-type and DP-type steel sheets for an auto-body. *Int. J. Mech. Sci.* **50**, 918–931 (2008).
115. Bleck, W., Papaefthymiou, S. & Frehn, A. Microstructure and tensile properties in dual phase and trip steels. *Steel Res. Int.* **75**, 704–710 (2004).
116. Yerra, V. A., Pradeep, S. A., Ozsoy, I. B. & Kothari, A. A systems approach to develop ultra lightweight composite door using fiber reinforced thermoplastics. *SPE ACCE 2018* 1–15 (2018).
117. Park, C., Kan, C. S. & Hollowell, W. T. Investigation of Opportunities for Lightweight Vehicles Using Advanced Plastics and Composites, DOT HS 811 692. (2012).
118. Office of Vehicle Safety Compliance. Laboratory Test Procedure for FMVSS 214S (STATIC) Side Impact Protection. (1992).
119. Herrmann, H. & Bucksch, H. Introduction to Fracture Mechanics David. *Dictionary Geotechnical Engineering/Wörterbuch GeoTechnik* 845–845 (2014). doi:10.1007/978-3-642-41714-6_130817
120. Strumberger, N., Se, D. & Zagreb, F. N. Strumberger, A. Gospocic, C. Bratulic: Polymeric Materials in Automobiles POLYMERIC MATERIALS IN AUTOMOBILES. (2005).
121. Eveno, E. & Gillespie, J. J. Resistance welding of graphite polyether ether ketone composites an experimental investigation. (1988).

122. Dubé, M., Hubert, P., Yousefpour, a. & Denault, J. Resistance welding of thermoplastic composites skin/stringer joints. *Compos. Part A Appl. Sci. Manuf.* **38**, 2541–2552 (2007).
123. Koutras, N., Villegas, I. F. & Benedictus, R. Influence of temperature on the strength of resistance welded glass fibre reinforced PPS joints. *Compos. Part A Appl. Sci. Manuf.* **105**, 57–67 (2018).
124. Xu, X. *et al.* In-situ curing of glass fiber reinforced polymer composites via resistive heating of carbon nanotube films. *Compos. Sci. Technol.* **149**, 20–27 (2017).
125. Of, I., Thermal, C., Polymers, B. O. F., Of, B. & Analysis, D. S. C. Characterization of Polymers using Differential Scanning Calorimetry (DSC) IMPORTANCE OF CHARACTERIZING THERMAL Characterization of Polymers using Differential Scanning Calorimetry (DSC). (2017).
126. Lafranche, E., Krawczak, P., Ciolczyk, J. P. & Maugey, J. Injection moulding of long glass fiber reinforced polyamide 66: Processing conditions/microstructure/flexural properties relationship. *Adv. Polym. Technol.* **24**, 114–131 (2005).
127. Vasanthan, N. Crystallinity determination of nylon 66 by density measurement and fourier transform infrared (FTIR) spectroscopy. *J. Chem. Educ.* **89**, 387–390 (2012).
128. Millot, C., Fillot, L. A., Lame, O., Sotta, P. & Seguela, R. Assessment of polyamide-6 crystallinity by DSC: Temperature dependence of the melting enthalpy. *J. Therm. Anal. Calorim.* **122**, 307–314 (2015).
129. Ageorges, C., Ye, L., Mai, Y.-W. & Hou, M. Characteristics of resistance welding of lap shear coupons. *Compos. Part A Appl. Sci. Manuf.* **29**, 911–919 (1998).

130. Chao, Y. J. Ultimate Strength and Failure Mechanism of Resistance Spot Weld Subjected to Tensile, Shear, or Combined Tensile/Shear Loads. *J. Eng. Mater. Technol.* **125**, 125 (2003).
131. Liebsch, A. *et al.* Adhesion Studies of Thermoplastic Fibre-Plastic Composite Hybrid Components Part 1: Thermoplastic-Thermoplastic-Composites. 68–73 (2018).
132. Suarez, S. A., Gibson, R. F., Sun, C. T. & Chaturvedi, S. K. The influence of fiber length and fiber orientation on damping and stiffness of polymer composite materials. *Exp. Mech.* **26**, 175–184 (1986).
133. ASTM INTERNATIONAL. ASTM D5868 Standard Test Method for Lap Shear Adhesion for Fiber Reinforced Plastic (FRP). *ASTM B. Stand.* **01**, 4–5 (2005).
134. Blackman, B. R. K., Hadavinia, H., Kinloch, A. J., Paraschi, M. & Williams, J. G. The calculation of adhesive fracture energies in mode I: Revisiting the tapered double cantilever beam (TDCB) test. *Eng. Fract. Mech.* **70**, 233–248 (2003).
135. BLACKMAN, B., DEAR, J. P., KINLOCH, A. J. & OSIYEMI, S. The calculation of adhesive fracture energies from double-cantilever beam test specimens. *J. Mater. Sci.* **10**, 253–254 (1991).
136. Whitney, J. M., Browning, C. E. & Hoogsteden, W. A DCB test for characterizing mode I delamination of composite materials. *J. Reinf. Plast. Chem.* **1**, 3–14 (1982).
137. ASTM. D5528-01 2001. Standard Test Method for Mode I Interlaminar Fracture Toughness of Unidirectional Fiber-Reinforced Polymer Matrix Composites. *Am. Soc. Test. Mater.* **01**, 1–12 (2010).

138. Siviour, C. R. & Jordan, J. L. High Strain Rate Mechanics of Polymers: A Review. *J. Dyn. Behav. Mater.* **2**, 15–32 (2016).
139. Reis, J. M. L. *et al.* Analysis of the cyclic tensile behaviour of an elasto-viscoplastic polyamide. *Polym. Test.* **58**, 40–47 (2016).
140. Fleck, N. A., Stronge, W. J. & Liu, J. H. High Strain-Rate Shear Response of Polycarbonate and Polymethyl Methacrylate. *Proc. R. Soc. A Math. Phys. Eng. Sci.* **429**, 459–479 (2006).
141. Wu, S. R. & Cheng, J. Advanced development of explicit FEA in automotive. *Methods* **7825**, (1997).
142. Elices, M., Guinea, G. V., Gómez, J. & Planas, J. The cohesive zone model: advantages, limitations and challenges. *Eng. Fract. Mech.* **69**, 137–163 (2002).
143. Melosh, R. J. Finite Element Analysis of Automobile Structures. *SAE Trans.* **83**, 1341–1355 (1974).
144. Sun, L. *et al.* Application of 1D/3D finite elements coupling for structural. *J. Cent. South Univ. Technol.* **14**, 773–778 (2011).
145. Lanzerath, H., Nowack, N. & Mestres, E. Simulation Tool including Failure for Structural Adhesives in Full-Car Crash Models. *SAE Tech. Pap. Ser. 1*, (2010).
146. RADIOSS THEORY MANUAL 14.0 version-July 2015 Large Displacement Finite Element Analysis. (2015).
147. Pasligh, N., Schilling, R. & Bulla, M. Modeling of Rivets Using a Cohesive Approach for Crash Simulation of Vehicles in RADIOSS. *SAE Int. J. Transp. Saf.* **5**, 208–216

(2017).

148. Jadhav, A. P., Molligan, D., Andersen, S. & John, W. American Society for Composites – 22 nd Annual Technical Conference September 17-19 , 2007 , Seattle , Washington Cover Sheet Title: Effect of Surface Preparation on Environmental Durability of Adhesive-Bonded Metallic Surfaces ASC Technical Division : D. (2007).
149. Powers, D. A. Interaction of Water with Epoxy. *Sandia Natl. Lab.* 1–57 (2009).
150. Highway Traffic Safety Administration, N. & Department of Transportation, U. 2016 Data: Summary of Motor Vehicle Crashes. 1–8 (2016).
151. Gotsch, S. What's Driving Total Loss Frequency? *Certified Collateral Corporation* (2015). Available at: <https://www.cccis.com/2015/11/13/whats-driving-total-loss-frequency/>.
152. Gilabert, F. A. *et al.* Composite Micro-Scale Model Accounting for Debonding , Strain Rate-Dependence and Damage Under Impact Using an Explicit Finite Element Solver. *ECCM17 - 17th Eur. Conf. Compos. Munich, Ger. 26-30th June 2016* 26–30 (2016).